Graphene Quantum Dots: Gaining Control over the Valley Degree of Freedom

Von der Fakultät für Mathematik, Informatik und Naturwissenschaften der

RWTH Aachen University

zur Erlangung des akademischen Grades eines Doktors der Naturwissenschaften genehmigte Dissertation

vorgelegt von

Diplom-Physiker Nils Michael Freitag, MBA

aus Pittsburgh, Pennsylvania, USA

Berichter: Univ.-Prof. Dr. rer. nat. Markus Morgenstern
Univ.-Prof. Dr. sc. ETH Christoph Stampfer

Tag der mündlichen Prüfung: 27.04.2017

Diese Dissertation ist auf den Internetseiten der Universitätsbibliothek online verfügbar.

Contents

1. Introduction **5**

2. Measurement techniques **9**

2.1. Scanning tunneling microscopy and spectroscopy 9

2.1.1. The tunneling effect - revealing the atomic topography 10

2.1.2. Differential conductance spectroscopy 13

2.1.3. Mapping spectroscopy peaks 15

2.2. Transport measurements 18

3. Graphene characteristics **19**

3.1. Atomic lattice, band structure and wave function properties of graphene 20

3.1.1. Density of states 24

3.2. Graphene in an external magnetic field 25

3.3. Si/SiO_2 and hexagonal BN substrates 27

3.4. Graphene sample preparation 29

3.5. Superstructure of commensurate graphene on hexagonal boron nitride . . 30

3.5.1. Limits of the density functional theory results 35

3.5.2. Investigating the density of states at zero magnetic field 36

3.5.3. Conclusion 42

4. Quantum dots in graphene **44**

4.1. Quantum dot terminology 45

4.2. Klein tunneling and electrostatic confinement in graphene 49

4.3. Confinement in gapped graphene 51

4.3.1. Patterned QDs 52

4.3.2. Bilayer graphene gapped by electric displacement fields 54

4.3.3. QD eigenstates in a large magnetic field 56

5. Tip-induced quantum dots in commensurate graphene on hBN **59**
5.1. The Coulomb staircase 61
5.1.1. Signature Coulomb peak sequence of an ideal graphene QD 64
5.2. Poisson calculations 65
5.2.1. Tip-induced potential in graphene 66
5.2.2. Coupling of the quantum dot to the other electrodes 68
5.3. Tight binding model 70
5.3.1. Assigning a valley to the TB wave functions 74
5.4. Spectroscopy at finite magnetic field 75
5.4.1. Onset of charging peaks 76
5.4.2. Capturing the influence of the graphene superstructure on orbital and valley splittings 79
5.4.3. Possible observation of local valley anti-crossings 83
5.4.4. Identification of defect charging peaks 85
5.4.5. Discussion of Landau level features in spectroscopy 86
5.5. Conclusion and transport device considerations 89

6. Graphene nanostructures produced by local anodic oxidation **92**
6.1. Preparation of nanostructures 95
6.2. Graphene ring structures 98
6.3. Coulomb blockade in a structured quantum dot 103
6.4. Conclusion 107

7. Summary **109**

8. Acknowlegements **111**

A. Appendix **113**

Bibliography **119**

List of Acronyms

2DES	two-dimensional electron system
AB	Aharonov-Bohm
ABR	Aharonov-Bohm ring
AFM	atomic force microscope (microscopy)
BLG	bilayer graphene
BZ	Brillouin zone
CP	charging peak
CVD	chemical vapor deposition
DCP	defect charging peak
DFT	density functional theory
DOS	density of states
DP	Dirac point
EBL	electron beam lithography
FFT	fast Fourier transform
FQHE	fractional quantum Hall effect
FWHM	full width at half maximum
GGA	generalized gradient approximation
GNR	graphene nanoribbon
GO	graphene oxide
GR	graphene ring
LAO	local anodic oxidation
LDA	local density approximation
LDOS	local density of states
MLG	monolayer graphene
QD	quantum dot
QHE	quantum Hall effect
RIE	reactive ion etching
RPA	random phase approximation
SDP	secondary Dirac point
SL	superlattice
SPM	scanning probe microscopy
SSB	sublattice symmetry breaking
STM	scanning tunneling microscope (microscopy)
STS	scanning tunneling spectroscopy
TB	tight binding
TEM	transmission electron microscopy
UCF	universal conductance fluctuation
UHV	ultra high vacuum
VHS	van Hove singularity
WGM	whispering gallery mode

1. Introduction

Semiconductor electronics are driving a huge development in information technology towards omnipresent digitization since the realization of the first transistor in 1947.[1,2] The discovery of graphene[3] in 2004 added a new candidate to the pool of materials competing to improve key properties of micro- and nano-electronic devices on the quest to continuously become faster, dissipate less power per active unit and require less space, also known as Moore's law.[4] Only one atomic layer thick, graphene embodies the ultimate size reduction in one dimension while combining high mechanical flexibility and strength (Young's modulus of 1 TPa)[5] with high electrical conductivity and comparatively low optical absorption (about 2.3 %).[6] Flexible electronics and conductive composite materials were among commonly proposed applications.[7–9] Being an all-surface material, graphene's environment strongly impacts its properties. This severely limited device homogeneity and required to transfer graphene from Si/SiO_2 to a better-suited substrate like hexagonal boron nitride (hBN) to achieve ballistic transport on the few 10 µm scale.[10] On the other hand, sensor applications become very appealing. For instance, sensitive Hall measurements allow to determine magnetic field strengths with much higher accuracy than before.[11] Exploration of the properties of graphene has kindled interest in other 2D crystals like dichalcogenides or layered oxides and their heterostructures.[8,9,12]

Graphene also remains highly interesting from a fundamental perspective. Opposed to other two-dimensional electron systems (2DES) realized in semiconductor heterostructures, graphene grants direct access to basically all scanning probe microsocopy (SPM) techniques. Especially scanning tunneling microscopy (STM) and spectroscopy (STS) on 2DESs has been limited for instance, to those induced by surface doping of n-InAs(110)[13] or n-InSb(110)[14] by Cs. The inherent disorder poses limits on the observation of delicate quantum phase transitions like the fractional quantum Hall effect (FQHE).[15] In principle, graphene could be the key to capture the local nature of these effects. The charge carriers in graphene are quasiparticles that behave as chiral fermions, which are additionally free of rest mass, a property usually encountered for elementary particles such

as photons and neutrinos. In graphene, the chiral property is not the spin, but the sublattice degree of freedom. The electrons in graphene come with an additional degree of freedom which is also formally analogous to the physical spin, called *valley pseudospin*. In this unique disguise, graphene's charge carriers enrich the physics of, for instance, the quantum hall effect (QHE)[16–19] or localization in 2D.[20–22] Moreover, graphene has been called a tabletop test environment for high energy physics,[7,18] since its effective fine structure constant is three orders of magnitude larger[23–26] than in quantum electrodynamics. Therefore experiments mimicking hardly attainable settings in the context of astro, relativistic particle or nuclear physics become tangible. For instance, the large magnetic fields of white dwarfs,[27–29] neutrino oscillations,[30] Zitterbewegung,[31–33] Klein tunneling[34,35] and the atomic collapse in case of supercritical charge[36–40] have been the subject of proposals or conducted experiments.

Graphene has also sparked some enthusiasm in the quantum computing community. Quantum bits (qubits) are the primitive building blocks of quantum computers. In principle, they can solve certain problems much more efficiently, popular examples being prime factoring[41] and searching in unsorted data.[42] There has been significant progress on, for instance, qubits in superconductors.[43–46] Graphene presents a promising host material for spin qubits, which have been intensively researched in III-V semiconductor heterostructures like GaAs/AlGaAs.[47–49] There, strong hyperfine and spin-orbit interaction limit spin coherence times,[50,51] though nuclear spin bath polarization[52] results in times exceeding 200 µs and tailored gate sequences[53] provide some additional counteraction. On the other hand, graphene's carbon is a light element creating negligible spin-orbit interaction.[54,55] Graphene can also be grown from an isotopically purified ^{12}C source, thereby eliminating the about 1.1 % of ^{13}C atoms carrying nuclear spins in natural carbon.[56,57] This leads to expected spin decoherence times limited by phonon-mediated spin relaxation in the range of milliseconds.[58–61] The same objective is also pursued by using group IV host materials like Si and Ge and prototype qubits have been demonstrated.[62,63] Here, one of the drawbacks is the requirement to lift the additional valley degree of freedom. Though this is also an issue in graphene, controlling the valley pseudospin also offers the possibility to operate qubits within the valley space. Again, long coherence times on the order of milliseconds are expected.[64] On paper, graphene's properties look quite promising. However, the challenge of creating well-defined QDs which allow their exploitation remains.

The aforementioned Klein tunneling renders purely electrostatic confinement in mono-

layer graphene difficult. Hence, imposing physical boundaries and thus gaps due to size quantization by carving out nanostructures from pristine graphene sheets appeared as appealing solution, because the existent tool-box of semiconductor nanostructuring techniques could be applied. However, graphene's surface sensitivity makes it highly susceptible to lithography process residues. As the latter also hamper the investigation of graphene by STM, I explored an alternative resist-free patterning technique (chap. 6): local anodic oxidation (LAO). A negatively biased metallic tip of an atomic force microscope (AFM) dissociates water molecules in the water meniscus forming between tip and sample under ambient conditions. Moving the tip thus allows writing arbitrary oxide patterns on the sample surface. LAO was previously employed to create nanostructures in, for instance, GaAs/AlGaAs heterostructures.[65,66] I successfully structured graphene rings and QDs, while the defining cuts can be as narrow as 10-15 nm and no structural change is observed for the rest of the flake. However LAO, like most other lithography techniques, lacks control over the generated atomic edge configuration. The disordered edges of patterned graphene devices have been identified as the main source of uncontrolled charge localization and thus crucial limitation to device performance.[67] Hence, I did not observe Aharonov-Bohm oscillations and the measurements on the QD were limited to Coulomb blockade physics without the regular substructure of excited states, alike most of the literature.[67]

Looking for an alternative approach to confine Dirac electrons, inducing band gaps by an external magnetic field seems appealing. At a moderate field of $B = 2\,\mathrm{T}$ the first Landau gap in graphene already reaches a comparatively large value of about 50 meV. Adding a gate-induced band bending then allows to confine electrons in QDs without physical edges. Since the potential disorder needs to be smaller than the gap size, I investigate a graphene flake transferred to hBN. The great advantage of using an STM tip-induced confinement potential is its maneuverability, such that the QD can, for instance, also be used as a local probe.[68,69] Transport measurements on the LAO structured QD exhibit an irregular charging peak sequence with addition energies of $3-4\,\mathrm{meV}$. Measuring the Coulomb staircase in the tip-induced QDs by means of STS reveals addition energies of $10-20\,\mathrm{meV}$ at 7 T and a preferential grouping of Coulomb peaks in quadruplets (chap. 5). This footprint of a sequence of well-defined orbital QD states shows that the QD energy level spectrum exhibits large and regular orbital splittings which separate quadruplets of QD states. Their additional spin-valley substructure manifests itself as separation of quadruplets into doublets, while the experiments find

the impact of the valley splittings to dominate over the Zeeman splitting in accordance with theoretical expectations.

I characterize the QDs by utilizing the two main tuning knobs of my experiment: the external magnetic field and the position of the induced QD within the superstructure of commensurate graphene on hBN (13.8 nm periodicity). Varying the magnetic field reveals the onset of confinement between $1 - 2\,\mathrm{T}$ and Landau levels (LLs) with non-zero index as the origin of the confined electron and hole states. The QD wave functions inherit a peculiar property of the bulk LL wave functions, as exchanging the valley index for a particular orbital state corresponds to swapping the wave function amplitudes between the two sublattices. Thus, moving the trapped electrons across the sample and subjecting them to a substrate-induced breaking of the local sublattice symmetry directly effects the magnitude of the observed valley splittings. The STM allows to map the QD properties, thereby uncovering signatures of local avoided valley crossings and a tunability of the valley splitting beyond 7 meV on the scale of 10 nm. These values surpass the highest reported values for any potentially nuclear spin free host material by more than one order of magnitude (Si/SiO_2, $500\,\mu\mathrm{eV}$).[70] On the one hand, these controlled valley splittings show a road toward spin qubits in graphene. On the other hand, these findings may be seen in analogy to singlet-triplet transitions in spin qubits subjected to local magnetic field gradients,[71,72] thus allowing to harness the valley or a combination of spin and valley degree of freedom in novel graphene quantum devices.

2. Measurement techniques

Before getting involved with the physics of graphene quantum dots, it is mandatory to discuss the employed probing techniques and a specially developed data analysis method for spectroscopy series, which was key to identify spatial variations in the quantum dot's addition energy spectrum. Therefore, this chapter reviews the principles of STM and STS (sec. 2.1), describes a peak tracing algorithm developed to map peak energies in STS series (sec. 2.1.3) and briefly states details relevant to the conducted transport measurements (sec. 2.2).

2.1. Scanning tunneling microscopy and spectroscopy

Gaining insight on the electronic structure of solids on the nanometer scale contributes immensely to the fundamental understanding of many physical phenomena. In 1982, the invention of the STM by Binning and Rohrer,[73,74] in this sense, started a new era in surface science research. The addition of the atomic force microscope (AFM) five years later[75] further extended the capabilities in the growing field of SPM. While the early measurements were concerned with imaging the atomic topography,[76] nowadays STS providing spectroscopic information of the local density of states (LDOS) with atomic resolution is the main focus. It is the key to delve into effects like superconductivity, the Kondo-effect, the QHE[16,17] or supercritical charge.[40] Other applications range from single atom manipulation,[77,78] imaging of chemical reactions[79,80] or differing spin populations[81,82] to time-resolved measurements on the sub ns scale.[83–85] Many experiments have to be conducted in a controlled environment at low temperatures, since contamination of the sample surface and thermal activation either limit the observation or undermine the formation of the sought-after state. Therefore, STMs are often integrated into ultra-high vacuum (UHV, i.e., $p < 1 \times 10^{-9}\,\mathrm{mbar}$) low temperature (down to $T = 10\,\mathrm{mK}$)[86] systems.

Our home-built STM setup[87] utilizes liquid helium as cooling agent ($T \approx 4.2\,\mathrm{K}$) and a pressure of $p \approx 1 \times 10^{-10}\,\mathrm{mbar}$. The STM's base temperature is $T \approx 8\,\mathrm{K}$ due to the heat load of additional wiring required to fit a high-frequency compatible STM unit.[85] Additionally, the setup allows to apply a $|B| \leq 7\,\mathrm{T}$ field perpendicular to the sample surface as well as smaller in-plane magnetic fields in both directions (3 T, 1 T). In the following I will address the main concepts behind STM and STS. Readers seeking a broader introduction should consider Refs. [88, 89].

2.1.1. The tunneling effect - revealing the atomic topography

Electron tunneling is one of the most basic concepts in quantum mechanics. In STM, we consider an electronic tip and sample state at energy ε with wave functions Ψ_{tip} and Ψ_{s}, respectively. They are separated by a potential barrier of width Z and height $\bar{\Phi} \approx (\Phi_{\mathrm{tip}}+\Phi_{\mathrm{s}})/2$, where Φ_{tip} and Φ_{s} are the work function of tip and sample, respectively. Both states will decay exponentially inside the barrier, but if it is narrow enough (i.e., a couple of Å) both states will have a finite overlap and electrons can tunnel between Ψ_{tip} and Ψ_{s}. The corresponding transmission probability in WKB approximation to first order[90] is $T \propto e^{-2\kappa Z}$, with the inverse decay length

$$\kappa = \sqrt{\frac{2m_e}{\hbar^2}\left(\Phi_{\mathrm{eff}} - \varepsilon\right)}\,, \tag{2.1}$$

where $\Phi_{\mathrm{eff}} = \bar{\Phi}+eV_{\mathrm{tip}}/2$ captures the impact of an applied tip voltage V_{tip} on the effective barrier height. T governs the tunneling current[90]

$$I = \int_0^{eV_{\mathrm{tip}}} \rho_{\mathrm{s}}(\boldsymbol{r},\varepsilon)\,\rho_{\mathrm{tip}}(\boldsymbol{r},\mp eV_{\mathrm{tip}} \pm \varepsilon)\,T(\varepsilon, eV_{\mathrm{tip}}, \boldsymbol{r})\,d\varepsilon \tag{2.2}$$

at the location $\mathbf{r}$ of the tip with respect to the sample. Here, one assumes elastic tunneling at $V_{\mathrm{tip}} \ll \Phi_{\mathrm{eff}}/e$. The LDOS of tip ρ_{tip} and sample ρ_{s} in between their electrochemical potentials μ_{tip} and μ_{s}, that is, within the bias window $eV_{\mathrm{tip}} = \mu_{\mathrm{tip}} - \mu_{\mathrm{s}}$, carry I (blue arrows in Fig. 2.1). The upper and lower signs in the argument of ρ_{tip} correspond to $\mu_{\mathrm{tip}} > \mu_{\mathrm{s}}$ (i.e., $V_{\mathrm{tip}} < 0$, Fig. 2.1a) and $\mu_{\mathrm{tip}} < \mu_{\mathrm{s}}$ (i.e., $V_{\mathrm{tip}} > 0$, Fig. 2.1b), respectively. States in the upper part of the bias window contribute more strongly to I since the barrier is lower for them. Tersoff and Hamann[91,92] amended the one-dimensional model to treat elastic tunneling in three dimensions more accurately by

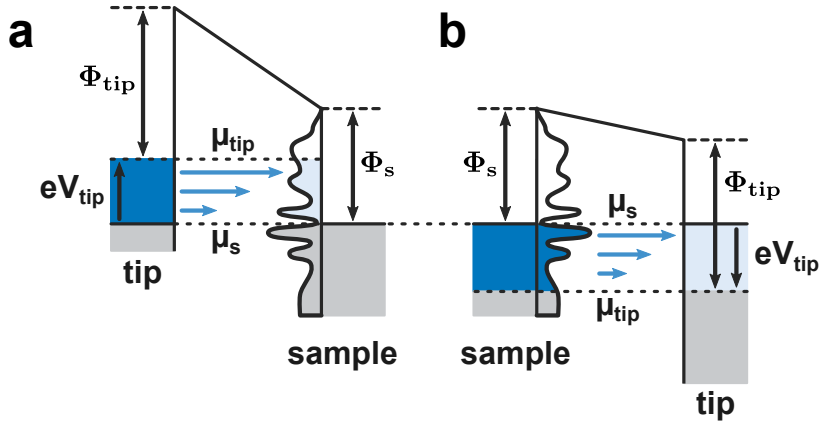


Figure 2.1.: **Energy diagram for tunneling between an STM tip and a sample.** Work function of tip Φ_{tip} and sample Φ_{s} marked by double arrows. Gray, blue or white filled areas depict DOS of tip (assumed flat) and sample, as labeled at the bottom. Applied tip voltage V_{tip} (black vertical arrow) opens a bias window between the electrochemical potentials of tip μ_{tip} and sample μ_{s} (black dotted lines). Electrons from occupied states (dark blue filled areas) can tunnel (light blue arrows) into available unoccupied states of the other electrode (light blue filled areas). **(a)** For $\mu_{\mathrm{tip}} > \mu_{\mathrm{s}}$, electrons tunnel from the tip to the sample. **(b)** For $\mu_{\mathrm{tip}} < \mu_{\mathrm{s}}$, electrons tunnel from the sample to the tip.

incorporating an *s*-type tip orbital (e.g., Au tips). Many metallic tips like Tungsten or Pt/Ir tips, however, tunnel also via *p* or *d* orbitals close to μ_{tip}, which show higher spatial resolution. Here, Chen found an elegant description based on different order derivatives of the orbital wave functions leading to adjusted κ values.[93–95] Fortunately, I (eq 2.2) retains its general structure and is sufficient to discuss the features in my experiments.

The exponential dependency of T and thus I on Z, that is, the tip-sample separation, is the great trump when designing a feedback loop to navigate the STM tip with subatomic precision relative to the sample. In constant current mode, a local variation of ρ_{s} within the bias window will be compensated by a counteracting Z shift of the tip, issued by the piezo-motors. Rastering the tip across the sample and logging Z will thus produce a map of the integrated LDOS within the bias window. Since the LDOS is strongly correlated with the atomic positions, this explains referring to such images as the *topography*. Figure 2.2 portrays two examples recorded on graphene on hBN (panel a) and Au(111) showing the typical *heringbone* surface reconstruction[96] (panel b).

Moreover, $I(Z)$ curves allow to sensitively crosscheck the tip-sample interaction. Ideally, $\Phi_{\mathrm{eff}} \approx 5\,\mathrm{eV}$ is the only free parameter and thus $2\kappa \approx 2.3\ \mathrm{\AA}^{-1}$ (eq 2.1). If the decay is significantly stronger (i.e., $2\kappa > 2.3\ \mathrm{\AA}^{-1}$), attractive forces between tip and sample

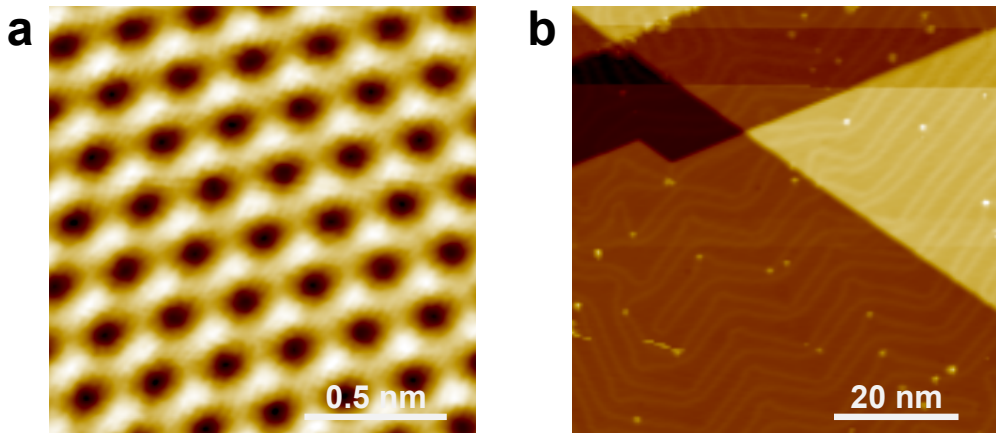


Figure 2.2.: **Exemplary constant-current STM images of graphene and Au(111).** **(a)** Atomically resolved $1.5 \times 1.5\,\mathrm{nm}^2$ STM image of graphene on hBN taken at $T = 8\,\mathrm{K}$. Bright dots stem from one atomic sublattice of the graphene honeycombs. $V_{\mathrm{tip}} = 300\,\mathrm{mV}$, $I = 300\,\mathrm{pA}$. **(b)** STM image of a Au(111) surface with different terraces featuring the fcc-hcp *heringbone* reconstruction[96] (parallel brighter lines). Darker stripe at the top due to tip change. Image recorded at $V_{\mathrm{tip}} = 480\,\mathrm{mV}$, $I = 300\,\mathrm{pA}$.

reduce the effective Z by deforming the tip and/or sample. Since graphene easily buckles and is not strongly attached to its usually insulating substrates, lifting of the sample is expected to dominate in this case.[29]

Finally I want to briefly address the tip preparation. First, tungsten tips were prepared by microchemical etching of wires. The microtips were then reshaped by controlled indentation into the surface of a Au(111) crystal,[97] thereby forming a Au apex of a few 10 nm in length. Typically $V_{\mathrm{tip}} = 9\,\mathrm{V}$ during the procedure and thus $I \approx 8\,\mathrm{mA}$ due to an additional $1\,\mathrm{k}\Omega$ resistor in series. I then check $I(Z)$ curves and characterize the tips by exploiting the topographic and spectroscopic features of the Au(111) surface reconstruction.[96]

2.1.2. Differential conductance spectroscopy

Starting from the tunneling current in eq 2.2, we can derive the contributions to the differential conductance[89]

$$\frac{dI}{dV_{\mathrm{tip}}} \propto e\rho_{\mathrm{tip}}(0)\rho_{\mathrm{s}}(eV_{\mathrm{tip}})T(eV_{\mathrm{tip}}, V_{\mathrm{tip}}) \tag{2.3}$$

$$+ \int_0^{eV_{\mathrm{tip}}} \frac{\partial\rho_{\mathrm{tip}}(\varepsilon - eV_{\mathrm{tip}})}{\partial V_{\mathrm{tip}}}\rho_{\mathrm{s}}(\varepsilon)T(\varepsilon, V_{\mathrm{tip}})d\varepsilon \tag{2.4}$$

$$+ \int_0^{eV_{\mathrm{tip}}} \rho_{\mathrm{tip}}(\varepsilon - eV_{\mathrm{tip}})\rho_{\mathrm{s}}(\varepsilon)\frac{\partial T(\varepsilon, V_{\mathrm{tip}})}{\partial V_{\mathrm{tip}}}d\varepsilon \tag{2.5}$$

for the case $V_{\mathrm{tip}} < 0$. As ρ_{tip} is favorably featureless, the second term is neglected. The reduction of the barrier height with increasing V_{tip} enters in the third term. It produces an exponential background to the LDOS features of the sample in the first term. Thus focusing on the dI/dV modulation reveals the structure of ρ_{s}. However, this assumes V_{tip} does not alter ρ_{s}. For instance, a tip-induced band bending will modify the position of ρ_{s} with respect to μ_{s}, thus, for instance, states dropping out of the bias window would cause additional dips in dI/dV. Moreover, charging of a tip-induced QD also shifts ρ_{s} relative to the bias window giving rise to Coulomb peaks in dI/dV (see sec. 5.1). Essentially, the modulation of the dI/dV signal can have other sources than a variation of ρ_{s} at μ_{tip} while sweeping V_{tip}.

Practically, the dI/dV spectra are measured by lock-in detection of the tunneling current change due to adding a sinusoidal modulation V_{mod} to V_{tip}. In this thesis, I use a frequency of $f_{\mathrm{mod}} = 1223\,\mathrm{Hz}$ and amplitudes of $2 - 7.3\,\mathrm{mV_{rms}}$ for that purpose. In measurements of QD charging sequences, I optimized V_{mod} for well separated charging peaks at maximum signal-to-noise ratio. Prior to sweeping V_{tip} for every spectrum, the tip is stabilized at the stabilization voltage V_{stab} and current I_{stab}. Then the feedback loop is switched off for the acquisition of the $I(V_{\mathrm{tip}})$ and $dI/dV(V_{\mathrm{tip}})$ spectrum. Whenever I plot $(dI/dV)/I_0$, I divide every point of the dI/dV spectrum by the first current value I_0 of the measured $I(V)$ curve. This normalization compensates small remaining variations in tip-sample distance after stabilization, which are due to inherently imperfect feedback loop operation or residual mechanical noise.

Compared to usual dI/dV measurements, where the tip-sample distance is kept constant after stabilization (fixed-Z mode), the tip slightly approaches the sample at a rate

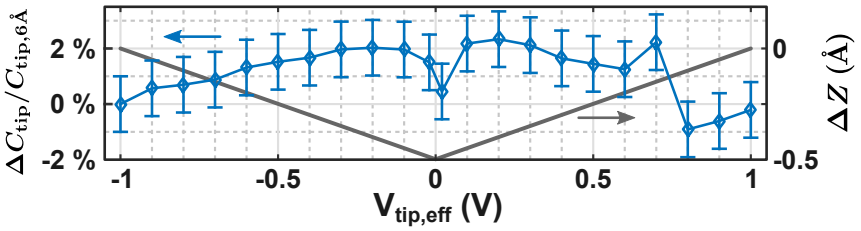


Figure 2.3.: **Change in capacitance between tip and tip-induced graphene QD in the varied-Z mode.** Relative change of the tip to dot capacitance $\Delta C_{\mathrm{tip}} = C_{\mathrm{tip,VarZ}} - C_{\mathrm{tip,6Å}}$ with respect to the capacitance $C_{\mathrm{tip,6Å}}$ at a fixed tip-sample separation $Z = 6$ Å. During the varied-Z spectroscopy, the tip approaches at a rate of 0.5 Å/V. Poisson calculation conducted for a tip radius of $r_{\mathrm{tip}} = 120\,\mathrm{nm}$ and a dot radius of $r_{\mathrm{dot}} = 25\,\mathrm{nm}$. $V_{\mathrm{tip,eff}}$ denotes the applied tip voltage. The error bars reflect the convergence criterion of the Poisson solver concerning the iteration-by-iteration threshold in the change of the induced charge, which is used to calculate the capacitance. More details in section 5.2.

of 50 pm/V in the varied-Z mode. Thus the tip approaches the sample by $\Delta Z = 0.5$ Å while sweeping the voltage from 1 V to 0 V and retracts the same distance while continuing to sweep to -1 V. This increases the dynamic range of the differential conductivity, that is, the visibility of features for small V_{tip} improves, since the increasing barrier height is counteracted by a smaller Z keeping T roughly constant. In turn, graphene's linear density of states (at 0 T) will not appear in its usual 'V-shape' in dI/dV, but comparatively flat. The additionally ensued change in tip to sample capacitance, derived from my Poisson-solver results and shown in Figure 2.3, amounts to below 2.5 %. It was thus neglected in the analysis of the tip-induced QD (chap. 5), since the capacitance uncertainty due to the uncertainty in tip radius is larger (Fig. 5.7).

Generally, V_{mod} will impact the energy resolution of the experiment, which can be expressed by[98]

$$\Delta E \approx \sqrt{(3.3 k_{\mathrm{B}} T)^2 + (2.5 e V_{\mathrm{mod}})^2}\,, \tag{2.6}$$

where the first term is due to thermal broadening of the Fermi distribution. Consequently, the reduction of both, temperature and V_{mod}, aids achieving higher energy resolution. Additionally, if the signal-to-noise ratio and the acquisition time do not pose obstacles, one should aim for $eV_{\mathrm{mod}} \approx k_{\mathrm{B}}T$. Especially the time for a spectroscopy series often is limited due to the sheer number of spectra. For instance, recording 60×60 spectra with 1000 points resolution in voltage and a raster time of 10 ms (Lock-In integration time 3 ms) requires a total of about 10 hours. Significantly increasing the energy resolution thus costs several more hours, which always has to be weighted with

the setup's stability concerning, for instance, (thermal) drift.

2.1.3. Mapping spectroscopy peaks

In many settings, it is highly insightful to locally trace the energy of electronic states. Their footprint in STS are peaks, which can also be generated by charging of localized states[68,99,100] and various measurement artifacts, for instance, mechanical noise. While a human is generally well suited to weed out erroneous peaks and identify the same peak in different dI/dV spectra, this task becomes impossible to handle manually with increasing spatial resolution, that is, number of spectra collected on a fine grid. For instance, more than half a million peaks had to be processed in the one spectroscopy series portrayed in section 5.4.2.

Hence, I trained an army of monkeys[1] to do the job. They operate on an algorithm which I devised to mimic the human ability to identify errors in an image. There are two main assumptions behind the algorithm. First, the position of the peaks changes smoothly and more or less uniformly across the sample, that is, it is possible to define a sensible maximum pixel-by-pixel variation δ_{px}. Second, the peak sequence is generally well ordered across the sample, that is, numbering the peaks going from zero towards higher $|V_{\mathrm{tip}}|$ is a good first approximation for the finally determined index. The following description omits many of the details in favor of a comprehensive overview of the key properties.

Prior to applying the algorithm, the relevant peaks have to be identified. Figure 2.4 shows the different stages of the process. For every spectrum of an STS series ($N \times N$ grid), a peak finder (simple first order criterium based) identifies peaks, which are then fitted by a Gaussian to extract their position and FWHM. The resulting peak list is then filtered based on certain *cut criteria*: (i) the peaks have to be within a certain V_{tip} interval, (ii) their FWHM needs to be within a certain interval (i.e., $10 - 20\,\mathrm{mV}$), (iii) consecutive peaks need to have a minimum spacing (i.e., $15\,\mathrm{mV}$). The cropped peaks are saved as backup in a *category B* peak matrix. The peaks which pass make up the $N \times N \times L$ *category A* peak matrix, where the third dimension corresponds to the peak index l. Every $N \times N \times 1$ matrix layer corresponds to an initial peak map. Single pixel within the map are identified by their coordinates (m,n).

We now unleash the algorithm, starting with $l = 1$. The peak map will contain

[1] The semiconductor transistor breed commanded by MATLAB.

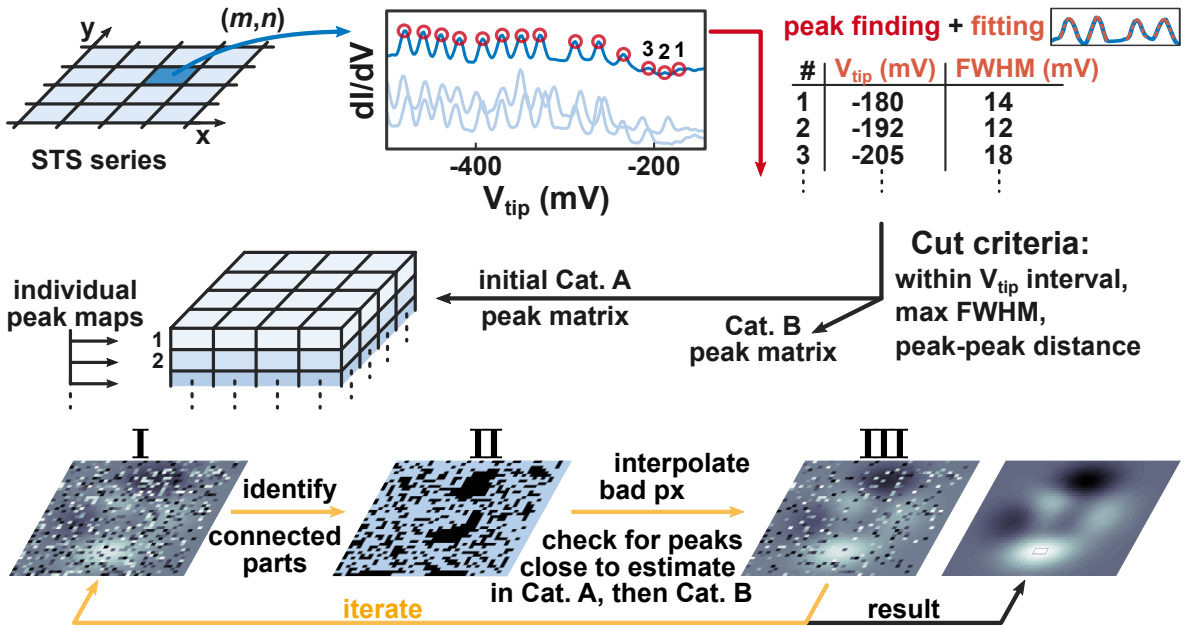


Figure 2.4.: **Flow diagram of the peak tracing algorithm.** First row: For every spectrum of an STS series a peak list is generated by a peak fitting procedure (examples in the top right box). Every spectrum is identified by its coordinates (m, n) within the grid. Second row: The peak lists are filtered according to the shown cut criteria to create the peak matrices category A and B. The first serves as starting point for the algorithm. Third row: The images **I**,**II** and **III** showcase a generated initial peak map, identified connected (blue area) as well as erroneous parts (black px, actual result found by the algorithm) and the peak map after replacing some erroneous px, respectively. The last image represents the ideal final map.

numerous erroneous pixel, as showcased for the image marked **I** in Figure 2.4. Besides the quality of the spectra, this depends on the cut criteria and can be in excess of 50 % of all px. Nonetheless, it is possible to identify smoothly connected areas by naked eye. The algorithm starts with a pixel which is smoothly connected to at least three of its neighbors, that is, the top, bottom, left and right pixel are no more than δ_{px} away (typically $\delta_{\mathrm{px}} \approx 5\,\mathrm{mV}$). Then it adds all neighboring pixel within δ_{px} to this initial patch and iterates this process. Figuratively speaking: A wetting layer of height δ_{px} spreads from the starting point and all dry points are called disconnected. If there are no more connected neighbors and a significant portion of the image has not been analyzed (i.e., 10 %), the algorithm selects a new appropriate starting pixel and continues. Finding multiple isolated patches is actually typical. Too small patches are also ignored. The result of applying this procedure to image **I** is marked **II** in Figure 2.4. We see, a large fraction of the intact image is successfully identified (light blue area).

In the next step, the algorithm tries to find substitutions for the erroneous pixel. First it generates an estimate for every pixel by interpolation from the correct pixel. If the present peak position lies within a certain interval of this estimate, the peak remains in category A. If not, the algorithm first looks for a replacement in category A at higher l, that is, the peak finder possibly identified peaks prior to the desired sequence. If it is successful at some higher index $l = l_\mathrm{r}$, all peaks in the peak list at (m,n) with $l < l_\mathrm{r}$ will be moved to category B and the peaks with $l \geq l_\mathrm{r}$ move down in index, that is, $l \to l - l_\mathrm{r} + 1$. Otherwise, category B at (m,n) is searched and, if found, the peak in the map is exchanged with the match from category B. In case no alternative peak can be found a token is inserted and all l in the list at (m,n) are incremented by one assuming the spectrum lacks an adequate peak. Note that by fixing the peak map with $l = 1$ we actually improve all maps with higher l whenever a peak sequence at some (m,n) moves up or down.

After this first round of replacements, we have to address those error pixel which are not detected by the 'wetting layer' approach. For instance, let us consider the analog of a screw dislocation in a crystal. There, the layer index of two specific neighboring atoms differs by one and the burgers vector appears similar to a helix or the threads of a screw. Here, we find two neighboring pixel which are more than δ_px apart, but we can find a smooth path connecting the two pixel which circles around the step. However, the map will still look discontinuous at least for these two pixel. I employ different median and gradient filters to identify these pixel. Then the same replacement procedure as stated above is performed. Eventually, this completes one full replacement iteration (we have reached image **III** in Fig. 2.4) and the algorithm starts over. If no pixel was replaced during the last iteration, the peak map with index l is final and the algorithm moves on to map $l + 1$.

The final peak matrix allows to investigate local changes in single peak energies as well es peak splittings. Actually, any property of such a peak becomes mappable, for instance, the life time of a state via the peak's FWHM. While I will investigate charging peak sequences of a tip-induced QD (chap. 5), Landau level spectroscopy, local variations in spin splittings, or a superconducting gap could also be interesting applications. Generally, whenever using a peak finder and defining a certain interval is not enough, for instance, due to occasionally recorded error peaks, the algorithm should prove beneficial. Of course the effectiveness of the algorithm depends on choosing appropriate parameters. Fortunately, evaluating a couple of exemplary spectra is usually sufficient

to find sensible boundaries for peak spacings, the FWHM and δ_{px}, which is obviously sensitive to the experimental resolution. The algorithm is surprisingly fault tolerant, that is, it can deal with significantly more than 50 % erroneous pixel in the first map. Hence, one should try weakening the cut criteria to include more potential peaks, if too many pixel remain blank in the final peak maps. The algorithm is applicable to any problem where peak positions or, more generally, some quantities vary smoothly in a 2D space. However, peaks which only occur in a part of this space, cross or split are so far difficult to deal with. The resulting artifacts in the maps are on the one hand undesired, but, on the other, may also provide important clues.

2.2. Transport measurements

All transport measurements were carried out in a ^{3}He-bath cryostat, which is described in detail in Ref. [101]. It provides a base temperature of $T \leq 290\,\mathrm{mK}$ and a maximum magnetic field of $B = 10\,\mathrm{T}$. A total of 24 contacts can be separately connected via a connector box on the top of the insert. All contacts can be grounded, floated or low-pass filtered (cutoff frequency $f_{\mathrm{c}} = 1\,\mathrm{kHz}$) individually.

Measurements in 2-point geometry were carried out in two ways. Firstly, a constant current source was used to drive a current I through the sample. It is connected to two BNC sockets of the connector box and additionally the voltage V between these two sockets is measured by a voltmeter (*34401A*, Agilent) via two T adapters. Ohm's law $R = V/I$ then yields the total resistance of the circuit including that of the sample, the contacts and the wiring. The second method utilizes home-built symmetric I-V converters. They apply a DC and/or AC source-drain voltage V_{SD} to the sample, which is divided by a factor of 10^2 and 10^4, respectively, on the input side. The I-V converters directly output the resulting current with a chosen gain of $10^5 \ldots 10^{10}\,\mathrm{V/A}$. A Lock-In amplifier (*SR830*, Stanford Research Systems) provides the AC signal ($f < 100\,\mathrm{Hz}$), while all DC signals, including gate voltages, are applied by highly stable voltage sources (*7651*, Yokogawa). DC outputs are fed to voltmeters after being low-pass filtered ($f_{\mathrm{c}} = 3\,\mathrm{Hz}$), while the differential conductance dI/dV is extracted by a Lock-In amplifier from the raw signal.

3. Graphene characteristics

This chapter has been published in parts in:

Electrostatically Confined Monolayer Graphene Quantum Dots with Orbital and Valley Splittings
N. M. Freitag, L. A. Chizhova, P. Nemes-Incze, C. R. Woods, R. V. Gorbachev, Y. Cao, A. K. Geim, K. S. Novoselov, J. Burgdörfer, F. Libisch, M. Morgenstern
Nano Letters **2016**, *16*, 5798-5805
© 2016 American Chemical Society

In 2004, the isolation of a single layer of graphite, now known as graphene,[3] came as a surprise, in part because the Mermin-Wagner theorem[102] doomed it and any purely two-dimensional crystal unstable. Before its discovery, many of its properties were already investigated, since it had served as starting point in the theoretical description of graphite[103,104] and carbon nanotubes.[105] As showcased in the introduction, graphene has many strong traits with respect to mechanical, optical or electrical applications, while also offering intriguing insight on more fundamental phenomena.

This chapter captures the main properties of graphene related to my experiments. Broader treatises on the subject are found in Refs. [26, 106, 107]. In section 3.1, I will start out with the crystal lattice of monolayer graphene (MLG) and deal with the resulting wave functions, band structure and density of states (DOS). The application of a strong external magnetic field significantly changes these properties (sec. 3.2), which will be key to localize charge carriers as portrayed in chapter 5. I will also discuss Si/SiO_2 and hexagonal boron nitride (hBN) substrates (sec. 3.3), since the properties of actual graphene devices crucially depend on their interaction with their immediate environment. Though this is often the limiting factor for device homogeneity, it also allows to introduce a new periodicity to the system by aligning the crystal lattices of graphene and the substrate. The appropriate graphene sample preparation techniques are addressed in

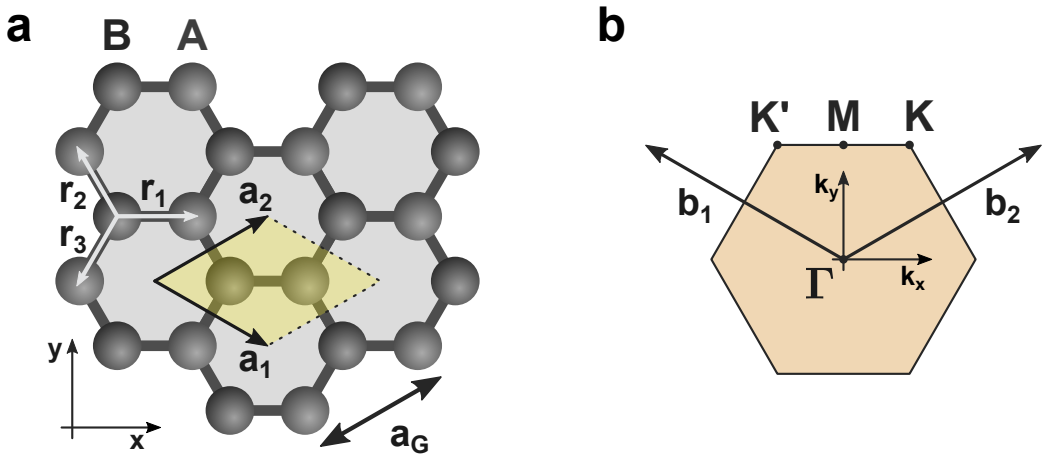


Figure 3.1.: **Crystal lattice and first Brillouin zone of graphene.** **(a)** Honeycomb lattice structure of graphene: sublattices marked B (darker gray) and A (lighter gray); nearest neighbor vectors $\mathbf{r}_1$, $\mathbf{r}_2$, $\mathbf{r}_3$; lattice vectors $\mathbf{a}_1$, $\mathbf{a}_2$; unit cell, semi-transparent yellow diamond; lattice constant $a_\mathrm{G} = 2.459\,\text{Å}$.[108] **(b)** First Brillouin zone of graphene: reciprocal lattice vectors $\mathbf{b}_1$, $\mathbf{b}_2$; high-symmetry points $\mathbf{\Gamma}$, $\mathbf{M}$, $\mathbf{K}$, $\mathbf{K}'$ marked by dots.

section. 3.4. The last section will then consider the structure of commensurate graphene on hBN from an experimental and theoretical perspective (sec. 3.5).

3.1. Atomic lattice, band structure and wave function properties of graphene

Graphene's honeycomb lattice structure (Fig. 3.1a) is described by a triangular Bravais lattice with a lattice constant of $a_\mathrm{G} = 2.459\,\text{Å}$[108] and a two-atom basis consisting of sublattice A and B. Correspondingly, the first Brillouin zone (BZ) also has hexagonal symmetry (Fig. 3.1b). It features the high-symmetry point $\mathbf{\Gamma}$ at $\mathbf{k} = 0$, two inequivalent $\mathbf{K}$ and $\mathbf{K}'$ points at the corners and three inequivalent $\mathbf{M}$ points in the middle of the BZ edges (only one marked). The originally $1s^2 2s^2 2p^2$ configured carbon atoms sp^2 hybridize in the x-y plane to form covalent σ bonds with their neighbors at relative angles of 120°. The unhybridized $2p_z$ orbitals overlap comparatively weakly forming π bonds. The strongly differing overlap of the π and σ bonds leads to a large 12 eV separation of the bonding and anti-bonding σ bands at the Γ point, while the π bands govern the low energy properties around the Fermi energy and thus the electronic transport.

In the most simple tight binding (TB) approximation of the π bands, the wave func-

tion is a linear combination of p_z orbitals $\phi(\mathbf{r})$ centered at the atom positions. Using $\mathbf{R} = n_1\mathbf{a}_1 + n_2\mathbf{a}_2$ ($n_1, n_2 \in \mathbb{Z}$), while $\mathbf{r} = 0$ on a B sublattice site, one gets[109,110]

$$\Psi_{\mathbf{k}}(\mathbf{r}) = \frac{1}{\sqrt{N}} \sum_{\mathbf{R}} e^{i\mathbf{k}\mathbf{R}} [\mathcal{A}\phi(\mathbf{r} - \mathbf{R} + \mathbf{r}_1) + \mathcal{B}\phi(\mathbf{r} - \mathbf{R})], \tag{3.1}$$

where $\mathcal{A}$ and $\mathcal{B}$ are the sublattice amplitudes on sublattice A and B, respectively, $\mathbf{r}_1$ is the nearest neighbor vector (Fig. 3.1a) and N the number of lattice sites. Eq 3.1 can be written as

$$\Psi_{\mathbf{k}}(\mathbf{r}) = e^{i\mathbf{k}\mathbf{r}} u_{\mathbf{k}}(\mathbf{r}) \tag{3.2}$$

and fulfills Bloch's theorem since $u_{\mathbf{k}}(\mathbf{r})$ is lattice periodic. Besides the kinetic energy, the graphene lattice Hamiltonian includes all the potentials of the carbon atoms $V_0(\mathbf{r})$ and thus reads[110]

$$H = \frac{p^2}{2m} + \sum_{\mathbf{R}} [V_0(\mathbf{r} - \mathbf{R} + \mathbf{r}_1) + V_0(\mathbf{r} - \mathbf{R})]. \tag{3.3}$$

Solving the eigenvalue problem $H\Psi_{\mathbf{k}}(\mathbf{r}) = \varepsilon(\mathbf{k})\Psi_{\mathbf{k}}(\mathbf{r})$ by including only nearest neighbor hopping and neglecting second order terms in the overlap integrals yields the energy dispersion relation[110]

$$\varepsilon(\mathbf{k}) = \pm t_{\mathrm{NN}} \sqrt{1 + 4\cos^2\left(\frac{k_{\mathrm{x}} a_{\mathrm{G}}}{2}\right) + 4\cos\left(\frac{k_{\mathrm{x}} a_{\mathrm{G}}}{2}\right)\cos\left(\frac{\sqrt{3}k_{\mathrm{y}} a_{\mathrm{G}}}{2}\right)}, \tag{3.4}$$

where

$$t_{\mathrm{NN}} = \int d^3r \phi(\mathbf{r} - \mathbf{r}_1) V_0(\mathbf{r} - \mathbf{r}_1) \phi^*(\mathbf{r}) \tag{3.5}$$

is the nearest neighbor hopping amplitude ($t_{\mathrm{NN}} \approx 3\,\mathrm{eV}$)[106] and the $\pm$ distinguishes between the conduction and valence band. The result is plotted in Figure 3.2a. Stemming from the distinction of bonding and antibonding bands, the conduction (petrol) and valence band (orange) are also referred to as π^* and π band, respectively. However, we will see that this simple distinction does not prevail in the low energy electronic wave functions. The energy difference is largest at $\mathbf{\Gamma}$ (i.e., $6t_{\mathrm{NN}}$), while their touching points at $\mathbf{K}$ and $\mathbf{K}'$ are called Dirac points. These main features do not change upon including next-nearest neighbor hopping ($t_{\mathrm{NNN}} \approx -0.1t_{\mathrm{NN}}$)[26,106,111] in Figure 3.2b (same scale, origins leveled). However, now we see an electron-hole asymmetry arising. Every carbon

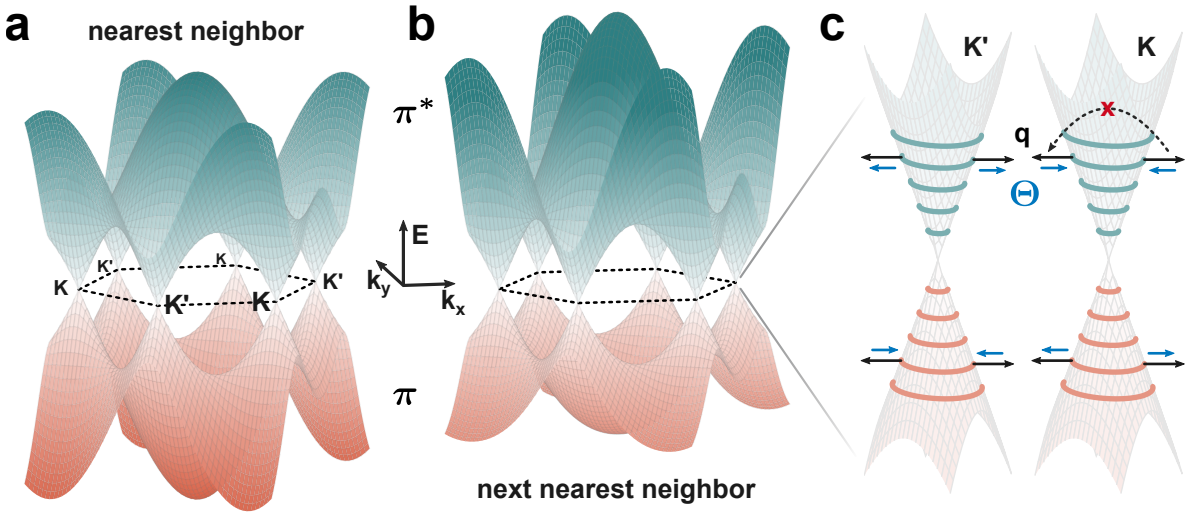


Figure 3.2.: **Band structure of graphene.** **(a)** π and π^* band, as labeled, of MLG from *nearest neighbor* TB according to eq 3.4 with $t_{\mathrm{NN}} = 3\,\mathrm{eV}$. Dotted line marks edge of first BZ. $\mathbf{K}$ and $\mathbf{K}'$ points labeled. **(b)** Same as panel **a** (same scale, origin vertically aligned to panel **a**) but from *next nearest neighbor* TB[106] with $t_{\mathrm{NNN}} = -0.1 t_{\mathrm{NN}}$. **(c)** Zoom onto Dirac cones around E_{F} at $\mathbf{K}'$ and $\mathbf{K}$, as labeled. Colored rings represent equi-energy lines. Bottommost and topmost ring mark $E = \pm 260\,\mathrm{meV}$. Black arrows mark wave vector $\mathbf{q}$ measured from the respective $\mathbf{K}'$ or $\mathbf{K}$ point. Blue arrows mark the projection $\mathbf{\Theta}$ of the pseudospin vector onto $\mathbf{q}$. Black dashed arrow marks intravalley backscattering process, which is prohibited (red 'x') due to the orthogonality of states with opposite $\mathbf{\Theta}$.

atom contributes one electron to the π bands, thus the valence band is completely filled and the Fermi energy resides exactly at the Dirac points.

Since the transport properties of graphene are governed by an energy interval of roughly 1 eV around E_{F}, the further evaluation can be restricted to the bands around $\mathbf{K}'$ and $\mathbf{K}$. Expanding H in eq 3.3 linearly around $\mathbf{K}$, that is, $\mathbf{k} = \mathbf{K} + \mathbf{q}$ and only first order terms in $|\mathbf{q}|a_{\mathrm{G}}$ are taken into account, yields[109,110]

$$\hbar \nu_{\mathrm{F}} \begin{pmatrix} 0 & q_{\mathrm{x}} - i q_{\mathrm{y}} \\ q_{\mathrm{x}} + i q_{\mathrm{y}} & 0 \end{pmatrix} \begin{pmatrix} \mathcal{A}_{\mathbf{q}} \\ \mathcal{B}_{\mathbf{q}} \end{pmatrix} = \varepsilon \begin{pmatrix} \mathcal{A}_{\mathbf{q}} \\ \mathcal{B}_{\mathbf{q}} \end{pmatrix}, \tag{3.6}$$

where $\nu_{\mathrm{F}} = 3 t_{\mathrm{NN}} a_{\mathrm{G}} / 2\hbar \approx 10^6\,\mathrm{m/s}$ is the Fermi velocity and the components of the spinor $\Psi_{\mathbf{K}} = (\mathcal{A}_{\mathbf{q}}, \mathcal{B}_{\mathbf{q}})$ give the relative amplitudes of the wave function on sublattice A and B. Using the Pauli-matrices in two dimensions $\boldsymbol{\sigma} = (\sigma_{\mathrm{x}}, \sigma_{\mathrm{y}})$ the Hamiltonian in eq 3.6 reads[26,110]

$$H_{\mathbf{K}} = \hbar \nu_{\mathrm{F}} \mathbf{q} \cdot \boldsymbol{\sigma}. \tag{3.7}$$

Note that the Schrödinger equation thus effectively takes the form of the Dirac equation with an adjusted speed of light ν_F. Moreover, $\boldsymbol{\sigma}$ does not act on the real spin but on the sublattice space such that $\Psi_\mathbf{K}$ is referred to as sublattice pseudospin vector.[106] The eigenvalues for the simplified $H_\mathbf{K}$

$$\varepsilon(\mathbf{q}) = \pm\hbar\nu_\mathrm{F}|\mathbf{q}| \tag{3.8}$$

finally reveal that graphene's electrons exhibit a linear dispersion (Fig. 3.2c) making them massless quasirelativistic fermions. This is yet another example of electrons disguising their elementary character in very specific solid state settings,[112] others being, for instance, excitons, majorana excitations[113–116] and the fractional charge of composite fermions.[117–119] Another good quantum number for such quasiparticles is the helicity η. The operator of helicity $\eta_\mathbf{q} = \mathbf{q}\cdot\boldsymbol{\sigma}/|\mathbf{q}|$ projects the sublattice pseudospin vector onto its direction of motion. There are only two eigenvalues $\eta = \pm$, meaning the sublattice pseudospin projection $\boldsymbol{\Theta}$ is either parallel ('+') or antiparallel ('−') to the momentum (Fig. 3.2c). Additionally, there is a correspondence of helicity and chirality (i.e., handedness) for massless particles.[106] Therefore, electrons ($\varepsilon > 0$) at $\mathbf{K}$ are right-handed ($\eta = +$) while holes ($\varepsilon < 0$) are left-handed ($\eta = -$). Again, there is a link to particle physics, where massless neutrinos are strictly left-handed and antineutrinos are right-handed.

Now if we consider the situation at $\mathbf{K}' = -\mathbf{K}$, that is, $H_{\mathbf{K}'} = -\hbar\nu_\mathrm{F}\mathbf{q}\boldsymbol{\sigma}^* = H^*_\mathbf{K}$, the dispersion relation (eq 3.8) does not change. Consequently, the states at $\mathbf{K}'$ and $\mathbf{K}$ are degenerate, which gives rise to an additional twofold valley degree of freedom and the valley pseudospin $\xi = +$ at $\mathbf{K}$ and $\xi = -$ at $\mathbf{K}'$. Also η inverts, that is, electrons and holes have opposite chirality at $\mathbf{K}$ and $\mathbf{K}'$. By defining the band index $\lambda = \pm$ for the conduction and valence band, respectively, we see that the different indexes relate as $\lambda = \xi\eta$. Since states of opposite chirality are orthogonal, backscattering ($\mathbf{q}\rightarrow$-$\mathbf{q}$) vanishes on smooth potentials (Fig. 3.2c), because they only provide small $\Delta\mathbf{k}$ and thus cannot couple the two valleys (i.e., no intervalley scattering).[106,109,110] In real graphene samples, random strain fluctuations manage to reinstall intravalley backscattering to some extent.[120] We can gain additional insight by considering the wave functions in the two valleys[26]

$$\Psi_{\mathbf{K},\lambda} = \begin{pmatrix}\mathcal{A}_\mathbf{q}\\ \mathcal{B}_\mathbf{q}\end{pmatrix} = \frac{1}{\sqrt{2}}\begin{pmatrix}e^{-i\varphi_q/2}\\ \lambda e^{i\varphi_q/2}\end{pmatrix} \tag{3.9}$$

and

$$\Psi_{\mathbf{K}',\lambda} = \begin{pmatrix} \mathcal{A}'_{\mathbf{q}} \\ \mathcal{B}'_{\mathbf{q}} \end{pmatrix} = \frac{1}{\sqrt{2}} \begin{pmatrix} e^{i\varphi_{\mathbf{q}}/2} \\ -\lambda e^{-i\varphi_{\mathbf{q}}/2} \end{pmatrix} \tag{3.10}$$

while the angle $\varphi_{\mathbf{q}} = \arctan(q_\mathrm{x}/q_\mathrm{y})$ of $\mathbf{q}$ with the k_x-axis effectively describes a phase. One characteristic of a spinor is that a 2π phase rotation of $\varphi_{\mathbf{q}}$ changes the sign of the wave function, which indicates a phase of π, commonly known as Berry's phase.[121] Interestingly, Berry's phase in bilayer graphene (BLG) is 2π.[122]

3.1.1. Density of states

The linear dispersion derived in the previous section distinctly alters the DOS in graphene compared to the two-dimensional semiconductor case with parabolic dispersion (constant DOS). In order to find the number of electronic states dN at energy E per unit area, we consider a ring on one Dirac cone (compare Fig. 3.2c) with radius q, width dq and thus area $2\pi q dq$. A single state in 2D has the area $(2\pi)^2/L^2$, where L is the length of a square sample. Straightforwardly, under consideration of the fourfold spin-valley degeneracy,

$$dN = 4 \cdot \frac{1}{L^2} \cdot 2\pi q dq \cdot \frac{L^2}{(2\pi)^2} \overset{\text{eq 3.8}}{=} \frac{2E}{\pi\hbar^2\nu_\mathrm{F}^2} dE \tag{3.11}$$

and thus the DOS in graphene $D(E) = dN/dE$ is linear in E. By integrating from the Dirac point up to a certain energy E, we can hence calculate the charge carrier concentration $N(E)$ and find[110]

$$N(E) = \frac{2}{\pi\hbar^2\nu_\mathrm{F}^2} \int_0^E E' dE' = \frac{E^2}{\pi\hbar^2\nu_\mathrm{F}^2}. \tag{3.12}$$

In conclusion, graphene's DOS vanishes towards the Dirac point, thus screening is strongly reduced. In turn, any charge in the environment of graphene will cause a comparatively strong band shift and electrostatic disorder from the substrate leads to the formation of electron-hole puddles if E_F is close to the Dirac point.[123–128] Such an energy dependent screening ability is called quantum capacitance and will be an issue in section 5.2.

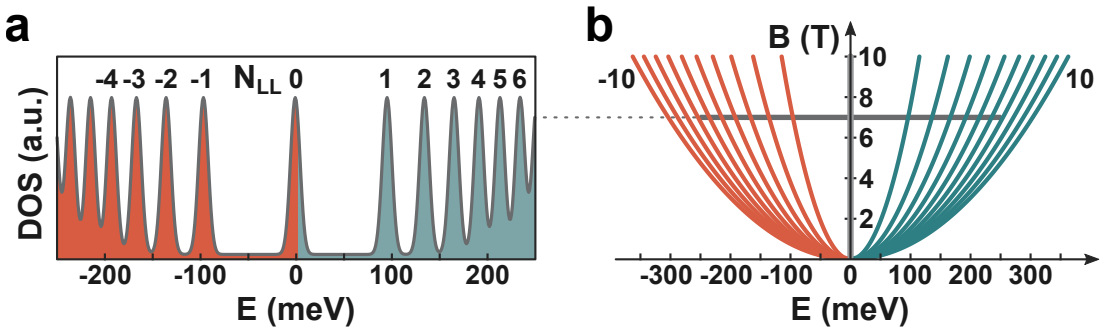


Figure 3.3.: **Landau levels in graphene (a)** DOS of graphene in a perpendicular magnetic field of $B = 7\,\mathrm{T}$. Position of Landau levels (LLs) calculated according to eq 3.13 with $\nu_\mathrm{F} = 1 \times 10^6\,\mathrm{m/s}$. LLs portray Gaussian broadening with a 5 meV sigma width, are labeled by their index N_LL, and orange/petrol filling marks states with hole/electron character. **(b)** LL fan for $N_\mathrm{LL} = -10, \ldots, 10$, also calculated for $\nu_\mathrm{F} = 1 \times 10^6\,\mathrm{m/s}$. Gray horizontal bar marks section shown in panel **a**.

3.2. Graphene in an external magnetic field

An external magnetic field B applied perpendicular to the graphene plane will force the electrons onto cyclotron orbits. For low B the electrons will not complete a full orbit without scattering, that is, $\omega_\mathrm{C}\tau \gg 1$, where ω_C is the cyclotron frequency and τ the mean time between scattering events. However, the vector potential of the magnetic field will add an Aharonov-Bohm phase[110,129] to any scattering path, thereby modifying the interference condition for counterpropagating electrons on closed phase-coherent paths. Measuring the magnetoresistance allows to extract the strength of different scattering processes, while an decreasing/increasing magnetoresistance at low field corresponds to weak localization[130–133]/ antilocalization.[134] Contrary to a conventional 2DES, graphene's pseudospin supports weak antilocalization,[22,105] however, especially early experiments mainly observed weak localization[101,135,136] due to various impeding (e.g., intervalley) scattering mechanisms.[20,21,137]

Significantly increasing B to the point where the electrons complete at least one cyclotron orbit without being scattered, that is, now $\omega_\mathrm{C}\tau = \mu B \approx 1$, where μ is the charge carrier mobility, imposes the same condition for constructive self-interference on all electrons. In analogy to the Bohr-Sommerfeld quantization for atoms, the quantization of the cyclotron motion leads to a condensation of graphene's DOS into highly degenerate

Landau levels (LLs) at discrete energies $E_{N_{\mathrm{LL}}}$, which read for graphene,[26,138]

$$E_{N_{\mathrm{LL}}} = \mathrm{sgn}(N_{\mathrm{LL}})\sqrt{2e\hbar\nu_{\mathrm{F}}^2|BN_{\mathrm{LL}}|} \tag{3.13}$$

$$= \mathrm{sgn}(N_{\mathrm{LL}})\hbar\omega_{\mathrm{c}}\sqrt{N_{\mathrm{LL}}}, \tag{3.14}$$

where ν_{F} is the Fermi velocity, $N_{\mathrm{LL}} \in \mathbb{Z}$ is the LL index and $\omega_{\mathrm{c}} = \sqrt{2e\nu_{\mathrm{F}}^2|B|/\hbar}$ is the cyclotron frequency. Figure 3.3 shows the according DOS at $B = 7\,\mathrm{T}$, for $\nu_{\mathrm{F}} = 1 \times 10^6\,\mathrm{m/s}$, and assumed Gaussian broadening in panel a, while panel b portrays $E_{N_{\mathrm{LL}}}(B)$ for $N_{\mathrm{LL}} = -10, \ldots, 10$. Compared to a 2DES with parabolic band structure, where $\omega_{\mathrm{c}} = eB/m^*$, $E_{N_{\mathrm{LL}}} = \hbar\omega_{\mathrm{c}}(N_{\mathrm{LL}} + 1/2)$ and thus the LL energy is proportional to B and N_{LL}, graphene exhibits a square root dependency on B and N_{LL} (Fig. 3.3b). Interestingly, a 2DES with huge Rashba spin-orbit coupling also exhibits a graphene-like LL spectrum.[139] Graphene's quasi-relativistic charge carriers also form an unusual LL at zero energy, which is comprised of electron and hole states and is a direct consequence of the Berry phase of the sublattice pseudospin (see Fig. 3.3a). Another feature are the different wave function amplitudes on sublattice A and B for the bulk LL eigenstates[26]

$$\Psi^{\mathbf{K}}_{N_{\mathrm{LL}}} = \begin{pmatrix} \Psi^{\mathrm{A}}_{|N_{\mathrm{LL}}|-1} \\ \Psi^{\mathrm{B}}_{|N_{\mathrm{LL}}|} \end{pmatrix} \quad \text{and} \quad \Psi^{\mathbf{K}'}_{N_{\mathrm{LL}}} = \begin{pmatrix} \Psi^{\mathrm{A}}_{|N_{\mathrm{LL}}|} \\ \Psi^{\mathrm{B}}_{|N_{\mathrm{LL}}|-1} \end{pmatrix}. \tag{3.15}$$

For each valley, this leads to sublattice polarized states for $N_{\mathrm{LL}} = 0$, because the part of the wave function with subscript $|N_{\mathrm{LL}}| - 1 = -1$ does not exist. Peculiarly, all other valley polarized LLs with $|N_{\mathrm{LL}}| \geq 1$ exhibit different orbital states on either sublattice, where the orbitals are interchanged in the other valley.

The square-root LL spectrum emphasizes the first Landau gaps. For instance at $B = 7\,\mathrm{T}$, the first Landau gap $\Delta_{01}^{\mathrm{LL}} = E_1 - E_0 \approx 100\,\mathrm{meV}$ in graphene, but $\Delta_{01}^{\mathrm{LL}} \approx 15\,\mathrm{meV}$ for $m^* = 0.05 - 0.07m_e$ as found in InGaAs/InP and GaAs/AlGaAs heterostructures.[140,141] Ultimately, they can provide robust confinement for graphene QDs (see sec. 4.3, chap. 5) and enable the observation of the QHE and Shubnikov-de-Haas oscillations[142] at room temperature.[143] Within the quantum Hall regime, transport experiments with QDs need to take the formation of edge channels into account (see Fig. 5.20). To briefly discuss their origin (details see, e.g., Ref. [110]), we consider a sample of width $2w$ and a length much lager than w (Fig. 3.4b). The confining edge potential will shift the energies of electron/hole LLs upwards/downwards toward the sample edge (Fig. 3.4a). Thereby

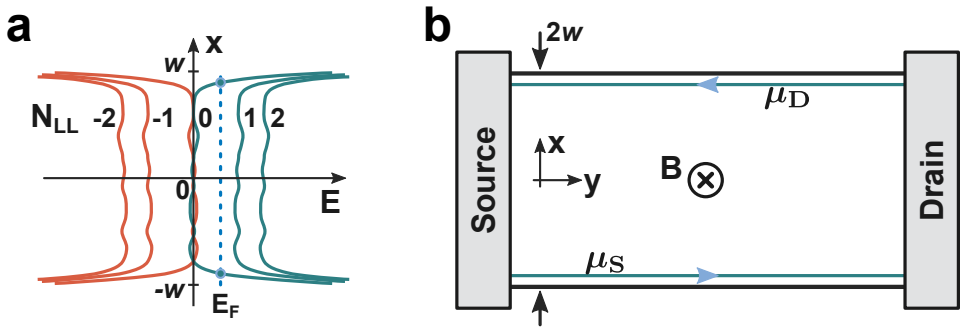


Figure 3.4.: **Edge channels in the quantum Hall regime (a)** Schematic real space energy diagram for LLs with index $N_{\mathrm{LL}} = \pm 2,\ \pm 1,\ 0$ portraying a line cut across a sample of width $2w$, aligned to panel **b**. Modulation of the LL energy inside the bulk reflects potential disorder. E_{F} lies within a LL gap (dotted blue line) . Circles mark selected crossing points of a LL with E_{F} and thereby the position of a corresponding edge channel in panel **b**. **(b)** Edge channel configuration in a sample of width $2w$ and E_{F} in a LL gap, as labeled and defined in panel **a**. Blue arrows indicate direction of electron motion. There is no backscattering between edge channels and their electrochemical potentials match that of source μ_{S} and drain μ_{D}, as labeled.

1D conductive channels, which do not exhibit backscattering due to their chirality, are formed along the edge (horizontal petrol lines in Fig. 3.4b) where the LLs cross E_{F} (circles in Fig. 3.4a), which are therefore called *edge channels*. Backscattering between the edge channels of opposite sample edges is only possible if E_{F} coincides with the energy of an extended state of the bulk (center of a LL).

3.3. Si/SiO_2 and hexagonal BN substrates

Initially, graphene samples were exfoliated and processed on standard Si/SiO_2 wafers.[3,18,19] The 90 nm or 300 nm thick thermally oxidized SiO_2 top-layer serves two purposes: (i) interference effects ease the optical identification of graphene flakes[144] and (ii) it insulates the graphene from the degenerately doped Si back gate electrode.[3] However, dangling bonds, trapped charges, SiO_2 surface optical phonons[145,146] and the surface roughness-induced graphene corrugation[124,147–152] of a few nm severely limited the performance of graphene devices,[120,153–155] such that mobilities hit a wall slightly above 10 000 $\mathrm{cm}^2/\mathrm{Vs}$.[19,26,154]

On substrate, mobilities finally surmounted this limit with the introduction of hBN as additional layer between SiO_2 and graphene.[154] Just like graphite, hBN is a layered crystal with weak van-der-Waals forces acting between the layers. The individual layers

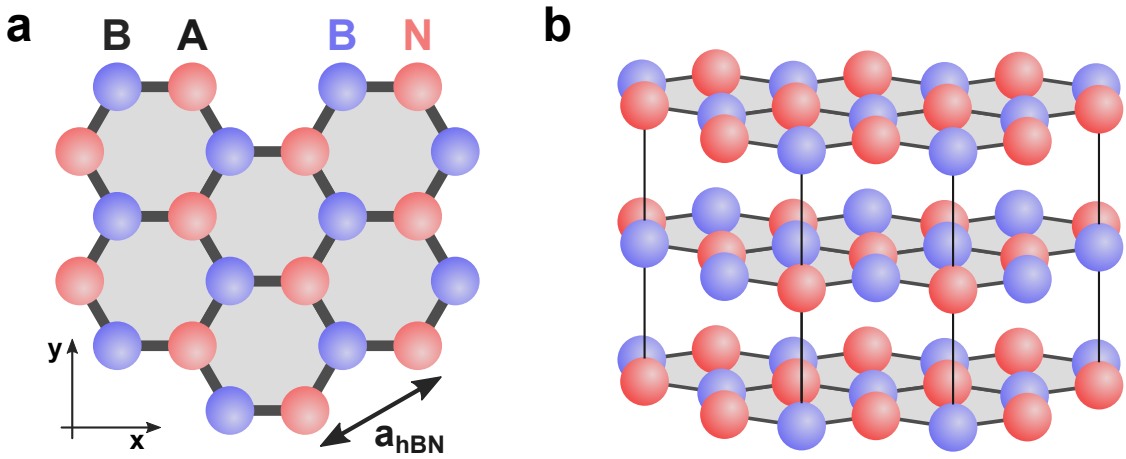


Figure 3.5.: **Crystal lattice of hBN. (a)** Honeycomb lattice structure of a single hBN layer: Sublattices B and A are labeled and are occupied by boron (B, blue) and nitrogen (N, red) atoms, respectively. Lattice constant $a_{\mathrm{hBN}} = 2.505\,\text{Å}$.[156] **(b)** Three layers of AA' stacked hBN, i.e., a B atom always sits on top of a N atom in the adjacent layer and vice versa. Vertical lines are guides to the eye.

exhibit the same honeycomb lattice structure as graphene, while the B and N atoms substitute one of the graphene sublattices each (see Fig. 3.5a). The lattice constant $a_{\mathrm{hBN}} = 2.505\,\text{Å}$[156] is about 2 % larger than that of graphene. Adjacent layers prefer AA' (eclipsed) stacking,[157,158] with B atoms residing over N atoms (see Fig. 3.5b). The large band gap of about 6 eV[159] makes hBN transparent for visible light and suitable as insulating gate dielectric ($\varepsilon_{\mathrm{hBN}} \approx \varepsilon_{\mathrm{SiO_2}} = 3 - 4$).[154,160] It presents a far superior substrate to SiO_2,[153,154] because it is atomically flat, relatively free of dangling bonds and charge traps and thus greatly reduces disorder for graphene's electrons.[125,161,162] Its high-energy optical phonon modes[154] are also beneficial, since they are barely excited at 300 K Moreover, to avoid contamination by adsorbates, hBN serves as a capping layer[163] in hBN/G/hBN heterostructures.[164] There is, however, room for improvement during crystal growth. The remaining oxygen and carbon defects (density $< 1 \times 10^{18}\,\text{atoms/cm}^3$)[165] can be charged[166–168] electrically and optically, cause hysteresis in large gate voltage sweeps[166] and create electrostatic potential disorder and even localized states in the graphene.[169–171]

3.4. Graphene sample preparation

Often, graphene samples for transport experiments are still prepared by exfoliation from graphite crystals by the 'scotch tape method',[3] while more recently graphene grown by chemical vapor deposition (CVD) has rivaled or even exceeded the performance of exfoliated graphene if transferred correctly.[10] The isolation of graphene flakes started out on Si/SiO_2 substrates, but it is nowadays transferred to the cleaner and less corrugated substrate hBN (see also sec. 3.3). The polymer based, flake-by-flake transfer technique[154,163,172,173] required intermediate annealing after the transfer of every layer and was later simplified by Wang et al.[164] and Zomer et al.[174] to solely rely on the van der Waals interaction between the two crystals in contact, also called the polymer free 'dry-transfer' technique. The different components are separately exfoliated on SiO_2 and successively picked up by a polymer-coated mask to assemble a stack (e.g., G/hBN). In the next step, the stack is placed on the designated bottommost layer (e.g., hBN) forming the desired heterostructure (i.e., hBN/G/hBN). Finally, the mask is detached by melting the polymer layer. In an effort to copy this technique, I designed and implemented a heating stage for our clean room's mask aligner based on the design used in Groningen by N. Tombrosh and P. Zomer.[173] The benefit of this approach is that only the topmost layer will have been in contact with the polymer. The technique is also referred to as 'stamping'[174] and allows to assemble stacks much more quickly and with comparatively high success rate. However, there is one important drawback in terms of SPM accessibility. To receive a graphene flake of highest quality, it needs to be picked up by an hBN flake. To come out on top, the entire stack has to be flipped keeping the polymer as substrate. There is also the rather challenging option of directly growing graphene on top of hBN on Cu or Ni.[175–178]

The solution to the flipping problem is exfoliation of the graphene on a separate polymer coated mask. Bringing a graphene flake into contact with a hBN flake on Si/SiO_2 results, in most of the cases, in delamination of the graphene from the polymer. By using a resist free contacting technique it is now possible to create a sample which has never been in contact with solvents. There are two candidates: Indium soldering[101,179,180] and shadow mask evaporation. The samples used in the LAO experiments (chap. 6, e.g., Fig. 6.7a) were contacted by In. Here, the sample is placed on a heating stage underneath a microscope. Micro-manipulators are used to pull In needles (tip diameter $\sim \mathcal{O}(\mu m)$, length of $0.5 - 1\,cm$) from a molten droplet of In (melting at $T \approx 156.6\,°C$).[181] Placing

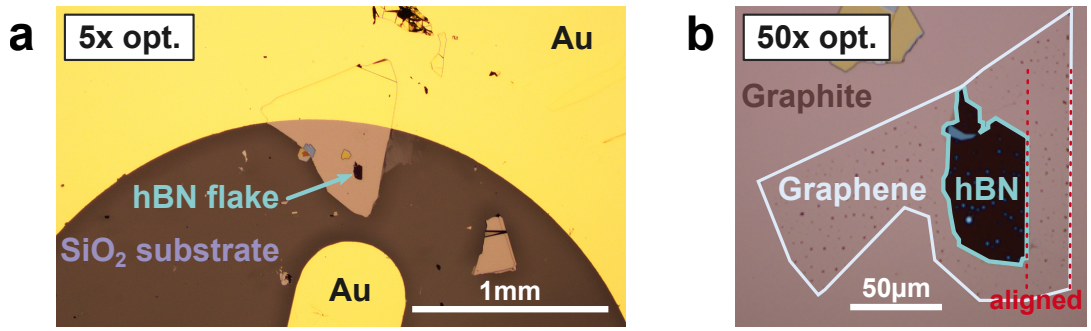


Figure 3.6.: **Images of the crystallographically aligned graphene-on-hBN sample.** The sample stack is made up of graphite, hBN (30 nm) and graphene (aligned to the hBN), as labeled in panel **b**. Cr/Au (2 nm/100 nm) contacts marked 'Au' are evaporated through a shadow mask. **(a)**/**(b)** 5×/50× enlarged optical image of the sample.

the needles on the graphene flake with µm precision creates contacts. However, the main drawback of this technique lies in an oxide barrier of the contacts forming under ambient conditions, which regularly yields contact resistances in excess of 100 kΩ.

Meanwhile, shadow mask evaporation is employed to improve the contacts and omit heating the sample over several hours in air. However, applying more than four contacts requires processing individual shadow masks rather than using, for instance, standard transmission electron microscopy (TEM) grids. The technique was used on the commensurate graphene sample investigated by STM (sec 3.5, chap. 5). The graphite/hBN/MLG stack (Fig. 3.6b) was prepared by the Manchester group which exfoliated graphite flakes on a SiO_2 substrate, followed by two consecutive dry transfers[182] of 30 nm thick hBN and MLG. The latter was crystallographically aligned to the hBN with a precision better than 1° (see Fig. 3.6b).[183] Moreover, the graphite layer serves as additional screening layer for the SiO_2, contact to the graphene and safe landing platform for the STM tip, since missing the graphene flake and approaching an insulating substrate would damage the tip.

3.5. Superstructure of commensurate graphene on hexagonal boron nitride

As discussed in section 3.3, one layer of hBN is isostructural[157,158] to graphene and has an only about 2 % larger lattice constant.[108,156] Hence, one observes moiré lattices with different periodicity depending on their relative crystal orientation when forming

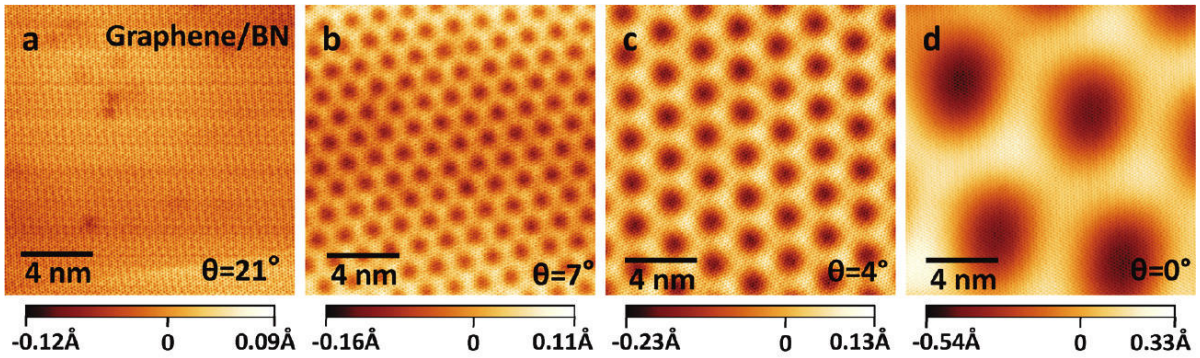


Figure 3.7.: **Moiré structures of graphene on hBN.** STM topography images for different misalignment angles θ, as labeled. **(a)** $V_{\text{tip}} = -0.15\,\text{V}$, $I = 0.1\,\text{nA}$, $V_{\text{BG}} = -25\,\text{V}$. **(b)** $V_{\text{tip}} = -0.15\,\text{V}$, $I = 0.2\,\text{nA}$, $V_{\text{BG}} = 0\,\text{V}$. **(c)** $V_{\text{tip}} = -0.15\,\text{V}$, $I = 0.2\,\text{nA}$, $V_{\text{BG}} = -6\,\text{V}$. **(d)** $V_{\text{tip}} = -0.15\,\text{V}$, $I = 0.15\,\text{nA}$, $V_{\text{BG}} = -3\,\text{V}$. Error on $\theta = \pm 1°$. Adapted with permission from Decker, R. et al. *Nano Lett.* **2011**, *11*, 2291–2295.[161] Copyright (2011) American Chemical Society.

a bilayer[125,161,175,183–187] as portrayed in Figure 3.7. However, one has to distinguish two phases:[183] (i) the incommensurate phase, where both crystal lattices remain almost undistorted and (ii) the commensurate phase, where the graphene lattice adjusts to fit n graphene to m hBN lattice constants such that $\frac{n}{m} \in \mathbb{Q}$. This adjustment goes hand in hand with the expansion of areas of favorable stacking configuration. The commensurate-incommensurate transition[183] occurs at a critical misalignment angle of about 1°, which corresponds to a moiré lattice constant of about 10 nm. Importantly, as soon as the graphene lattice adapts, the resulting superstructure is no longer described by a plain moiré lattice. Its broken inversion symmetry results in opposite directions of current flow in the **K** and **K′** valley, which gives rise to the valley Hall effect.[188] I will focus on the commensurate phase, since my STM measurements were carried out on such a sample.

Two components determine the interaction between the C atoms and the hBN layer:[191] first, different onsite potentials for the two carbon atoms; second, a difference in interlayer hybridization of different C atoms with the B and N atoms. Their competition will favor the C atom on B over the one on the hBN hollow site for a smaller interlayer separation, because the gain in kinetic energy due to the stronger orbital hybridization outweighs the gain in potential energy on the hollow site.[191] For a larger separation, the onsite potential becomes determining and the C above the hBN hollow site is preferred. Thus, among others, the interlayer separation is a crucial factor in determining the fa-

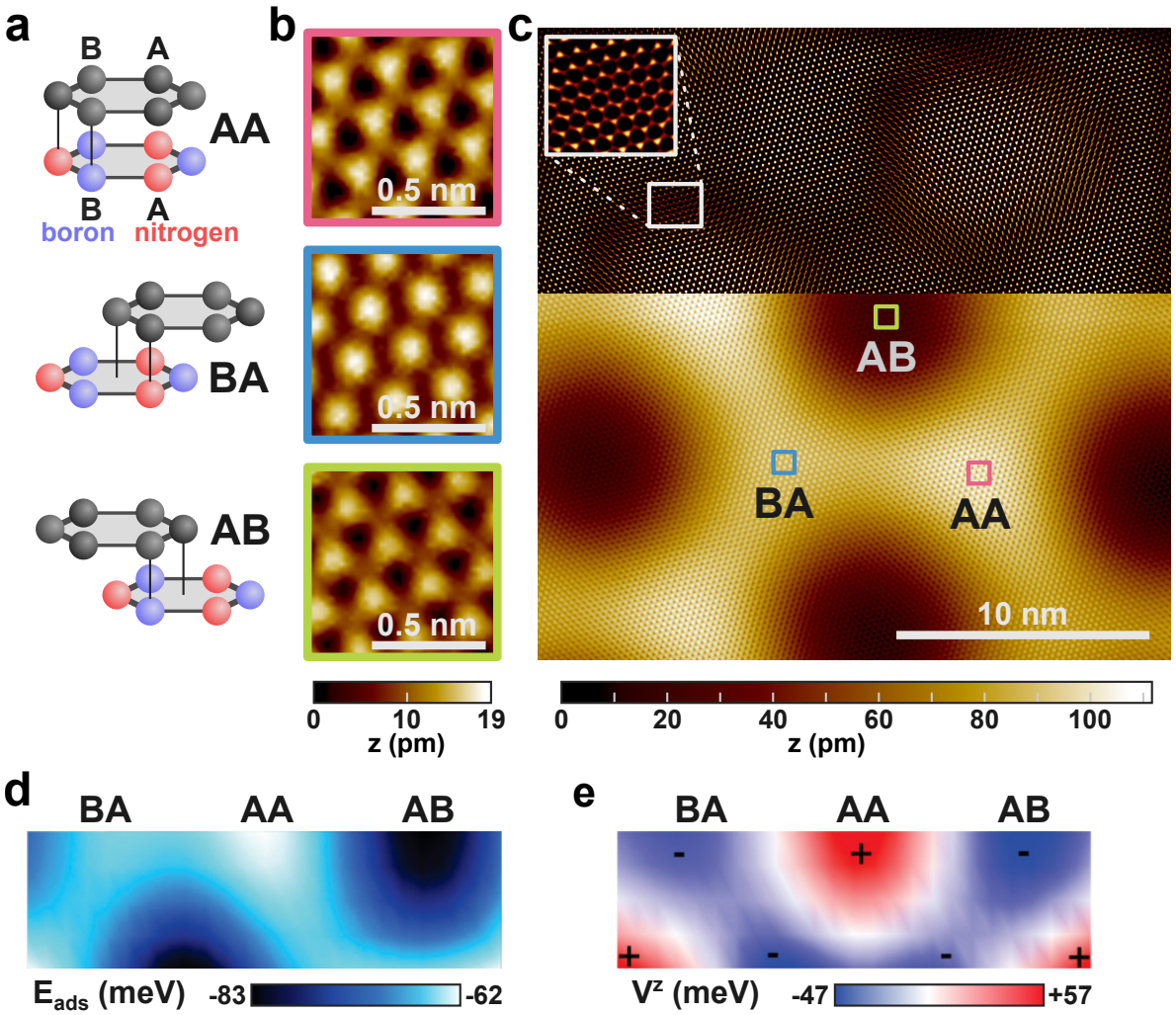


Figure 3.8.: **Details of the superstructure of commensurate graphene on hBN** **(a)** The three high-symmetry stacking orders of graphene on hBN labeled AA, BA and AB from top to bottom. For AA stacking, the two sublattices for both layers are labeled A and B. Carbon, boron and nitrogen atoms colored gray, blue and red, respectively. Vertical lines are guides to the eye. **(b)** Zooms onto high-symmetry points in the STM topography image shown in panel **c** as marked by colored squares and aligned to panel **a**. Note the pronounced sublattice symmetry breaking. **(c)** Bottom part shows raw STM topography image of the commensurate graphene superstructure on hBN. $V_{\mathrm{tip}} = 400\,\mathrm{mV}$, $I = 1\,\mathrm{nA}$, $I(Z)$ yields $2\kappa = 5.7 \pm 0.1\ \mathrm{\AA}^{-1}$. Colored squares mark zooms in panel **b** and high-symmetry points labeled by their stacking order AB, BA, AA. Top part shows the Fourier filtered image, where only first and second order contributions with the periodicity of the graphene lattice constant a_{G} were included (see Fig. 3.1a). Note the nearly circular boundary region between AA and AB/BA stacking, indicating a switching of the sublattice with high intensity (see inset). **(d,e)** Adsorbtion energy E_{ads} and sublattice symmetry breaking potential V^{z} per unit cell for commensurate graphene on hBN as calculated by DFT[189] with an adequate van der Waals potential (RPA correlation energy evaluated within the adiabatic connection fluctuation-dissipation theorem[190]). High-symmetry stacking orders labeled BA, AA, AB. Reprinted figure with permission from Sachs, B. et al. *Phys. Rev. B* **2011**, *84*, 195414.[189] Copyright (2011) by the American Physical Society.

vored stacking[191] and impacts any observable sublattice symmetry breaking (SSB) in STM. The main features of the superstructure become intuitively clear by keeping in mind that the position above a N atom is the least desirable. The three high-symmetry configurations are illustrated in Figure 3.8a: (i) AA stacking, with C on B and C on N, (ii) BA stacking, with C on N and C on the hBN hollow site and (iii) AB stacking, with C on B and C on the hBN hollow site. The DFT calculations by Sachs et al.[189] (Fig. 3.8d and sec. 3.5.1) identify AB stacking as most favorable (-83 meV/unit cell) and BA (-65 meV/unit cell) as only slightly better than AA stacking (-62 meV/unit cell). Their findings corroborate other ab-initio calculations,[192] which also find the repulsive C-N interaction, being about two to three times larger than the C-B repulsion,[193] to dominate the adsorbtion energy between the graphene and the hBN layer. This results in a lower adsorbtion energy per graphene unit cell for AB stacking compared to the other two configurations (Fig. 3.8d).

The variation of the adsobtion energy E_{ads} determines the corrugation of the graphene sheet and nicely matches the STM topography image in the lower part of Figure 3.8c. In Figure 3.8c, for instance, I measure a peak-to-peak height corrugation $\Delta z_{\mathrm{SS}} = z(AA) - z(AB) = 85 \pm 3\,\mathrm{pm}$. Generally I find $\Delta z_{\mathrm{SS}} = 90 \pm 10\,\mathrm{pm}$ (error reflects variation for 10 different topography images recorded with 4 different tips and also varying micro-tips; scan parameter range $V_{\mathrm{tip}} = -0.240{-}1\,\mathrm{V}$, $I = 7{-}700\,\mathrm{pA}$), in close agreement with values reported by Decker et al.[161] (see Fig. 3.7d). The STM tip will pull on the graphene due to van der Waals and electrostatic forces,[29,151,194] which could lead to an exaggeration of Δz_{SS} in the measurements if, for instance, areas with low adsorbtion energy are lifted more strongly than those with high adsorbtion energy. $I(Z)$ curves are a good indicator of lifting (see sec. 2.1.1). Indeed, frequently, measurements with comparatively steep $I(Z)$ curves, that is, $2\kappa > 3.5\ \mathrm{\AA}^{-1}$ (e.g., Fig. A.5a), exhibit $\Delta z_{\mathrm{SS}} > 100\,\mathrm{pm}$ and maximum values of $\Delta z_{\mathrm{SS}} = 125 \pm 5\,\mathrm{pm}$.[1] For more regular $I(Z)$ curves, different tip shapes and varying V_{tip} or I only have an impact within the stated uncertainty range, thus much smaller values of Δz_{SS} are unlikely. Hence, the experimental values clearly disagree with the predicted smaller $\Delta z_{\mathrm{SS}} \approx 20\,\mathrm{pm}$ in different DFT calculations.[189,195]

While the superstructure formation contributes a slowly varying, sublattice independent potential term $V^0(\mathbf{r})$, largely caused by the long range corrugation, the variations on the atomic scale due to the B and N atoms lead to a SSB term with amplitude V^{z} (see

[1] Measured at $V_{\mathrm{tip}} = 220\,\mathrm{mV}$, $I = 250\,\mathrm{pA}$. Increasing the tip-sample distance by going to $V_{\mathrm{tip}} = 400\,\mathrm{mV}$ and $I = 7\,\mathrm{pA}$ reduced Δz_{SS} to $87 \pm 7\,\mathrm{pm}$.

Fig. 3.8e). Formally, the potential energy in the Dirac Hamiltonian takes the form[196]

$$H_{\mathrm{pot}} = V^0(\mathbf{r}) \cdot \sigma_0 \otimes \tau_0 + V^{\mathrm{z}}(\mathbf{r}) \cdot \sigma_{\mathrm{z}} \otimes \tau_0, \tag{3.16}$$

where the unit matrix σ_0 (τ_0) and the Pauli matrix σ_z act on the A-B sublattice (valley) degree of freedom. The sign of V^z inverts going from AA to AB/BA (Fig. 3.8e). Sublattice A becomes energetically less favorable as it shifts its position from on top of a B atom to a N atom/hollow site (see Fig. 3.8a). Looking for this sublattice contrast in experiment, I Fourier filter the top part of the STM image in Figure 3.8c and only include first and second order components in the graphene lattice periodicity a_{G}. There is a clear circular boundary of lower intensity around AA stacked areas (high LDOS on sublattice A) across which the sublattice contrast inverts, while AB and BA stacked areas (high LDOS on sublattice B) are continuously connected matching the DFT predictions in Fig. 3.8e. This is all the more surprising, since in this case the tip lifts the graphene significantly by about 55 pm (see Figure A.1). On the one hand, this increases the interlayer separation with respect to equilibrium and thus alters the carbon onsite energies. On the other hand, it induces strain and thereby contributes an additional SSB through the pseudo Zeeman effect.[29] Moreover, this is the only measurement which matches the DFT this nicely. Other images recorded at smaller I, different/inverted V_{tip} or with another tip showcase, for instance, weak or absent SSB on AB, identical SSB for all stackings or the same SSB on BA and AA. In Fig. 3.8b, the zooms on to the high-symmetry points emphasize the details of the sublattice symmetry breaking. While the bright sublattice has a triangular appearance for AA and AB stacking, it looks round for BA stacking.

Because the elastic energy needed to stretch the graphene to conform with the hBN lattice amounts to 40 meV/two carbon atoms and thus outweighs the gain in adhesion energy of 14 meV/two carbon atoms for AB stacking[189] with respect to the average adhesion energy, a superstructure forms. The favored expansion of AB stacked areas induces tensile strain, which is compensated in the compressed and slightly lifted BA and AA areas. The additional out-of-plane corrugation does not significantly release in-plane strain. We can deduce an upper bound for this relaxation by estimating that a change of $\Delta z \approx 80$ pm happens on a length of 4 nm (transition between, e.g., AB and AA). Therefore, the lattice only relaxes by $\sqrt{0.08^2 + 4^2}/4 = 0.02\,\%$.

3.5.1. Limits of the density functional theory results

Above, I have pointed out some agreement of DFT derived potentials and experiment, however, there is also significant disagreement in parts pointing to physics not captured accurately by DFT so far. The incompatibility of theory and experiment is to some extent expected, because DFT in the local-density approximation (LDA) and generalized gradient approximation (GGA) fails to reproduce van-der-Waals forces and other long-range correlations accurately.[197,198] Sachs et al.[189] employed the random phase approximation (RPA) to determine the equilibrium separation of graphene and hBN for the different stacking orders more accurately, however, the size of the graphene superstructure unit cell exceeds the computational limits of this method. So far, there simply is no appropriate method to consistently implement the full structural relaxation and DOS calculations within one framework. Hence, the derived equilibrium geometries for commensurate graphene on hBN probably underestimate the corrugation significantly, because they do not include strain effects, which occur on the moiré unit cell length scale.

Purely isotropic strain creates an additional scalar potential,[199,200] while shear components can be captured by a gauge field resulting in a pseudomagnetic field[200] and thus contributions to V^{z}.[29] Additionally, the interlayer distance is a crucial parameter for the onsite potential of the carbon atoms. While a change in magnitude due to a change in distance is the quite obvious result of large scale molecular dynamics calculations by van Wijk et al.,[193] calculations by Xu et al.[191] also imply the possibility of a sign change in the SSB. To some extend stuck in this predicament, theory can only try to fit the potentials to experiment. Nonlocal measurements of the Hofstadter butterfly could be reproduced by next-nearest neighbor TB.[196] There, V^0 was based on Figure 3.8d (i.e., E_{ads}) and expanded by adding a Gaussian with an amplitude of $-100\,\mathrm{meV}$ and FWHM of 7 nm to AB stacking (inferred from second order perturbation theory in Ref. [184]) and taking V^{z} from Ref. [189] (same as Fig. 3.8e). DFT[195] favors a different V^0, where AB and BA stacking with respect to AA stacking have the same amplitude but opposite sign, that is, $V^0 = \pm 60\,\mathrm{meV}$, respectively. Strain was modeled by expanding (compressing) the graphene lattice on AB (AA, BA) areas. Here, slight changes to the misalignment of graphene and hBN will change the local strain but probably leave the macroscopic transport properties largely unaffected. These results thus cannot serve as reliable reference for models dealing with local properties on the scale of the superstructure unit

cell.

In conclusion, there are still serious loopholes in the theoretical treatment of commensurate graphene on hBN. Especially the uncertainty in the atomic structure quite possibly underestimates the local role of strain for slight misalignment $\theta < 1°$. To this end, superstructure lattice deformations (e.g., Fig. 5.14a) add even more complexity when trying to reproduce local measurements. Nonetheless, STM experiments provide a good indication for various parameters in question and the later portrayed tip-induced QDs (see chap. 5) capture intriguing details related to V^0 and V^z and thus help to understand the MLG/hBN system better.

3.5.2. Investigating the density of states at zero magnetic field

Generally, a slowly varying periodic potential on a scale much larger than the graphene lattice constant introduces a new supercell in real space. According to the zone folding in reciprocal space, new high-symmetry points are created in the band structure giving rise to multiple minibands and secondary Dirac points (SDPs) at the supercell Brillouin zone boundaries.[201–204] Depending on the periodic potential, the SDPs can be isotropic or anisotropic and exhibit more or less pronounced gaps surrounded by van Hove singularities (VHS).[196,205,206] In principle, lithographically defined patterns[201,207] and moiré patterns forming due to crystallographic misalignment should have a similar impact. Due to their structural compatibility, substrates with hexagonal lattices,[208] for instance, decoupled twisted bilayer graphene,[209–213] Iridium[214–216] or hBN,[100,125,161,184] are of particular interest. The induced VHS have been probed , for instance, by Raman spectroscopy.[217] Measurements of the Hofstadter-Butterfly effect[218] reveal the SDPs[219–221] and even Zak-type cloning of third-generation Dirac points.[222] Reports of a gap at the original DP, mostly assumed to be of about 30 meV, have been inconsistent throughout the experimental literature.[125,183,185,219,223–225] Similarly, early DFT calculations[226] predicted a gap of about 50 meV, while including a graphene-hBN lattice mismatch diminishes the gap by restoring sublattice symmetry on average.[227,228] However, structural relaxation of graphene and hBN, and many-body effects resurrect the gap yielding values of $7 - 20$ meV.[192,206,229] Recently, Xu et al.[191] argued that depending on the strength of the Coulomb onsite repulsion and the graphene-hBN interlayer spacing an interaction-induced state can close or enhance the gap. There has also been a spread in the predictions of the position of the valance and conduction band SDPs,

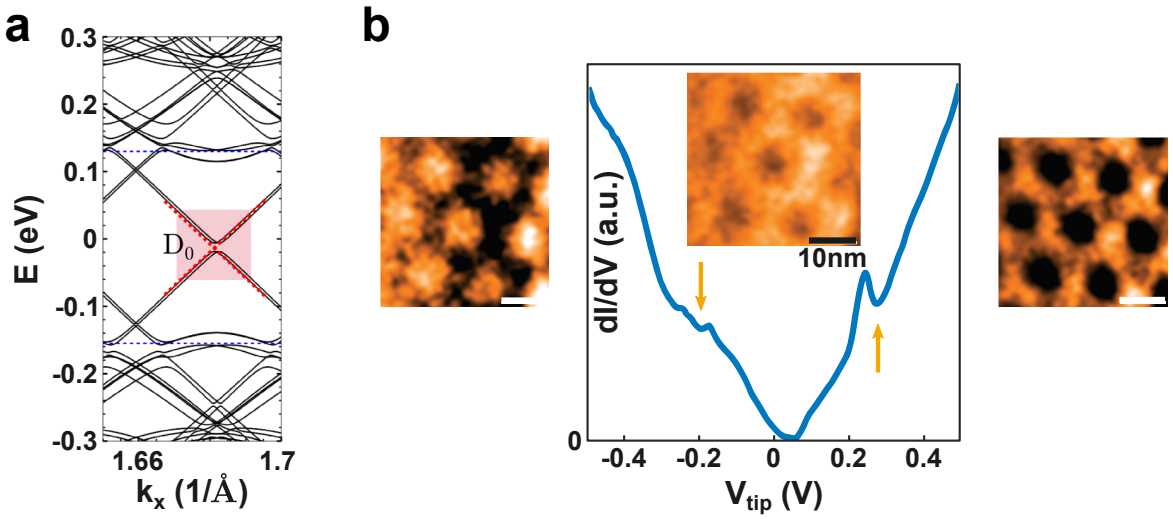


Figure 3.9.: **Expected DOS of commensurate graphene on hBN. (a)** Cut through the band structure ($k_y = 0$) of bulk graphene (13.8 nm superlattice wave length) within the reduced zone structure of the superlattice (SL) calculated using a third-nearest-neighbor TB model. Sublattice independent potential amplitude on AB stacking, −100 meV, zero for AA and BA. Sublattice symmetry breaking potential shown in Fig. 3.8e is implemented. Details see Ref. [196]. Red dashed line shows a fit to the main Dirac cone (red region). Blue dashed lines mark SDPs. **(b)** Central plot: experimental dI/dV curve for a SL wavelength of 13.4 nm; orange arrows, SDPs. Three images show $\Delta dI/dV$ maps, recorded 270 mV below (left), at (middle) and 330 mV above (right) the DP. All scale bars 10 nm. No clue in original publication concerning position of the high-symmetry points. Panel **a**: Reprinted figure with permission from Chizhova, L. A. et al. *Phys. Rev. B* **2014**, *90*, 165404.[196] Copyright (2014) by the American Physical Society. Panel **b**: Adapted by permission from Macmillan Publishers Ltd: Yankowitz, M. et al. *Nat. Phys.* **2012**, *8*, 382–386, copyright (2012).[184]

which lie in the range of −200 . . . −150 meV and 130 . . . 200 meV (compare blue dashed lines, Fig. 3.9a), respectively.[184,196,203,206,230,231] Moreover, the valence band SDP is generally expected to show a stronger DOS feature. Again, structural relaxation reduces the DOS signature of both SDPs.[206]

The LDOS of graphene on hBN with small misalignment angles has been captured in two STM experiments.[125,184] In particular, Yankowitz et al.[184] measured a sample with 13.4 nm superstructure wavelength. As portrayed in Figure 3.9b, they report that for energies below the SDP in the valence band ($V_{\text{tip}} - V_{\text{DP}} \approx 230$ mV, right arrow) a hexagonal pattern of increased LDOS forms (right image, $V_{\text{tip}} - V_{\text{DP}} = 330$ mV). In the conduction band above the SDP ($V_{\text{tip}} - V_{\text{DP}} \approx -220$ mV, left arrow) the contrast inverts (left image, $V_{\text{tip}} - V_{\text{DP}} = -270$ mV). The contrast is strongly reduced for energies in

between the SDPs (center image). However, the authors of Ref. [184] do not clearly link the contrast inversion center to a high-symmetry stacking configuration.

I compare these results to spectroscopy series of my own. In Figure 3.10k the mean of 9×9 single spectra, recorded in the areas marked by identically colored squares in Figure 3.10b, are portrayed. While there are generally more dI/dV features, the dips at $V_{\mathrm{tip}} \approx 180\,\mathrm{mV}$ and $V_{\mathrm{tip}} \approx -180\,\mathrm{mV}$ (orange arrows) can possibly be interpreted as the valence and conduction band SDPs, respectively. The reduced spacing compared to Ref. [184] could to some extent be due to the larger SL wave length of about 13.8 nm in my case. Plots of the LDOS above (Fig. 3.10c-d) and below (Fig. 3.10j) the SDPs do not reproduce the expected LDOS inversion discussed above. For the valence band it seems like the LDOS is reduced on AA areas (Fig. 3.10j), while in the conduction band AB areas portray decreased LDOS (Fig. 3.10c-d).

In the region in between the SDPs (Fig. 3.10e-i), AA stacking is the contrast inversion center showing either higher (panels e,f,i) or lower LDOS (panels g,h) with respect to AB and BA stacking. In parts, a shift of the LDOS patterns with respect to the high symmetry points is observed. This could point towards additional strain contributions. In another spectroscopy series (see Figure A.5), again AA and AB areas are either higher or lower in intensity with respect to the other stacking configurations. LDOS plots (Fig. A.5c-h) also show significant changes in the contrast close to the DP. There, the conduction band features higher LDOS for AB areas (Fig. A.5c), while the valence band exhibits reduced LDOS close to AA stacking (Fig. A.5h), similar to Figure 3.10j. Hence, there is no contrast inversion for a high-symmetry point as suggest by Yankowitz et al.[184] However, the $I(Z)$ characteristic for that series (Fig. A.5a, compare to Fig. 3.10a) indicates additional lifting of the graphene by the STM tip,[29] probably inducing additional features in the dI/dV signal and obscuring the SDPs.

In Figure 3.10g,h one can also see a pronounced stripe pattern, while Figure 3.10d portrays more of a checkerboard pattern. Both are attributed to a sublattice contrast, which is sampled by the comparatively coarse spectroscopy grid and thereby produces an aliasing effect. The stripe pattern inverts close to the DP (compare orange lines in Figure 3.10g,h) and at $V_{\mathrm{tip}} \approx 210\,\mathrm{mV}$ the same pattern as in Figure 3.10h is observed (not shown). Atomically resolved STS series corroborate this finding (e.g., Fig. A.6). This does not agree with Slotman et al.,[230] who predict significantly differing sublattice wave function amplitudes of their TB quasieigenstates only close to the SDPs (case of perfect crystallographic alignment).

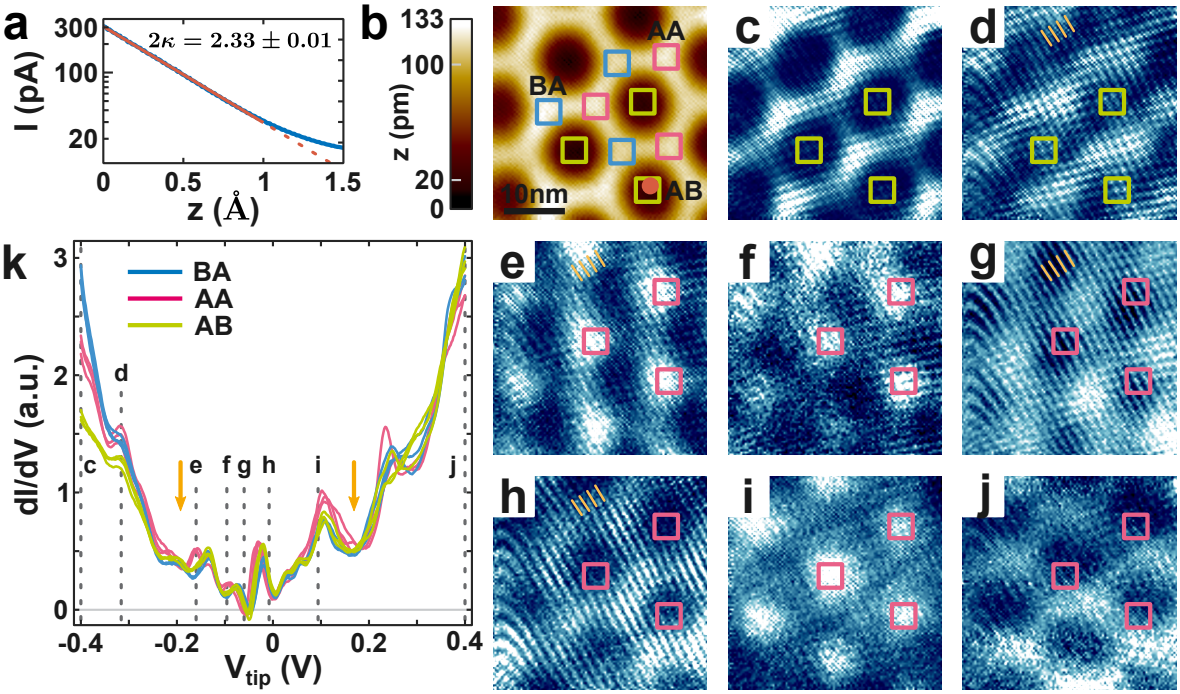


Figure 3.10.: **LDOS of commensurate graphene on hBN at zero magnetic field.** **(a)** Mean of five $I(Z)$ curves (blue) taken at the position marked by a red dot in panel **b**. $V_{stab} = 400\,\mathrm{mV}$, $I_{stab} = 300\,\mathrm{pA}$. Red line marks linear fit yielding 2κ as labeled. Solid part marks range used for fitting. **(b)** $35{\times}35\,\mathrm{nm}^2$ STM topography image recorded at $V_{tip} = 400\,\mathrm{mV}$, $I_{set} = 300\,\mathrm{pA}$. Colored squares mark areas where spectra in panel **k** were recorded (blue: BA, magenta: AA, green: AB). Red dot marks position where $I(Z)$ curve in panel **a** was recorded. **(c-j)** dI/dV maps extracted from a series of spectra taken on a 100×100 grid in the area shown in panel **b**. Spectroscopy (fixed-Z, series S541) parameters: $V_{stab} = 400\,\mathrm{mV}$, $I_{stab} = 300\,\mathrm{pA}$, $V_{mod} = 7.3\,\mathrm{mV_{rms}}$ and $B = 0\,\mathrm{T}$. V_{tip}, as labeled in panel **k**, in alphabetic order of the panels: $-400\,\mathrm{V}$, $-316\,\mathrm{mV}$, $-160\,\mathrm{mV}$, $-96\,\mathrm{mV}$, $-60\,\mathrm{mV}$, $-8\,\mathrm{mV}$, $94\,\mathrm{mV}$ and $400\,\mathrm{mV}$. Green and magenta squares mark AB and AA stacked areas respectively. Orange lines in panels **d**,**e**,**g**,**h** mark identical positions to emphasize shift in stripe pattern. **(k)** Nine locally averaged dI/dV spectra (9×9 single spectra) from the areas marked by colored squares in panel **b**. Dotted vertical lines mark V_{tip} of the dI/dV maps shown in panels **c-j**, as labeled. V_{tip} axis is the same as in Fig. 3.9b.

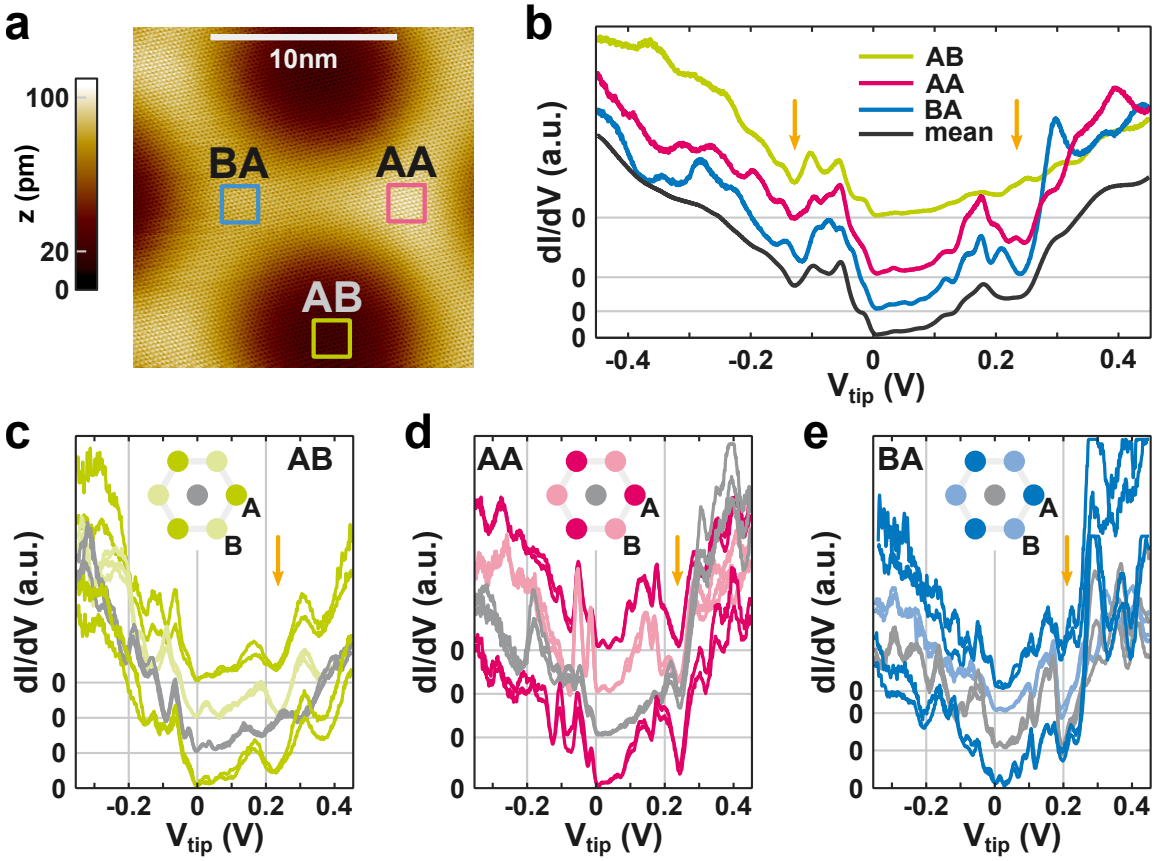


Figure 3.11.: **LDOS variation on the atomic scale at zero magnetic field.** **(a)** $18.3 \times 18.3\,\mathrm{nm}^2$ STM topography image. $V_{\mathrm{tip}} = -450\,\mathrm{mV}$, $I_{\mathrm{set}} = 0.9\,\mathrm{nA}$. Colored squares mark areas where spectra in panel **b-e** were recorded. **(b)** Three locally averaged dI/dV spectra (6×6 single spectra on $2.2 \times 2.2\,\mathrm{nm}^2$) from the AB (green), AA (magenta) and BA (blue) areas marked by colored squares in panel **a**. Black spectrum is average over 50×50 spectra taken over entire area of panel **a**. Spectroscopy (fixed-Z, series S47) parameters: $V_{\mathrm{stab}} = -450\,\mathrm{mV}$, $I_{\mathrm{stab}} = 0.9\,\mathrm{nA}$, $V_{\mathrm{mod}} = 5.5\,\mathrm{mV_{rms}}$. $I(Z)$ curves yield $2\kappa \approx 2.35\ \mathrm{Å}^{-1}$. Orange arrows indicate possible position of the SDPs. **(c-e)** dI/dV spectra extracted from a series of spectra taken within the colored squares in panel **a**. Spectroscopy (fixed-Z, series S3, S42, S40) parameters: $V_{\mathrm{stab}} = -350\,\mathrm{mV}$, $I_{\mathrm{stab}} = 0.8\,\mathrm{pA}$, $V_{\mathrm{mod}} = 5.5\,\mathrm{mV_{rms}}$. Dark colored spectra (2 each), sublattice A; light colored spectra (3 each), sublattice B; gray spectra (3 each), hollow site, as sketched in the upper part of the panels. Spectra for different positions are vertically offset for clarity, light gray horizontal lines mark zero dI/dV.

Switching of the sublattice contrast is indeed observed at various energies. We can additionally investigate another set of spectroscopy series which allow to assess LDOS variations on the atomic scale. Figure 3.11a shows the area covered by a spectroscopy series from which the averaged spectra in Figure 3.11b are extracted. The conduction band SDP at $V_{\mathrm{tip}} \approx -120\,\mathrm{mV}$ appears for all stackings, while it seems suppressed in the valence band at $V_{\mathrm{tip}} \approx 220\,\mathrm{mV}$ for AB stacking. Generally the valence band SDP DOS feature is more pronounced in the literature,[195,232] however, the LDOS for AB stacking is unavailable making the interpretation of the suppression cumbersome. Averaging over the entire area (black curve) retains both SDP features. They appear shifted with respect to Figure 3.10k, which might be due to a differing local doping. Figure 3.11c-e portray single spectra from atomically resolved spectroscopy series recorded inside the AB, AA and BA areas in Figure 3.11a marked by green, magenta and blue squares, respectively. The dark and light colored spectra were recorded close (within experimental resolution) to the A and B sublattice, respectively. The gray curves stem from the hollow site. Multiple spectra for every position are plotted to convey local variations in the measurements.

For AB stacking (Fig. 3.11c) we see that the valence band SDP LDOS dip (orange arrow) is visible on the atoms, but shifted for the hollow site explaining the weak appearance in the averaged curve (green, Fig. 3.11b). Moreover, the dips in both conduction and valence band seem to be more pronounced on the B sublattice. For AA stacking (Fig. 3.11d) the SDP features appear sharper, while sublattice B shows close to zero dI/dV for both SDPs and sublattice A only in the valence band (orange arrow). Only the hollow site shows an additional dip at $V_{\mathrm{tip}} \approx -0.2\,\mathrm{V}$, which also appears for AB (Fig. 3.11c) and BA stacking (Fig. 3.11e). However, in the latter case the feature is also found on the A sublattice. It is again the B sublattice and the hollow site which portray a more pronounced valence band SDP.

There are two more noteworthy features: (i) a double peak structure above E_{F} (i.e., $V_{\mathrm{tip}} < 0\,\mathrm{V}$), which is most pronounce for AA stacking (Fig. 3.11d) and (ii) additional dips in dI/dV slightly below $V_{\mathrm{tip}} = 0.4\,\mathrm{V}$ (best seen in Fig. 3.11c,e), which could stem from higher generation DPs. However, the lack of LDOS spectra on the atomic scale in the literature make it generally difficult to compare the results. STS always probes the LDOS at a distinct position within the atomic lattice and the observed significant local changes make it tough to compare to calculated DOS plots. Interestingly, STS measurements[233] and theory[234] concerning twisted BLG at small misalignment angles (Fig. 3.12) portray

some similarities. Here, additional nondispersive flat bands develop at the DP for certain magic twist angles due to modulated interlayer hopping.[235–237] This kinetic term is frequently dismissed[204] for the hBN/graphene bilayer, since the hBN bands are situated far from E_F. The twisted bilayer measurements in Figure 3.12c show a double peak structure above E_F, which is most pronounced for AA stacking. Slightly changing the misalignment shifts the position and relative amplitude of the peaks (Fig. 3.12b). Minimal misalignment of my graphene/hBN sample and local changes therein might cause the similar spectroscopic features to arise. This asks for more detailed theoretical analysis of the graphene/hBN interlayer hopping, especially for misalignment angles slightly different from 0°. There has also been a recent study on C defects in the topmost hBN layer and their effect on the LDOS.[238] Hybridization with a graphene C atom results in additional peaks close to E_F, which could therefore also account for some of the STS features.

3.5.3. Conclusion

In summary, the analysis of the sublattice contrast of commensurate graphene on hBN reproduces a very similar structure to the one expected from DFT in some cases. There, the sign of the sublattice symmetry breaking potential inverts going from AA to AB or BA stacking. Different tips and imaging parameters, however, yield alternate sublattice contrast. While the superstructure topography closely resembles the calculated adsorbtion energy, I find an about four times larger value for the corrugation, that is, $90 \pm 10\,\mathrm{pm}$, in agreement with STM measurements in Ref. [161]. Molecular dynamics calculations by van Wijk et al.[193] yield closer values of 30-35 pm. STS measurements portray a rich LDOS structure without a gap at the primary DP, which varies on the superstructure as well as on the atomic scale. This does not match the results of Ref. [184] (Fig. 3.9b), which portrays a much more straightforward change in LDOS with energy. While their own theoretical model reproduces their results, San-Jose et al.[232] only attain similar LDOS patterns by excluding pseudogauge fields. They are likely to be relevant due to strains of the order of 2% and resulting pseudomagnetic fields[206,232] of $5-50\,\mathrm{T}$ within the superstructure. Though obviously dependent on the local strain distribution, they further enrich the electronic structure which agrees much better with my general observations. My specific LDOS patterns do not match those calculated in Ref. [232]. However, tip-sample interaction effects, especially lifting of the graphene, can alter the

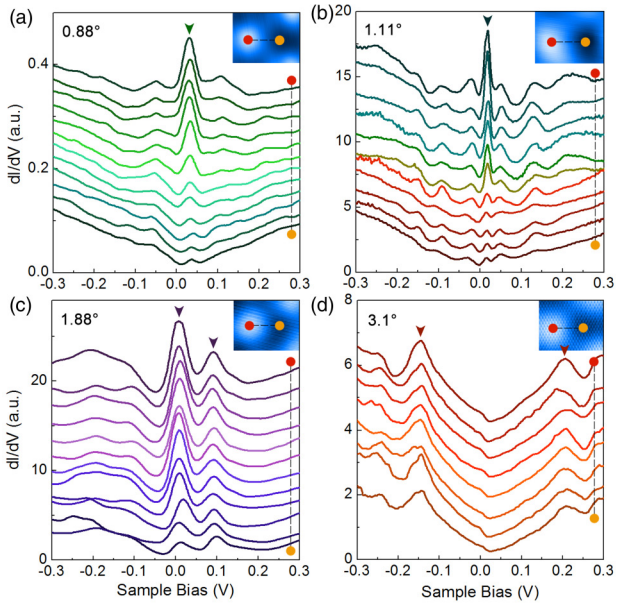


Figure 3.12.: **Scanning tunneling spectroscopy on twisted bilayer graphene.** **(a-d)** Spatial evolution of dI/dV spectra along the dashed lines in STM images of the insets for the twisted bilayers with $\theta = 0.88 \pm 0.03°$ (panel **a**), $\theta = 1.11 \pm 0.05°$ (panel **b**), $\theta = 1.88 \pm 0.08°$ (panel **c**), and $\theta = 3.1 \pm 0.1°$ (panel **d**). The VHSs of the twisted bilayers are marked by arrows in the spectra. For the 1.88° and 3.1° bilayers, the two peaks with energy spacing of 80 and 350 meV, respectively, are the two low-energy VHSs. For the 1.11° and 0.88° samples, a pronounced peak mainly localized in the AA-stacking regions is observed at the charge neutrality point of the spectra, indicating the emergence of nondispersive flat bands. The FWHMs of the peaks for the 1.11° and 0.88° bilayers are 18 and 30 meV, respectively. Reprinted figure with permission from Yin, L. J. et al. *Phys. Rev. B* **2015**, *92*, 081406.[233] Copyright (2015) by the American Physical Society.

local strain significantly[29,194] and thus hamper the observation of the unperturbed sample structure. It is also likely that some of the dI/dV structures stem from tip states. Nonetheless, features which obviously vary on the atomic scale should stem from the sample. The comparison to experiments on twisted bilayer graphene hints at a possibly stronger graphene/hBN interlayer hopping than generally assumed. Also C defects in the hBN can contribute additional LDOS peaks close to E_F.[238]

4. Quantum dots in graphene

This chapter aims at gaining a general understanding of QDs, their characterization and results from the literature, while chapters 5 and 6 portray my own experimental results. A small island of graphene which is only weakly coupled to its environment presents a quasi zero-dimensional electron system or a so-called QD. Here, the diameter of the QD is smaller than the coherence length, which has two important consequences: (i) there are only discrete energy levels (i.e., orbitals) due to size quantization and (ii) the Coulomb interaction between the individual electrons will strongly impact the energy separation of different charge states (sec. 4.1). In GaAs,[239] well-defined QD confinement potentials have been realized which mimic that of a nucleus and thus the QD energy level spectrum is similar to that of real atoms. Hence, those QDs are sometimes called artificial atoms.[240,241]

Confinement in graphene is naturally challenging, as conventional, purely electrostatic electron traps cannot efficiently confine massless Dirac electrons.[34] This phenomenon is called Klein tunneling (see sec. 4.2). Circumventing it by patterning QDs into graphene failed to reproduce the GaAs confinement quality.[67] Energy spectra lack a well-defined orbital structure and there are no signs of the valley degeneracy. While disorder in the bulk was eventually ruled out (see, e.g., Refs. [67, 242–244]), the uncontrolled edge termination and edge structure resulting from the patterning process were identified as main source of undesired localization and scattering. An extensive review on this topic can be found in Ref. [67]. The literature on approaches to introduce smooth confinement in graphene will also be reviewed in the following sections, while addressing purely electrostatically confined whispering gallery modes (WGMs)[170,171,245] and BLG gapped by electric displacement fields.[246–248]

The alternative approach of our choice relies on combining a gap opening magnetic field with a local electrostatic potential (sec. 4.3).[249,250] This smooth electrostatic confinement, comparable to that of conventional gate-induced semiconductor 2DES QDs,[241] has received surprisingly meager attention over the years. It has been difficult to implement

it in exfoliated graphene flakes on Si/SiO_2 substrates, because vertical gate structures defining the QD need to be applied to the flake. The option of pre-patterned bottom gates within the substrate was unfeasible, since the exfoliation of flakes is a random process. Top gates require an additional dielectric layer, which, if deposited by evaporation, would have further reduced the graphene homogeneity in addition to the negative influence of the SiO_2 substrate. The rise of hBN and transferable hBN/graphene/hBN heterostructures overcome these obstacles, but so far no such device has been reported.

Closely related experiments have been concerned with localization in the QH regime. It is well established that the existence and robustness of QH phenomena are intimately linked to disorder.[17,251] Scanning single-electron transistor measurements on a semiconductor 2DES by Ilani et al.[252] were the first to shed light on the local formation of dots and antidots in the valleys and hills of the disorder potential. The same technique was later also applied to graphene by Martin et al.[123,253] revealing the strong impact of Coulomb interactions on localization and screening even though the mobility is two to four orders of magnitude smaller than in high-mobility GaAs samples.[254–257] More highly resolved STM studies on the general QHE in semiconductors[14,258] and graphene on SiC,[259,260] graphite,[261–264] SiO_2[265] and hBN[266] were corroborated by the observation of confinement in disorder or defect induced potentials of, for instance, graphite[267,268] and graphene on graphite,[269,270] on SiO_2,[152] on SiC[271] and on hBN.[194,272] Also probed by STM, strain induced pseudomagnetic fields[28,29,200] can lead to localization.[194] Additionally, transport measurements on metal contact induced pnp junctions[273] and a suspended graphene nanoribbon (GNR)[274] have observed the formation of QDs in the disorder potential at high magnetic fields. However, the challenge of tuning the confinement potential deliberately and characterizing the confined states has remained.

4.1. Quantum dot terminology

In this section I will introduce the important quantities related to QDs, while mainly following Ref. [110]. Within the rather intuitive capacitance model, the electron interaction on the dot and its coupling to additional electrodes is captured by capacitances C_j, where $j = 1, 2, \ldots, J$ denotes the electrodes. Therefore it neglects any more complex electron-electron interaction, for instance, exchange interaction, and assumes that the electrostatic repulsion of the electrons on the QD, that is, the charging energy, increases

by the same value for every additional electron. The results of the capacitance model are identical to those of the constant interaction model.[110] In Figure 4.1a the capacitances between the QD and the source C_S, the drain C_D and the gate electrodes C_{G_i} comprise the total capacitance of the QD $C_\Sigma = \sum_j C_j = C_\mathrm{S} + C_\mathrm{D} + \sum_i C_{\mathrm{G}_i}$. If all capacitances are known, this allows to calculate the (additional) charging energy $E_\mathrm{C} = e^2/C_\Sigma$ required to add an electron to the QD. Under the assumption that the single particle energy levels $\varepsilon_n^{(0)}$ have been obtained from the solution of the quantum mechanical problem with all electrode voltages $V_j = 0$ (i.e., the QD is confined by pure geometrical means), the total energy of the QD with N electrons reads

$$E(N) = \sum_{n=1}^{N} \varepsilon_n^{(0)} + \frac{e^2 N^2}{2C_\Sigma} + |e| N \sum_{j=1}^{J} \frac{C_j}{C_\Sigma} V_j. \tag{4.1}$$

Defining the electrochemical potential to add an electron to a QD with $N-1$ electrons as

$$\mu_N = E(N) - E(N-1) \tag{4.2}$$

$$= \varepsilon_N^{(0)} + \frac{e^2}{C_\Sigma}\left(N - \frac{1}{2}\right) + |e| \sum_{j=1}^{J} \alpha_j V_j \tag{4.3}$$

offers a simple physical interpretation. The chemical potential $\varepsilon_N^{(0)}$ is required to occupy the next single-particle energy state. The second term reflects the total electrostatic repulsion of the electrons on the QD and the last term portrays the impact of a changing electrode voltage V_j, while its effectiveness is captured by the electrode lever arm $\alpha_j = C_j/C_\Sigma$. Note that necessarily $\sum_j \alpha_j = 1$. In most experiments, the electrochemical potential of the QD is continuously tuned by a gate and subsequent changes in the number of electrons on the QD are detected. The respective gate voltage distances ΔV_G capture the addition energy required to add the $N+1$st electron to the dot

$$E_\mathrm{add}(N) = \mu(N+1) - \mu(N) = \Delta + E_\mathrm{C}, \tag{4.4}$$

where Δ is the single particle energy level spacing and $e\alpha_\mathrm{G}\Delta V_\mathrm{G} = E_\mathrm{add}$ is used for conversion.

Suppose the experimental conditions allow us to resolve integer changes in the oc-

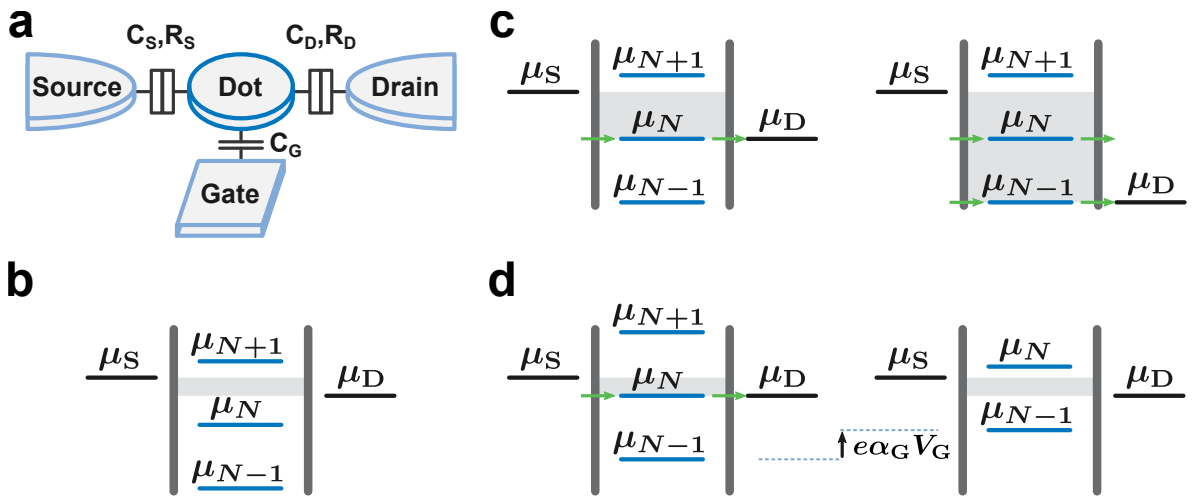


Figure 4.1.: **Modeling transport through a QD. (a)** Sketch of a QD, which is separated from source and drain leads by tunneling barriers with capacitance C_S and C_D and resistance R_S and R_D, respectively. An additional gate capacitively couples to the QD via C_G. **(b)** Schematic relating the electrochemical potentials of source μ_S, drain μ_D, and the QD μ_n (blue lines) for $n = N-1$, N, or $N+1$ electrons on the QD. The difference of μ_S and μ_D (light gray area) marks the bias window. **(c)** Left panel: sufficiently lowering μ_D with respect to panel **b** makes transport via μ_N possible allowing electrons to tunnel (green arrows) from the source to the QD and further to drain. Right panel: Upon reaching $\mu_N - 1$ with μ_D, two charge states may contribute to current in parallel. **(d)** Left panel: μ_N resides inside the bias window. Right panel: By lowering the gate voltage V_G the electrochemical potential of the QD is increased by $e\alpha_G V_G$, where α_G is the gate lever arm. The QD is in the Coulomb blockade regime.

cupation number of the QD, that is: (i) the QD is only weakly coupled to source and drain, ensuing a conductance via the QD of less than e^2/h, and (ii) temperature is small compared to the charging energy, that is, $k_B T \ll E_C = e^2/C_\Sigma$. If additionally (iii) $k_B T \ll \Delta$, then the single-level transport regime is reached. Figure 4.1b corresponds to the energy level structure of the QD system in Figure 4.1a. A finite source-drain bias voltage $V_{SD} = \mu_S - \mu_D$ separates the electrochemical potentials of source μ_S and drain μ_D. This opens a so-called transport bias window (light gray area). As no energy level resides inside the bias window in Figure 4.1b, no transport occurs and this situation is referred to as Coulomb blockade. Now, if we increase the bias window such that a charge state enters, like in Figure 4.1c, an additional electron can tunnel from the source onto the QD (i.e., $N-1 \to N$) and again to the drain electrode (i.e., $N \to N-1$) giving rise to a conductance resonance. Since in the first panel μ_{N+1} lies outside the bias window, an electron raising μ_{N-1} to μ_N will block the QD for any further electron until it

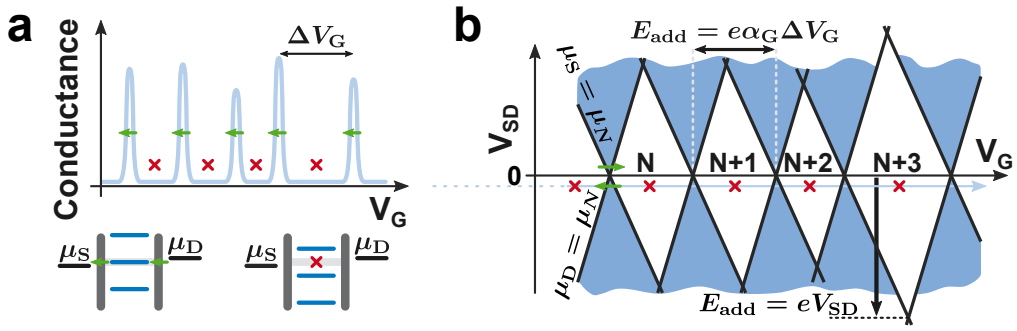


Figure 4.2.: **Schematic relating Coulomb peaks and Coulomb diamonds.** **(a)** Conductance resonances in a gate voltage V_G sweep for small negative bias $V_{SD} = \mu_S - \mu_D$, i.e., $eV_{SD} \ll E_{add}$, corresponding to a horizontal cut through the Coulomb diamonds in panel **b**. Bottom sketches: left, whenever a QD energy level (blue horizontal line) resides between μ_S and μ_D a Coulomb peak appears in the conductance which are marked by green arrows; right, QD in Coulomb blockade, marked by red crosses in the conductance. **(b)** Sketch of the conductance for a single QD in the V_G-V_{SD} plane: blue, finite conductance; white, no conductance; N, $N+1$, $N+2$, $N+3$, occupation number of the QD within the Coulomb diamonds; light blue horizontal arrow, line cut shown in panel **a**; vertical and horizontal black arrows, V_G spacing and V_{SD} value used to extract the addition energy E_{add} as labeled (α_G, gate lever arm). Exemplarily, green arrows indicate direction of current flow and red crosses mark Coulomb blockade regime as defined in panel **a**.

leaves the QD again, which coins the term sequential single-electron tunneling. Further increasing the bias window in the second panel of Figure 4.1c, we see that transport via more (here, two) charge states becomes possible. In Figure 4.1d we keep the bias window constant with respect to Figure 4.1b, but shift the electrochemical potential of the QD up by applying a gate voltage V_G (eq 4.1) to allow transport via μ_N. A further decrease of V_G (second panel) will restore Coulomb blockade again. Thus the sequence of Coulomb peaks produced by a V_G sweep (schematically Fig. 4.2a) will resolve the energy level spectrum of the QD.

Obviously, the size of the bias window will influence the V_G interval in which the QD is conductive. Systematically mapping the conductance in the V_G-V_{SD} plane (schematically Fig. 4.2b) reveals areas with exponentially suppressed conductance,[275] the so-called Coulomb diamonds.[276–278] Within a Coulomb diamond the number of electrons is fixed to an integer number. The edges of the Coulomb diamonds mark the alignment of a QD energy level with either the source ($\mu_S = \mu_N$) or drain ($\mu_D = \mu_N$) electrochemical potential. Different slopes m_1 and m_2 of these lines result from different capacitive couplings to source and drain. In turn, this allows to extract α_S and α_D whenever drain

or source are grounded, respectively. If V_{SD} is applied antisymmetrically, then only $\alpha_S - \alpha_D$ is attainable. However, $1/\alpha_G = |\Delta m| = |m_1 - m_2|$ is independent of the bias configuration.

There are two ways to extract E_{add} from the Coulomb diamonds. First, the touching points of the Coulomb diamonds for $V_{SD} \approx 0\,V$ mark the coincidence of an energy level with μ_S and μ_D. Thus one only needs to convert the distance in gate voltage ΔV_G of two adjacent touching points (black horizontal arrow in Fig. 4.2b) via $E_{add} = e\alpha_G \Delta V_G$, although α_G has to be determined independently. Secondly, the upper and lower tip of a Coulomb diamond mark the bias value where one energy level is aligned to μ_S and another level to μ_D. Hence, on directly finds $E_{add} = eV_{SD}$, as marked by the vertical arrow in Figure 4.2b. For near constant contributions from E_C, the size of the Coulomb diamonds will only vary for significant contributions from Δ to E_{add}. Thus, graphene's fourfold degeneracy would appear as a regular pattern of three smaller diamonds followed by a larger one (see also Fig. 5.4). This basic description of Coulomb diamonds excludes features arising from, for instance, excited states[276,277,279] or cotunneling,[280–282] since they were not observed in my experiments.

4.2. Klein tunneling and electrostatic confinement in graphene

Confinement of relativistic particles touches upon the so-called Klein paradox.[283] It describes the unimpeded penetration of an electron through a potential barrier of width D and height V_0, in case V_0 exceeds the electron's rest energy.[34] Hole-like states inside the barrier align with their conjugated states outside the barrier[284–286] enabling electrons to travel though the barrier as positrons. Owing to their vanishing rest mass, that is, the lack of a band gap, this condition is always fulfilled for electrons in graphene[34] as sketched in Figure 4.3a,b. Hence, Klein tunneling[34,287,288] through any electrostatic potential which is smooth on the atomic scale and thus does not couple the two valleys hinders electron confinement.[26,249,289–292]

Contrasting the case of free electrons in vacuum, momentum conservation and the preservation of chirality make Klein tunneling highly anisotropic in graphene. In particular, the scattering probability for an electron and a hole state from the same valley with identical wave vector is null, because they feature opposite chirality and are thus

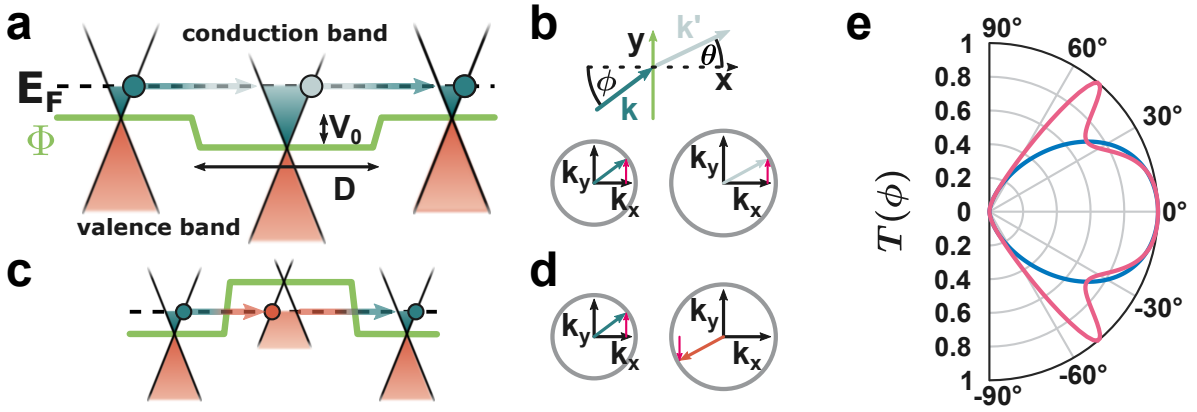


Figure 4.3.: **Klein tunneling in graphene.** **(a)** Sketch of an electrostatic potential Φ (green line) creating a barrier of width D and height V_0. Φ locally shifts the band structure as indicated by the three displaced Dirac cones: petrol, conduction band; orange, valence band. Electrons at the Fermi energy E_F (dark petrol circle) can penetrate the barrier by occupying a different state (gray circle). **(b)** Refraction of the electron at the potential barrier (green arrow). Initial wave vector k, petrol arrow; angle of incidence, ϕ; refracted wave vector, k'; angle of refraction, θ. Left and right circle portray Fermi surface around one K point outside and inside the barrier, respectively. Magenta arrow indicates conserved wave vector component k_y, parallel to the barrier. **(c)** Same as panel **a**, but sketch shows an npn junction. Electron passes the potential barrier as a hole (orange circle). **(e)** Transmission coefficient for a npn barrier with parameters $D = 100\,\mathrm{nm}$, $V_0 = 200\,\mathrm{meV}$. $E_F = 40\,\mathrm{meV}$ (blue line) and $E_F = 80\,\mathrm{meV}$ (magenta line).

orthogonal (see also sec. 3.1). The preservation of this quantity also restricts vertical tunneling between decoupled graphene layers.[293,294] On the other hand, the momentum component parallel to the potential barrier has to be conserved.[35] Therefore, as sketched in Figure 4.3a, $k_y = k_F \sin(\phi) = k_F \sin(\theta) = k'_y$, where ϕ is the angle of incidence and θ the angle of refraction. Since, in general, the Fermi circle inside and outside of the potential barrier will differ in radius, the electron will be refracted. This argument also illustrates the unimpeded transmission in case of normal incidence. For arbitrary ϕ, the transmission coefficient in the limit of a high barrier (i.e., $|V_0| \gg |E_F|$) reads[34]

$$T(\phi) = \frac{\cos(\phi)^2}{1 - \cos\left(D \cdot \sqrt{(V_0 - E_F)^2/(\hbar v_F)^2 - k_y^2}\right)^2}, \tag{4.5}$$

while $k_y = \frac{E_F}{\hbar v_F} \sin(\phi)$. Two examples of $T(\phi)$ are plotted in Figure 4.3e. While the transmission for normal incidence is equal to unity, the additional structure towards larger ϕ also depends on the relation of the Fermi wave length and D. Furthermore,

for $\phi \approx \pm\pi/2$ the transmission becomes very small. This creates the possibility to trap electrons which repeatedly glance off a circular potential, while slowly varying potentials are more efficient.[295] In terms of quantum mechanics, these are states which are well described by an angular momentum quantum number m. STM experiments have confirmed the existence of electrostatically confined small-m states[170,171] as well as WGMs[245] for high m. However, the reported dwell times are extremely short, that is, below 200 fs (< 14 fs in Ref. [170]). Alternatively, it has been suggested to create zero-energy modes[296] by tuning the electrochemical potential outside of the confinement area exactly to the Dirac point and thus creating a barrier region of vanishing DOS. Obviously, this approach is highly susceptible to any disorder and evanescent modes[297] could also facilitate a finite conductivity. Nevertheless, guiding electrons along a GNR defined by detuning a narrow stripe of graphene from the Dirac point has been demonstrated.[298] Similarly, waveguides have been defined in pnp and npn channels.[299] While pure electrostatic confinement is exhausted at this point, I will now turn to the various approaches which utilize a gap in the electronic spectrum of graphene.

4.3. Confinement in gapped graphene

There are basically three main strategies utilizing energy gaps to confine electrons in graphene which will be addressed in sections 4.3.1 - 4.3.3. Robust confinement demands gaps in excess of the potential disorder. Minimum values of the potential fluctuations in suspended samples reach down to 1 meV,[300] while STM measurements on hBN[125,161,162] indicate values of $5 - 10$ meV (one standard deviation). Confining electrons in patterned nanostructures by size quantization (see Fig. 4.4a,b) is the most straightforward approach from a technological point of view. Width modulation along a ribbon of graphene, in principle, allows to tailor the confinement gap (particle in a box). Thereby, electrons can be trapped on small patches of graphene bordered by constrictions, which only allow tunnel-coupling to source and drain leads. In regularly AB stacked bilayer graphene, an electric displacement field D opens up a band gap[301,302] (see Fig. 4.4c,d) and can be used to tune the conductivity in field-effect transistors.[302–307] Finally graphene's Dirac LL spectrum provides a large gap between LL zero and one, that is, already about 50 meV (eq 3.13) at a moderate magnetic field of 2 T (see Fig. 4.4e,f). Additional vertical gates could be used to define QDs.

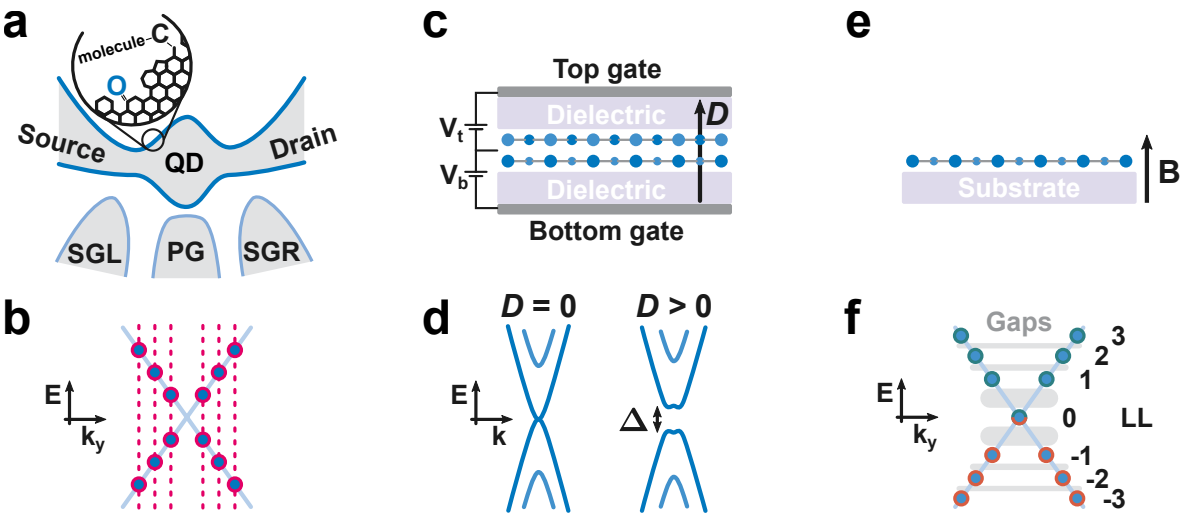


Figure 4.4.: **Three gap opening mechanisms in graphene.** **(a)** Sketch of a width-modulated, patterned graphene QD structure, where constrictions separate the QD from the source and drain leads. Additional gates: plunger gate (PG), side gates left (SGL) and right (SGR). Magnified details showcase edge imperfections created during fabrication: edge roughness, reconstruction and binding of oxygen (blue O) or other molecules. **(b)** Sketch of MLG band structure (light blue lines) at a K point in the k_y direction. Size quantization restricts k_y values to the vertical dashed magenta lines and the remaining states are marked by dots. **(c)** BLG encapsulated by two arbitrary dielectric layers separating it from a top and bottom gate. Applying gate voltages V_t and V_b will create a displacement field D **(d)** Sketch of the band structure of bilayer graphene at a K point. For finite D a band gap Δ opens up. **(e)** Sketch of a MLG subjected to a perpendicular magnetic field B. **(f)** MLG band structure (like panel **b**) under the influence of Landau quantization. Blue and red circles mark electron and hole Landau levels (LLs), respectively, labeled by their index $-3 \ldots 3$. Gray stripes indicate Landau gaps.

4.3.1. Patterned QDs

Electron beam lithography (EBL) and reactive ion etching (RIE) have been perfected in processing semiconductor samples over decades and are widely available. Other niche techniques include LAO[308,309] (see chap. 6), He ion[310] and electron beam sculpting,[311,312] and growth of in-plane hBN-graphene heterostructures.[313,314] While the first three are time-consuming, there have been no reports on devices produced by the latter. I will give an overview of conducted experiments on patterned QDs and refer to Refs. [67, 315] for an extensive review. The idea behind width-modulated graphene nanostructures as sketched in Figure 4.4a is that size confinement opens up an energy gap E_g. For GNRs the gap is theoretically[316–320] and experimentally[321–323] found to be inversely proportional

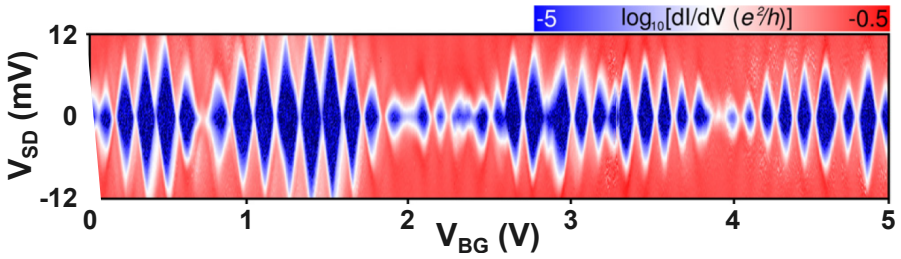


Figure 4.5.: **Coulomb diamonds of an etched BLG QD.** Logarithmic plot of the conductance of a BLG QD with 40 nm diameter (see Refs. [67, 324]) as function of source drain voltage V_{SD} and back gate voltage V_{BG}. $T = 1.3\,\mathrm{K}$, all side gates are grounded. Adopted from Bischoff, D. et al. *Appl. Phys. Rev.* **2015**, *2*, 031301, with the permission of AIP Publishing.[67]

to the width of structure W, that is, $E_{\mathrm{g}}(W) = \alpha/W$, with α in the range of $0.2-1.5\,\mathrm{eVnm}$ depending on the model. Separating the dot from source and drain leads by narrow constrictions with larger E_{g} thereby allows to trap charge carriers on the wider graphene island. Adjacent graphene electrodes can serve as gates (compare Fig. 4.4a).

Besides many examples of more or less irregular Coulomb blockade measurements[67] (see Fig. 4.5, Fig. 6.8d), QDs have exhibited excited states on numerous occasions[67,325] and the related cotunneling has been observed in a few devices.[326–328] Charge detection as a method to read out spin qubits in, for instance, GaAs based double QD systems,[52,329] was first demonstrated by Güttinger et al.[330] Unlike using a second QD for charge detection,[331] they utilized the coupling to a proximate GNR.[330,332] The scheme can also be used for time resolved charge detection and Ref. [333] assessed the charge detector back action on the QD. Moreover, charge relaxation times of 60-100 ns were found by Volk et al.[332] In B field dependent measurements an electron-hole crossover[326,327,334] was detected and the Zeeman splitting was determined,[335,336] while the spin filling sequence did not show a favored spin orientation. Double QDs, in principle designed to realize spin qubits, have shown the expected hexagonal patterns in stability diagrams and finite bias triangles.[337,338]

Though many methods and designs from semiconductor QD experiments have successfully been adopted, results have stayed behind the high expectations. This observation is further corroborated by experiments on GNRs, where, in principle, only the transverse modes are quantized. Transport generally exhibits less regular Coulomb diamonds[322,323,339–342] than found in QDs. This behavior is explained by percolation through electron and hole puddles being disconnected by gapped areas and forming

separate QDs, whose form is additionally energy dependent.[322,343] The expected quantized conductance[317,344–348] has only been observed in the case of a very short suspended GNR.[349]

We see that carving out nanostructures from graphene leaves behind severed edges hosting localized states and crippling the control over the electronic properties. TEM[350,351,354–356] and STM measurements[352,357] of graphene edges, as those shown in Figure 4.6a-c, portray the multitude of realized edge (re)configurations, while tight binding calculations[353,358,359] give a feeling of the strong impact of minor edge roughness (see Fig. 4.6d). It is known from studies on graphite that graphene edges are notoriously reactive and various functional groups can easily bond.[360,361] Of course this can also be exploited in desired functionalization.[362–365] Single missing atoms, protrusions and dents are frequently observed, for instance, at graphite step edges even after repeated annealing[352] (Fig. 4.6c). Hence, it seems impossible to free GNRs, QDs or their constrictions from parasitic localized states. Near perfect edges have so far only been achieved in bottom-up processes like molecular self-assembly of GNRs[366] or unzipping CNTs.[367,368] While STM confirmed the existence of an edge state in the latter case,[369] transport measurements did not go beyond comparatively clean Coulomb diamonds without signs of orbital splittings.[370]

4.3.2. Bilayer graphene gapped by electric displacement fields

Theoretically, displacement fields open a band gap in regular AB stacked BLG with maximum values of $0.25 - 0.3\,\mathrm{eV}$.[21,371,372] Early experiments on SiO_2, with gate structures only covering a strip of the sample, deduced effective transport gaps in the range of a few meV, even at displacement fields up to $2.5\,\mathrm{V/nm}$.[305] Later, $80-130\,\mathrm{meV}$ were reported at displacement field of $|0.85| - |1.23|\,\mathrm{V/nm}$ in hBN encapsulated samples with fully covering top gates.[306,307] In contrast, gap values extracted from angle-resolved photo emission spectroscopy (ARPES)[301] infrared microspectroscopy[302] and SdH-oscillations[373] are in excess of $200\,\mathrm{meV}$. The strong discrepancy between transport and optical absorption measurements on the same sample,[302] that is, a maximum resistance of $\approx \frac{h}{2e^2}$ for a gap of about $250\,\mathrm{meV}$, showcases the existence of parasitic conduction channels inside the gap, especially for the more narrow gate structures. Suspended BLG samples portray increased homogeneity,[374–376] but remaining disorder in the band gap,[300,377,378] edge conductance[379] or domain walls of AB and BA stacked areas[380–382] possibly facilitate

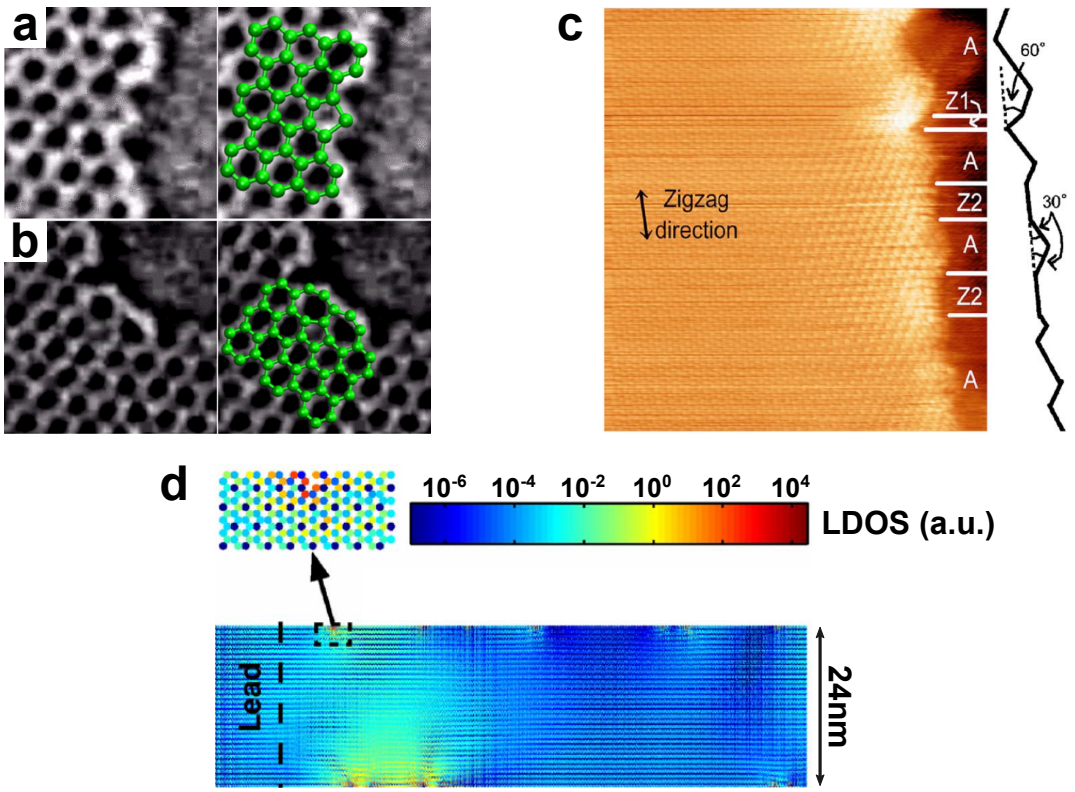


Figure 4.6.: **Atomic reconstructions and localization at graphene edges.**
(a,b) Aberration-corrected TEM image of free-standing MLG (see Ref. [350] for details). Panel **a** and **b** show pentagon and pentagon/heptagon reconstructions, respectively. **(c)** STM image ($14.8\times13.4\,\mathrm{nm}^2$) of a graphite edge after repeated cycles of heat treatment at 800 °C in UHV and subsequent hydrogenation, recorded at $V_{\mathrm{tip}} = -20\,\mathrm{mV}$, $I = 0.7\,\mathrm{nA}$. **(d)** Calculated LDOS at $E = -54\,\mathrm{meV}$ in an armchair GNR of 24 nm width, 150 nm length and 1% defect concentration at the edge (atom removed). Reprinted figure with permission from Koskinen, P. et al. *Phys. Rev. B* **2009**, *80*, 073401 (panel **a,b**),[351] Kobayashi, Y. et al. *Phys. Rev. B* **2006**, *73*, 125415 (panel **c**),[352] Evaldsson, M. et al. *Phys. Rev. B* **2008**, *78*, 161407 (panel **d**).[353] Copyright (2009, 2006, 2008) by the American Physical Society.

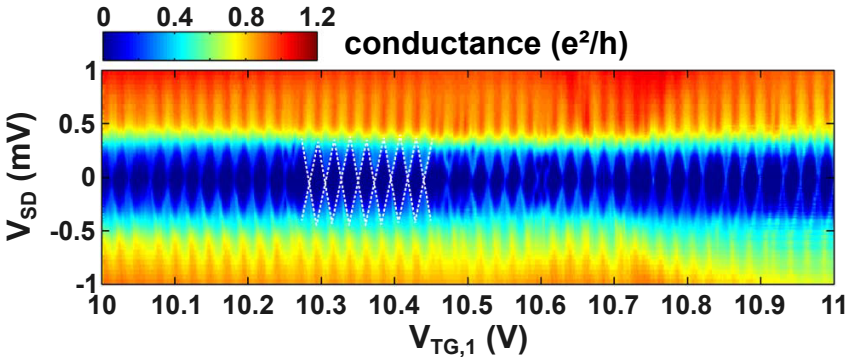


Figure 4.7.: **Coulomb diamonds of an electrostatically defined BLG QD.** Conductance of a BLG QD, defined by a back gate (BG) and a split top gate, as function of source drain voltage V_{SD} and one top gate $V_{\mathrm{TG},1}$. Lithographic dot diameter of 400 nm, $V_{\mathrm{BG}} = -14.4\,\mathrm{V}$, $V_{\mathrm{TG},2} = 11\,\mathrm{V}$, $B = 5.2\,\mathrm{T}$, $T = 110\,\mathrm{mK}$. $E_{\mathrm{C}} \approx 0.4\,\mathrm{meV}$. Adapted by permission from Macmillan Publishers Ltd: Allen, M. T. et al. *Nat. Commun.* **2012**, *3*, 934, copyright (2012).[247]

the residual conductance. Experiments employing corbino-like geometries[383,384] actually disagree with the edge conductance model. Unless a method is developed to eradicate the domain walls, reliably integrating multiple gate-induced QDs on the same bilayer graphene flake is prone to fail. Though single electrostatically defined QDs exhibiting Coulomb blockade have been reported,[246–248] they still lack control over the spin and valley degree of freedom of an individual state. An example of nicely regular Coulomb diamonds without the expected fourfold symmetry is shown in Figure 4.7, notably, recorded at $B = 5.2\,\mathrm{T}$.

4.3.3. QD eigenstates in a large magnetic field

Landau quantization, as discussed in section 3.2, and the entailed Landau gaps (see Fig. 4.4f) present the basis for an alternative confinement scheme, which has been addressed theoretically in multiple publications[249,250,292,385–391] starting in 2007. Introducing a local electrostatic potential $\Phi_{\mathrm{gr}}^{\mathrm{el}}$ in graphene will create states which peak inside of it, however, due to Klein tunneling these states have extended oscillatory tails.[250] The uniform magnetic field suppresses these tails exponentially through the Landau gaps and thereby creates confined states. The eigenenergy of these states $\varepsilon_i(\Phi_{\mathrm{gr}}^{\mathrm{el}})$ will shift with respect to the bulk LL energies (eq 3.13), that is, $\Phi_{\mathrm{gr}}^{\mathrm{el}}$ breaks the orbital degeneracy of the LLs.[270] Of course the exact shape of $\Phi_{\mathrm{gr}}^{\mathrm{el}}$ is pivotal for the resulting energy level spectrum and the single-particle orbitals.

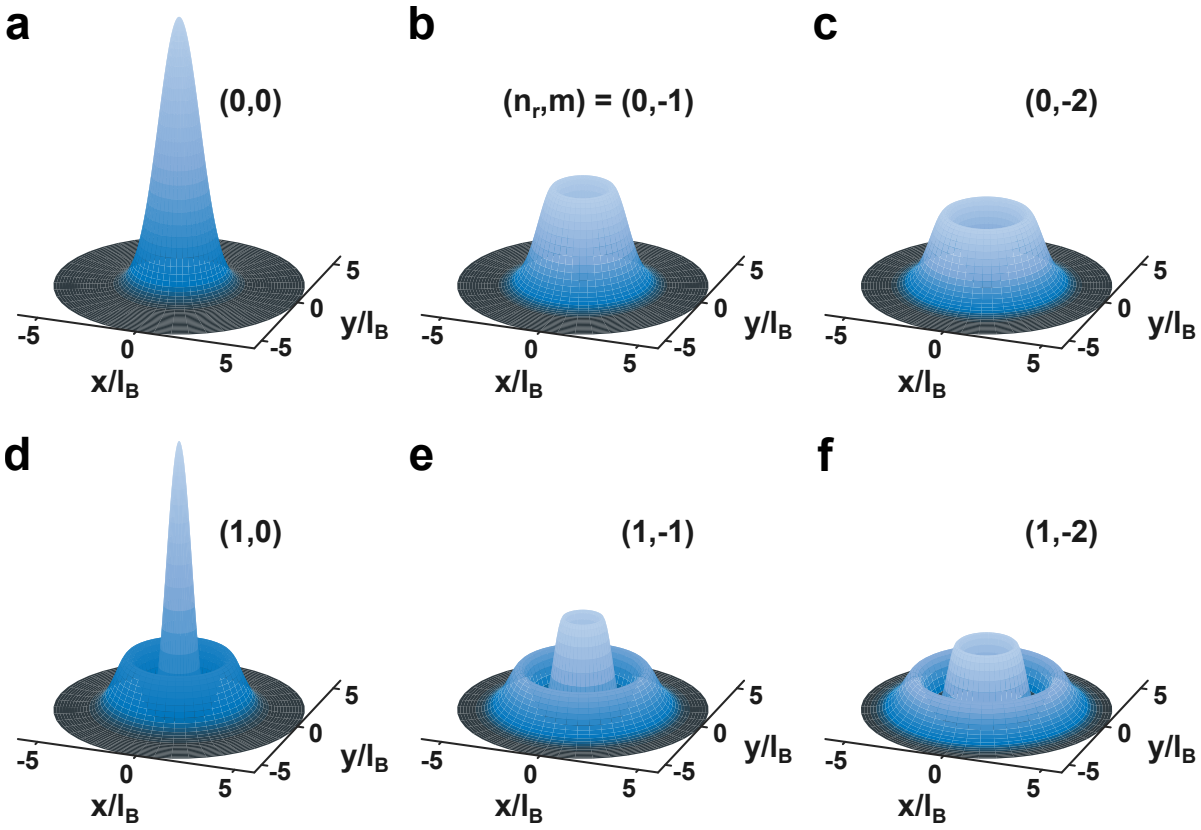


Figure 4.8.: **Landau level wave functions in the symmetric gauge. (a-f)** Square of the wave functions $|\Psi_{n_r,m}|^2$ (see eq 4.9) for different radial n_r and angular momentum m quantum numbers as labeled. Plots cover an area with radius $6 \cdot l_B$. Height scale identical for all plots, color scaled individually.

I will next describe the QD states and the energy level spectrum theoretically. The tip-induced potential will modify the bulk LL wave functions (eq 3.15), though the QD states inherit their general structure. Inspecting the ideal, unperturbed wave functions makes it easier to categorize the TB wave functions later, for instance, with respect to their valley index and angular momentum. The bulk LL wave functions on one sublattice provided in Ref. [26] read

$$\Psi_{N_{LL}}(\xi) = 2^{-N_{LL}/2}(N_{LL}!)^{-1/2} \exp(-\xi^2/2) H_{N_{LL}}(\xi), \tag{4.6}$$

where $\xi = y/l_B - l_B k$ is a dimensionless length scale, $l_B = \sqrt{\hbar/eB}$ is the magnetic length and $H_{N_{LL}}$ is a Hermite polynomial. Amending the wave functions in eq 4.6 by a factor of $\pi^{-1/4}$ makes them so called Hermite functions, which are then orthonormal and satisfy

the differential equation of a one-dimensional quantum mechanical harmonic oscillator

$$\Psi''_{N_{\mathrm{LL}}}(r) + (2N_{\mathrm{LL}} + 1 - r^2)\Psi_{N_{\mathrm{LL}}}(r) = 0. \tag{4.7}$$

This was derived by Landau in 1930,[392] while solving the Schrödinger equation for a free electron in a homogeneous magnetic field, which boils down to the harmonic oscillator problem. Therefore, the wave functions in the symmetric gauge

$$\vec{A} = \frac{B}{2}(-y, x) \tag{4.8}$$

can be derived from the known Fock-Darwin states[241,393–395] and in polar coordinates read[396]

$$\Psi_{n_\mathrm{r},m}(r,\theta) = \frac{e^{-im\theta}}{\sqrt{2\pi}l_\mathrm{B}}\sqrt{\frac{n_\mathrm{r}!}{(n_\mathrm{r}+|m|)!}}e^{-\frac{1}{4}\frac{r^2}{l_\mathrm{B}^2}}\left(\frac{1}{\sqrt{2}}\frac{r}{l_\mathrm{B}}\right)^{|m|} L_{n_\mathrm{r}}^{|m|}\left(\frac{1}{2}\frac{r^2}{l_\mathrm{B}^2}\right), \tag{4.9}$$

where $L_n^m(x)$ is a generalized Laguerre polynomial and $n_\mathrm{r} \in \mathbb{N}_0$ and $m \in \mathbb{Z}$ are the radial and angular momentum quantum number, respectively. Two wave functions with $(n_\mathrm{r}, \pm m)$ only differ by a phase factor $e^{-im\theta}$. In Figure 4.8 I show a few examples of the squared wave function $|\Psi_{n_\mathrm{r},m}|^2$, which are scaled to the characteristic length l_B. While n_r determines the number of radial nodes, increasing $|m|$ increases the distance of the first maximum to the center. Identifying the possible combinations for a given N_{LL}[250,396,397] yields the restriction

$$|N_{\mathrm{LL}}| = n_\mathrm{r} + 1/2 \cdot (m + |m|)\,, \tag{4.10}$$

with $0 \leq n_\mathrm{r} \leq |N_{\mathrm{LL}}|$ and $m \leq |N_{\mathrm{LL}}|$. Note that without an additional potential, for instance, resulting from disorder or being tip-induced, the different m states are degenerate. Adding such a potential, states with small $|m|$ exhibiting the most central probability density (see Fig. 4.8) will shift more strongly in energy than states with higher $|m|$ as long as the potential is not smooth on the scale of a few l_B. This will lead to the observation of orbital splittings in chapter 5.

5. Tip-induced quantum dots in commensurate graphene on hBN

This chapter has been published in parts in:

Electrostatically Confined Monolayer Graphene Quantum Dots with Orbital and Valley Splittings
N. M. Freitag, L. A. Chizhova, P. Nemes-Incze, C. R. Woods, R. V. Gorbachev, Y. Cao, A. K. Geim, K. S. Novoselov, J. Burgdörfer, F. Libisch, M. Morgenstern
Nano Letters **2016**, *16*, 5798-5805
© 2016 American Chemical Society

So far, I have portrayed that various approaches to create graphene QDs mainly based on nanostructuring or gate-induced gapping of bilayer graphene have not overcome fundamental limitations in device control. While the measurements show Coulomb blockade physics, the detrimental effects of edge roughness in patterned devices or remaining disorder in the displacement gap of BLG prohibit the control over the spin or valley degree of freedom of the QD state. Hence, one of the main requirements for qubit applications in graphene[58,60] has not been met yet.

Local probe techniques like STM offer to manipulate the band structure of weakly screened materials beneath the tip by acting as a gate electrode. Even though this perturbation is generally undesired, it can be utilized to confine charge carriers in semiconductors[68,258,398,399] and map the interaction of the sample with the tip-induced QD.[69,400] In graphene, however, the lack of a band gap results in extremely short dwell times[170,171] ($< 200\,\mathrm{fs}$) for purely electrostatic confinement.

In this chapter I will discuss the creation and characterization of smoothly confined quantum dots in graphene on hBN, which avoid many previously discussed drawbacks, that is, substrate and edge disorder, and exhibit a greatly improved control over the con-

fined wave functions. The electrons are trapped by a combination of LL gaps and an electrostatic potential.

As sketched for my experiments in Figure 5.1a, an STM tip is the source of the smooth confinement potential $\Phi_{\mathrm{gr}}^{\mathrm{el}}(r)$ (green line). The corresponding band bending $E_{\mathrm{gr}}(r)$ and resulting formation of the QD is portrayed in Figure 5.1b. Landau quantization in the perpendicular external magnetic field forms band gaps, the largest being the LL_0-$\mathrm{LL}_{\pm1}(7\,\mathrm{T}) \approx 100\,\mathrm{meV}$ gap. By lifting the orbital degeneracy of the bulk graphene LLs, the tip-induced potential embeds localized states (thin blue lines) within this gap. In principle, such a smooth symmetric confinement potential creates a well-ordered sequence of orbitals and suppresses intervalley scattering, because it changes only slowly on the atomic scale.

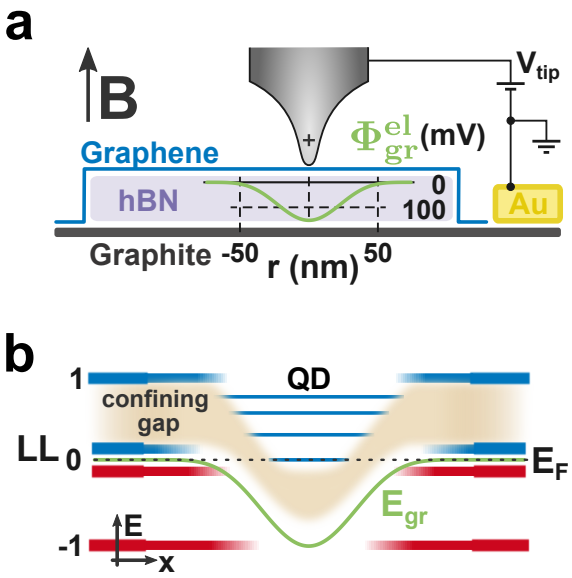


Figure 5.1.: **Confinement in LL gaps.** **(a)** Sketch of my experiment. A 30 nm thick hBN layer partially separates the graphene from the graphite layer. The applied tip voltage V_{tip} induces a potential $\Phi_{\mathrm{gr}}^{\mathrm{el}}(r)$ (green line) in the graphene, calculated as solution of Poisson's equation (sec. 5.2). The external magnetic field B induces Landau quantization. **(b)** Real space energy diagram aligned to panel **a**: states belonging to electron (hole) LLs, blue (red); bulk LLs, 1, 0, -1; local band bending E_{gr}, green line; QD states embedded in the LL_0-LL_{+1} gap, thin blue lines; Fermi energy E_{F}, black dotted line.

By sweeping the tip voltage, confined states are gated across the Fermi energy and create sequences of charging peaks in dI/dV by means of Coulomb staircases (sec. 5.1). The predominant grouping of these Coulomb peaks in quadruplets (sec. 5.4) reflects the fourfold spin-valley degeneracy of graphene (sec. 5.1.1). The varying stacking orders and strain configurations of commensurate graphene on hBN locally render a different sublattice energetically favorable, thus confined states of valley index $\mathbf{K}$ and $\mathbf{K}'$ will separate in energy. Whenever this valley splitting significantly exceeds the Zeeman splitting and temperature, I observe an additional separation of quadruplets into doublets (sec. 5.4.2). In principle, this makes these QDs suitable as building blocks for spin qubits. Moreover, the STM allows to raster the trapped electrons across the graphene superstructure. Thereby I

can map the changes in orbital and valley splittings. On the one hand, this reveals the giant tunability of the valley splitting of more than 7 meV, exceeding the highest reported values[70] for any potentially nuclear spin-free host material by more than an order of magnitude. On the other hand, higher orbital states exhibit signatures of local avoided valley crossings (sec. 5.4.3), which indicates superpositions of **K** and **K′** states. Moving the QD fast enough such that states evolve coherently across the anti-crossing would even also allow for Landau-Zener-Stückelberg interferometry.[401,402] Moreover, the observed valley splitting gradients potentially enable all-electric gate operations on qubit states utilizing the valley degree of freedom.[64,403–405]

Since there is no independent probe of the tip-induced QD enabling the determination of its lateral extent or the confinement potential, I use a Poisson solver to estimate the tip-induced potential and the capacitive couplings of the QD to surrounding electrodes (sec. 5.2). Florian Libisch and Larisa Chizhova implemented the derived tip-induced potential within their TB framework[196,406] to model the QD within the commensurate graphene (sec. 5.3), which provides viable insight on the details of the confined states. Additionally, I cover the impact of charging of hBN defect states on my measurements (sec. 5.4.4), LL features observed in STS (sec. 5.4.5) and finally draft a transport device scheme (sec. 5.5) based on the showcased confinement mechanism.

5.1. Probing the QD addition energy spectrum with the STM - the Coulomb staircase

So far, I have discussed the characterization of QDs in a transport configuration, implicitly focusing on nanostructured graphene QDs. I will now relate these to STM measurements on their tip-induced counterparts and present a detailed microscopic picture of the tip-QD interaction. Figure 5.2a shows a sketch of the STM configuration. The graphene surrounding the dot and the STM tip serve as source and drain electrodes, respectively. Vertical tunnel-coupling of the QD states to the graphite electrode is virtually null due to the 30 nm thick BN flake.[407] In contrast to many transport measurements, the two involved tunneling barriers are strongly asymmetric. While the dot-graphene tunnel-coupling will be some multiple of h/e^2, that is, $R_{\mathrm{gr}} < 1\,\mathrm{M\Omega}$, the vacuum tunneling barrier to the tip is $R_{\mathrm{tip}} \approx 1\,\mathrm{G\Omega}$. Therefore, electrons will tunnel much faster between the QD and graphene than to or from the tip. Consequently, I also neglect any

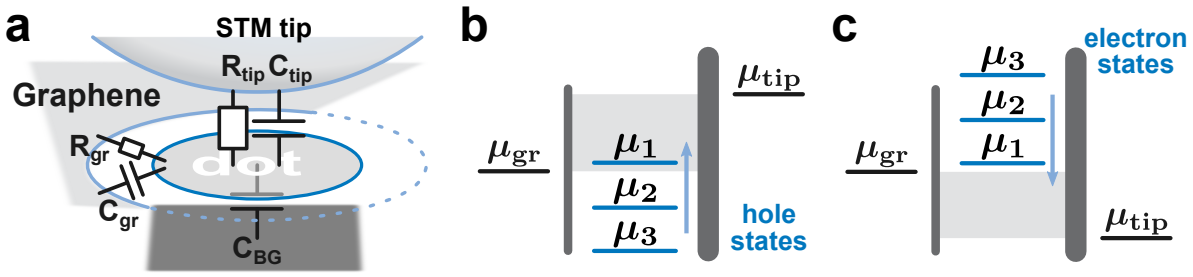


Figure 5.2.: **Schematic STM measurement configuration for a tip-induced QD.** **(a)** Sketch of an STM tip above a graphene sheet (light gray) and a back gate (BG) electrode (dark gray). The tip-induced QD, labeled 'dot', couples to the surrounding graphene via a tunneling resistance R_{gr} and capacitance C_{gr}, to the tip via R_{tip} and C_{tip} and to the BG via C_{BG}. **(b,c)** Energy diagram relating the electrochemical potential of graphene μ_{gr}, different QD charge states (blue lines) μ_{N} and tip μ_{tip}. Light gray box marks the bias window. Vertical gray lines represent the tunneling barriers, while their relative size indicates $R_{\mathrm{tip}} \gg R_{\mathrm{gr}}$. Light blue arrows indicate the gating effect of the tip on the QD states upon further increasing (panel **b**) or decreasing (panel **c**) μ_{tip}.

additional resistances in series (Au-electrode, graphite, bulk graphene) or any effect of the DOS of bulk graphene or graphite.

The close proximity of the metallic tip and the induced QD, that is, about 6 Å tip-sample distance, makes the tip an efficient gate. Consequently, changes in V_{tip} strongly influence the QD energy level spectrum. Ultimately, the QD disappears for vanishing electric field between tip and graphene. If the electrochemical potential of the tip μ_{tip} exceeds that of graphene μ_{gr} (Fig. 5.2b), the tip will be negatively charged and hole states localize underneath the tip. By further increasing μ_{tip} these states will be gated into the bias window from below. This means that μ_N will never coincide with μ_{tip} and therefore it is impossible to directly capture the energies of the QD states in dI/dV_{tip} spectra. The analogous case for confined electrons is portrayed in Figure 5.2c.

However, exploiting the gating capabilities of the STM tip opens up a different detection scheme. Adopting the argument from Ref. [100], I will extend the above stated picture for the case of electron confinement, that is, positive V_{tip}, since the reasoning is analogous for hole confinement. Increasing V_{tip} (orange arrow in Fig. 5.3) shifts the states underneath the tip energetically down. States originating from LLs with positive index are embedded in the LL_0-LL_{+1} gap which provides electrostatic confinement (Fig. 5.3a, see also Fig. 5.1b). Within the bias window $eV_{\mathrm{tip}} = \mu_{\mathrm{gr}} - \mu_{\mathrm{tip}}$, electrons tunnel from the sample into unoccupied states of the tip. One current path (dashed

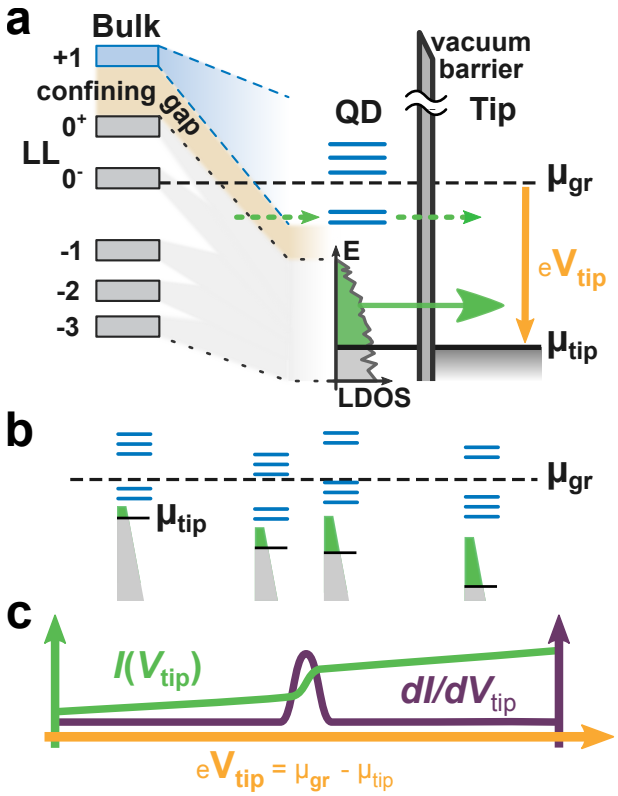


Figure 5.3.: **Sketch of the Coulomb staircase.** The chemical potentials of graphene μ_{gr} (black dashed line) and tip μ_{tip} (black solid line) define the bias window eV_{tip}, within which graphene states tunnel into empty tip states. There are two current paths available: (i) a weak one (green dashed arrow) via quantum dot states (blue lines), (ii) a dominant one (solid green arrow) via states strongly coupled to the graphene bulk (marked LDOS). Left: bulk graphene LLs away from the tip-induced band bending. **(b)** Schematic diagram of change in QD energies (blue lines) and quasi-continuous LDOS underneath the tip (green and gray triangle) for increasing V_{tip} from left to right. Between the second and third frame, the QD changes its charge state shifting the energy of the QD states and the entire LDOS upwards. **(c)** Tunneling current I displaying the staircase (green line) and differential conductance dI/dV (purple line) for increasing V_{tip} (aligned with panel **b**).

green arrow Fig. 5.3a) passes through states of the QD (blue lines). The other stronger current path (solid green arrow Fig. 5.3a) originates from the quasi-continuous LDOS at lower energies where energetically overlapping LL states strongly couple to the graphene bulk. Though increasing V_{tip} gates QD states down (Fig. 5.3b), the Coulomb gap around E_{F} always separates the highest occupied from the lowest unoccupied state, prohibiting continuous charging of confined states. It is only when the next unoccupied level crosses μ_{gr} that the QD is charged by an additional electron. The electrostatic repulsion due to its charge abruptly increases the Hartree energy of all states, thereby shifting additional graphene states from below μ_{tip} into the bias window (Fig. 5.3b, central transition). Consequently, the tunneling current I increases which translates to a charging peak in dI/dV_{tip} (Fig. 5.3c). This mechanism is called Coulomb staircase[408] and has been observed previously, for instance, for charging of clusters within an STM experiment.[409] In essence, charging peaks in dI/dV signal the coincidence of a charge level of the QD with μ_{gr}[99] and thus provide a clear signature of the addition energy spectrum of the QD.

5.1.1. Signature Coulomb peak sequence of an ideal graphene QD

In graphene QDs, lifting the orbital, valley or spin degeneracy impacts the energy level spectrum. Figure 5.4a portrays the case where, for instance, the confinement potential exclusively induces an orbital splitting Δ_1^{o}. The two split states remain spin and valley degenerate (indicated by the four small black arrows). Subsequently filling these states with electrons by gating them across E_{F} will produce the Coulomb peak sequence shown in Figure 5.4b. The first four peaks are split by E_{C}, because the single particle energy contribution to E_{add} is zero. Since the fifth electron has to occupy the next orbital, that is, now Δ^{o} contributes to E_{add}, the fourth and fifth peak show a larger spacing. More generally, in the case of graphene peaks will group in quadruplets.

By introducing a sublattice-discriminating substrate interaction, for instance, by aligning graphene to hBN, one can create an additional valley splitting Δ^{τ} as sketched in Figure 5.4d. Consequently, the quadruplets will exhibit a generally differing additional splitting, reducing the spacing of adjacent quadruplets. As shown in Figure 5.4c, Δ^{o} cannot be unambiguously determined from the quadruplet spacing in this case, while Δ^{τ} is attainable. Subjecting the QD to an external B field, which naturally also contributes to Δ^{o},[393] will add a Zeeman splitting Δ^{σ}. If $\Delta^{\tau} \ll \Delta^{\sigma}$, quadruplets should again split into doublets, but here one expects no difference between the quadruplets. If $\Delta^{\tau} \gg \Delta^{\sigma}$,

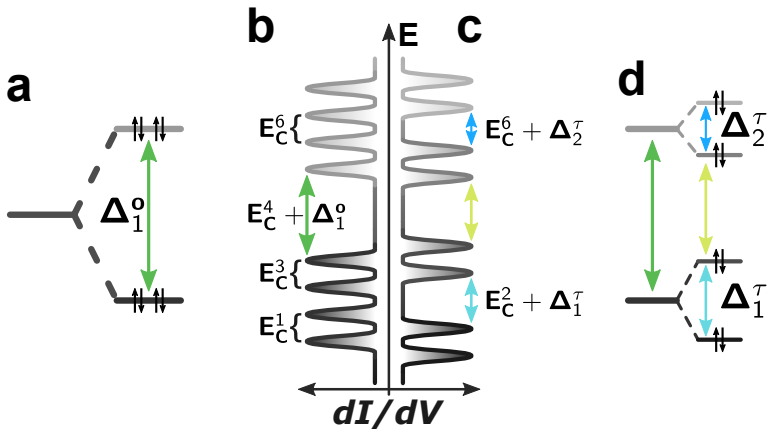


Figure 5.4.: **Single particle energy spectrum and Coulomb peak sequence.** **(a)** Energy level diagram for the first two orbital states of a graphene QD exhibiting an orbital splitting Δ_1^o. Both orbitals are fourfold degenerate, as indicated by black arrows representing physical spin. **(b,c)** Charging peak sequence in the differential conductance dI/dV corresponding to the level diagrams in panel **a** and **d**, respectively. Charging peaks are separated by the addition energy $E_{\mathrm{add}}^i = E_{\mathrm{C}}^i + \Delta_i$, where $E_{\mathrm{C}}^i \approx E_{\mathrm{C}}$ is the charging energy and Δ_i is comprised of Δ_j^o and/or the valley splittings Δ_k^τ. In panel **b** quadruplet ordering showcases a dominant Δ_1^o, while Δ_k^τ become sizable in panel **c**, further separating quadruplets into doublets. **(d)** Same as panel **a**, but including additional Δ_k^τ. The spin splitting Δ^σ is neglected, as $\Delta^\sigma < \Delta_k^\tau, \Delta_j^o, E_{\mathrm{C}}$ in experiment.

Δ^σ only adds a minor contribution to the splitting within the valley-split doublets. Figure 5.4 purposely shows the situation later encountered in graphene on hBN, where at 7 T Δ^o is about $4 - 10$ meV, Δ^τ is generally smaller but locally up to 10 meV and thus exceeds $\Delta^\sigma = g\mu_{\mathrm{B}}B \approx 800\,\mu\mathrm{eV}$ ($g = 2$).

5.2. Poisson calculations

Investigating tip-induced QDs in an STM setup with no additional gates lacks an independent probe of the tip-sample interaction. Moreover, the tip cannot access the environment of the QD. Therefore, I estimate the electrostatic couplings of the different electrodes in Poisson calculations. Without this information the tip lever arm α_{tip} remains unknown and it is not possible to deduce E_{add} from the measured peak spacings in V_{tip}. Additionally, the form of the tip-induced potential in graphene $\Phi_{\mathrm{gr}}^{\mathrm{el}}(r)$ was required for the TB calculations of the confined states in section 5.3.

Poisson calculations using the finite-difference method were implemented in Matlab

based on Ref. [410] and adopted for cylinder symmetric problems. Starting point for the solver was a program written by Christian Holl, which I modified quite thoroughly. The problem is modeled in the $\rho - z$ plane by (i) the edge boundary conditions, being either of the Dirichlet (fixed potentials), Neumann ($d\Phi^{\mathrm{el}}/d\vec{n} = 0$, where $\vec{n}$ is the outward-pointing unit normal vector) or constant normal gradient type ($d^2\Phi^{\mathrm{el}}/d\vec{n}^2 = 0$); (ii) assigning different dielectric constants, for instance, $\varepsilon_{\mathrm{hBN}} = 4$ for hBN and $\varepsilon_{\mathrm{gr}} = 2.5$ for graphene; (iii) defining materials with free charges, here, graphene's DOS (eq 3.11) and temperature through the Fermi Dirac distribution; (iv) setting up other electrodes with fixed Φ_{el} like the tip, effectively amending the Dirichlet boundary conditions. The induced charge density $q(\mathbf{r})$ on the graphene electrodes and the electrostatic potential solution $\Phi_{\mathrm{el}}(\mathbf{r})$ to Poisson's equation related by

$$\Delta\Phi_{\mathrm{el}}(\mathbf{r}) = -\frac{q(\mathbf{r})}{\varepsilon}, \tag{5.1}$$

where $\varepsilon = \varepsilon_0 \cdot \varepsilon_{\mathrm{r}}$, are found by iterating two steps. First, $\Phi_{\mathrm{el}}(\mathbf{r})$ is found by numerical matrix inversion. Then charges are redistributed according to this $\Phi_{\mathrm{el}}(\mathbf{r})$. Typically only 10-15% of the change relative to the last iteration is used to achieve smooth convergence. This is done until the relative changes in $\Phi_{\mathrm{el}}(\mathbf{r})$ and $q(\mathbf{r})$ drop below a threshold value, typically 0.2-0.5 % integrated over the whole QD. The next two sections will portray the results for $\Phi^{\mathrm{el}}_{\mathrm{gr}}(r)$ and the capacitance between the QD and the other electrodes.

5.2.1. Tip-induced potential in graphene

A typical set of parameters to simulate $\Phi^{\mathrm{el}}_{\mathrm{gr}}(r)$ includes a tip radius $r_{\mathrm{tip}} = 120\,\mathrm{nm}$, a tip opening angle $\gamma = 30°$, a tip sample distance $Z = 6\,\text{Å}$, the thickness of the hBN layer $t_{\mathrm{hBN}} = 30\,\mathrm{nm}$, the dielectric constants of hBN $\varepsilon_{\mathrm{hBN}} = 4$ and graphene $\varepsilon_{\mathrm{gr}} = (4+1)/2 = 2.5$, a magnetic field $B = 0\,\mathrm{T}$ or $7\,\mathrm{T}$ modifying the DOS of graphene, which additionally incorporates $\sigma = 3\,\mathrm{meV}$ Gaussian disorder broadening and a temperature of $T = 8\,\mathrm{K}$. The grounded graphite is modeled by the boundary condition $\Phi^{\mathrm{el}}(z = 0\,\mathrm{nm}) = 0\,\mathrm{V}$. Figure 5.5a shows an exemplary converged solution of the resulting potential (color code) with the potential within the graphene layer $\Phi^{\mathrm{el}}_{\mathrm{gr}}(r)$ shown as green overlay.

I perform calculations with varying tip potential to find the relation $\Phi^{\mathrm{el}}_0(V_{\mathrm{tip,eff}})$ in Figure 5.5b, which I use to translate tip-induced potential amplitudes Φ^{el}_0 to tip voltages and vice versa. Here, I use the effective tip voltage $V_{\mathrm{tip,eff}} = V_{\mathrm{tip}} + \Delta\Phi/e$, to simplify

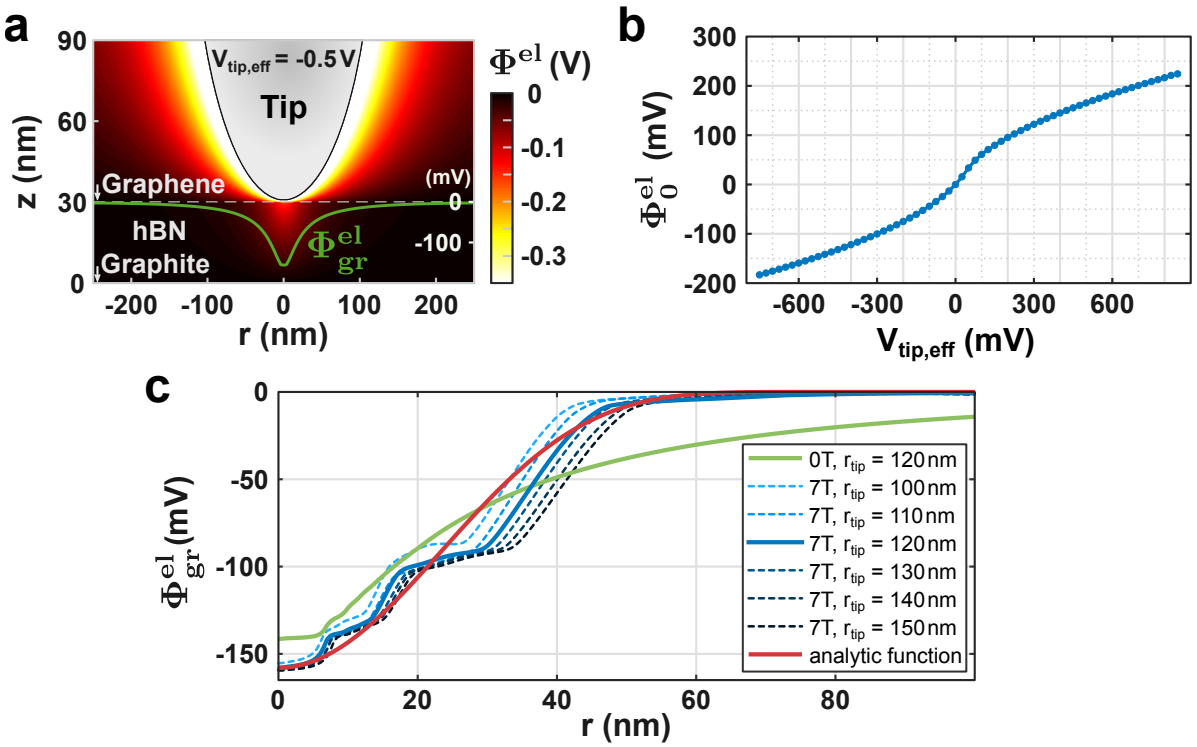


Figure 5.5.: **Poisson calculations of the tip-induced potential.** **(a)** Converged numerical solution of Poisson's equation modeling the STM tip ($r_{\mathrm{tip}} = 120\,\mathrm{nm}$, tip-sample distance $Z = 6\,\text{Å}$) over graphene ($\varepsilon_{\mathrm{gr}} = 2.5$, $\nu_{\mathrm{F}} = 1 \times 10^6\,\mathrm{m/s}$) on hBN ($\varepsilon_{\mathrm{hBN}} = 4$, $t_{\mathrm{hBN}} = 30\,\mathrm{nm}$) on graphite (potential fixed to ground) at $B = 0\,\mathrm{T}$. Induced confinement potential in the graphene layer $\Phi^{\mathrm{el}}_{\mathrm{gr}}(r)$ as green overlay (axis on the right). **(b)** Tip-induced potential amplitude Φ^{el}_0 depending on the effective applied tip voltage $V_{\mathrm{tip,eff}}$, which includes possible work function differences between graphene and tip at $B = 0\,\mathrm{T}$. Every dot corresponds to a separate calculation. **(c)** Change in $\Phi^{\mathrm{el}}_{\mathrm{gr}}(r)$ for varying r_{tip} and applied magnetic fields. Red curve portrays the potential used in the TB calculation corresponding to eq 5.2, which is adapted to the $\Phi^{\mathrm{el}}_{\mathrm{gr}}(r)$ at 7 T.

the discussion by making the applied tip voltage V_{tip} independent of any work function difference $\Delta\Phi = \Phi_{\mathrm{tip}} - \Phi_{\mathrm{graphene}}$, which only presents an offset. Note, since in the measurements $|V_{\mathrm{tip}}| \leq 1\,\mathrm{V}$, it is sufficient to consider the capacitive coupling of the QD to the surrounding graphene and to the BG within $|\Phi^{\mathrm{el}}_0| < 300\,\mathrm{mV}$ (sec. 5.2.2).

I also estimate the effect of B on the band bending. Therefore I implement LLs into graphene's DOS at energies following eq 3.13, degeneracy $n_{\mathrm{LL}} = 4 \times \frac{e}{hB}$, and smoothed by a Gaussian with standard deviation $\sigma = 3\,\mathrm{meV}$. The main effect of the increased DOS close to E_{F} is a reduction of the radial tail of the induced potential, as seen in Figure 5.5c.

I use the results at $B = 7\,\mathrm{T}$ to deduce an analytic function for the induced potential

(red curve in Fig. 5.5c) reading

$$\Phi_{\mathrm{gr}}^{\mathrm{el}}(\Phi_0^{\mathrm{el}}, r) = \Phi_0^{\mathrm{el}} \cdot \cos\left(\frac{\pi r}{2\Phi_0^{\mathrm{el}}} \cdot \frac{10^6}{0.32 + \left(\frac{0.005 + \left|\Phi_0^{\mathrm{el}}\right|}{0.04}\right)^{-1.2}}\right)^5, \tag{5.2}$$

r in [m] is the radial distance to the center of the tip. This simplifies the implementation into the TB calculations (sec. 5.3), because Φ_0^{el} is the only free parameter. The cosine shape was motivated by work of Maksym et al.,[387] while the regularly suggested Gaussian[250] would only suit tips with very small radii $r_{\mathrm{tip}} \leq 20\,\mathrm{nm}$. The tip radius is the main parameter to match theory and experiment. Using $\Phi_{\mathrm{gr}}^{\mathrm{el}}(r)$ from a tip with $r_{\mathrm{tip}} = 70\,\mathrm{nm}$ in the TB calculations did not reproduce the experimental observations, that is, too few states crossed E_{F} in the relevant V_{tip} interval. However, for a larger tip with $r_{\mathrm{tip}} = 120\,\mathrm{nm}$, we reach agreement. Also note that the results for $\Phi_{\mathrm{gr}}^{\mathrm{el}}(r)$ only vary slightly for $100\,\mathrm{nm} \leq r_{\mathrm{tip}} \leq 150\,\mathrm{nm}$ as shown in Figure 5.5c. In the same plot the size of the QD can be estimated from the FWHM of $\Phi_{\mathrm{gr}}^{\mathrm{el}}(r)$ resulting in a radius of $r_{\mathrm{dot}} = 25 \pm 5\,\mathrm{nm}$. This will be used in the next section to deal with the capacitive coupling of the QD to the other electrodes.

5.2.2. Coupling of the quantum dot to the other electrodes

After estimating the dot radius, I can calculate the capacitances of the dot to the other electrodes to eventually deduce $\alpha_{\mathrm{tip}} = C_{\mathrm{tip}}/C_{\Sigma}$, where C_{Σ} is the total capacitance of the dot. Three different scenarios (Fig. 5.6) are employed to find the contributing capacitance between QD and tip C_{tip}, QD and surrounding graphene C_{gr} and QD and back gate C_{BG}. One electrode is set to a fixed potential Φ^{el} and via the induced charge Q on the other I can calculate $C = Q/\Phi^{\mathrm{el}}$. The different boundary conditions are indicated in Figure 5.6. In case of C_{BG} (Fig. 5.6c), the top boundary models the constant electric field in front of an infinitely extended charged plate. Graphene is always modeled with its bulk density of states (eq 3.11). For C_{tip} (Fig. 5.6a) and C_{BG} (Fig. 5.6c) I fixed the tip potential Φ_{tip} and BG potential Φ_{BG}, respectively, and extract the induced charge on the QD (blue). For C_{gr} (Fig. 5.6b) Φ_{QD} is fixed and the induced charge within a cutoff radius of 50 nm into the surrounding graphene is used.

The impact of different parameters, that is, $r_{\mathrm{tip}} = 100 - 150\,\mathrm{nm}$, $r_{\mathrm{dot}} = 20 \pm 5\,\mathrm{nm}$,

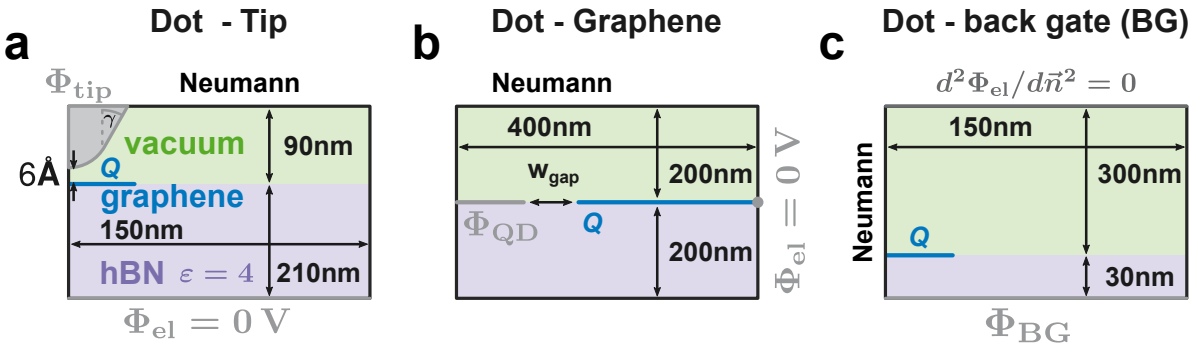


Figure 5.6.: **Sketches of the simulation domain used in the Poisson calculations.** **(a-c)** Q indicates on which electrode the induced charge was determined to calculate $C = Q/U$. Green areas: vacuum ($\varepsilon = 1$); violet areas: hexagonal boron nitride (hBN, $\varepsilon = 4$); blue lines: graphene ($\varepsilon = 2.5$); gray lines, gray area or gray dot: Dirichlet boundary condition; black boundaries: Neumann boundary condition, as labeled. Panel **a**: QD-tip capacitance was extracted for fixed tip potential Φ_{tip}. Typical tip-sample distance, 6 Å, as labeled; tip opening angle, $\gamma = 30°$; tip radius varied within $5-150$ nm. Panel **b**: QD-graphene capacitance was extracted for fixed QD potential Φ_{QD}. Width of the gap between the QD and the surrounding graphene w_{gap}, black double arrow, as labeled. Panel **c**: QD-BG capacitance was extracted for fixed BG potential Φ_{BG}. The top boundary condition captures the constant electric field in front of an infinite charged plate.

$w_{gap} = 5 - 20$ nm, $Z = 5 - 7.5$ Å and finite doping $\delta n = 0 - 1.2 \times 10^{15}\,\mathrm{m}^{-2}$, on the capacitances is investigated and the main results are summarized in Figure 5.7. An effect arising from graphene's linear DOS, so-called quantum capacitance,[123,319,411–413] manifests itself as reduced capacitance around the Dirac point. The largest contribution to C_Σ stems from C_{tip}, followed by C_{BG} and C_{gr}. While Z (6 % change in stated range, compare Fig. 2.3) and w_{gap} (Fig. 5.7b) have a comparatively weak impact within the stated boundaries, r_{tip} (Fig. 5.7a) and especially r_{dot} (Fig. 5.7a,c) dominate the uncertainty of the derived capacitances. Doping and, weakly, temperature ensue an asymmetry in $C(V_{eff,tip})$ and generally increase the capacitances and reduce quantum capacitance effects compared to the case with no doping (see Fig. 5.7c, dashed lines 40 meV hole doping). As we want to extract E_{add} via α_{tip} from charging peak distances in the spectra, it is sufficient to consider the V_{tip} range where these are observed, that is, $|V_{tip,eff}| > 150$ mV. I state the values at $V_{tip,eff} = -0.2$ V, where, considering the QD's diameter of 55 nm and a slight p-doping, $C_{tip} = 8 \pm 1.5$ aF, $C_{BG} = 5 \pm 1$ aF, $C_{gr} = 3.5 \pm 0.7$ aF and thus $C_\Sigma = 16.5 \pm 3.2$ aF. Now I can calculate α_{tip}, which is portrayed in Figure 5.8. The similar behavior of all capacitances reduces the quantum capacitance effect on α_{tip}, which remains nearly constant away from the Dirac point. Es-

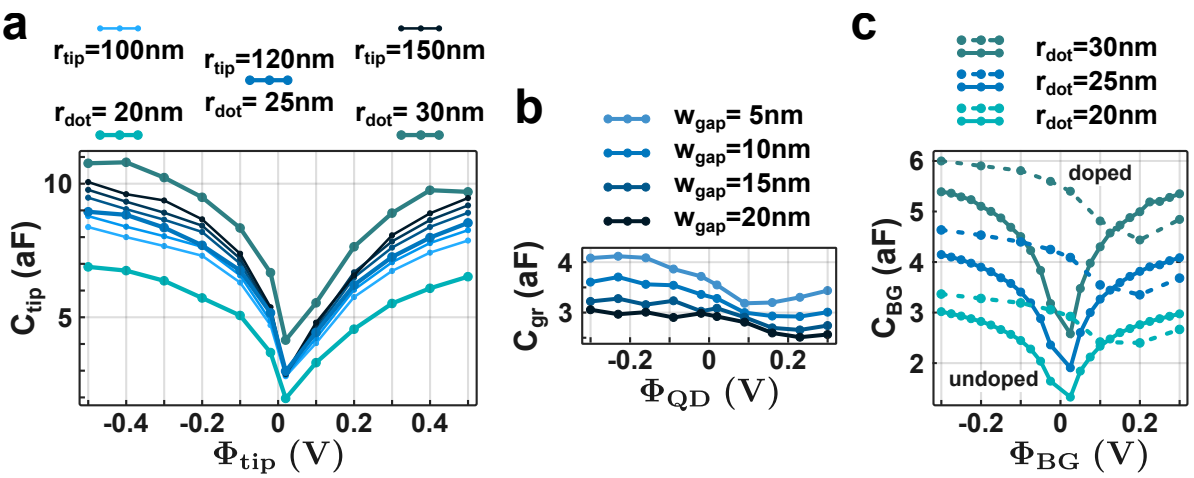


Figure 5.7.: **Simulated capacitive couplings of the tip-induced QD.** For all calculations, $T = 8\,\mathrm{K}$ and potential fluctuations incorporated by Gaussian smoothing of the DOS with $\sigma = 3\,\mathrm{meV}$. **(a)** QD-tip capacitance C_{tip} simulated as sketched in Fig. 5.6a. Thick lines show C_{tip} for fixed $r_{\mathrm{tip}} = 120\,\mathrm{nm}$ and $r_{\mathrm{dot}} = 20, 25, 30\,\mathrm{nm}$, as labeled above. Thin lines are results for fixed $r_{\mathrm{dot}} = 25\,\mathrm{nm}$ and $r_{\mathrm{tip}} = 100 \ldots 150\,\mathrm{nm}$, in steps of 10 nm. Doping $\delta n = 2 \times 10^{14}\,\mathrm{m}^{-2}$. **(b)** QD-graphene capacitance C_{gr} simulated as sketched in Fig. 5.6b. C_{gr} was calculated for a fixed $r_{\mathrm{dot}} = 25\,\mathrm{nm}$ and different widths of the gap w_{gap} between the QD and the surrounding graphene, as labeled above. $\delta n = 2 \times 10^{14}\,\mathrm{m}^{-2}$. Same scale as panel **c**. **(c)** QD-BG capacitance C_{BG} simulated as sketched in Fig. 5.6c. C_{gr} was calculated for different r_{dot} as labeled. Solid lines mark simulations with no doping and dotted lines with $\delta n = 1.2 \times 10^{15}\,\mathrm{m}^{-2}$ (i.e., a 40 meV shift in E_{F}), respectively.

pecially in the relevant regime of the observed charging peaks I find $\alpha_{\mathrm{tip}} = 0.51 \pm 0.03$. This value is close to a value reported by Jung et al.[152] ($\alpha_{\mathrm{tip}} = 0.56$) for a similar system with an STM tip above graphene in the QH regime.

5.3. Tight binding model

The TB calculations portrayed in this section were carried out by Florian Libisch and Larisa Chizhova, while their interpretation was a joint effort. They calculate eigenstates of a $120\,\mathrm{nm} \times 100\,\mathrm{nm}$ commensurate graphene flake on hBN using third-nearest neighbor TB,[406] where the substrate interaction enters via a periodic superstructure potential and local strain effects leading to varying hopping matrix elements t,[196] parametrized from DFT calculations.[189,414] As portrayed in section 5.2.1, we approximate Φ_0^{el} and $\Phi_{\mathrm{gr}}^{\mathrm{el}}(r)$ by a classic electrostatic solution of Poisson's equation (Fig. 5.5a) with the tip radius r_{tip} as fit parameter. Comparing calculated charging energies to experiment yields a plausible

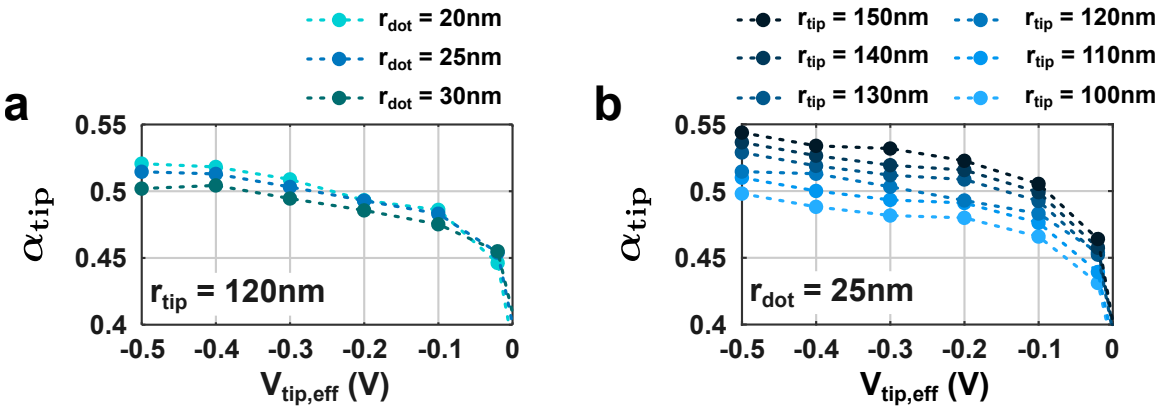


Figure 5.8.: **Effect of quantum capacitance on α_{tip}.** **(a)** Change in tip lever arm α_{tip} due to a changing dot radius r_{dot} at constant tip radius $r_{\mathrm{tip}} = 120\,\mathrm{nm}$. **(b)** Change in α_{tip} for varying r_{tip} at constant $r_{\mathrm{dot}} = 25\,\mathrm{nm}$. $\delta n = 2 \times 10^{14}\,\mathrm{m}^{-2}$.

value of $r_{\mathrm{tip}} \approx 120\,\mathrm{nm}$ implying a FWHM of the QD confinement potential of 55 nm at 7 T (see Fig. 5.5c). I independently determine the initially free parameter E_{F} from the position of LL_0 in STS as $E_{\mathrm{F}} = -40 \pm 5\,\mathrm{meV}$ (see sec. 5.4.5). Accordingly, the graphene is p-doped. Note that varying E_{F} within the stated uncertainty range (see blue horizontal bar in Figure 5.9a) leads to no qualitative changes in the predictions of their model. They use open boundary conditions to simulate the coupling of the flake to the surrounding graphene. Consequently, eigenstates will feature complex eigenvalues $E_l = \varepsilon_l + i\Gamma_l/2$, where the real part ε_l represents the resonant energies and the imaginary part Γ_l the coupling to the delocalized bulk states.[359] Thus we can readily distinguish states that are spread out over the flake (large Γ_l) from those localized near the tip (small Γ_l). We color code Γ_l in Figure 5.9a for a calculation with the tip-induced potential centered on an AB stacked area. At $B = 7\,\mathrm{T}$ and vanishing band bending ($\Phi_0^{\mathrm{el}} = 0$), we find only delocalized states whose eigenenergies cluster around the bulk LL energies (eq 3.13, Fig. 5.9a). As we increase Φ_0^{el}, states begin to localize at the tip and shift in energy, with smaller Γ_l (darker curves) pointing to stronger localization (see Fig. 5.9a). Comparing hole states originating from LL_{-1} for negative and positive Φ_0^{el}, we find, as expected, stronger localization in case of negative Φ_0^{el}. The potential is always attractive to one kind of charge carriers which will localize underneath the tip. The other kind is repelled by the induced potential (see also Ref. [250]) which results in stronger coupling to the bulk. In section 5.3.1, I will classify our TB wave functions in terms of the quantum numbers N, n_{r} and m by comparing sublattice A and B separately to the ideal Fock-Darwin states of

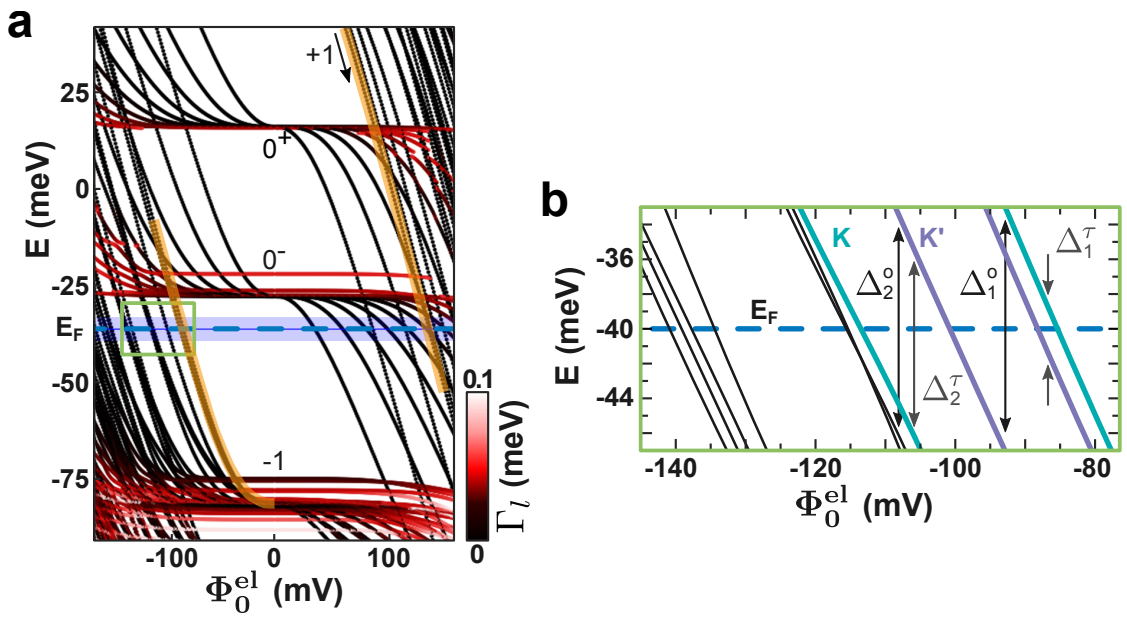


Figure 5.9.: **Tight binding eigenenergies of the tip-induced QD. (a)** TB eigenenergies of a $120 \times 100\,\mathrm{nm}^2$ graphene sample with open boundaries as function of tip-induced potential amplitude Φ_0^{el} at $B = 7\,\mathrm{T}$. The tip-induced potential (red line in Fig. 5.5c) is centered on an AB area slightly offset from the center of the sample (see, e.g., Fig. 5.10b). BA and AA yield very similar behavior, not shown. Line color encodes coupling to the boundary (imaginary part Γ_l of eigenenergies): black (red) indicates strong (weak) localization underneath the tip. States from $\mathrm{LL}_{\pm 1}$ and the split LL_0 are labeled by ± 1 and 0, respectively. The LL_0 splitting, induced by the sublattice dependent potential V^{z} of the hBN, reduces the confining gap to $E_{0^-} - E_{-1} \approx 50\,\mathrm{meV}$. First states crossing E_{F} from $\mathrm{LL}_{\pm 1}$ are highlighted in orange. Uncertainty in E_{F} indicated as blue horizontal bar (sec. 5.4.5). The green rectangle marks the zoom shown in panel **b**. **(b)** Zoom into area marked by a green box in panel **a**. Colored lines identify valley **K** (cyan) and **K′** (purple) (see sec. 5.3.1). First two orbital Δ_j^{o} and valley Δ_k^{τ} splittings marked by arrows.

section 4.3.3 and Figure 4.8. As expected, small angular momentum states are the first ones to localize with increasing Φ_0^{el}, in line with calculations in Ref. [385]. Since the radial extent of the wave functions grows for the first couple of states crossing E_{F}, as expected for increasing m (compare Fig. 5.9b-e), we expect E_{C}^i to decrease towards higher peak indices at fixed B. Delocalized states remain at bulk LL energies (red horizontal lines in Fig. 5.9a). Besides the applied B naturally lifting the orbital degeneracy in QDs,[393] the TB results allow to estimate the orbital $\Delta_{\mathrm{j}}^{\mathrm{o}}$ and valley splittings $\Delta_{\mathrm{k}}^{\tau}$. First we see that according to Figure 5.9b the valley index orders as **K**-**K′** for the first pair of states and as **K′**-**K** for the second pair on the AB-stacked area. The calculation therefore predicts a valley splitting of about $\Delta_1^{\tau} = 3\,\mathrm{meV}$ for the first orbital state. We can also

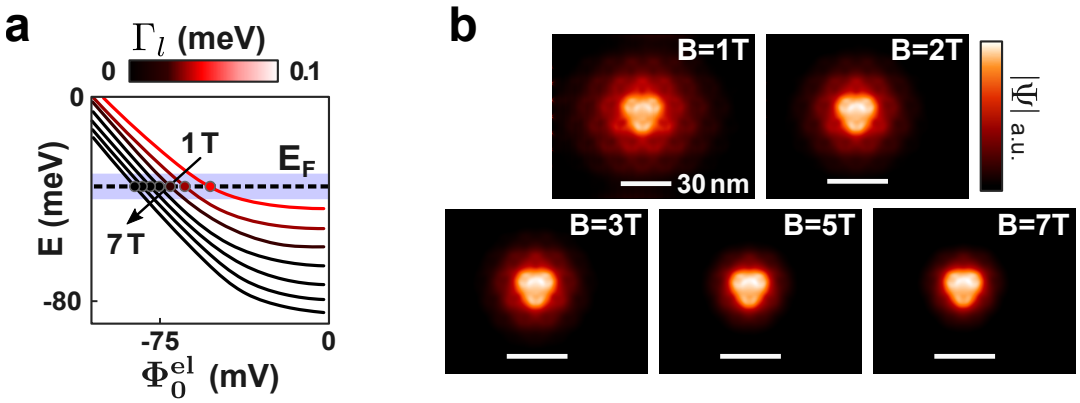


Figure 5.10.: **Main impact of the magnetic field on the tight binding results.** **(a)** Energy of first confined hole state as function of induced potential amplitude Φ_0^{el} for different integer valued B as marked. $\Phi_{\mathrm{gr}}^{\mathrm{el}}(r)$ according to eq 5.2 (red line in Fig. 5.5c). At larger B, the state crosses E_{F} (dashed line, blue bar represents uncertainty) at larger Φ_0^{el} and thus the corresponding onset tip voltage V^* for charging peaks shifts to larger negative values. Color codes imaginary part of the eigenenergy Γ_l at $\varepsilon_l = E_{\mathrm{F}}$ as in Fig. 5.9a. **(b)** Calculated $|\Psi| = \sqrt{|\psi_{\mathrm{A}}|^2 + |\psi_{\mathrm{B}}|^2}$ of the first confined hole state (same as panel **a**) when crossing E_{F} at different B as labeled. The state originates from LL_{-1}, i.e., $V_{\mathrm{tip}} < 0\,\mathrm{V}$ when crossing. All scale bars identical.

distinguish two regimes in the sequence of spin degenerate states crossing E_{F} for negative Φ_0^{el}. The first regime (Fig. 5.9b) exhibits $\Delta_k^{\tau} \lesssim \Delta_j^{\mathrm{o}} \lesssim E_{\mathrm{C}}^i$, while the second at higher Φ_0^{el} is characterized by densely spaced states, thus $\Delta_j^{\mathrm{o}} \approx \Delta_k^{\tau} \ll E_{\mathrm{C}}^i$. The sequence within the first regime corresponds to about five orbital pairs from valley **K** and **K′**, in line with about five quadruplets in our experimental spectra (see labels '4' in Fig. 5.12a and ΔV sequences in Fig. 5.12b,c). Within the employed TB model, the strength of the valley splitting is dominated by the sublattice symmetry breaking term V^{z} due to the hBN substrate.[196]

Figure 5.10 portrays the main impact of a changing magnetic field in the TB simulations. Here, we use a constant shape of the potential albeit its width might change with B in the experiment (see Fig. 5.5c). First, the bulk LL_{-1} energy moves away from E_{F} with increasing B ($\Phi_{\mathrm{gr}}^{\mathrm{el}} = 0\,\mathrm{mV}$ in Fig. 5.10a), thus gating the first hole state to E_{F} requires larger Φ_0^{el}. Additionally, a strong reduction of Γ_l is found with increasing magnetic field, corresponding to the suppression of the radial tail of the wave function as visible in Figure 5.10b and indicating the onset of strong localization in the QD between 1 and 3 T (Fig. 5.10a).

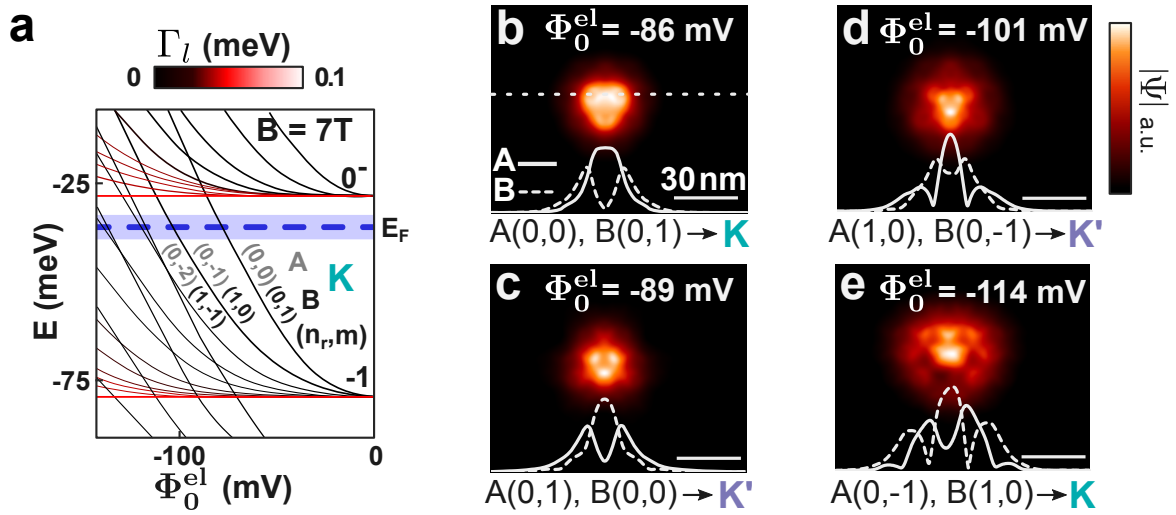


Figure 5.11.: **Identifying the valley of tight binding eigenstates. (a)** Schematic of eigenstate energies for valley **K** deduced from Fig. 5.9a. LL_{0^-} and LL_{-1} are marked. Color codes imaginary part of the eigenenergy Γ_l as in Fig. 5.9a. Blue horizontal bar marks uncertainty in E_F. State labels correspond to radial and angular momentum quantum number (n_r, m) on sublattice A and B colored differently, as marked. **(b-e)** Color plot of the TB wave function amplitude $|\Psi| = \sqrt{|\psi_A|^2 + |\psi_B|^2}$ of the first four states crossing E_F on the hole side. Φ_0^{el} at the crossing point $\varepsilon_l(\Phi_0^{el}) = E_F$ is marked. Solid (dashed) white lines are line cuts along the dotted white line in panel **b** for contributions from sublattice A (B), as marked. Below the plots, (n_r, m) combinations on sublattice A and B, and associated valley (eq 4.10) are added. All scale bars identical.

5.3.1. Assigning a valley to the TB wave functions

In order to classify the TB wave functions in terms of N, n_r and m, we consider sublattice A and B separately. Tracing the states back to their LL of origin reveals N, constraining possible $n_r \leq N$. The value of n_r is then determined by counting radial minima in sublattice dependent line cuts of the wave function amplitude (Fig. 5.11b-d). The distance of the first radial maximum from the center of the wave function is afterwards sufficient to order the possible m numbers of the LL (eq 4.10). Additionally, the (n_r, m) combinations need to be consistent with N differing by one on the two sublattices (eq 3.15). For instance, the line cuts in Figure 5.11b portray $(n_r, m) = (0, 0)$ and $(0, 1)$ on sublattice A and B, respectively. Figure 5.11c-e additionally shows that the roles of the two sublattices interchange for the first and second pair of states. Inserting n_r and m in eq 4.10 yields the valley index, where states with $N_A = N_B - 1$ and $N_B = N_A - 1$ are assigned to valley **K** and **K′**, respectively. For valley **K** more states are labeled by

their (n_r, m) combinations in Figure 5.11a.

5.4. Spectroscopy at finite magnetic field

In this section I present STS measurements on the QDs. The external magnetic field B induces Landau quantization, which allows to capture Dirac electrons in the LL gaps electrostatically by inducing a smooth local band bending using the STM tip. Well-defined graphene QDs, in principle, portray charging peak (CP) sequences with preferential grouping into quadruplets (see sec. 5.1.1). This embodies fourfold spin-valley degenerate QD states which are separated by orbital splittings Δ^o. Additional spin Δ^σ or valley splittings Δ^τ induce a subtle substructure within the quadruplets. The TB calculations allow to crosscheck the onset of localization with B (expected between 1 T and 3 T) and the CP positions in V_{tip} for varying B. The latter should shift outwards in voltage for increasing B for states originating from LLs with $|N| > 0$ due to the increase in bulk LL energies ($\propto \sqrt{B}$, eq 3.13). Finally, probing different positions within the graphene superstructure by moving the tip and, thus, the QD is expected to impact the addition energy spectrum of the QD. Potentially such local changes can be used as a tuning knob for Δ^τ.

Figure 5.12a shows three exemplary dI/dV spectra, acquired at $B = 7\,\mathrm{T}$ at the positions marked by correspondingly colored dots in the stylized graphene superstructure topography at the top. The spectra were adjusted to same vertical scale by dividing dI/dV by the first value I_0 of the respective $I(V)$ curve (sec. 2.1.2). I observe pronounced, regularly spaced peaks for $V_{tip} < -170\,\mathrm{mV}$ and $V_{tip} > 500\,\mathrm{mV}$. A closer look at the sequences reveals the expected grouping in quadruplets, which can still be distinguished up to the 20^{th} peak. This grouping becomes even more evident by directly comparing the voltage difference between adjacent peaks ΔV in Figure 5.12b,c: ΔV between quadruplets is up to twice as large as ΔV within the quadruplets indicating $\Delta_j^o \lesssim E_C^i$ while Δ_k^τ and Δ^σ are significantly smaller.

To further elucidate grouping patterns, I measure 6400 dI/dV spectra at equidistant positions within a $60\,\mathrm{nm} \times 60\,\mathrm{nm}$ area, thus, probing all areas of the superstructure. The median ΔV values (orange circles in Fig. 5.12b,c) portray the robust ordering into quadruplets on the hole side, implying Δ_j^o generally dominates over Δ_k^τ and Δ^σ. On the electron side of the spectra the sequences are disturbed by a few additional CPs of

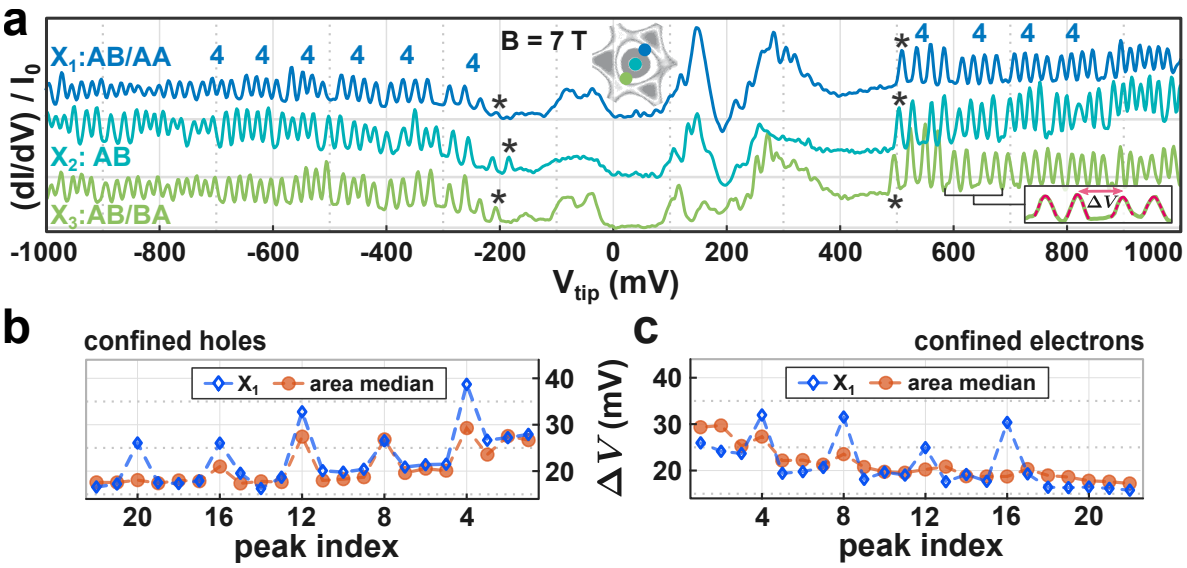


Figure 5.12.: **Spectroscopy at B = 7 T revealing quadruplet ordering of CPs.** **(a)** Representative differential conductance spectra $dI/dV(V_{\mathrm{tip}})$, normalized by the first value I_0 of the respective $I(V_{\mathrm{tip}})$ curve (sec. 2.1.2). Recording positions, as sketched at the top, are: X_1, between AA and AB (blue); X_2, on AB (cyan); X_3, between AB and BA (green). Spectra on other regions (e.g., AA, BA) look similar. Series S500, varied-Z, $V_{\mathrm{stab}} = 1\,\mathrm{V}$, $I_{\mathrm{stab}} = 700\,\mathrm{pA}$, $V_{\mathrm{mod}} = 4.2\,\mathrm{mV_{rms}}$, $B = 7\,\mathrm{T}$. Quadruplets of peaks are marked by '4' and the first CP on either V_{tip} side by an asterisk. Curves are offset for clarity, while horizontal gray lines mark $dI/dV = 0\,\mathrm{S}$. Inset shows a zoom with Gaussian fits (dashed lines) used to extract distances between adjacent peaks ΔV as marked. **(b,c)** Distances ΔV as function of consecutive peak index, for spectrum X_1 (blue, error bars smaller than symbol size) and the median values for 80×80 spectra (orange) recorded on $60 \times 60\,\mathrm{nm}^2$ (see Fig. 5.14a).

defect states in the hBN substrate[169] which are identified by their characteristic spatial development (see sec. 5.4.4). This limits the comparability of the electron and hole sector and hides possible smaller electron-hole asymmetries in the data. The dI/dV features in between the CPs most likely capture contributions from multiple orbital states of each LL, which are lifted in degeneracy by the tip-induced potential, but cannot be identified unambiguously (see sec. 5.4.5 and also sec. 3.5.2).

5.4.1. Onset of charging peaks

Tuning the bulk LL energies (eq 3.13) by varying B allows to illuminate different key aspects of the confinement mechanism. On the one hand, the observation of CPs requires (i) sufficiently large Landau gaps to overcome the potential disorder and (ii) the states

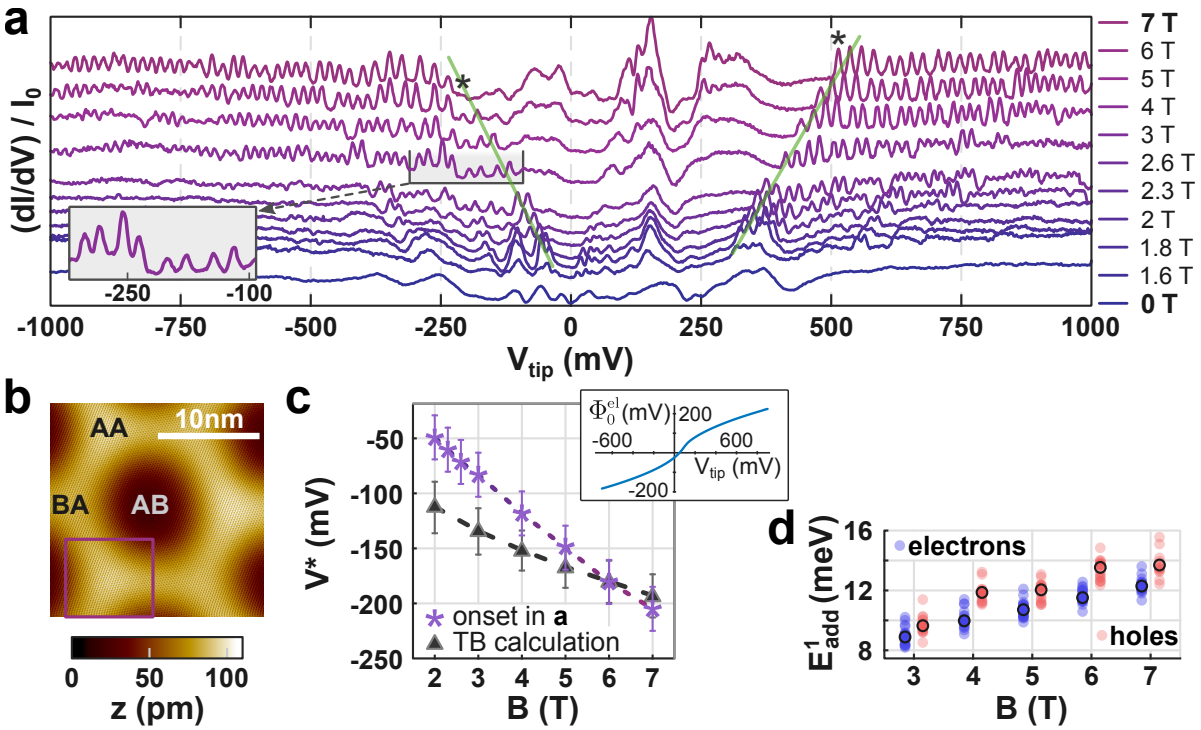


Figure 5.13.: **Occurence of CPs with magnetic field.** **(a)** dI/dV spectroscopy in the vicinity of the AA stacked area marked in panel **b** at varying B, marked on the right. Four spatially adjacent spectra (2x2 grid) taken within the violet area in panel **b** are averaged and the ones for $B > 0\,\mathrm{T}$ are offset by a value proportional to $\sqrt{B}$. Series S502-512, varied-Z, $V_{\mathrm{stab}} = 1000\,\mathrm{mV}$, $I_{\mathrm{stab}} = 700\,\mathrm{pA}$, $V_{\mathrm{mod}} = 4.2\,\mathrm{mV_{rms}}$. $I(Z)$ curves yield $2\kappa = 2.33 \pm 0.01\ \mathrm{Å}^{-1}$. Green lines are guides to the eye, marking the onset voltage of CPs V^*. At 7 T an asterisk marks the first CP on either side. Inset shows zoom onto marked peaks. **(b)** STM image (raw data) recorded at $V_{\mathrm{tip}} = 400\,\mathrm{mV}$, $I_{\mathrm{set}} = 0.3\,\mathrm{nA}$. Violet square marks AA area where spectra in panel **a** were recorded. **(c)** Comparison between measured and calculated V^*. Inset shows the required $\Phi_0^{\mathrm{el}}(V_{\mathrm{tip}})$ for conversion of Φ_0^* to V^*. It is taken from a Poisson-solver (sec. 5.3) including a reasonable work function difference of $\Delta\Phi = 50\,\mathrm{meV}$ between graphene and tip. Error bars for measured V^* reflect typical variation of V^* on AA areas across a few superstructure unit cells. Error bars for calculation arise from the uncertainty in E_{F}. **(d)** Plot of the B dependance of $E^1_{\mathrm{add}} \approx E^1_{\mathrm{C}}$ of 20 spectra (semitransparent dots) in the vicinity of an AA area. Data points are recorded at integer valued B fields (in Tesla), but displayed slightly shifted to the left (electrons, blue) and to the right (holes, red) for clarity. Median values are encircled in black.

localized underneath the tip need to fit into the tip-induced potential. On the other hand, the confined states need to be gated to E_F from the bulk LL energies, thus requiring larger $|V_{tip}|$ for higher B if $N_{LL} \neq 0$ as discussed in section 5.3. I will therefore compare the B dependence of the onset voltage of CPs V^* in theory and experiment.

Indeed, experimentally V^* shifts towards higher $|V_{tip}|$ for increasing B (green lines Fig. 5.13a), thus gating the first state to E_F requires stronger band bending for higher B. Since the curves for $B > 0\,T$ are offset proportional to $\sqrt{B}$, the straight line connecting the first CPs reveals that the energy distance of the first state to E_F scales with $\sqrt{B}$. This corresponds to the increase in bulk LL energies for $N \neq 0$ (eq 3.13), strongly suggesting those LLs as source of the confined states. The observed asymmetry in V^* is explained by a p-doping of the sample (determined from the position of LL_0, see sec. 5.4.5). While the evolution of states with Φ_0^{el} in the calculations (Fig. 5.9a) is approximately symmetric with respect to $\Phi_0^{el} \rightarrow -\Phi_0^{el}$, a shifted E_F induces an asymmetry in the first crossing points of $LL_{\pm 1}$ states with the Fermi level Φ_0^* for electrons and holes (see orange highlighted lines in Fig. 5.9a). In Figure 5.13c I compare V^* and Φ_0^* from the Tb calculations (see Fig. 5.10a) which is adopted by using the $V_{tip}(\Phi_0^{el})$ dependence from the Poisson solver (inset Fig. 5.13c, Fig. 5.5b). Care must be taken to correctly account for the work function difference between the tip and the sample: the tip's work function $(4.5 - 4.8\,eV)$[68,415] exceeds that of graphene (4.5 eV), placing electric field neutrality in the positive V_{tip} sector. Moreover, it definitely has to lie in between the two CP regimes because the QD vanishes without band bending. Using a plausible work function difference of +50 meV in Figure 5.13c leads to satisfactory agreement between the theoretical predictions for the first state crossings and the experimental V^*. Recall that the TB model does not consider the change of the form of the confinement potential with B. It sticks to the 7 T estimate (Fig. 5.5c), albeit $\Phi_{gr}^{el}(r)$ in the experiment becomes more extended for smaller B (Fig. 5.5c), which would aid the gating of localized states having a larger lateral size (increasing l_B). Hence, this would decrease the theoretical values of $|V^*|$ for small B and further improve agreement.

The first clear CPs in experiment appear at around 2 T (Fig. 5.13a), nicely agreeing with the predicted $1-3\,T$ range (sec. 5.3). First signatures are already visible at 1.6 T (Fig. 5.13a, $V_{tip} \approx 350\,mV$), where the first LL gap has a value of about 46 meV (eq 3.13). Though a LL_0 gap would reduce this value, it can be interpreted as upper bound for the potential fluctuations on a scale of $10-20\,nm$. This agrees with values estimated from the local variation of the onset of CPs (see sec. 5.4.2), that is, the eigenenergy variation of

the first confined state. Moreover, it coheres with the local changes of the V_{tip} position of the Dirac point in other STM measurements of graphene on hBN (maximally 40-50 meV on about 20 nm).[125,161]

These finding are further corroborated by comparing the diameter of the LL state $d_n = 2\sqrt{2n+1}\cdot l_{\mathrm{B}}$, being $d_1 = 89\,\mathrm{nm}$ (63 nm) for LL_1 at 1 T (2 T), with the FWHM of $\Phi^{\mathrm{el}}_{\mathrm{gr}}(r)$ being 55 nm. At higher B, the diameter of the first QD state wave function is dominated by l_{B} rather than by the width of $\Phi^{\mathrm{el}}_{\mathrm{gr}}(r)$. The compression of the wave function for increasing B (Fig. 5.10b) also manifests itself as increase in addition energy, for instance, for $E^1_{\mathrm{add}} = E^1_{\mathrm{C}} + \Delta^\sigma$ in Figure 5.13d, where the increase in E^1_{add} with B of about 4 meV cannot be explained by that of Δ^σ, being 460 µeV between 3 T and 7 T. Consequently, increased Coulomb repulsion between electrons due to stronger compression and thus larger E^1_{C} dominates $E^1_{\mathrm{add}}(B)$. I observe a similar monotonic increase for the other E^i_{add} with odd index i, where $E^i_{\mathrm{add}} = E^i_{\mathrm{C}} + \Delta^\sigma$ with negligible Δ^σ, independent of the position of the QD.

The inset in Figure 5.13a portrays slight deviations from the pure quadruplet ordering, which will be treated in the next section.

5.4.2. Capturing the influence of the graphene superstructure on orbital and valley splittings

As already observed in Figure 5.12a and emphasized by the inset in Figure 5.13a, quadruplets sometimes split up into doublets depending on the position of the tip. Moreover, dI/dV maps within the CP regime show characteristic patterns on the scale of the superstructure. I will employ the peak tracing algorithm portrayed in section 2.1.3 to reveal the spatial modulation of the individual peak voltages. By subtracting consecutive voltage maps we can finally generate maps of the addition energies.

Figure 5.14b shows a dI/dV map recorded at $V_{\mathrm{tip}} = 1\,\mathrm{V}$, that is, deep in the CP regime, and thus bright features identify positions where the tip has gated a confined state to E_{F}. Consequently, we understand circular or any line-like feature as equi-energy lines of a certain QD state. Overlaying a topography contour from Figure 5.14a, we see a clear tendency of the features to center on AB areas. The shift to the top right in the lower left corner is attributed to a sloping background potential. Moreover, lines never cross, as would be expected for charging of defect states (see sec. 5.4.4), but rather merge between the AB areas. This essentially proves that the spatial charging patterns

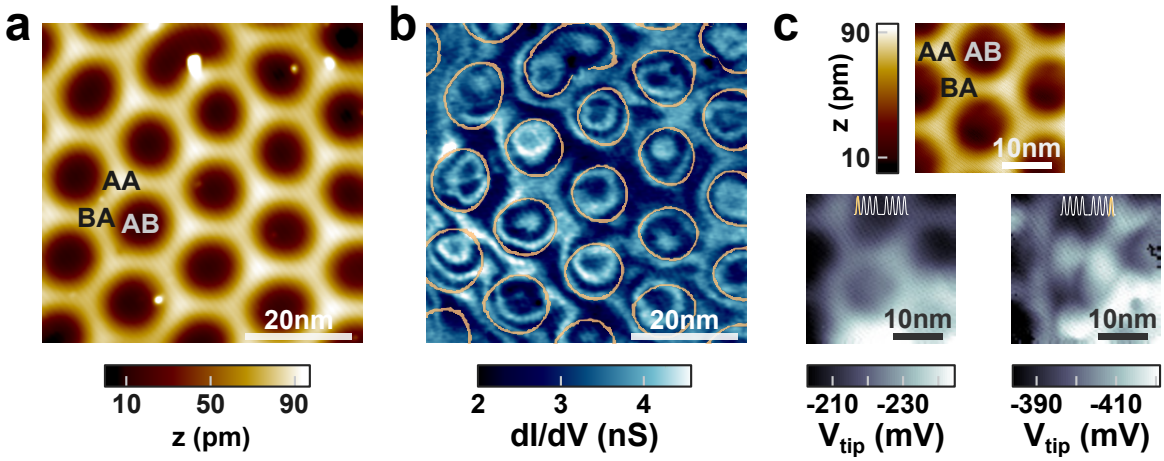


Figure 5.14.: **Local variation of CP features.** **(a)** STM image recorded at $V_{\mathrm{tip}} = 1\,\mathrm{V}$, $I_{\mathrm{set}} = 0.7\,\mathrm{nA}$, $B = 7\,\mathrm{T}$. **(b)** Corresponding dI/dV image with orange topography contour (about half of maximum height) overlay extracted from panel **a**. Same parameters as in panel **a** and $V_{\mathrm{mod}} = 4.2\,\mathrm{mV_{rms}}$. **(c)** Top: STM topography image recorded at $V_{\mathrm{tip}} = 510\,\mathrm{mV}$, $I_{\mathrm{set}} = 0.4\,\mathrm{nA}$, $B = 7\,\mathrm{T}$. Note, panel **a** and **c** are scanned with a relative rotation of 185°. Bottom: Two tip voltage maps tracing the first (left) and eighth (right) hole CP in a spectroscopy series covering the area shown at the top (Series S817, varied-Z, $V_{\mathrm{stab}} = 1\,\mathrm{V}$, $I_{\mathrm{stab}} = 750\,\mathrm{pA}$, $V_{\mathrm{mod}} = 2.7\,\mathrm{mV_{rms}}$; $I(Z)$ curves yield $2\kappa = 3.50 \pm 0.02\ \mathrm{Å}^{-1}$).

arise from the superstructure-induced modulation of the eigenenergies of the confined states of a tip-induced QD.

In order to gain a clearer picture of this eigenenergy modulation, we need to trace the position of every single CP in V_{tip} across the sample. Therefore I collect dI/dV spectra on a regular grid and link the CPs from different spectra, that is, assign their correct index to them, to produce voltage maps for every CP. Figure 5.14c showcases the result for a highly resolved spectroscopy series. The left V_{tip} map for the first hole CP is nicely modulated in correspondence to the superstructure topography at the top. AB areas appear darker in the V_{tip} map, that is, here it requires less gating by the tip for the first confined state to reach E_{F}. This is in fact equivalent to the observation of the features being centered on AB areas (Fig. 5.14b), because this is where the CP first appears. Suggested by the TB results (Fig. 5.11b), I expect the first state to cross E_{F} to be the most circular symmetric one, which, thus, most straightforwardly probes the local electrostatic potential.[68,69] Hence, it is not surprising that the V_{tip} map resembles the adsorbtion energy landscape (Fig. 3.8d) with a variation of about $V_{\mathrm{tip}}(\mathrm{AB}) - V_{\mathrm{tip}}(\mathrm{AA}) \approx 15\,\mathrm{mV} \cdot \alpha_{\mathrm{tip}} \approx 7.5\,\mathrm{meV}$ within one superstructure unit cell.

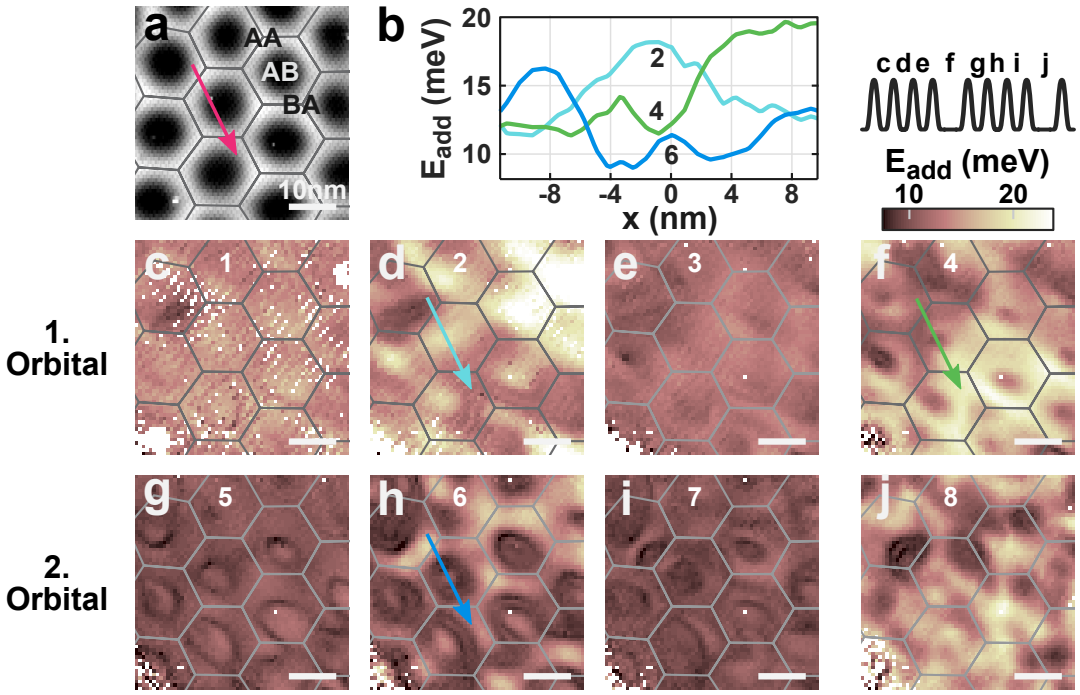


Figure 5.15.: **Addition energy maps.** **(a)** STM image of the $45 \times 45\,\mathrm{nm}^2$ area for which panels **c-j** are shown. $V_{\mathrm{tip}} = 400\,\mathrm{mV}$, $I_{\mathrm{set}} = 300\,\mathrm{pA}$, $B = 7\,\mathrm{T}$. Magenta arrow corresponds to blue and green arrows in panels **d**, **f**, **h**. Honeycomb gray grid lines adapted to topography for comparison to panels **c-j**. **(b)** Line cuts along arrows in panels **d**, **f**, **h**: E^2_{add}, light blue; E^4_{add}, green; E^6_{add}, dark blue. **(c-j)** Addition energy maps (labeled by their index at the top, extracted from the spectroscopy series S500, see Fig. 5.12 for details) for the addition of the first eight holes to the tip-induced QD shown for the area in panel **a**. The panels are also identified in the schematic CP sequence on the top right. Data recorded at $B = 7\,\mathrm{T}$. Honeycomb gray grid from panel **a**. Same scale bar as panel **a**.

As seen for the right V_{tip} map in Figure 5.14c (eighth hole CP), less straightforward patterns are found probably due to less symmetric wave functions and electron-electron interaction at higher occupation numbers.

Next, I create $45\,\mathrm{nm} \times 45\,\mathrm{nm}$ maps of the addition energies at 7 T by subtracting consecutive CP voltage maps and converting them via $\alpha_{\mathrm{tip}} = 0.51$. We directly see that maps of $E^{\mathrm{i}}_{\mathrm{add}}$ with odd index i generally appear weakly modulated compared to those with even i (compare Fig. 5.15c-j, see Fig. A.7 for higher orbitals). This links the odd transitions to spin filling within one valley,[100] since the spin splitting is expected to be spatially homogeneous except for possible exchange enhancement. Dark line features most probably originate from the local crossing of states, which will be discussed in section 5.4.3. The residual spatial variation below 1 meV (one standard deviation of the

median values of $E_{\mathrm{add}}^{3,5,7}$) within the assessed area (Fig. 5.15a) is attributed to local changes in the charging energy or subtle differences in the exchange enhancement.[260,400,416] On the contrary, addition energy maps for even i are more strongly modulated on the scale of the superstructure, as seen in Figure 5.15d,f,h,j (compare to Fig. 5.15a). In detail I find: (i) local maxima at AB stacking for E_{add}^{2}, (ii) E_{add}^{4} exhibits local minima with weak halos in the AB area, (iii) E_{add}^{6} resembles a honeycomb pattern connecting AA and BA areas, while a local maximum at AB stacking is also present. Figure 5.15b shows exemplary linecuts in $E_{\mathrm{add}}^{2,4,6}$ showcasing their variation on the scale of the superstructure unit cell exceeds 7 meV. The slight offset of the line cut with respect to the high-symmetry points of the superstructure is attributed to an offset of the capacitive center of the tip to the tunneling tip. Moreover, by subtracting the charging energy ($E_{\mathrm{C}} \approx 8-10\,\mathrm{meV}$) we see that absolute values of the valley splitting of up to 10 meV are attainable (see also Fig. 5.15d,h).

These observations lead to two main conclusions concerning possible qubit applications. Realizing a spin qubit within one valley of the first orbital ensures a comfortable separation from higher excitations due to the large valley splitting. However, the greater novelty lies within the captured valley splitting gradients. This, in principle, allows to conduct gate operations within the valley degree of freedom by utilizing electric gates to slightly shift the QD position.[71,72] I also note, that while the valley splittings are not completely regular with respect to the superstructure, there barely are homogeneous areas. Therefore there is no need for precise gate alignment during the fabrication of gate structures.

So far the patterns in $E_{\mathrm{add}}^{\mathrm{i}}$ for even i could not be precisely reproduced by TB. For example, while Figure 5.15h looks symmetric around AB, the calculation using DFT based TB parameters favors AA stacking as point of symmetry. Most probably, either the strain configuration of the ideal superstructure is not correctly parametrized or slight distortions of the superstructure in experiment already have a significant impact on the sublattice symmetry breaking and thus E_{add}. Indications for the latter explanation are most prominent in the lower right corner of Figure 5.15h. Here it seems like the symmetry of the pattern changes, now connecting AB and BA areas. Though the superlattice seems to be horizontally stretched in this region (see Fig. 5.15a), it is not certain which area is the least disturbed. Towards the top of the images the pattern changes again, which is apparently connected to the superlattice defect just outside of the frame (compare Fig. 5.14a, more vertical stretching on the left). This variability and the generally

observed local variation of spectroscopic features might actually have the same origin: local changes in the strain configuration. While their impact on the topography is minor, they seem to strongly impact the sublattice symmetry breaking V^z through the pseudo Zeeman effect[29] and thereby the valley splittings.

5.4.3. Possible observation of local valley anti-crossings

As pointed out in the previous section, the addition energy maps linked to spin filling (odd index) show distinct dark lines starting to be pronounced with the second orbital. Figure 5.16d-f highlights these features within the second quadruplet. Since V^z inverts going from AA to AB or BA stacking (see Fig. 3.8), it is plausible to expect crossings of states from different valleys.

The footprint of such a crossing in single particle energies and thus addition energies is derived in Figure 5.16a. On the left, we start with two spin split states per valley. Moving the QD closer to the crossing, the valley splitting Δ^6 (blue arrow) decreases, while the spin splittings Δ_5 and Δ_7 remain constant. Passing through the crossing creates a dip-peak-dip structure in Δ_6, while dips in Δ_5 and Δ_7 should coincide with the peak in Δ_6 (Fig. 5.16b). Coupling of the states at the crossing points by, for instance, the confinement potential, will create avoided crossings.

Line cuts of E_{add}^{5-7} are shown in Figure 5.16c and clearly reproduce the characteristic features of Figure 5.16b. How-

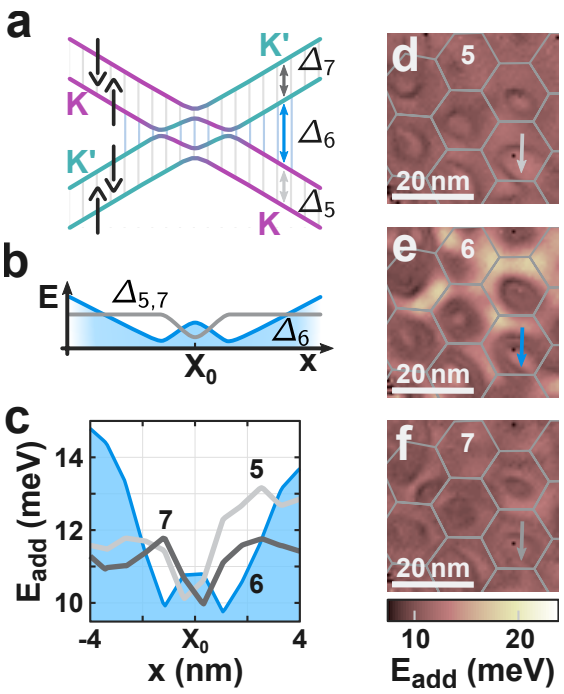


Figure 5.16.: **Signatures of a local valley anti-crossing.** **(a)** Schematic showing the crossing of states within the second orbital for a changing position of the QD. States belonging to valley **K** and **K′** are colored cyan and magenta, respectively. Black arrows indicate physical spin orientation. Single particle energy splittings Δ_{5-7} are marked by double arrows. **(b)** Schematic behavior of Δ_{5-7}, as labeled, derived from panel **a**. X_0 marks center of the crossing. **(c)** Linecuts along correspondingly colored arrows in panels **d-f** through E_{add}^{5-7}, as labeled. **(d-f)** Addition energy maps for the fifth through seventh hole transition. Arrows mark linecuts shown in panel **c**. Centers of honeycomb grid identify AB stacking (see Fig. 5.15a). All same color scale.

ever, we see dips in Δ_5 and Δ_7 of about 2 meV, thus exceeding the maximum value within the simple model, which is given by $\Delta^\sigma \approx 800\,\mu$eV. As the intermediate peak in Δ_6 is only about 1 meV high (maximum value also Δ^σ), there must be additional effects shifting the eigenenergies or lowering of the charging energy. In the center of the crossing (marked X_0 in Fig. 5.16b,c) the spin filling sequence is $\uparrow\uparrow\downarrow\downarrow$. Pauli exclusion therefore reduces the e-e repulsion and thus E_C. If we conjecture a drop in E_C of about 1 meV for the fifth and seventh transition, that is, E_C does not drop for E^6_add, this would account for the discrepancy. However, it is not possible to draw any conclusions on the size of the anti-crossings.

For higher orbitals, these footprints are observed more frequently in the addition energy maps (e.g., Fig. A.7), while also occurring for the orbital transitions in between quadruplets. Consequently the spin transitions show even richer patterns with counterparts in either the valley or orbital transitions. The features are not observed on the electron side (see Fig. A.8) and they are additionally obscured by charging of defect states in the hBN,[169] which will be addressed in the next section. Especially, the crossing in the second orbital is highly interesting from a fundamental point of view. Driving a state through such an anti-crossing allows to create a superposition of valley states. The probability to remain in the same valley after the sweep (a so-called Landau-Zener transition) is known as Landau-Zener probability and was originally treated in the context of atomic collisions by Landau,[417,418] Zener,[419] Stückelberg[420] and Majorana.[421] It depends on the size of the avoided crossing and the sweep speed. Systematically investigating such transitions by means of Landau-Zener-Stückelberg interferometry[401,422,423] allows to access coherence times of two-level systems as well as their energy-level structure.

I note that there is a peculiar twist to the portrayed observations on the hole and electron CPs. While it becomes increasingly difficult to match CPs for holes in some areas (see lower left corners of E_add maps in Fig. 5.15 and Fig. A.7), this is less of an issue for electrons (Fig. A.8). Additional investigations of the TB eigenstates might reveal differences in the electron and hole wave functions. Experimentally, the asymmetry in V_tip with respect to the onset of CPs might offer a different explanation. The tip-induced potential amplitude is more than 50 meV larger for electrons before the QD is actually charged (Fig. 5.9). Perhaps the confinement potential thereby inhibits the redistribution of the probability density to areas of favorable stacking and thus limits relative changes in the eigenenergies. Moreover, the p-doping leaves LL_0 unoccupied slighly above E_F (see sec. 5.4.5). This could lead to a significantly different screening of the tip depending

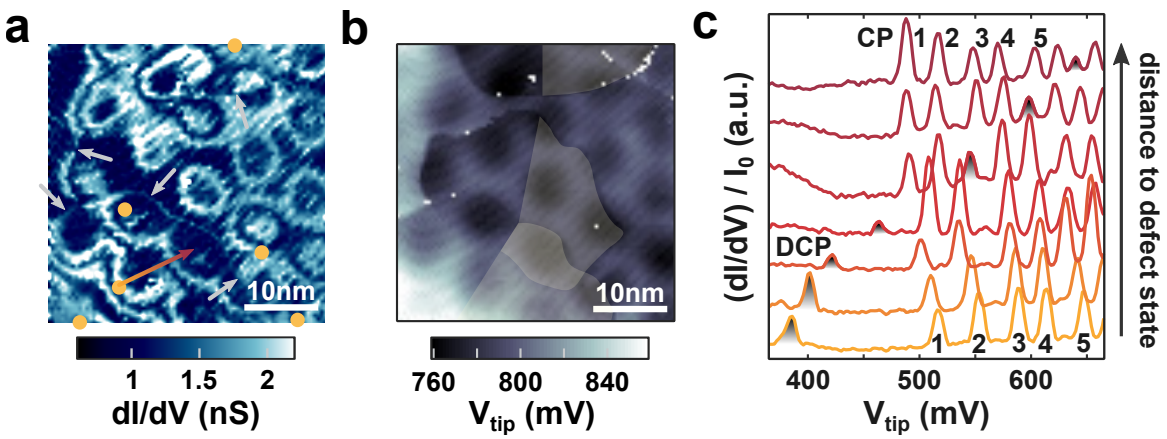


Figure 5.17.: **Defect charging peaks (DCPs) in the differential conductance.** **(a)** dI/dV map for $V_{\mathrm{tip}} = 812\,\mathrm{mV}$ (extracted from spectroscopy series S500, $V_{\mathrm{stab}} = 1\,\mathrm{V}$, $I_{\mathrm{stab}} = 700\,\mathrm{pA}$, $V_{\mathrm{mod}} = 4.2\,\mathrm{mV_{rms}}$ and $B = 7\,\mathrm{T}$). Discontinuity lines of the charging pattern marked by gray arrows stem from DCPs. Orange dots mark location of first occurrence of the DCPs. Orange to red fading arrow indicates where spectra in panel **c** were taken. **(b)** V_{tip} map of the 13^{th} electron CP. Darker areas with sharp boundaries (half of each area marked by yellow overlay) are caused by a DCP. **(c)** dI/dV spectra, normalized by initial current I_0, recorded while laterally moving the tip away from a defect state along orange-to-red arrow in panel **a**. The CP originating from the defect state is highlighted and labeled DCP. The first five CPs of the tip-induced QD are marked CP1-5.

on the V_{tip} polarity leading to better screening for $V_{\mathrm{tip}} > 0\,\mathrm{V}$. However, measurements with adjustable Fermi energy, that is, with an operational back gate, are required to decide on these conjectures.

5.4.4. Identification of defect charging peaks

Besides the already discussed CPs originating from the tip-induced QD, similar but distinctly different additional spectroscopic features stemming from the charging of defect states probably within the hBN are observed. In dI/dV maps faint lines appear (gray arrows, Fig. 5.17a), which act as discontinuity with respect to the QD charging patterns. The area enclosed by such lines grows for increasing V_{tip} amplitude. In maps of the V_{tip} position of the CPs the corresponding areas appear offset (yellow overlay, Fig. 5.17b). In contrast to the QD features, these areas overlap for large enough V_{tip}. This is the typical behavior seen for charging of localized defect states by an STM tip.[99,424] In this case, they most probably stem from impurities in the hBN layer, which were previously reported by Wong et al.[169] to produce 'ring defects' in dI/dV maps. The respective de-

fect level lies above the Dirac point, which agrees with my almost exclusive observation of defect charging peaks (DCPs) for positive V_{tip}.

In contrast to charging of tip-induced QD states, V_{tip} needs to be increased to charge the same defect state as the tip moves away, because the capacitive coupling to the state weakens. Such a sequence of dI/dV spectra, where the tip laterally moves away from the emergence point of such a DCP is portrayed in Figure 5.17c. Its height is suppressed with respect to the adjacent CPs, which fits the weaker impact that a more distant charge has on the LDOS beneath the tip (detection mechanism see sec. 5.1). As soon as the DCP mixes with the QD CPs, the CP sequence will be offset by one. From which index on a specific spectrum is offset depends on the distance to the defect state, where the spectrum is recorded. This blurs the fourfold sequence of the median values in Figure 5.12c, since for higher charging peak indexes, that is, higher V_{tip}, spectra in a larger area around the defect will incorporate the corresponding DCP. The ideal quadruplet transitions for the median values washes out and later even shift towards higher peak transition indexes (Fig. 5.12c, e.g., $12 \rightarrow 13$, $16 \rightarrow 17$).

5.4.5. Discussion of Landau level features in spectroscopy

For some tips I find dI/dV spectra portraying an apparent LL sequence at $B = 7\,\mathrm{T}$ like in Figure 5.18a for $V_{\mathrm{tip}} > -100\,\mathrm{mV}$. I do not observe LLs for $V_{\mathrm{tip}} < -100\,\mathrm{mV}$ since charging peaks set on earlier for $V_{\mathrm{tip}} < 0$, which in turn is due to LL_{-1} being closer to E_{F} than LL_{+1} (see discussion of asymmetric onset of charging peaks in sec. 5.4.1). Plotting the squared LL peak energies for spectra A and B in Figure 5.18b, we see that they do not correspond to the ideal LL energies (E_N) of eq 3.13 ($\nu_{\mathrm{F}} = 1 \times 10^6\,\mathrm{m/s}$). However, they show a square root dependency and if I include the gating effect of the tip by multiplying E_N by $1 + \alpha_{\mathrm{tip}} = 1.51$ (schematically Figure 5.18c), I see agreement. I conclude that the dI/dV features have to originate from states which are gated by the tip, thus they need to be sufficiently localized underneath the tip and I do not probe them at the bulk LL energies. The only exception is LL_0, since the effect of the tip-induced potential is very limited for small electric fields (work function difference compensated at $V_{\mathrm{tip}} \approx -50\,\mathrm{mV}$, sec. 5.4.1).

The distinct peaks in the spectra may be explained by dominant contributions to dI/dV from the states with $m = 0$ (peak in the wave function amplitude at $r = 0$, Fig. 4.8) originating from the respective LLs.[258,270] These are not the confined QD states

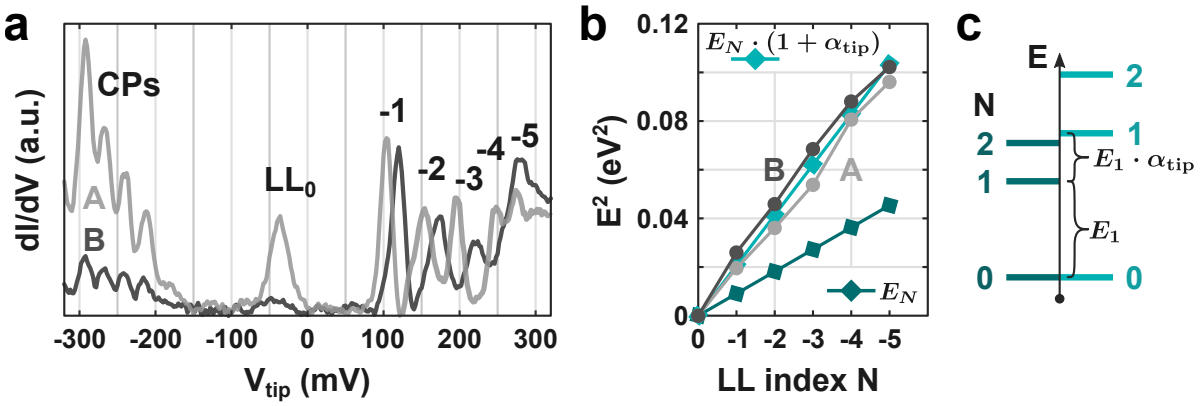


Figure 5.18.: **Landau level signatures in the differential conductance.** **(a)** Two dI/dV spectra taken at different locations, averaged over trace and retrace, recorded at $B = 7\,\mathrm{T}$, $V_{\mathrm{stab}} = 400\,\mathrm{mV}$ and $I_{\mathrm{stab}} = 200\,\mathrm{pA}$. Contributions from states with $m = 0$ originating from LLs with $N = 0, \ldots, -5$ are marked, as well as charging peaks (CPs). Contribution from LL_{-4} for spectrum B only visible as shoulder. **(b)** Comparison of the squared measured peak energies deduced from panel **a** (light and dark gray) to the squared ideal LL energies (E_N, petrol) calculated from eq 3.13 ($\nu_{\mathrm{F}} = 1 \times 10^6\,\mathrm{m/s}$). Additionally the calculated values are plotted after multiplication with a factor of $1 + \alpha_{\mathrm{tip}} = 1.51$ (cyan). **(c)** Schematic of the ideal LL energies (left) and expected energies in dI/dV (right), where the latter are shifted by the gating effect of the tip to $(1 + \alpha_{\mathrm{tip}})$-times larger energies.

responsible for the charging peaks in the positive sector (electron confinement), as these already occupied states will not cross E_{F} for increasing V_{tip}. However, at least the '-1' peak will lead to changing peaks in the negative V_{tip} sector. Dominating $m = 0$ states are only observed if (i) the tip tunnels very close to its capacitive center and (ii) the confining potential is very close to circularly symmetric around this center. If either condition is flawed, various angular momentum states will contribute to dI/dV and multiple peaks per LL will be observed.[270] Quantitatively, misalignment smaller than the magnetic length will already lead to significant contributions of $m \neq 0$ states (compare line cuts in Figure 5.11b-d). As charging patterns in maps of the dI/dV signal reveal the same symmetry as the graphene superstructure, I can estimate the relative shift of tunneling and capacitive center. I commonly find shifts of a few nm. This explains why the majority of dI/dV spectra feature a very rich structure in the charging peak 'gap'. However, without knowing the exact confinement potential everywhere, linking spatially varying contributions of the peaks to distinct m states cannot be done reliably.

Next, I point out a few similar observations which have been reported in the literature. For instance, strained graphene on Rh has also exhibited unconventional splitting

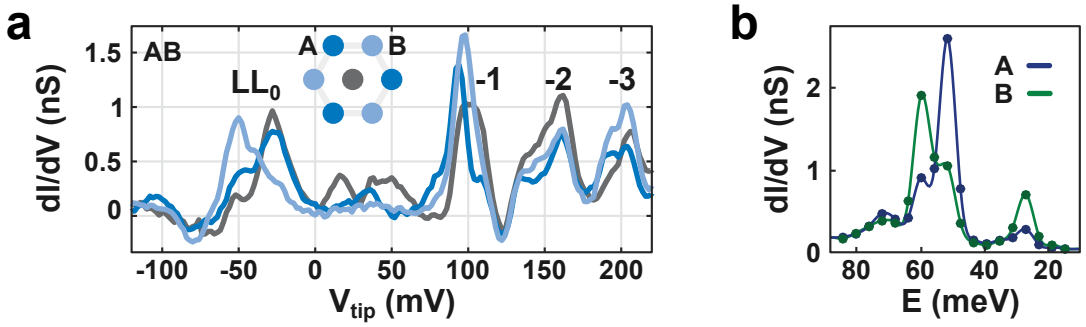


Figure 5.19.: **Sublattice contrast of Landau level zero.** **(a)** dI/dV spectra, averaged over two equivalent positions, recorded at $B = 7\,\mathrm{T}$, $V_{\mathrm{stab}} = 300\,\mathrm{mV}$, $I_{\mathrm{stab}} = 100\,\mathrm{pA}$ (varied-Z spectroscopy series S459, AB stacking, $I(Z)$ curves yield $2\kappa = 3.31 \pm 0.04\ \mathrm{Å}^{-1}$). As sketched in the center, spectrum on sublattice A, dark blue; on sublattice B, light blue; on hole site, gray. Landau level (LL) zero labeled LL_0 and the two peaks are split by about 25 meV. Peaks attributed to higher LLs labeled by their LL index -1,-2,-3. **(b)** Average dI/dV spectra obtained on sublattice A and B of graphene on SiC at $B = 8\,\mathrm{T}$. E axis inverted for clarity of comparison to panel **a**. Adapted by permission from Macmillan Publishers Ltd: Miller, D. L. et al. *Nat. Phys.* **2010**, *6*, 811–817, copyright (2010).[271]

of LLs and an increased visibility of hole LLs compared to electron LLs.[425] Inhomogeneous strain patterns arising from the deformation of the graphene superstructure might have a similar effect. The observation of LL features is limited to the hole side in my measurements. Though the induced band bending is most probably the limiting factor, a comparable mismatch in visibility has also been observed in graphene on SiC. There, electron LLs show a much stronger signal.[260]

I frequently find a splitting in the LL_0 feature as seen in Figure 5.19a. The position of the LL_0 peak is linked to the position being either on sublattice A (dark blue curve), B (light blue) or the hollow site (gray), while the splitting amounts to approximately 25 meV. The gap between LL_{0+} and LL_{0-} in TB is about 40 meV (Fig. 5.9). Again, this could point to insufficiently captured details of the strain or sublattice symmetry breaking potential term. Such a splitting has been previously interpreted as valley splitting of LL_0 ($\approx$ 11 meV, Fig. 5.19b), while the responsible sublattice symmetry breaking was induced by a misaligned second graphene layer on SiC.[271] Corroborating measurements on SiC and highly oriented pyrolytic graphite at $B = 8\,\mathrm{T}$ by Wang et al.[426] yield very similar values of 13 meV and 16 meV, respectively. The effect is most pronounced for LL_0, because its wave functions link valley and sublattice most strongly (see eq. 3.15, sec. 3.2).

The LL features additionally allow to estimate E_F. Since I find LL_0 peaks always in the unoccupied states sector (i.e., $V_{tip} < 0\,V$), $E_F = -40 \pm 5\,meV$ (Fig. 5.18a) is used to determine the coincidence of states with E_F in the TB calculations.

5.5. Conclusion and transport device considerations

In summary, I have realized graphene quantum dots without physical edges via electrostatic confinement in magnetic field using low disorder graphene crystallographically aligned to a hexagonal boron nitride substrate. I observe more than 40 charging peaks in the hole and electron sector arranged in quadruplets due to orbital splittings. The first few peaks on the hole and electron side show an additional doublet structure traced back to lifting of the valley degeneracy. Note that such a lifting is key for the use of graphene quantum dots as spin qubits [58]. Tight binding calculations[196,406] quantitatively reproduce the orbital splitting energy of $4-10\,meV$ as well as the first orbital's valley splitting energy of about $3\,meV$ for AA stacking by assuming a tip potential deduced from an electrostatic Poisson calculation. The latter also allows to estimate the capacitances of the dot to the tip ($C_{tip} \approx 8 \pm 1.5\,aF$), the surrounding graphene ($C_{gr} \approx 3.5 \pm 0.7\,aF$) and to the back gate graphite electrode ($C_{BG} \approx 5 \pm 1\,aF$). Thus the total capacitance of the QD amounts to $C_\Sigma \approx 16.5 \pm 3.2\,aF$, which in turn yields a charging energy of $E_C \approx 10\,meV$ and a tip lever arm of $\alpha_{tip} = 0.51$. The tip radius is the only remaining fitting parameter and is determined by matching the onset of charging peaks in tip voltage and the orbital splittings to the experimental values. With $r_{tip} = 120\,nm$ the full width at half maximum of the induced potential is $55\,nm$ at $7\,T$. At $2\,T$ the diameter of a LL_1 state compares favorably to this value, which agrees well with the experimental onset of charging peaks in experiment and the tight binding calculations.

The results demonstrate a much better controlled confinement by combining magnetic and electrostatic fields than previously found in graphene. I further exploit the sensitivity of the quantum dot states to their environment to map the effect of the graphene superstructure on orbital and valley splittings. The most exciting findings concern the local variation of the valley splittings for confined holes: (i) within the first orbital, locally values of $10\,meV$ are reached and (ii) strong changes of up to $7\,meV$ on the scale of a few nm are found, while (iii) from the second orbital on, signatures of local valley crossings are unveiled. While (i) is very encouraging for the realization of spin qubits,

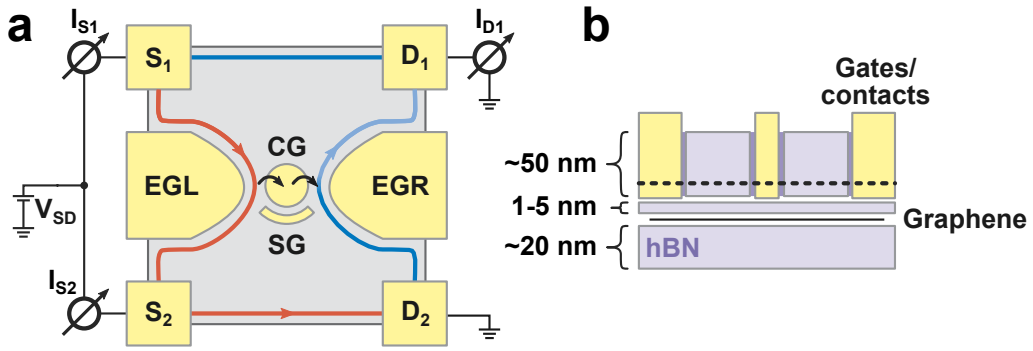


Figure 5.20.: **Draft of a transport device building on electrostatic confinement in the QH regime. (a)** Top-view of the proposal: Graphene flake, gray square; source contacts, S_1 and S_2; drain contacts, D_1 and D_2; edge gate left, EGL; edge gate right, EGR; center gate, CG; side gate, SG; edge states at source/drain potential, red/blue. Black arrows indicate hopping of an electron from the left edge channel to the right via the QD underneath CG. **(b)** Side view of the device structure. Graphene is encapsulated by two hBN layers. The topmost hBN layer is pre-structured according to the gate geometry. Holes later accommodate the gate electrodes and contacts (yellow). Black dashed line indicates cut shown in panel **a**.

(ii) and (iii) open up the field for valley based quantum computation by using gate structures which shift the QD's position. Here, it would be highly interesting to assess the decoherence times for the valley degree of freedom predicted to be $\mathcal{O}(1\,\mathrm{ms})$,[64] for instance, by employing Landau-Zener-Stückelberg interferometry.

Importantly, building QDs and qubits based on this confinement approach requires devices operating in the quantum Hall regime. In particular, edge states replace conventional source and drain leads. Fortunately, there is a great wealth of experiments in semiconductor heterostructures dedicated to the investigation and manipulation of edge states,[427–429] for instance, revealing quasiparticles with fractional charge in the fractional quantum hall regime.[117–119] Edge states can generally be guided by electrostatic gates, as sketched in Figure 5.20a. Here, I use side gates (EGL and EGR) to bring the edge states from the left and right sample edge into proximity with the QD, which is induced by the central gate CG with a diameter of about 100 nm. Tuning the voltages on EGL and EGR should also mediate the tunnel-coupling of the edge states to the QD. Now we apply the bias voltage V_{SD} to the source contacts S_1 and S_2, and ground the drain contacts D_1 and D_2. The current I_{S2} will convey the usual longitudinal conductance in the quantum Hall regime and is not concerned with the current via the QD. Due to the chirality of the edge states, current can only flow in one direction along an edge channel (here, counterclockwise). Thus, only I_{S1} and I_{D1} capture the current via the QD and

should yield the same absolute value. Finally, the side gate SG could be used to slightly shift the QD position.

This scheme can be easily expanded to accommodate two QDs in series. One main issue in this design is the contacting of the gates. Leads on top of a hBN/graphene/hBN heterostructure need to be much more distant from the graphene than the actual gate electrode. This could be accomplished by stacking two different hBN layers on top of the graphene, as shown in Figure 5.20b. The first is only a few nm thin to ensure strong coupling of the electrodes to the graphene. The second layer is much thicker, that is, about 50 nm, and is structured[430–432] before stacking to contain holes in form of the gates. Consequently the gate leads will be separated from the graphene.

6. Graphene nanostructures produced by local anodic oxidation

This chapter has been published in parts in:

Graphene quantum dots: wave function mapping by scanning tunneling spectroscopy and transport spectroscopy of quantum dots prepared by local anodic oxidation
M. Morgenstern, N. M. Freitag, A. Vaid, M. Pratzer, M. Liebmann
Physica Status Solidi RRL: Rapid Research Letters **2016**, *10*, 24-38
© 2016 WILEY-VCH Verlag GmbH & Co. KGaA, Weinheim

and has been accepted for publication in parts in:

Graphene Quantum Dots probed by Scanning Tunneling Microscopy
M. Morgenstern, N. M. Freitag, A. Nent, P. Nemes-Incze, M. Liebmann
Annalen der Physik
© 2017 WILEY-VCH Verlag GmbH & Co. KGaA, Weinheim

AFM lithography employing LAO has been developed to create nanostructures on the surface of semiconductors starting with silicon[433–435] and has been applied to titanium films,[436] GaAs/AlGaAs heterostructures[65,66,437,438] and carbon nanotubes.[439] Although STMs are also used for LAO,[440] AFMs are generally more convenient to operate and being able to image partially insulating samples is clearly advantageous. Experiments on graphene by Giesbers et al.[308] stimulated work in our research group towards STM compatible resists-free nanostructures. After pre-studies by Markus Liebmann, myself and quite a few bachelor students,[441–447] I investigated rings structures and QDs. LAO, in principle, offers several advantages over the combination of EBL and RIE.

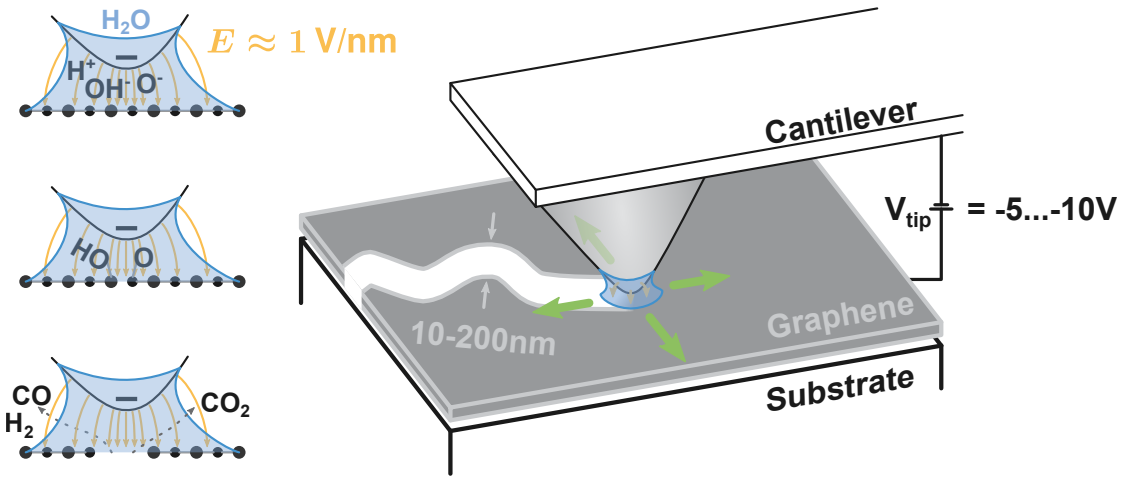


Figure 6.1.: **Principle of LAO.** The tip at the end of an AFM cantilever is brought into contact with a graphene sample in ambient conditions. A water meniscus (blue area) forms and by applying a strong negative tip voltage V_{tip} the graphene is locally oxidized. The piezo controlled navigation of the tip (green arrows) allows to create arbitrary patterns (white stripe). Left: Sketch of the LAO reaction. Sufficiently high electric fields $E \approx 1\,\mathrm{V/nm}$ (field lines indicated by orange arrows) facilitate the dissociation of water molecules into H^+, OH^- and O^- ions (first frame). The oxidative ions can react with the graphene leading to partial oxidation (second frame). Continuing the oxidation finally leads to gasification of the carbon in form of CO and CO_2 molecules (third frame). H_2 is released in any case.

Once contacted by either micro-soldering or shadow mask evaporation (see sec. 3.4), the structuring is accomplished using only the AFM. This enables in-situ crosschecks of the structures. Moreover, the rest of the graphene flake is not contaminated with resist or solvent residues during the process. The latter are especially burdensome when engaging the sample with an STM tip. I will describe the method comprehensively here and refer the reader to broader introductory reviews[448–450] and a review designated to carbon allotropes and especially graphene[451] for additional information.

The basic principle of LAO under ambient conditions is sketched in Figure 6.1. As the conductive tip of an AFM is brought into contact with the sample, a water meniscus[452] forms due to the ever-present water film on the sample,[453] which acts as an electrolyte. Controlling the humidity of the air thus presents a tuning knob for the size of the meniscus.[452] By applying a negative tip voltage below a threshold of $V_{\mathrm{tip}} = -5 \ldots -4\,\mathrm{V}$,[334,336] water molecules dissociate[454] in an electric field of about $1\,\mathrm{V/nm}$ and oxygen and hydroxyl oxidative ions can react with the sample surface. The reaction is limited to a small area underneath the cusp of the tip, because there the elec-

tric field is the strongest and the anions reach the graphene most quickly.[455] The piezoactuators of the AFM allow to navigate the tip with nm-precision, thus arbitrary patterns can be produced on the surface, for instance, modeling quantum point contacts,[334,456,457] nanoribbons,[458,459] Aharonov-Bohm rings[458] and QDs[309,334,336] with feature sizes down to 10 nm.[457] Regulating the scan speed (typically $50-200\,\mathrm{nm/s}$) mediates the reaction time and therefore presents a handle on the width of the produced lines.[459] Typical widths range from a few tens of nm to 200 nm, while the radius of the tip apex and the relative humidity (via the water meniscus) also have a strong impact.[460] Adjusting the speed can also be used to only partially oxidize a stripe of graphene (so-called pseudocuts), instead of removing it completely by gasification of carbon (see Fig. 6.1).[451] The degree of oxidation and thus the size of the induced transport gap (up to 4 eV)[461] also increases with increasing $|V_{\mathrm{tip}}|$,[456] while partially oxidized lines consisting of graphene or graphene oxide nanoislands harbor localized states.[461] Finally, the load force F_{load} of the cantilever adds a mechanical component to the process. With higher F_{load}, the tip plows through the fractured graphene leaving rubble at the sides of the resulting cuts (see Fig. 6.3b). The degree of scratching is controlled by the cantilever deflection set-point S_{Def} [V]. It translates to the cantilever deflection $\Delta z = \sigma_{\mathrm{Cant}} S_{\mathrm{Def}}$ via a cantilever specific deflection sensitivity σ_{Cant} [nm/V]. The latter can be approximated by $\sigma_{\mathrm{Cant}} = \frac{l_{\mathrm{Cant}}}{2}\,\mathrm{V}^{-1}$, where l_{Cant} is the length of the cantilever. Using the force constant of the cantilever D_{f} and Hook's law one obtains

$$F_{\mathrm{load}} = D_{\mathrm{f}} \cdot \Delta z. \tag{6.1}$$

Obviously, many parameters can be varied to try and reduce feature size, improve control and reliability of the LAO process. For instance, tapping mode AFM can be used instead of contact mode to reduce ablation of the tip.[458,459] Inverting the polarity of V_{tip} leads to hydrogenation of the graphene[462] and equally insulating structures, if catalytic Pt/Ir tips are used. In the majority of experiments, highly doped Si tips are used,[308,458,459,461] partly because coatings like TiN[463] or Ti/Pt[441,447] appear to degrade faster and leave contaminants behind. Park et al.[464] applied LAO in a different atmosphere and thus exchanged the active electrolyte with, for instance, isopropyl alcohol or methyl alcohol, reducing the cut width down to 3 nm in case of methyl alcohol. By modulating the amplitude of V_{tip} between zero and a set point between 15 and 30 V, structuring electrically isolated graphene is possible.[458,465] Using an STM for structuring, Tapasztó et al.[340] could control the atomic edge configuration of only 3 nm wide

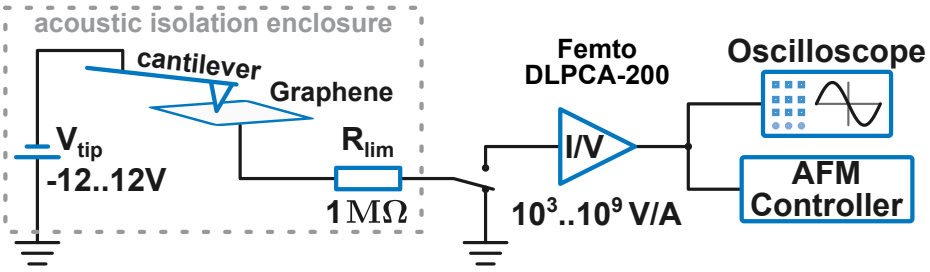


Figure 6.2.: **LAO electronic circuitry.** The internal AFM voltage source can apply tip voltages V_{tip} in the range of $-12 \ldots 12\,\mathrm{V}$. The resistor R_{lim} is used to limit the current flowing during the LAO process. Optionally, a variable gain I/V converter (*DLPCA-200*, Femto) can be connected in series to view the current on an oscilloscope and capture it by feeding it to an auxiliary port of the AFM controller unit.

nano-ribbons. It is also possible to start out with a highly resistive sheet of graphene oxide (GO) and locally reduce it to create conductive structures.[466,467]

6.1. Preparation of nanostructures

Graphene flakes were exfoliated on 300 nm SiO capped Si wafers and contacted by indium soldering (see sec. 3.4). LAO was performed by employing contact-mode AFM (*Dimension Icon*, Bruker) inside an acoustic isolation enclosure. The latter also simplified controlling the relative humidity (RH), generally maintained at 60%, by utilizing an additionally installed humidity control unit (*miniClima EBC11*, Long Life for Art). I used highly n-doped Si cantilevers (NSC18) with an intermediate $D_{\mathrm{f}} = 2.8\,\mathrm{N/m}$, resonance frequency $\omega_{\mathrm{res}} = 75\,\mathrm{kHz}$ and $\sigma_{\mathrm{Cant}} = 112\,\mathrm{nm/V}$. They are stiffer than specialized contact mode cantilevers (e.g., CSC17, $D \approx 0.2\,\mathrm{N/m}$) and thus allow capturing tapping mode images at reasonable speed in between individual structuring steps, when V_{tip} is set to zero. High resolution tapping mode images were acquired using NSC15 cantilevers ($D_{\mathrm{f}} = 40\,\mathrm{N/m}$, $\omega_{\mathrm{res}} = 325\,\mathrm{kHz}$). The electric circuitry is sketched in Figure 6.2. The internal voltage source of the AFM can apply voltages in the range of $\pm 12\,\mathrm{V}$ to the tip. A current limiting resistor $R_{\mathrm{lim}} = 1\,\mathrm{M\Omega}$ is added to avoid damage to the graphene or the tip. The current flowing during the oxidation I_{LAO} can be simultaneously monitored by either using an I/V converter (*DLPCA-200*, Femto) in series or measuring the voltage drop across R_{lim}. In principle this also allows to perform conductive AFM.[447] The crucial observation for making cuts or pseudocuts, also made by Puddy et al.[336] and Zijlstra,[447]

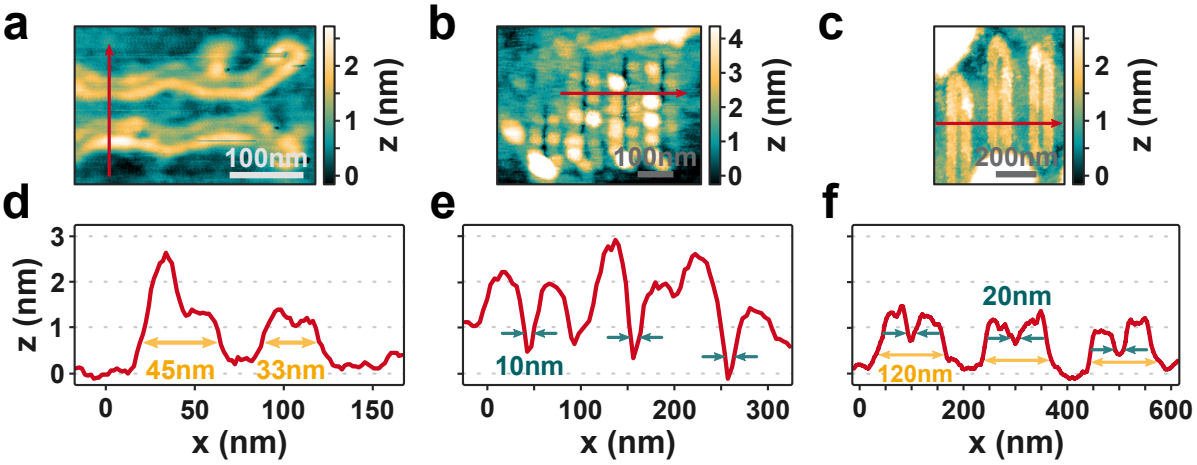


Figure 6.3.: **Pseudocuts and cuts produced by LAO. (a-c)** AFM tapping mode topography images. Red arrows mark line cuts shown in the panels below. Panel **a**: Narrow elevations produced with LAO parameters: RH = 60%, $V_{\mathrm{tip}} = -9.7\,\mathrm{V}$, $v_{\mathrm{tip}} = 200\,\mathrm{nm/s}$, $F_{\mathrm{load}} = 25\,\mathrm{nN}$. Panel **b**: Narrow cuts produced with LAO parameters: RH = 60%, $V_{\mathrm{tip}} = -9.5\,\mathrm{V}$, $v_{\mathrm{tip}} = 200\,\mathrm{nm/s}$, $F_{\mathrm{load}} = 22\,\mathrm{nN}$. Panel **c**: Wide elevations produced with LAO parameters: RH = 65%, $V_{\mathrm{tip}} = -6\,\mathrm{V}$, $v_{\mathrm{tip}} = 200\,\mathrm{nm/s}$, $F_{\mathrm{load}} = 25\,\mathrm{nN}$. **(d-f)** Line cuts marked by red arrows in the panels above and all drawn to same vertical scale. Orange double arrows mark width of pseudocuts, as labeled. Panel **e**: All petrol arrow pairs mark a distance of 10 nm. Panel **f**: All petrol arrow pairs mark a distance of 20 nm and all orange double arrows a distance of 120 nm.

is that I_{LAO} has to vanish during the process ($I_{\mathrm{LAO}} < 100\,\mathrm{pA}$, otherwise $I_{\mathrm{LAO}} \approx 1\,\mu\mathrm{A}$). Probably, the oxidation within the water meniscus continuously disconnects the part of the tip directly in contact with the sample from the surrounding graphene.[468] Hence V_{tip} mainly drops at the tip-sample interface and sustains the required electric field.

Before patterning the final structure, working parameters have to be found. In every new processing session, V_{tip}, v_{tip} and the amplitude set-point are widely varied. One should bare in mind that final parameters result from this time consuming procedure and are to some extent, random, because the tip-sample system cannot be sufficiently controlled. I typically employed V_{tip} between -6 and $-10\,\mathrm{V}$ and v_{tip} between 25 and 200 nm/V. My F_{load} in the range of 0.1 to 32 nN is comparable to values used in Refs. [334, 445, 447, 462], but significantly lower than, for instance, in Refs. [336, 442].

Figure 6.3 on the one hand portrays a few examples of produced pseudocuts (Fig. 6.3a,c) and cuts (Fig. 6.3b), while on the other hand showcasing the difference in results for almost identical parameters (Fig. 6.3a vs. Fig. 6.3b). The elevations in Figure 6.3a are among the most narrow ever produced. As seen in Figure 6.3d, their width ranges be-

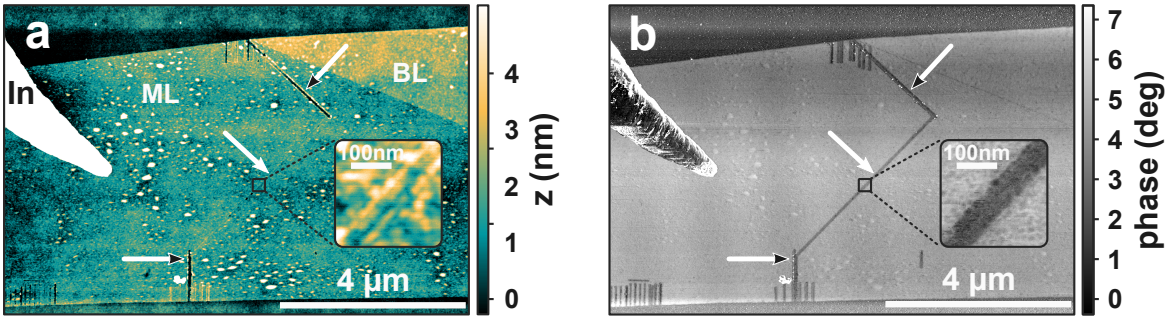


Figure 6.4.: **Pseudocut with attached full cuts. (a)** Tapping mode AFM topography of the middle section of the graphene on SiO_2 sample S129. Image was linewise aligned (median of differences method). Monolayer (ML) and bilayer (BL) part of the flake and Indium contact (In) are labeled. Numerous cuts and pseudocuts at the edge of the flake exemplify the process of finding adequate parameters. Pseudocut (marked by white arrow) was produced with LAO parameters: RH = 50%, $V_{\mathrm{tip}} = -7\,\mathrm{V}$, $v_{\mathrm{tip}} = 120\,\mathrm{nm/s}$, $F_{\mathrm{load}} = 31\,\mathrm{nN}$. The cuts connecting the edge of the flake and the pseudocut (marked by arrows with black filled heads) were produced with LAO parameters: RH = 48%, $V_{\mathrm{tip}} = -7\,\mathrm{V}$, $v_{\mathrm{tip}} = 50\,\mathrm{nm/s}$, $F_{\mathrm{load}} = 5\,\mathrm{nN}$ on the next day and the oxidation was repeated once. Inset shows zoom into area marked by the black square from a separate measurement. Full color scale is 1.76 nm. **(b)** Phase image corresponding to panel **a**. Image was linewise aligned (median value method). Inset shows zoom into area marked by a black square from a separate measurement. Full color scale is 5.26 deg.

tween $30 - 45\,\mathrm{nm}$ and their height is about 1.1 nm. The latter is a very typical value, as can be seen by comparing to the other line cuts (Fig. 6.3e,f), which have an identical height scale. In comparison, even though reducing V_{tip} to $-9.5\,\mathrm{V}$ and F_{load} to 22 nN, cuts were produced in Figure 6.3b. Their width of about 10 nm (Fig. 6.3e) is probably limited by the tip geometry. In the last example (Fig. 6.3c), wide, homogeneous pseudocuts of about 120 nm width (Fig. 6.3f) were structured. The reduced $V_{\mathrm{tip}} = -6\,\mathrm{V}$ limited the degree of oxidation and largely pertained graphene's mechanical stability. The tip was still quite sharp judging from the about 20 nm wide depression in the center (petrol arrows Fig. 6.3f), but did not plow through the partially oxidized graphene.

Next, I will demonstrate that cuts and pseudocuts can be successfully combined in one structure. A pseudocut, purposely distanced from the flake edges, serves as active element, while cuts separate the source and drain lead. Figure 6.4a shows a tapping mode AFM topography image of an Indium contacted graphene flake on SiO_2 and Figure 6.4b the corresponding phase image. The MLG part was used for LAO and the short lines perpendicular to the flake edges are the result of finding adequate parameters. First, the about 4 µm long pseudocut is drawn (fully white arrow Fig. 6.4a,b) using the parameters

RH = 50%, $V_{\mathrm{tip}} = -7\,\mathrm{V}$, $v_{\mathrm{tip}} = 120\,\mathrm{nm/s}$ and $F_{\mathrm{load}} = 31\,\mathrm{nN}$. It is barely visible in the topography but clearly visible in the phase image (see insets Fig. 6.4) and appears to be nicely homogeneous over almost its entire length. Next, I increase the oxidation time by reducing the scan speed to $v_{\mathrm{tip}} = 50\,\mathrm{nm/s}$ and repeat the process once to produce the attached cuts (marked by arrows with black heads in Fig. 6.4). The upper cut is actually incomplete and exemplifies the limited reproducibility of the method. Transport measurements of this structure revealed a gap of about 2.6 eV at $T = 120\,\mathrm{K}$ (see Fig. A.2), compatible with values reported by Masubuchi et al.[461]

In conclusion, LAO can be used to create nanostructures, while the most narrow features are attained with pseudocuts. Moreover, it allows to define electrodes on the 10 µm scale, which is crucial to apply contacts to the sample. In the next sections I will discuss the transport measurements of a few nanostructures.

6.2. Graphene ring structures

The Aharonov-Bohm (AB) effect[129,469,470] beautifully portrays the wave nature of electrons in a quantum interference experiment, which was first realized by Webb et al.[471] in a single metal ring. Electrons entering a ring-like structure as shown in Figure 6.5a,b from the left may exit on the right by either traversing through the upper or lower arm. Initially, these two partial waves will interfere constructively leading to a maximum in the transmission. In an external magnetic field B the magnetic flux $\phi = B \cdot A$ threads the mean area A enclosed by the two arms and both partial waves will accumulate an opposite AB phase $|\Delta\varphi_{\mathrm{AB}}| = \pi\frac{\phi}{\phi_0}$,[110] where $\phi_0 = h/e$ is the magnetic flux quantum. Consequently, their interference will oscillate between constructive and destructive with a period of

$$\Delta B_{\mathrm{AB}} = \frac{\phi_0}{A} = \frac{h/e}{A}, \tag{6.2}$$

which is also observed in the transmission through the ring. For an Aharonov-Bohm ring (ABR) with inner radius r_{in} and outer radius r_{out} eq 6.2 reduces to $\Delta B_{\mathrm{AB}} = 2\hbar/(e\bar{r}^2)$, where $\bar{r} = (r_{\mathrm{in}} + r_{\mathrm{out}})/2$ is the mean radius.

As pointed out in the context of weak localization (sec. 3.2), interference of phase-coherent scattering paths is special in graphene. Upon rotating the electron wave vector adiabatically by 2π, the ML graphene wave function (eq 3.9) accumulates an additional Berry phase[121] of π due to its sublattice pseudospin property (see also sec. 3.1). This

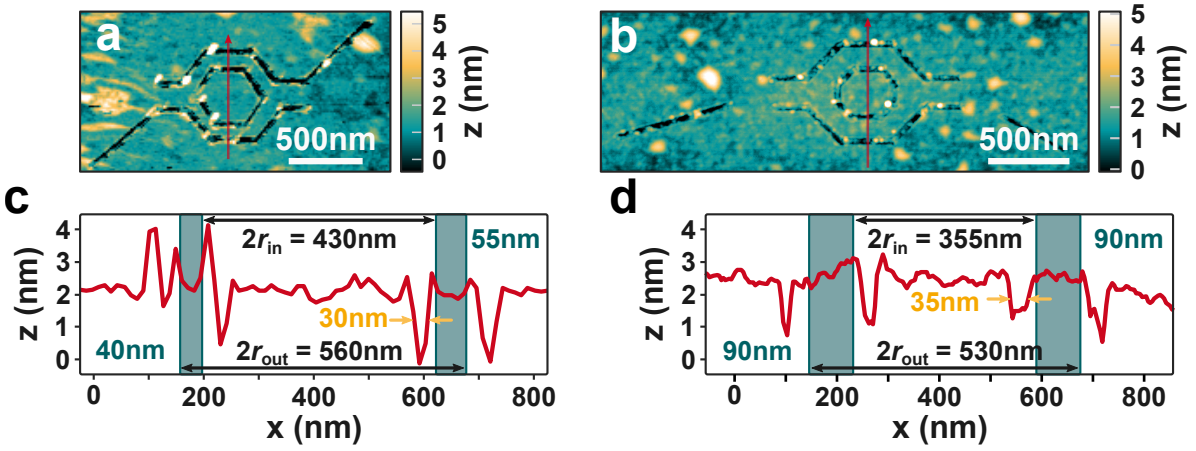


Figure 6.5.: **Graphene rings (GRs) produced by LAO. (a)** GR structured into MLG (sample L328, zone 1) by Nent[442] with LAO parameters: RH = 42%, $V_{\mathrm{tip}} = -7\,\mathrm{V}$, $v_{\mathrm{tip}} = 150\,\mathrm{nm/s}$, $F_{\mathrm{load}} = 300\,\mathrm{nN}$. Cuts are $30 - 35\,\mathrm{nm}$ wide (see panel **c**). Red arrow marks line cut in panel **c**. **(b)** Bilayer GR (sample S129) structured using LAO parameters: RH = 48%, $V_{\mathrm{tip}} = -7\,\mathrm{V}$, $v_{\mathrm{tip}} = 200\,\mathrm{nm/s}$, $F_{\mathrm{load}} = 5\,\mathrm{nN}$, inner ring radius 150 nm, outer ring radius 300 nm. Cuts are about 35 nm wide (see panel **d**). Red arrow marks line cut in panel **d**. **(c,d)** Line cuts along the red arrows in above panels. Left/right petrol vertical boxes, width (petrol labels) of the lower/upper arm of the GR (in panel **d**, the left box ignores remaining GO which makes the cut appear too narrow); upper/lower black horizontal double arrows, effective inner/outer diameter of the GR as labeled; orange arrow pair, cut width as labeled at a position where the full cut width appears in the line cut (compare panel **a**,**b**).

additional phase difference leads to destructive interference of the two paths and suppresses the transmission for vanishing B.[472] In BLG Berry's phase is 2π.[122] Hence one expects a peak in the transmission for $B = 0\,\mathrm{T}$.[473–475]

The AB effect in semiconductors is well established since 1987.[476–478] AB oscillations in graphene (see Ref. [479] for a review) were successfully observed in EBL and RIE patterned ABRs,[480–486] antidot lattices[487] and, recently, in a dual-gated hBN/MLG/hBN sample, where the ABR was gate defined.[298] In the latter case, the defining electrostatic potential guides the electrons along the ring while exploiting the suppression of Klein tunneling for grazing incidence (see Fig. 4.3e). Moreover, the scattering is valley-preserving as a minimum in conductivity is observed for $B = 0\,\mathrm{T}$ around the Dirac point.

Figure 6.5a,b portrays the LAO structured graphene rings (GRs) to be discussed here. After I prepared and contacted the ML graphene flake on SiO_2, the structuring of the GR in Figure 6.5a was carried out by A. Nent[442] utilizing a different AFM (Anfatec) but the

same cantilever type (NSC18). Besides the upper arm being slightly wider than the lower (55 nm vs. 40 nm) and some remaining rubble (bright white dots), narrow, $30 - 35$ nm wide cuts were achieved. With $r_{\mathrm{in}} \approx 215$ nm and $r_{\mathrm{out}} \approx 280$ nm (diameter measured, see Fig. 6.5c), $\bar{r} = 247.5$ nm and thus $\Delta B_{\mathrm{AB}} = 21.5$ mT. The bilayer GR in Figure 6.5b was structured with similar parameters, RH = 48%, $V_{\mathrm{tip}} = -7$ V, $v_{\mathrm{tip}} = 200$ nm/s, $F_{\mathrm{load}} = 5$ nN, though the load force was significantly smaller. The reduced rubble indicates that the tip thus removed less of the produced GO from the pseudocuts leading to the comparatively incomplete appearance of the cuts. Otherwise the structuring result looks homogeneous and the nicely symmetric GR should be sufficiently defined by the insulating GO. The measured $r_{\mathrm{in}} \approx 177$ nm and $r_{\mathrm{out}} \approx 265$ nm (see Fig. 6.5d) yield $\bar{r} = 221$ nm and $\Delta B_{\mathrm{AB}} = 27$ mT.

Figure 6.6a-c portrays the transport data on the monolayer GR. The back gate was broken thus only measurements with floating back gate electrode were conducted. Hence, the position of the Dirac point could not be obtained and I can only speculate that this sample is also p-doped. A constant source drain current $I_{\mathrm{SD}} = 10$ nA was applied and the 2-point magnetoresistance recorded. As expected, the data is symmetric for $-B \to B$. All measurements below about 3.2 K show massive negative magnetoresistance between -25 and 25 mT (Fig. 6.6a). This pronounced feature is observed in all four LAO structured GRs (compare Fig. 6.6d, Fig. A.3). The maximum resistance R_{max} (magenta diamonds, inset Fig. 6.6a) increases approximately linearly with decreasing T and saturates at about 1 K. This excludes WL and more generally quantum interference corrections in 2D as possible mechanism, because they are logarithmic in T.[110,135]

Peculiarly, R_{max} of the second GR on the same sample shows a very similar behavior (blue diamonds, inset Fig. 6.6a). If the effect would arise from localization effects within the nanostructures, it should be very sensitive to the individual scattering paths, that is, the geometry and atomic edge configuration are crucial. However, all LAO structured samples share Indium contacts. The superconducting critical temperature $T_{\mathrm{c}} = 3.41$ K (bulk value[488]) falls rights into the range between 3.1 K and 3.95 K (no intermediate values recorded) where the feature subsides. Moreover, the critical magnetic field[488] $B_{\mathrm{c}} = 28.57$ mT at zero T describes the width of the peak reasonably well. As deduced in my diploma thesis[101] from the T dependence of jumps in the resistivity of a MLG flake, B_{c} for In contacts is reduced by up to a factor of two, while $T_{\mathrm{c}} \approx 3.37$ K roughly matches the bulk value. This is plausible, because the small diameter of the contacts makes them less resilient against the external magnetic field. Very similar resistance

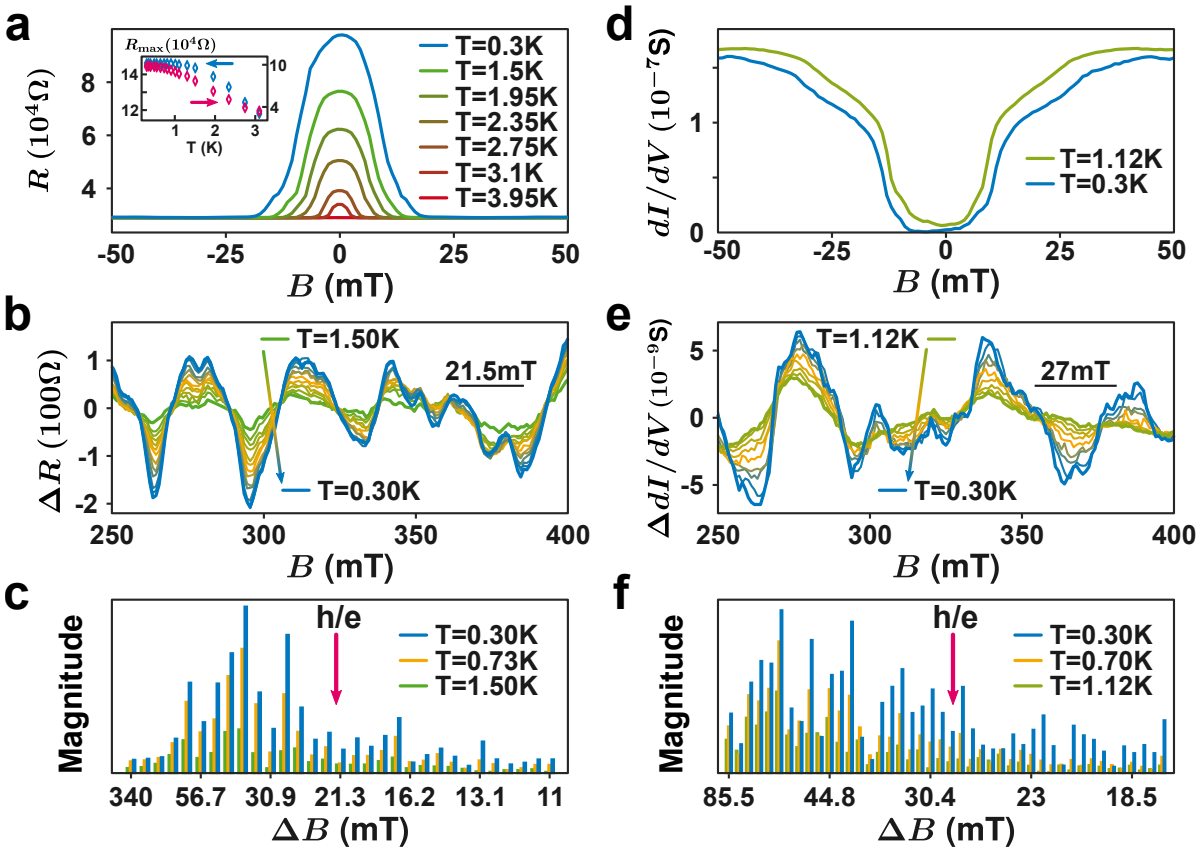


Figure 6.6.: **Transport characterization of graphene rings (GRs).** **(a)** 2-point resistance of the monolayer GR (sample L328, zone 1) around zero B for seven different T, as labeled. $I_{SD} = 10\,\text{nA}$ (constant current), back gate floating. Inset shows maximum resistance $R_{max}(T)$ for all curves with a central peak: magenta diamonds, this GR; blue diamonds, monolayer GR on the same sample (see Fig. A.3). **(b)** Same data as in panel **a** at different B after background subtraction (Savitzky-Golay filtered, 2nd order, 85 mT kernel) for $T = 1.5\,\text{K}$ (green), 1.31 K, 1.11 K, 1.01 K, 0.9 K, 0.8 K, 0.73 K, 0.64 K, 0.54 K, 0.49 K, 0.4 K, 0.34 K, 0.3 K (blue). Black bar marks expected AB period of 21.5 mT, as labeled. **(c)** FFT of the data in panel **b** for three different T, as labeled, in the range $B = 60 - 400\,\text{mT}$ excluding the central feature. Magenta arrow indicates expected AB period of 21.5 mT. **(d)** 2-point differential conductance $\mathrm{d}I/\mathrm{d}V$ of the bilayer GR (sample S129) around zero B for two different T, as labeled. $V_{SD} = 10\,\mu\text{V}$, $V_{mod} = 40\,\mu\text{V}$, $f_{mod} = 23.23\,\text{Hz}$, $V_{BG} = 20\,\text{V}$. **(e)** Same data as in panel **d** at different B after background subtraction (Savitzky-Golay filtered, 2nd order, 107 mT kernel) for $T = 1.12\,\text{K}$ (green), 1.03 K, 0.92 K, 0.8 K, 0.7 K, 0.55 K, 0.48 K, 0.36 K, 0.3 K (blue). Black bar marks expected AB period of 27 mT, as labeled. **(f)** FFT of the data in panel **e** for three different T, as labeled, in the range $B = 60 - 1000\,\text{mT}$ excluding the central feature. Magenta arrow indicates expected AB period of 27 mT.

jumps were found on the BLG sample for pairs of contacts not attached to the GR (see Fig. A.4). However, the mechanism behind the strong effect in the resistance is not understood, but also of no further relevance for the evaluation of the transport features outside of the affected B range.

In order to extract possible AB oscillations from the data, I perform a background subtraction. The background is generated by applying a second order Savitzky-Golay filter with an 85 mT kernel, which is approximately four times ΔB_{AB}. Figure 6.6b shows the temperature dependence of the exposed resistance fluctuations. Quite obviously, there is no dominant 21.5 mT period, which is corroborated by the absence of a corresponding peak in the fast Fourier transform (FFT) of the data (magenta arrow, Fig. 6.6) for B between 60 and 400 mT. Moreover the FFT shows that the relative magnitude of the frequency components remains largely unchanged while the absolute magnitude increases for decreasing temperature. Hence, there is no sign of entrant AB oscillations. The signal is dominated by UCFs,[135,489–492] which arise from the interference of random paths modified by B.

Though the bilayer GR was designed for a 4-point measurement, two contacts were not usable and thus only the 2-point differential conductivity was recorded. Firstly, the low conductivity (Fig. 6.6d) shows that the bottom graphene layer was fully affected by the LAO process. The same procedure for background subtraction is employed, this time with a 107 mT kernel. However, the differential conductivity fluctuations in Figure 6.6e show no modulation with the expected 27 mT period and no corresponding peak in the FFT (Fig. 6.6f) is observed. Different parameters were varied, that is, V_{BG} from -10 to 30 V, V_{AC} from 25 to 250 µV, but no regime with AB oscillations was found. Consequently the sample was abandoned in a timely manner.

In conclusion, LAO appears a cumbersome path to create graphene nanostructures for quantum interference experiments. The investigated GRs most probably suffer from rough edges as source of strong intervalley scattering and localization with detrimental consequences for the observation of AB oscillations. My experiments thus corroborate findings by Weng et al.[458] for the only other reported LAO structured GR. Close inspection of Figure 6.5a actually casts doubt on the transparency of the lower arm of the MLG device. Incompletely oxidized areas reduce the effective width of the entrance to the lower arm strongly below 40 nm, which could also explain the absence in that case. However, AB oscillations are not observed in any of the four investigated GRs. There might be a chance to observe AB oscillations in future GRs if they feature smaller radii

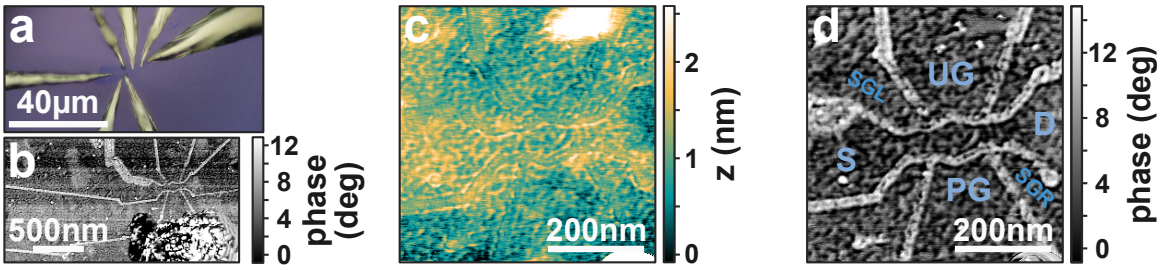


Figure 6.7.: **LAO structured multi-electrode QD with Indium contacts.** **(a)** Optical micrograph of sample IB01 showing the about 35 µm × 15 µm large graphene flake on a Si/SiO_2 substrate and seven micro-soldered Indium contacts. **(b)** Tapping mode AFM phase image showing multiple graphene electrodes separated by oxidized lines running towards the QD structure. **(c,d)** Tapping mode AFM topography and phase image, respectively, of a zoom onto the central QD structure. LAO parameters: RH = 60%, $V_{\mathrm{tip}} = -8.75\,\mathrm{V}$, $v_{\mathrm{tip}} = 200\,\mathrm{nm/s}$, $F_{\mathrm{load}} = 19\,\mathrm{nN}$. In **d** Contacted electrodes are labeled: Source (S), drain (D), side gate left (SGL) and right (SGR), and two plunger gates (PG, UG).

and perhaps only a large oxidized dot in the center produced without moving the tip.

6.3. Coulomb blockade in a structured quantum dot

In Figure 6.7 I portray a MLG QD produced by LAO, which has also been discussed in Ref. [309]. After exfoliation on Si/SiO_2, I micro-soldered (see sec. 3.4) seven Indium contacts onto the about 35 µm × 15 µm graphene flake (Fig. 6.7a). Figure 6.7b shows the vicinity of the QD with bright lines separating the different electrodes, which were mainly structured with the same LAO parameters as the QD (i.e., RH = 60%, $V_{\mathrm{tip}} = -8.75\,\mathrm{V}$, $v_{\mathrm{tip}} = 200\,\mathrm{nm/s}$, $F_{\mathrm{load}} = 19\,\mathrm{nN}$). The large chunk of debris at the bottom right stemmed from a nearby tip-crash, which damaged an In contact, and was later removed with the AFM tip. Figure 6.7c,d portray tapping mode AFM topography and phase images, respectively, of a zoom onto the central QD structure. The LAO parameters were optimized to generate the most narrow boundary structures possible. They are only about 15 nm wide and barely visible in the topography (Fig. 6.7c). However, the clear contrast in the phase image (Fig. 6.7d) confirms the successful partial oxidation and realization of source and drain leads, several side gates and two plunger gates. From this image I also extract the QD diameter of about 60 nm and the width of the constrictions of about 35 nm.

For the characterization of the QD V_{SD} was applied anti-symmetrically to source and

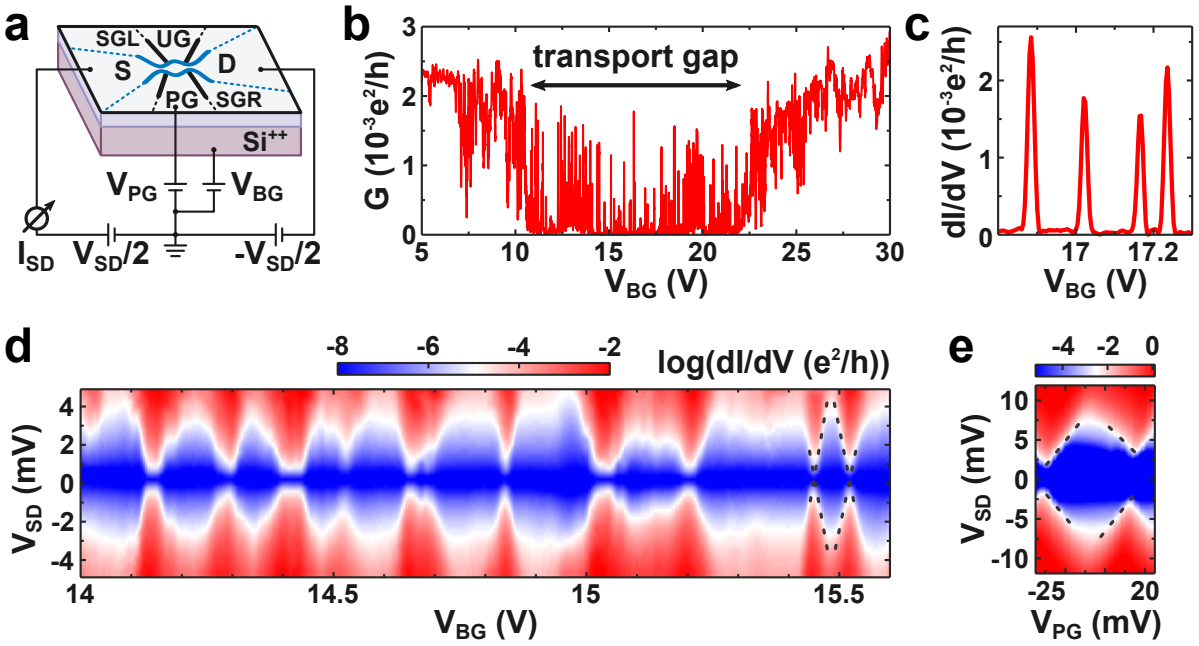


Figure 6.8.: **Transport characterization of a LAO structured QD. (a)** Sketch of the electrical circuit of the MLG QD on Si/SiO_2 (Sample IB01). Source (S), drain (D), lower plunger gate (PG), upper plunger gate (UG) and left/right side gate (SGL/SGR) electrode are labeled. All gate electrodes except the PG and BG were leaky, thus only V_{PG} and V_{BG} are sketched. V_{SD} is applied antisymmetrically and can include an AC component, which is used to measure the differential conductance dI_{SD}/dV_{SD} via a Lock-In amplifier (not shown). **(b)** Back gate trace recorded at $V_{SD} = 1.5\,\mathrm{mV}$, $T = 300\,\mathrm{mK}$, $V_{PG} = 0\,\mathrm{mV}$, all other electrodes floating. **(c)** Zoom into transport gap, showing a Coulomb peak sequence in dI_{SD}/dV_{SD} recorded at $V_{SD} = 0.5\,\mathrm{mV}$, $V_{mod} = 100\,\mu\mathrm{V_{rms}}$, $f_{mod} = 73.78\,\mathrm{Hz}$, $T = 1.2\,\mathrm{K}$, $V_{PG} = 0\,\mathrm{mV}$, all other electrodes floating. FWHM of the peaks about $15\,\mathrm{mV_{BG}}$. **(d)** Coulomb diamonds in a logarithmic plot of dI_{SD}/dV_{SD} recorded as function of V_{SD} and V_{BG} at $T = 1.2\,\mathrm{K}$, $V_{mod} = 100\,\mu\mathrm{V_{rms}}$, $f_{mod} = 73.78\,\mathrm{Hz}$, $V_{PG} = 0\,\mathrm{mV}$, all other electrodes floating. Diamond with dotted boundaries at $V_{BG} = 15.5\,\mathrm{V}$ was used to extract BG lever arm α_{BG}. The left (right) side of the diamond yields $\alpha_{BG,L} = 0.0736$ ($\alpha_{BG,R} = 0.0656$), thus $\alpha_{BG} = (\alpha_{BG,L} + \alpha_{BG,R})/2 \approx 0.07$. **(e)** Coulomb diamond in a logarithmic plot of dI_{SD}/dV_{SD} recorded as function of V_{SD} and V_{PG} at $T = 300\,\mathrm{mK}$, $V_{mod} = 30\,\mu\mathrm{V_{rms}}$, $f_{mod} = 73.78\,\mathrm{Hz}$, $V_{SGL} = V_S$, $V_{BG} = 14.8\,\mathrm{V}$, $V_{SGR} = V_D$, UG floating. Slopes of the diamond boundary, marked by dotted lines, yield $\alpha_{PG,L} = 0.152$ and $\alpha_{PG,R} = 0.137$.

drain (i.e., $V_{SD}/2 = V_S = -V_D$) and the 2-point conductance $G = I_{SD}/V_{SD}$ was measured (see also sec. 2.2). Figure 6.8b shows a back gate trace, recorded by varying V_{BG} at fixed $V_{SD} = 1.5\,\mathrm{mV}$ and $T = 300\,\mathrm{mK}$. The outer regions portray a transport regime of finite conductance, while the conductance partly vanishes and exhibits intermittent conductance resonances in the central region. This so-called transport gap at low carrier densities is governed by Coulomb blockade of the QD structure. Single Coulomb peaks in dI/dV are resolved in Figure 6.8c. They were measured by modulating V_{SD} with an amplitude of $V_{mod} = 100\,\mu\mathrm{V_{rms}}$ and frequency $f_{mod} = 73.78\,\mathrm{Hz}$. Collecting many such back gate traces at varying V_{SD} reveals partly overlapping Coulomb diamonds (Fig. 6.8d) of various size. This strongly suggests that contributions from multiple QDs in series enter the conductance signal.[322,341,493] Deformed diamonds indicate mixing of QD states with other localized states.[327] Moreover, the diamonds barely touch at zero V_{SD} which indicates that part of V_{SD} drops either at a QD or contact oxide barrier (see also sec. 3.4) in series.

The diamond marked by dashed lines in Figure 6.8d appears to originate from transport through a single charge state and its slopes yield a back gate lever arm of $\alpha_{BG} = 0.07$ (mean of left $\alpha_{BG,L} = 0.0736$ and right $\alpha_{BG,R} = 0.0656$ side, see also sec. 4.1). To deduce a total capacitance for the QD C_Σ from this I need to estimate the back gate capacitance C_{BG}. A circle with 60 nm diameter is the lower boundary for the effective QD area A_{QD}. However, since the QD constrictions are not much narrower than the QD itself, it might extend into the source and drain leads and cover an area of up to $60 \times 200\,\mathrm{nm}^2$. In the plate capacitor model this yields

$$C_{BG} = \varepsilon_0 \varepsilon_{SiO_2} \frac{A_{QD}}{t_{SiO_2}} = 0.425 \ldots 1.4\,\mathrm{aF}, \tag{6.3}$$

with $\varepsilon_{SiO_2} = 4$ and $t_{SiO_2} = 300\,\mathrm{nm}$. It is known, that due to fringe field amplification[494] eq 6.3 easily underestimates the capacitance of such nanostructures. Indeed, the Poisson solver cross-check in Figure 6.9 (see also sec. 5.2) yields a much larger capacitance for a circular graphene QD with $r_{dot} = 30\,\mathrm{nm}$ on 300 nm SiO_2. Obviously, the electric field lines (cyan arrows in Fig. 6.9a) deviate strongly from the idealized parallel alignment in the plate capacitor model. Excluding the two data points closest to the Dirac point in Figure 6.9c, that is, adjacent to zero V_{BG}, and thus neglecting effects of quantum capacitance, yields a mean $C_{BG} \approx 3.7\,\mathrm{aF}$. This value probably overestimates C_{BG}, because the surrounding graphene electrodes suppress the extended part of the electric

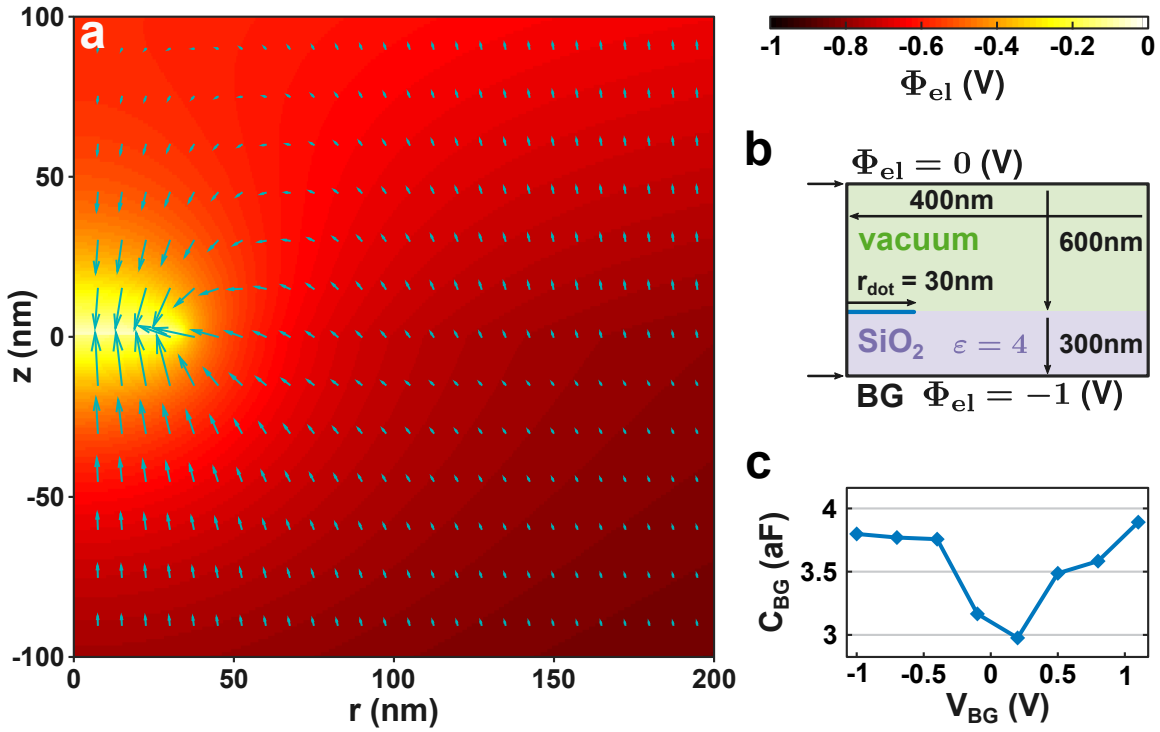


Figure 6.9.: **Visualizing fringe fields and estimating the back gate capacitance of the QD.** **(a)** Zoom into the electrostatic potential Φ_{el}, calculated as numerical, cylinder symmetric solution of Poisson's equation for the system sketched in panel **b**. QD extends from $r = 0 - 30\,\text{nm}$ at $z = 0\,\text{nm}$. Cyan arrows indicate electric field, calculated as gradient of Φ_{el}. **(b)** Sketch of the Poisson calculation. 300 nm SiO_2 ($\varepsilon = 4$) separate the back gate (BG) from the graphene QD (30 nm radius, $\varepsilon = 2.5$). The upper bound is fixed at $\Phi_{el} = 0\,\text{V}$ and the lower bound (BG) at, e.g., $\Phi_{el} = -1\,\text{V}$. The left and right boundary fulfill a Neumann boundary condition. **(c)** Back gate capacitance C_{BG} calculated from the induced charge Q_{QD} on the graphene QD for different V_{BG} ($C_{BG} = Q_{QD}/V_{BG}$).

field. However, using this value, $C_\Sigma = C_{BG}/\alpha_{BG} = 52.9\,\text{aF}$ and $E_C = e/C_\Sigma = 3\,\text{meV}$, which is in reasonable agreement with the $3 - 4\,\text{meV}$ observed in the measurements (height $e\Delta V_{SD}$ of Coulomb diamonds in Fig. 6.8d).

In principle various other side gates allow to tune the QD. However, all but PG turned out to be leaky, that is, exhibit a resistance of $\leq 10\,\text{M}\Omega$ to the rest of the structure. Hence, gate voltages of 1 mV will already induce leakage currents on the order of 100 pA, significantly disturbing the QD conductance signal. PG was used to record the Coulomb diamond at $V_{BG} = 14.8\,\text{V}$ in Figure 6.8e. Since the opening of the diamond on the right side effectively reduces the slopes of its boundaries (dotted lines), I use $\alpha_{PG} \approx 0.15$ from the left side of the diamond. This is a typical value for lateral gates also found in etched

graphene QDs.[315,330,332,495–497] The close proximity of PG and the QD, compared to the BG, explains the stronger gating.[315] By crudely estimating that the side gates on the left and right side each combined make up for an area equal to that of the PG, I find six electrodes with roughly the same coupling to the QD. Together with the back gate they add up to the total capacitance (i.e., $\sum_i \alpha_i = 6 \times 0.15 + 0.07 \approx 1$, see sec. 4.1).

On the contrary, considering the width of the diamond $\Delta U_{\mathrm{PG}} \approx 42\,\mathrm{mV}$ at zero V_{SD} translates to $C_\Sigma = e/(\alpha_{\mathrm{PG}} \cdot \Delta U_{\mathrm{PG}}) \approx 24\,\mathrm{aF}$, which disagrees with the previously estimated value of $C_\Sigma = 53\,\mathrm{aF}$. However, it is difficult to judge from a single diamond if $E_{\mathrm{add}} \approx E_{\mathrm{C}}$ and Figure 6.8d suggests that this is actually not the case.

In summary, it was possible to define a graphene QD with oxidized pseudocuts and measure the Coulomb blockade features of this device. The demonstrated feature sizes are amongst the smallest reported for etched graphene QDs.[315,324,498] Narrow boundaries, again at the limit of values reported for AFM LAO,[461] allow to bring gates very close to the target structures, that is, the QD or tunneling barriers. Unfortunately, a few electrodes were insufficiently insulated from the rest of the structures, thus future structuring attempts need to check the homogeneity of the boundaries more carefully. Ideally, less surgical parameters should be used to define the outer electrodes. The measured Coulomb diamonds are irregular and indicate that additional QDs in series and localized states contribute to the conductance. This behavior is also found in the other reported LAO structured graphene QD[334] and in the majority of experiments on etched graphene QDs.[67,244]

6.4. Conclusion

LAO enables the resist-free structuring of graphene and was employed to create graphene rings and QDs, which could potentially be investigated by STM. They were defined by insulating graphene oxide lines down to 15 nm in width and exhibit minimal feature sizes of 35 nm. Both values are at the lower end of reported values. Especially the multi-electrode QD is among the most complex structures reported in literature and even exhibits an operational graphene plunger gate; a novum for LAO structured QDs. Transport measurements on four graphene rings showed no sign of Aharonov-Bohm oscillations down to $T = 300\,\mathrm{mK}$, but were rather dominated by universal conductance fluctuations. The QD exhibits Coulomb blockade in a transport gap ranging from 10

to 22 V in back gate voltage. Irregular coulomb diamonds reveal addition energies of 3 to 4 meV, with no trace of orbital or valley splittings. In this sense, nanostructures produced by LAO are not superior to those created by electron-beam lithography and reactive ion etching. The only observed advantage is the increased resilience against uncontrolled charge rearrangements, which were very seldom encountered even in repeated back gate sweeps of 10 V.

Thus, edges resulting from the LAO process are effectively not advantageous with respect to those produced by electron-beam lithography and reactive ion etching when it comes to preserving the Dirac nature of the confined charge carriers. Disordered edges lead to uncontrolled charge localization[358] and intervalley scattering,[67,244] thereby crippling the control over confined states and quantum interference experiments. Within the frame of patterned graphene nanostructures, a possible solution might be to anneal the structures and thereby reconfigure the edges. Homogenizing the partially oxidized edges by controlled carbothermal etching in a dilute oxygen atmosphere[499–505] and subsequent (hydrogen) functionalization[506–510] might improve the edge characteristics. However, Indium contacts would not withstand this treatment and thus either the flake would have to be contacted differently for LAO structuring or one could employ tapping mode AFM LAO instead. The results emphasize that finding a less invasive confinement mechanism is mandatory to explore graphene's properties in nanostructures. One such approach realizing smooth confinement in graphene QDs was addressed in the previous chapter.

As a side note, LAO can potentially also structure next generation graphene/hBN heterostructures. Together with Zijlstra,[447] we could show that about 8 nm deep cuts can be structured into BN by LAO if the BN is covered by graphene and the process commences at the BN edge. Otherwise, the oxidation terminates about 3 nm into the BN, as observed by Grob.[511] In principle, this could reduce the SiO_2 induced disorder and improve the LAO nanostructures.

7. Summary

In an effort to circumvent rough edges and substrate induced potential disorder, I conducted STM and STS measurements on a commensurate MLG flake on hBN. An external magnetic field opens up Landau level gaps in the electronic spectrum and allows to trap electrons by a smooth tip-induced electrostatic potential. Poisson calculations in connection with next-nearest neighbor TB estimate a FWHM of 55 nm at $B = 7$ T for the confinement potential induced by an STM tip, with a radius of $r_{\mathrm{tip}} = 120$ nm. Charging peak sequences in dI/dV of more than 40 peaks on the electron and hole side reveal the addition energy spectrum of the created QDs. The onset of localization is found between 1-2 T. Typical addition energies at $B = 7$ T lie in the range of 10-20 meV. They are comprised of charging energies of about 10 meV, orbital splittings of 4-10 meV and valley splittings for the first/second orbital ranging from about 3 meV/7 meV on AA stacking to 8 meV/2 meV on AB stacking. The valley splittings surpass those reported for any potentially nuclear spin free host material by more than one order of magnitude (Si/SiO_2, 800 μeV).[70] The local disappearance and reappearance of a valley splitting around the AB area for the second orbital leaves traces of a valley crossing in maps of the addition energies, which is attributed to sublattice symmetry breaking interactions. Additional atomically resolved STS series find a sublattice symmetry breaking of 25 meV for LL_0 at 7 T.

The portrayed robust lifting of the valley degree of freedom embodies the first realization of a monolayer graphene QD meeting the prerequisites to be used in a spin qubit.[58] Additionally, moving the QD within the graphene superlattice (13.8 nm periodicity) supplies a highly effective tuning knob for the valley splitting and thereby establishes an inroad into quantum computation within valley space. In a next step, it would be highly interesting to assess spin and valley relaxation rates in transport measurements based on this confinement approach. Therefore, I propose a device design (Fig. 5.20) based on a hBN/MLG/hBN heterostructure using electrostatic gates to induce the QD, couple it to edge states and shift its position. Further STM experiments on samples with an

operational back gate should also elucidate the role of the position of the Fermi energy relative to the Landau level gaps with respect to the confinement strength and selection of the confined states. Moreover, taking the QD probe to other graphene heterostructures may reveal different sources impacting the eigenenergies. For instance, a WSe_2 substrate could induce strong spin-orbit interaction.

Nanostructures are also produced by local anodic oxidation of graphene flakes. They corroborate the general findings in the literature. I demonstrate precise structuring with feature sizes down to 10-30 nm, however, mono- and bilayer graphene rings with average diameters of 440 and 500 nm measured in 2-point configuration did not show signs of Aharonov-Bohm oscillations down to $T = 300$ mK. Transport measurements on a monolayer graphene QD with a diameter of 60 nm and multiple lateral gates exhibit irregular charging peak sequences with addition energies of $3 - 4$ meV. No orbital or valley splittings could be observed. Noteworthy is the comparatively strong resilience of LAO structures against uncontrolled charge rearrangements in large back gate voltage sweeps commonly observed in QDs structured by EBL and RIE.

8. Acknowlegements

Finally, I want to mention those having greatly impacted my time at the II. Institute of Physics B, RWTH Aachen University. Such an experience is foremost about the people, so I'd first like to thank Markus Morgenstern for his dedication as head of institute and providing me with many liberties during the course of my Ph. D. and Diploma thesis. Throughout, his demand for precision in the scientific discussion has presented a veritable challenge and he has always been the ultimate test for any 'home-grown' physical model. Whenever approached, he has been supportive and instantly responsive. All the best for future projects and may there be more exciting new physics around the next corner. A big thank you to Peter Nemes-Incze, the great Hungarian warrior, who joined to fight those hydralike enemies in the battles of interpreting experiments and coming up with invincible models. Good luck back in Hungary! Thanks to Christoph Stampfer for acting as second supervisor for my dissertation and providing stimulating comments and discussions on quantum dot physics and transport measurements in general. Another thanks goes out to the Vienna theory team, Florian Libisch, Larisa Chizhova, Tobias Reisch and Joachim Burgdörfer, for their key contributions to the success of the tip-induced QD project and their great hospitality during my visit. Here, a special thanks also to the Manchester group around Kostya Novoselov and Andre Geim for supplying the commensurate graphene sample.

Now, there are numerous colleagues, co-workers, employes and students who have in many ways contributed to the experiments, discussed physics problems or made my stay here more memorable. Since I think that the ordering of names should not be the main focus here, I will simply say thank you, for taking part in the after-lunch discussion club, table soccer, go-karting, cycling, running, board gaming, barbecuing, partying, wake-/snow-boarding, sailing or perhaps waterbomb slingshooting. For winning everlasting fame in the university wide institute Olympics. For being an office mate, the AFM/Raman/STM/EBL/tip-etching/clean room/you-name-it instructor, the excursion organizer, the skilled mechanic, the electronics guru, the one managing the liquid helium

shortage or defusing another Helium dewar bomb. For fun times with travel reimbursements, orders and time-sheets. And you, in one way or another, probably are (in reverse alphabetic order): Dominik Zijlstra, Frank Volmer, Uwe Wichmann (aka Sissi), Dinesh Subramaniam, Raoul Sous, Michael Schmitz, Lars Schreiber, Jörg Schirra, Dario Sarik, Frank Salz, Silke Rose, Wolfgang Retetzki Marco Pratzer, Mike Pezzotta, Christian Pauly, Fank Neubauer, Beate Nagel, Florian Muckel, Daniel Montag, Sascha Mohr, Simon Mathioudakis, Torge Mashoff, Marcus Liebmann, Ina Kürten, Philipp Küppers, Sebastian Kuhlen, Peter Kordt, Jens Kellner, Bernhard Kaufmann, Tjorven Johnsen, Felix Jekat, Lars van Hove, Arne Hollmann, Christian Holl, Helmut Hammers, Nina Grydzhuk, Martin Grob, Matthias Goldsche, Guido Geulen, Viktor Geringer, Alexander Georgi, Kilian Flöhr, Robert Feron, Marcus Eßer, Alexander Epping, Stephan Engels, Beatrix Dangela, David Cuma, Pascal Cerfontaine, Tim Botzem, Raphael Bindel, Priyamvada Bhaskar, Margarete Betger or Stefan Becker. Last, not least, I'd like to thank all the diligent electrons which participated in my experiments.

Finally, I also want to thank charming Julia for cutting me quite some slack whenever there were long hours in the lab or at the office and my family for their ongoing support since I took on studying physics.

A. Appendix

The appendix mainly provides a bit of extra information, while most of it are additional figures which did not make it to the main text. However, if certain readers want to look into the data, the references to spectroscopy series in figure captions like 'S500' are the original file names of the data sets. Their whereabouts can be retrieved in the folder of my dissertation in the excel sheet 'List of spectroscopy fields.xlsx'.

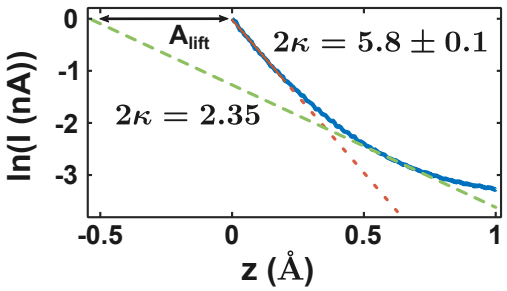


Figure A.1.: **Exemplary graphene lifting assessment.** Logarithmic plot of an $I(Z)$ curve (blue line); $V_{\mathrm{stab}} = -400\,\mathrm{mV}$, $I_{\mathrm{stab}} = 1\,\mathrm{nA}$. Orange solid line, linear fit yielding $2\kappa = 5.8 \pm 0.1$ Å^{-1}; orange dotted line, extrapolated fit; green dashed line, ideal $I(Z)$ curve with $2\kappa = 2.35$ Å^{-1}; black double arrow, graphene lifting height $A_{\mathrm{lift}} \approx 55\,\mathrm{pm}$.

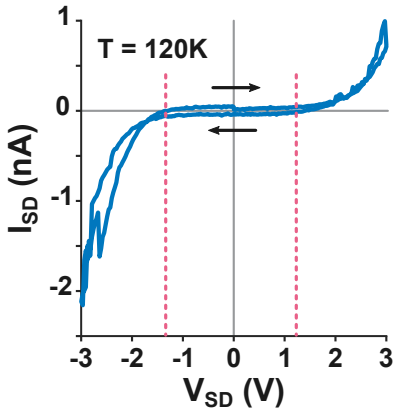


Figure A.2.: **GO gap.** 2-point I-V curve of the pseudocut shown in Fig. 6.4. $T = 120\,\mathrm{K}$ as labeled. Arrows mark sweep direction of V_{SD}. Magenta dotted lines mark gap of about 2.6 eV.

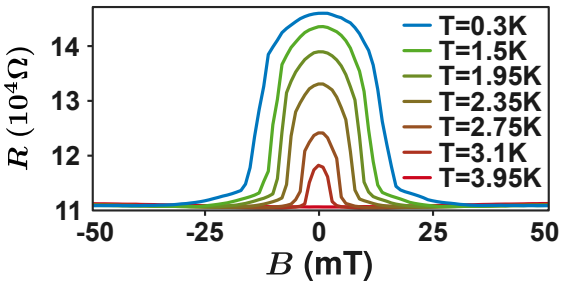


Figure A.3.: **Central magnetoresistance peak of another GR.** 2-point magnetoresistance of the GR structured by Hecking[445] (sample L328, zone 3) around zero B for different T as labeled. $I_{\mathrm{SD}} = 10\,\mathrm{nA}$ (constant current), back gate floating.

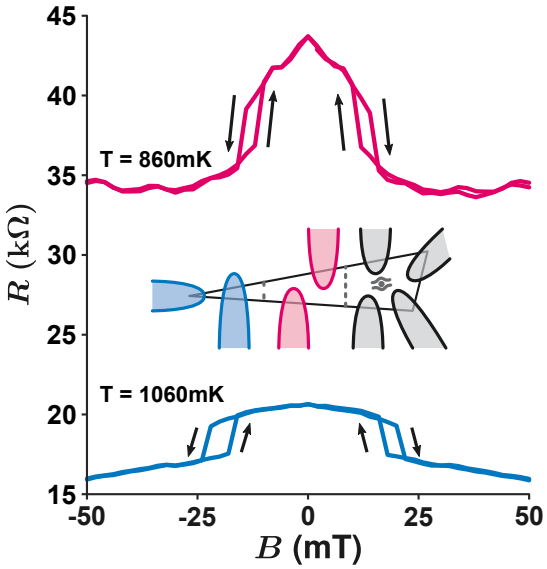


Figure A.4.: **Hysteretic magnetoresistance of graphene contacted by Indium.** 2-point magnetoresistance of the pairs of contacts marked by the same color as the curves in the central sample sketch. $V_{SD} = 1\,\mathrm{mV}$, temperature as labeled. Arrows mark sweep direction of the magnetic field B. Hysteresis is interpreted as delay between the transition of the contacts from superconducting to normal state (sweep to higher $|B|$) compared to regaining superconductivity (sweep to zero B).

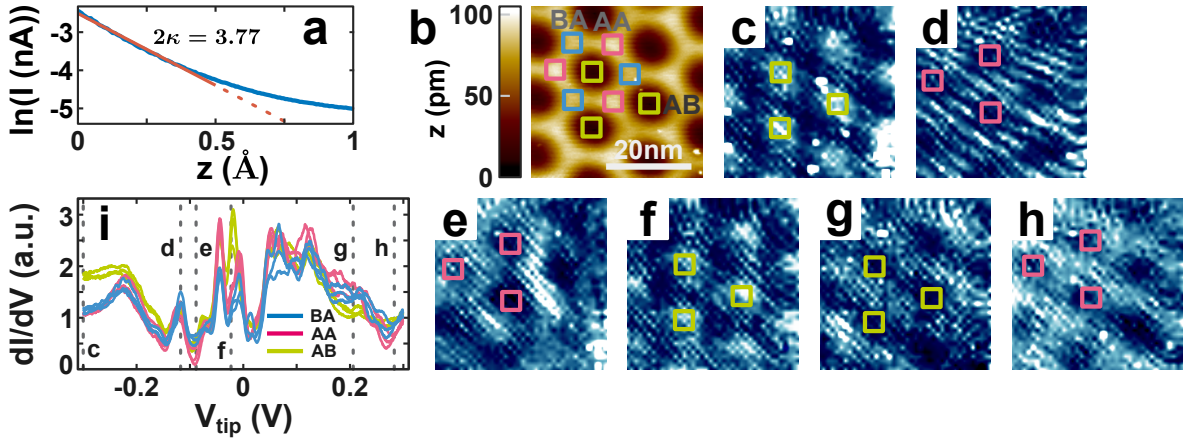


Figure A.5.: **LDOS of commensurate graphene on hBN at zero magnetic field.** **(a)** Mean $I(Z)$ curve of 5 consecutively acquired single curves. $V_{\mathrm{stab}} = 300\,\mathrm{mV}$, $I_{\mathrm{stab}} = 80\,\mathrm{pA}$. Red line marks linear fit yielding 2κ (error $\pm 0.03\,\mathrm{Å}^{-1}$), as labeled. Solid part marks range used for fitting. **(b)** $40 \times 40\,\mathrm{nm}^2$ STM image recorded at $V_{\mathrm{tip}} = 300\,\mathrm{mV}$, $I = 80\,\mathrm{pA}$. Colored squares mark areas where spectra in panel **i** were recorded. **(c-h)** dI/dV maps extracted from a series of spectra taken on a 40×40 grid in the area shown in panel **b**. Spectroscopy (varied-Z, series S184) parameters: $V_{\mathrm{stab}} = 300\,\mathrm{mV}$, $I_{\mathrm{stab}} = 80\,\mathrm{pA}$, $V_{\mathrm{mod}} = 5.5\,\mathrm{mV_{rms}}$, $B = 0\,\mathrm{T}$, tip approaches/retracts at $v_z = 100\,\mathrm{pm/V}$. V_{tip}, as labeled in panel **i**, in alphabetic order of the panels: $-300\,\mathrm{V}$, $-117.5\,\mathrm{mV}$, $-88.5\,\mathrm{mV}$, $-23\,\mathrm{mV}$, $206\,\mathrm{mV}$, $283.5\,\mathrm{mV}$. Contrast adapted for optimal visibility. **(i)** Nine locally averaged dI/dV spectra (3×3 single spectra on $2.3 \times 2.3\,\mathrm{nm}^2$) from the areas marked by colored squares in panel **b**. Magenta lines, AA stacking; green lines, AB stacking; blue lines, BA stacking. Dotted vertical lines mark V_{tip} of the dI/dV maps shown in panels **c-h**, as labeled.

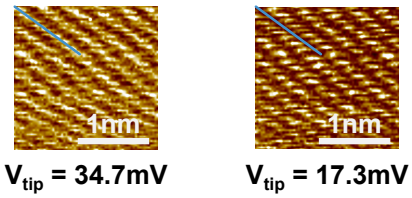


Figure A.6.: **Sublattice contrast inversion.** Maps of the dI/dV signal at the indicated V_{tip} taken from the spectroscopy series portrayed in Fig. 3.11 recorded on an AA stacked area. Stripe pattern shifts horizontally by about 1.8 Å. Blue lines are guides to the eye. Graphene lattice vertically distorted due to thermal drift.

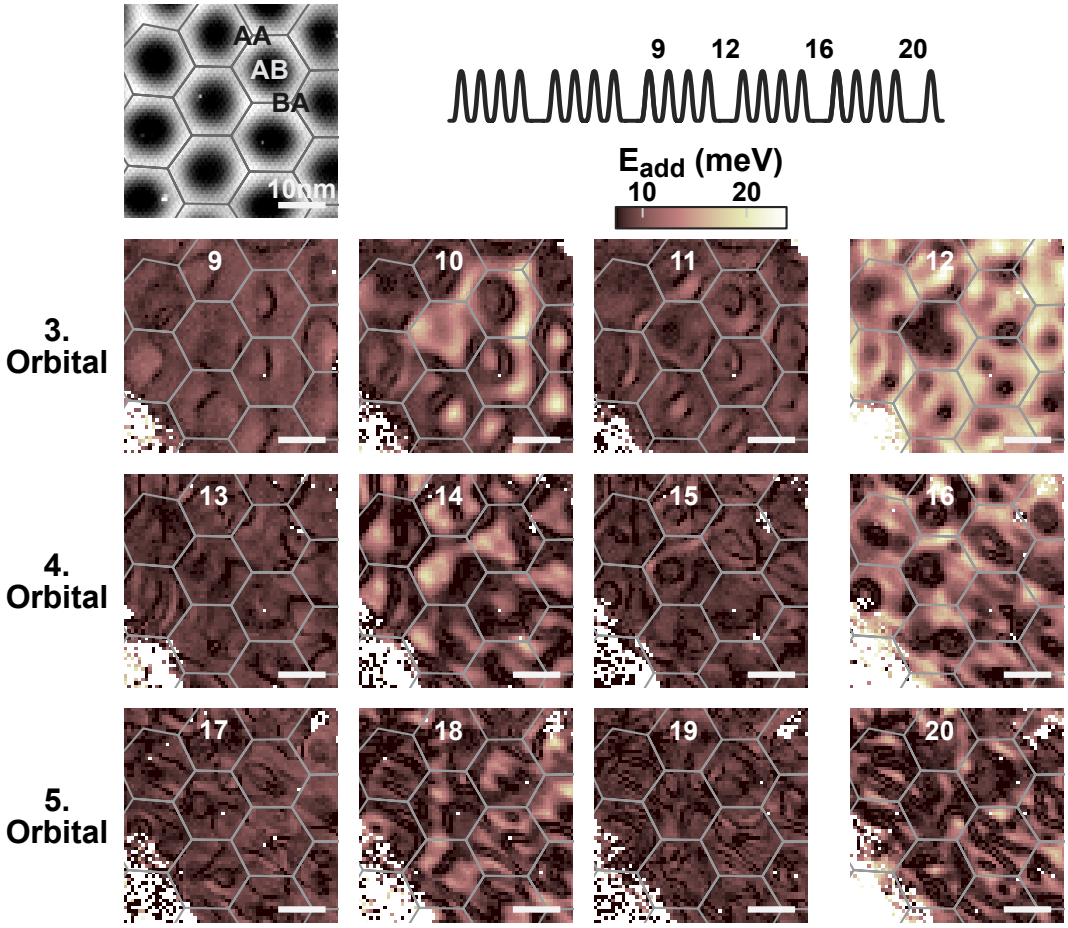


Figure A.7.: **Additional addition energy maps for confined hole states.** Top left shows STM image of the area where addition energy maps 9-20 for confined holes, as labeled, were recorded (see Fig. 5.15 for details). The first three columns of maps correspond to transitions within one QD orbital for every row, while the last column shows the addition energy required to add the first hole to the next orbital as indicated in the sketched charging peak sequence at the top. Honeycomb gray grid lines adapted to topography. All scale bars the same.

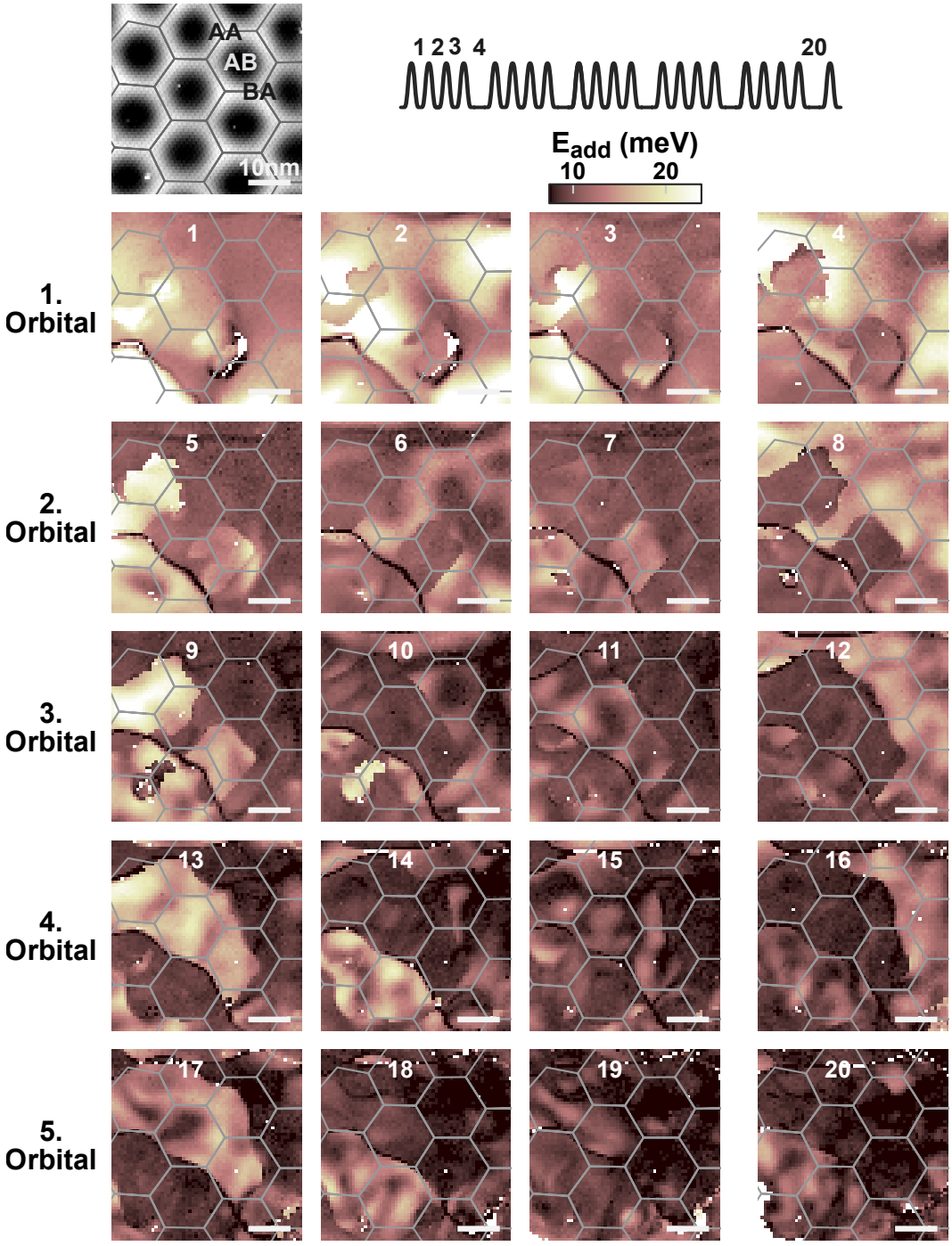


Figure A.8.: **Addition energy maps for confined electron states.** Top left shows STM image of the area where addition energy maps 1-20 for confined electrons, as labeled, were recorded (see Fig. 5.15 for details). The first three columns of maps correspond to transitions within one QD orbital for every row, while the last column shows the addition energy required to add the first electron to the next orbital as indicated in the sketched charging peak sequence at the top. Patches (map index shifted) and sharp lines in the maps are artifacts originating from defect charging peaks. Honeycomb gray grid lines adapted to topography. All scale bars the same.

Bibliography

(1) Bardeen, J.; Brattain, W. H. "The Transistor, A Semi-Conductor Triode" *Phys. Rev.* **1948**, *74*, 230–231.

(2) Riordan, M.; Hoddeson, L.; Herring, C. "The invention of the transistor" *Rev. Mod. Phys.* **1999**, *71*, S336–S345.

(3) Novoselov, K. S.; Geim, A. K.; Morozov, S. V.; Jiang, D.; Zhang, Y.; Dubonos, S. V.; Grigorieva, I. V.; Firsov, A. A. "Electric field effect in atomically thin carbon films" *Science* **2004**, *306*, 666–669.

(4) Moore, G. E. "Cramming More Components onto Integrated Circuits" *Electronics* **1965**, *38*, 114–117.

(5) Lee, C.; Wei, X.; Kysar, J. W.; Hone, J. "Measurement of the Elastic Properties and Intrinsic Strength of Monolayer Graphene" *Science* **2008**, *321*, 385–388.

(6) Nair, R. R.; Blake, P.; Grigorenko, A. N.; Novoselov, K. S.; Booth, T. J.; Stauber, T.; Peres, N. M. R.; Geim, A. K. "Fine structure constant defines visual transparency of graphene" *Science* **2008**, *320*, 1308–1308.

(7) Geim, A. K.; Novoselov, K. S. "The rise of graphene" *Nat. Mater.* **2007**, *6*, 183–191.

(8) Bonaccorso, F.; Colombo, L.; Yu, G.; Stoller, M.; Tozzini, V.; Ferrari, A. C.; Ruoff, R. S.; Pellegrini, V. "Graphene, related two-dimensional crystals, and hybrid systems for energy conversion and storage" *Science* **2015**, *347*, 1246501.

(9) Ferrari, A. C. et al. "Science and technology roadmap for graphene, related two-dimensional crystals, and hybrid systems" *Nanoscale* **2015**, *7*, 4598–4810.

(10) Banszerus, L.; Schmitz, M.; Engels, S.; Goldsche, M.; Watanabe, K.; Taniguch, T.; Beschoten, B.; Stampfer, C. "Ballistic Transport Exceeding 28 μm in CVD Grown Graphene" *Nano Lett.* **2016**, *16*, 1387–1391.

(11) Dauber, J.; Sagade, A. A.; Oellers, M.; Watanabe, K.; Taniguchi, T.; Neumaier, D.; Stampfer, C. "Ultra-sensitive Hall sensors based on graphene encapsulated in hexagonal boron nitride" *Appl. Phys. Lett.* **2015**, *106*, 193501.

(12) Geim, A. K.; Grigorieva, I. V. "Van der Waals heterostructures" *Nature* **2013**, *499*, 419–425.

(13) Morgenstern, M.; Klijn, J.; Meyer, C.; Wiesendanger, R. "Real-Space Observation of Drift States in a Two-Dimensional Electron System at High Magnetic Fields" *Phys. Rev. Lett.* **2003**, *90*, 056804.

(14) Hashimoto, K.; Sohrmann, C.; Wiebe, J.; Inaoka, T.; Meier, F.; Hirayama, Y.; Romer, R. A.; Wiesendanger, R.; Morgenstern, M. "Quantum Hall Transition in Real Space: From Localized to Extended States" *Phys. Rev. Lett.* **2008**, *101*, 256802.

(15) Tsui, D. C.; Stormer, H. L.; Gossard, A. C. "Two-Dimensional Magnetotransport in the Extreme Quantum Limit" *Phys. Rev. Lett.* **1982**, *48*, 1559–1562.

(16) Von Klitzing, K.; Dorda, G.; Pepper, M. "New Method for High-Accuracy Determination of the Fine-Structure Constant Based on Quantized Hall Resistance" *Phys. Rev. Lett.* **1980**, *45*, 494–497.

(17) Prange, R. E.; Girvin, S. M., *The Quantum Hall Effect*; Maryland Subseries: Based on Lectures at the University of Maryland, College Park; Springer: New York, 1990.

(18) Novoselov, K. S.; Geim, A. K.; Morozov, S. V.; Jiang, D.; Katsnelson, M. I.; Grigorieva, I. V.; Dubonos, S. V.; Firsov, A. A. "Two-dimensional gas of massless Dirac fermions in graphene" *Nature* **2005**, *438*, 197–200.

(19) Zhang, Y.; Tan, Y. W.; Stormer, H. L.; Kim, P. "Experimental observation of the quantum Hall effect and Berry's phase in graphene" *Nature* **2005**, *438*, 201–204.

(20) Khveshchenko, D. V. "Electron localization properties in graphene" *Phys. Rev. Lett.* **2006**, *97*, 036802.

(21) McCann, E.; Kechedzhi, K.; Fal'ko, V. I.; Suzuura, H.; Ando, T.; Altshuler, B. L. "Weak-localization magnetoresistance and valley symmetry in graphene" *Phys. Rev. Lett.* **2006**, *97*, 146805.

(22) Tikhonenko, F. V.; Kozikov, A. A.; Savchenko, A. K.; Gorbachev, R. V. "Transition between Electron Localization and Antilocalization in Graphene" *Phys. Rev. Lett.* **2009**, *103*, 226801.

(23) Katsnelson, M. I. "Nonlinear screening of charge impurities in graphene" *Phys. Rev. B* **2006**, *74*, 201401.

(24) Nomura, K.; MacDonald, A. H. "Quantum Hall Ferromagnetism in Graphene" *Phys. Rev. Lett.* **2006**, *96*, 256602.

(25) Das Sarma, S.; Hwang, E. H.; Tse, W.-K. "Many-body interaction effects in doped and undoped graphene: Fermi liquid versus non-Fermi liquid" *Phys. Rev. B* **2007**, *75*, 121406.

(26) Castro Neto, A. H.; Guinea, F.; Peres, N. M. R.; Novoselov, K. S.; Geim, A. K. "The electronic properties of graphene" *Rev. Mod. Phys.* **2009**, *81*, 109–162.

(27) Friedrich, S.; Ostreicher, R.; Schweizer, W. "Observation of flux and circular polarization spectra of white dwarfs with low magnetic fields" *Astron. Astrophys.* **1996**, *309*, 227–234.

(28) Levy, N.; Burke, S. A.; Meaker, K. L.; Panlasigui, M.; Zettl, A.; Guinea, F.; Castro Neto, A. H.; Crommie, M. F. "Strain-induced pseudo-magnetic fields greater than 300 tesla in graphene nanobubbles" *Science* **2010**, *329*, 544–547.

(29) Georgi, A. et al. "Tunable pseudo-Zeeman effect in graphene" *ArXiv e-prints* **2016**, arXiv:1611.06123.

(30) Xian, L. D.; Wang, Z. F.; Chou, M. Y. "Coupled Dirac Fermions and Neutrino-like Oscillations in Twisted Bilayer Graphene" *Nano Lett.* **2013**, *13*, 5159–5164.

(31) Katsnelson, M. I. "Zitterbewegung, chirality, and minimal conductivity in graphene" *Eur. Phys. J. B* **2006**, *51*, 157–160.

(32) Rusin, T. M.; Zawadzki, W. "Transient Zitterbewegung of charge carriers in mono- and bilayer graphene, and carbon nanotubes" *Phys. Rev. B* **2007**, *76*, 195439.

(33) Rusin, T. M.; Zawadzki, W. "Zitterbewegung of electrons in graphene in a magnetic field" *Phys. Rev. B* **2008**, *78*, 125419.

(34) Katsnelson, M. I.; Novoselov, K. S.; Geim, A. K. "Chiral tunnelling and the Klein paradox in graphene" *Nat. Phys.* **2006**, *2*, 620–625.

(35) Young, A. F.; Kim, P. "Quantum interference and Klein tunnelling in graphene heterojunctions" *Nat. Phys.* **2009**, *5*, 222–226.

(36) Pomeranchuk, I.; Smorodinsky, Y. "On the energy levels of systems with Z'137" *J. Phys. Ussr* **1945**, *9*, 97.

(37) Pereira, V. M.; Nilsson, J.; Castro Neto, A. H. "Coulomb Impurity Problem in Graphene" *Phys. Rev. Lett.* **2007**, *99*, 166802.

(38) Shytov, A. V.; Katsnelson, M. I.; Levitov, L. S. "Vacuum polarization and screening of supercritical impurities in graphene" *Phys. Rev. Lett.* **2007**, *99*, 236801.

(39) Shytov, A. V.; Katsnelson, M. I.; Levitov, L. S. "Atomic Collapse and Quasi-Rydberg States in Graphene" *Phys. Rev. Lett.* **2007**, *99*, 246802.

(40) Wang, Y.; Wong, D.; Shytov, A. V.; Brar, V. W.; Choi, S.; Wu, Q.; Tsai, H. Z.; Regan, W.; Zettl, A.; Kawakami, R. K.; Louie, S. G.; Levitov, L. S.; Crommie, M. F. "Observing atomic collapse resonances in artificial nuclei on graphene" *Science* **2013**, *340*, 734–737.

(41) Shor, P. W. "Polynomial-Time Algorithms for Prime Factorization and Discrete Logarithms on a Quantum Computer" *SIAM Review* **1999**, *41*, 303–332.

(42) Grover, L. K. "Quantum Mechanics Helps in Searching for a Needle in a Haystack" *Phys. Rev. Lett.* **1997**, *79*, 325–328.

(43) Mooij, J. E.; Orlando, T. P.; Levitov, L.; Tian, L.; van der Wal, C. H.; Lloyd, S. "Josephson Persistent-Current Qubit" *Science* **1999**, *285*, 1036–1039.

(44) Barends, R. et al. "Superconducting quantum circuits at the surface code threshold for fault tolerance" *Nature* **2014**, *508*, 500–503.

(45) Kelly, J. et al. "State preservation by repetitive error detection in a superconducting quantum circuit" *Nature* **2015**, *519*, 66–69.

(46) Neill, C. et al. "Ergodic dynamics and thermalization in an isolated quantum system" *Nat. Phys.* **2016**, *12*, 1037–1041.

(47) Koppens, F. H. L.; Buizert, C.; Tielrooij, K. J.; Vink, I. T.; Nowack, K. C.; Meunier, T.; Kouwenhoven, L. P.; Vandersypen, L. M. K. "Driven coherent oscillations of a single electron spin in a quantum dot" *Nature* **2006**, *442*, 766–771.

(48) Petta, J. R.; Johnson, A. C.; Taylor, J. M.; Laird, E. A.; Yacoby, A.; Lukin, M. D.; Marcus, C. M.; Hanson, M. P.; Gossard, A. C. "Coherent Manipulation of Coupled Electron Spins in Semiconductor Quantum Dots" *Science* **2005**, *309*, 2180–2184.

(49) Shulman, M. D.; Dial, O. E.; Harvey, S. P.; Bluhm, H.; Umansky, V.; Yacoby, A. "Demonstration of Entanglement of Electrostatically Coupled Singlet-Triplet Qubits" *Science* **2012**, *336*, 202–205.

(50) Dobers, M.; Vonklitzing, K.; Schneider, J.; Weimann, G.; Ploog, K. "Electrical Detection of Nuclear Magnetic-Resonance in Gaas-Alxga1-Xas Heterostructures" *Phys. Rev. Lett.* **1988**, *61*, 1650–1653.

(51) Khaetskii, A. V.; Loss, D.; Glazman, L. "Electron Spin Decoherence in Quantum Dots due to Interaction with Nuclei" *Phys. Rev. Lett.* **2002**, *88*, 186802.

(52) Bluhm, H.; Foletti, S.; Neder, I.; Rudner, M.; Mahalu, D.; Umansky, V.; Yacoby, A. "Dephasing time of GaAs electron-spin qubits coupled to a nuclear bath exceeding 200 μs" *Nat. Phys.* **2011**, *7*, 109–113.

(53) Cerfontaine, P.; Botzem, T.; DiVincenzo, D. P.; Bluhm, H. "High-Fidelity Single-Qubit Gates for Two-Electron Spin Qubits in GaAs" *Phys. Rev. Lett.* **2014**, *113*, 150501.

(54) Min, H.; Hill, J. E.; Sinitsyn, N. A.; Sahu, B. R.; Kleinman, L.; MacDonald, A. H. "Intrinsic and Rashba spin-orbit interactions in graphene sheets" *Phys. Rev. B* **2006**, *74*, 165310.

(55) Gmitra, M.; Konschuh, S.; Ertler, C.; Ambrosch-Draxl, C.; Fabian, J. "Band-structure topologies of graphene: Spin-orbit coupling effects from first principles" *Phys. Rev. B* **2009**, *80*, 235431.

(56) Balasubramanian, G.; Neumann, P.; Twitchen, D.; Markham, M.; Kolesov, R.; Mizuochi, N.; Isoya, J.; Achard, J.; Beck, J.; Tissler, J.; Jacques, V.; Hemmer, P. R.; Jelezko, F.; Wrachtrup, J. "Ultralong spin coherence time in isotopically engineered diamond" *Nat. Mater.* **2009**, *8*, 383–387.

(57) Chen, S.; Wu, Q.; Mishra, C.; Kang, J.; Zhang, H.; Cho, K.; Cai, W.; Balandin, A. A.; Ruoff, R. S. "Thermal conductivity of isotopically modified graphene" *Nat. Mater.* **2012**, *11*, 203–207.

(58) Trauzettel, B.; Bulaev, D. V.; Loss, D.; Burkard, G. "Spin qubits in graphene quantum dots" *Nat. Phys.* **2007**, *3*, 192–196.

(59) Fischer, J.; Trauzettel, B.; Loss, D. "Hyperfine interaction and electron-spin decoherence in graphene and carbon nanotube quantum dots" *Phys. Rev. B* **2009**, *80*, 155401.

(60) Recher, P.; Trauzettel, B. "Quantum dots and spin qubits in graphene" *Nanotechnology* **2010**, *21*, 302001.

(61) Struck, P. R.; Burkard, G. "Effective time-reversal symmetry breaking in the spin relaxation in a graphene quantum dot" *Phys. Rev. B* **2010**, *82*, 125401.

(62) Veldhorst, M.; Hwang, J. C. C.; Yang, C. H.; Leenstra, A. W.; de Ronde, B.; Dehollain, J. P.; Muhonen, J. T.; Hudson, F. E.; Itoh, K. M.; Morello, A.; Dzurak, A. S. "An addressable quantum dot qubit with fault-tolerant control-fidelity" *Nat. Nanotechnol.* **2014**, *9*, 981–985.

(63) Kawakami, E.; Scarlino, P.; Ward, D. R.; Braakman, F. R.; Savage, D. E.; Lagally, M. G.; Friesen, M.; Coppersmith, S. N.; Eriksson, M. A.; Vandersypen, L. M. K. "Electrical control of a long-lived spin qubit in a Si/SiGe quantum dot" *Nat. Nanotechnol.* **2014**, *9*, 666–670.

(64) Wu, G. Y.; Lue, N. Y.; Chang, L. "Graphene quantum dots for valley-based quantum computing: A feasibility study" *Phys. Rev. B* **2011**, *84*, 195463.

(65) Held, R.; Vancura, T.; Heinzel, T.; Ensslin, K.; Holland, M.; Wegscheider, W. "In-plane gates and nanostructures fabricated by direct oxidation of semiconductor heterostructures with an atomic force microscope" *Appl. Phys. Lett.* **1998**, *73*, 262–264.

(66) Fuhrer, A.; Lüscher, S.; Ihn, T.; Heinzel, T.; Ensslin, K.; Wegscheider, W.; Bichler, M. "Energy spectra of quantum rings" *Nature* **2001**, *413*, 822–825.

(67) Bischoff, D.; Varlet, A.; Simonet, P.; Eich, M.; Overweg, H. C.; Ihn, T.; Ensslin, K. "Localized charge carriers in graphene nanodevices" *Appl. Phys. Rev.* **2015**, *2*, 031301.

(68) Dombrowski, R.; Steinebach, C.; Wittneven, C.; Morgenstern, M.; Wiesendanger, R. "Tip-induced band bending by scanning tunneling spectroscopy of the states of the tip-induced quantum dot on InAs(110)" *Phys. Rev. B* **1999**, *59*, 8043–8048.

(69) Finkelstein, G.; Glicofridis, P. I.; Ashoori, R. C.; Shayegan, M. "Topographic mapping of the quantum hall liquid using a few-electron bubble" *Science* **2000**, *289*, 90–94.

(70) Yang, C. H.; Rossi, A.; Ruskov, R.; Lai, N. S.; Mohiyaddin, F. A.; Lee, S.; Tahan, C.; Klimeck, G.; Morello, A.; Dzurak, A. S. "Spin-valley lifetimes in a silicon quantum dot with tunable valley splitting" *Nat. Commun.* **2013**, *4*, 2069.

(71) Pioro-Ladriere, M.; Obata, T.; Tokura, Y.; Shin, Y. S.; Kubo, T.; Yoshida, K.; Taniyama, T.; Tarucha, S. "Electrically driven single-electron spin resonance in a slanting Zeeman field" *Nat. Phys.* **2008**, *4*, 776–779.

(72) Wu, X.; Ward, D. R.; Prance, J. R.; Kim, D.; Gamble, J. K.; Mohr, R. T.; Shi, Z.; Savage, D. E.; Lagally, M. G.; Friesen, M.; Coppersmith, S. N.; Eriksson, M. A. "Two-axis control of a singlet-triplet qubit with an integrated micromagnet" *Proc. Natl. Acad. Sci. U.S.A.* **2014**, *111*, 11938–11942.

(73) Binnig, G.; Rohrer, H.; Gerber, C.; Weibel, E. "Surface Studies by Scanning Tunneling Microscopy" *Phys. Rev. Lett.* **1982**, *49*, 57–61.

(74) Binnig, G.; Rohrer, H. "Scanning Tunneling Microscopy" *Helv. Phys. Acta* **1982**, *55*, 726–735.

(75) Binnig, G.; Quate, C. F.; Gerber, C. "Atomic Force Microscope" *Phys. Rev. Lett.* **1986**, *56*, 930–933.

(76) Binnig, G.; Rohrer, H.; Gerber, C.; Weibel, E. "7×7 Reconstruction on Si(111) Resolved in Real Space" *Phys. Rev. Lett.* **1983**, *50*, 120–123.

(77) Eigler, D. M.; Schweizer, E. K. "Positioning single atoms with a scanning tunnelling microscope" *Nature* **1990**, *344*, 524–526.

(78) Bartels, L.; Meyer, G.; Rieder, K. H. "Basic Steps of Lateral Manipulation of Single Atoms and Diatomic Clusters with a Scanning Tunneling Microscope Tip" *Phys. Rev. Lett.* **1997**, *79*, 697–700.

(79) Österlund, L.; Rasmussen, P. B.; Thostrup, P.; Lægsgaard, E.; Stensgaard, I.; Besenbacher, F. "Bridging the Pressure Gap in Surface Science at the Atomic Level: H/Cu(110)" *Phys. Rev. Lett.* **2001**, *86*, 460–463.

(80) Hendriksen, B. L. M.; Frenken, J. W. M. "CO Oxidation on Pt(110): Scanning Tunneling Microscopy Inside a High-Pressure Flow Reactor" *Phys. Rev. Lett.* **2002**, *89*, 046101.

(81) Wiesendanger, R.; Güntherodt, H. J.; Güntherodt, G.; Gambino, R. J.; Ruf, R. "Observation of vacuum tunneling of spin-polarized electrons with the scanning tunneling microscope" *Phys. Rev. Lett.* **1990**, *65*, 247–250.

(82) Bode, M.; Getzlaff, M.; Wiesendanger, R. "Spin-Polarized Vacuum Tunneling into the Exchange-Split Surface State of Gd(0001)" *Phys. Rev. Lett.* **1998**, *81*, 4256–4259.

(83) Loth, S.; Etzkorn, M.; Lutz, C. P.; Eigler, D. M.; Heinrich, A. J. "Measurement of Fast Electron Spin Relaxation Times with Atomic Resolution" *Science* **2010**, *329*, 1628–1630.

(84) Van Houselt, A.; Zandvliet, H. J. W. "*Colloquium* : Time-resolved scanning tunneling microscopy" *Rev. Mod. Phys.* **2010**, *82*, 1593–1605.

(85) Saunus, C.; Raphael Bindel, J.; Pratzer, M.; Morgenstern, M. "Versatile scanning tunneling microscopy with 120 ps time resolution" *Appl. Phys. Lett.* **2013**, *102*, 051601.

(86) Song, Y. J.; Otte, A. F.; Shvarts, V.; Zhao, Z.; Kuk, Y.; Blankenship, S. R.; Band, A.; Hess, F. M.; Stroscio, J. A. "Invited Review Article: A 10 mK scanning probe microscopy facility" *Rev. Sci. Instrum.* **2010**, *81*, 121101.

(87) Mashoff, T.; Pratzer, M.; Morgenstern, M. "A low-temperature high resolution scanning tunneling microscope with a three-dimensional magnetic vector field operating in ultrahigh vacuum" *Rev. Sci. Instrum.* **2009**, *80*, 053702.

(88) Wiesendanger, R., *Scanning probe microscopy and spectroscopy: methods and applications*; Cambridge University Press: 1994.

(89) Voigtländer, B., *Scanning probe microscopy: Atomic force microscopy and scanning tunneling microscopy*; Springer Berlin Heidelberg: 2015.

(90) Hamers, R. J. "Atomic-Resolution Surface Spectroscopy with the Scanning Tunneling Microscope" *Annu. Rev. Phys. Chem.* **1989**, *40*, 531–559.

(91) Tersoff, J.; Hamann, D. R. "Theory and Application for the Scanning Tunneling Microscope" *Phys. Rev. Lett.* **1983**, *50*, 1998–2001.

(92) Tersoff, J.; Hamann, D. R. "Theory of the scanning tunneling microscope" *Phys. Rev. B* **1985**, *31*, 805–813.

(93) Chen, C. J. "Theory of scanning tunneling spectroscopy" *J. Vac. Sci. Technol. A* **1988**, *6*, 319–322.

(94) Chen, C. J. "Tunneling matrix elements in three-dimensional space: The derivative rule and the sum rule" *Phys. Rev. B* **1990**, *42*, 8841–8857.

(95) Chen, C. J. "Origin of atomic resolution on metal surfaces in scanning tunneling microscopy" *Phys. Rev. Lett.* **1990**, *65*, 448–451.

(96) Chen, W.; Madhavan, V.; Jamneala, T.; Crommie, M. F. "Scanning Tunneling Microscopy Observation of an Electronic Superlattice at the Surface of Clean Gold" *Phys. Rev. Lett.* **1998**, *80*, 1469–1472.

(97) Voigtländer, B.; Cherepanov, V.; Elsaesser, C.; Linke, U. "Metal bead crystals for easy heating by direct current" *Rev. Sci. Instrum.* **2008**, *79*, 033911.

(98) Morgenstern, M. "Probing The Local Density Of States Of Dilute Electron Systems In Different Dimensions" *Surf. Rev. Lett.* **2003**, *10*, 933–962.

(99) Wildöer, J. W. G.; van Roij, A. J. A.; Harmans, C. J. P. M.; van Kempen, H. "Semiconductor band switching by charging a small grain with a single electron" *Phys. Rev. B* **1996**, *53*, 10695–10698.

(100) Freitag, N. M.; Chizhova, L. A.; Nemes-Incze, P.; Woods, C. R.; Gorbachev, R. V.; Cao, Y.; Geim, A. K.; Novoselov, K. S.; Burgdörfer, J.; Libisch, F.; Morgenstern, M. "Electrostatically Confined Monolayer Graphene Quantum Dots with Orbital and Valley Splittings" *Nano Lett.* **2016**, *16*, 5798–5805.

(101) Freitag, N. M. *Low-Temperature Transport Measurements on Indium Soldered Graphene*, Diploma Thesis, 2011.

(102) Mermin, N. D. "Crystalline Order in Two Dimensions" *Phys. Rev.* **1968**, *176*, 250–254.

(103) Wallace, P. R. "The Band Theory of Graphite" *Phys. Rev.* **1947**, *71*, 622–634.

(104) Slonczewski, J. C.; Weiss, P. R. "Band Structure of Graphite" *Phys. Rev.* **1958**, *109*, 272–279.

(105) Ando, T.; Nakanishi, T.; Saito, R. "Berry's phase and absence of back scattering in carbon nanotubes" *J. Phys. Soc. Jpn.* **1998**, *67*, 2857–2862.

(106) Goerbig, M. O. "Electronic properties of graphene in a strong magnetic field" *Rev. Mod. Phys.* **2011**, *83*, 1193–1243.

(107) Katsnelson, M., *Graphene: Carbon in Two Dimensions*; Cambridge University Press: 2012.

(108) Baskin, Y.; Meyer, L. "Lattice Constants of Graphite at Low Temperatures" *Phys. Rev.* **1955**, *100*, 544–544.

(109) Ando, T. "Theory of Electronic States and Transport in Carbon Nanotubes" *J. Phys. Soc. Jpn.* **2005**, *74*, 777–817.

(110) Ihn, T., *Semiconductor nanostructures : quantum states and electronic transport*; Oxford University Press: Oxford; New York, 2010.

(111) Kretinin, A.; Yu, G. L.; Jalil, R.; Cao, Y.; Withers, F.; Mishchenko, A.; Katsnelson, M. I.; Novoselov, K. S.; Geim, A. K.; Guinea, F. "Quantum capacitance measurements of electron-hole asymmetry and next-nearest-neighbor hopping in graphene" *Phys. Rev. B* **2013**, *88*, 165427.

(112) Venema, L.; Verberck, B.; Georgescu, I.; Prando, G.; Couderc, E.; Milana, S.; Maragkou, M.; Persechini, L.; Pacchioni, G.; Fleet, L. "The quasiparticle zoo" *Nat. Phys.* **2016**, *12*, 1085–1089.

(113) Majorana, E. "Teoria simmetrica dell'elettrone e del positrone" *Nuovo Cim.* **1937**, *14*, 171.

(114) Fu, L.; Kane, C. L. "Superconducting Proximity Effect and Majorana Fermions at the Surface of a Topological Insulator" *Phys. Rev. Lett.* **2008**, *100*, 096407.

(115) Mourik, V.; Zuo, K.; Frolov, S. M.; Plissard, S. R.; Bakkers, E. P. A. M.; Kouwenhoven, L. P. "Signatures of Majorana Fermions in Hybrid Superconductor-Semiconductor Nanowire Devices" *Science* **2012**, *336*, 1003–1007.

(116) Sun, H.-H. et al. "Majorana Zero Mode Detected with Spin Selective Andreev Reflection in the Vortex of a Topological Superconductor" *Phys. Rev. Lett.* **2016**, *116*, 257003.

(117) de-Picciotto, R.; Reznikov, M.; Heiblum, M.; Umansky, V.; Bunin, G.; Mahalu, D. "Direct observation of a fractional charge" *Nature* **1997**, *389*, 162–164.

(118) Saminadayar, L.; Glattli, D. C.; Jin, Y.; Etienne, B. "Observation of the $e/3$ Fractionally Charged Laughlin Quasiparticle" *Phys. Rev. Lett.* **1997**, *79*, 2526–2529.

(119) Reznikov, M.; Picciotto, R. d.; Griffiths, T. G.; Heiblum, M.; Umansky, V. "Observation of quasiparticles with one-fifth of an electron's charge" *Nature* **1999**, *399*, 238–241.

(120) Couto, N. J. G.; Costanzo, D.; Engels, S.; Ki, D. K.; Watanabe, K.; Taniguchi, T.; Stampfer, C.; Guinea, F.; Morpurgo, A. F. "Random Strain Fluctuations as Dominant Disorder Source for High-Quality On-Substrate Graphene Devices" *Phys. Rev. X* **2014**, *4*, 041019.

(121) Berry, M. V.; Mondragon, R. J. "Neutrino Billiards - Time-Reversal Symmetry-Breaking without Magnetic-Fields" *Proc. R. Soc. London, Ser. A* **1987**, *412*, 53–74.

(122) McCann, E.; Koshino, M. "The electronic properties of bilayer graphene" *Rep. Prog. Phys.* **2013**, *76*, 056503.

(123) Martin, J.; Akerman, N.; Ulbricht, G.; Lohmann, T.; Smet, J. H.; Von Klitzing, K.; Yacoby, A. "Observation of electron-hole puddles in graphene using a scanning single-electron transistor" *Nat. Phys.* **2008**, *4*, 144–148.

(124) Zhang, Y. B.; Brar, V. W.; Girit, C.; Zettl, A.; Crommie, M. F. "Origin of spatial charge inhomogeneity in graphene" *Nat. Phys.* **2009**, *5*, 722–726.

(125) Xue, J. M.; Sanchez-Yamagishi, J.; Bulmash, D.; Jacquod, P.; Deshpande, A.; Watanabe, K.; Taniguchi, T.; Jarillo-Herrero, P.; LeRoy, B. J. "Scanning tunnelling microscopy and spectroscopy of ultra-flat graphene on hexagonal boron nitride" *Nat. Mater.* **2011**, *10*, 282–285.

(126) Adam, S.; Jung, S. Y.; Klimov, N. N.; Zhitenev, N. B.; Stroscio, J. A.; Stiles, M. D. "Mechanism for puddle formation in graphene" *Phys. Rev. B* **2011**, *84*, 235421.

(127) Molitor, F.; Güttinger, J.; Stampfer, C.; Dröscher, S.; Jacobsen, A.; Ihn, T.; Ensslin, K. "Electronic properties of graphene nanostructures" *J. Phys.-Condens. Mat.* **2011**, *23*, 243201.

(128) Samaddar, S.; Yudhistira, I.; Adam, S.; Courtois, H.; Winkelmann, C. B. "Charge Puddles in Graphene near the Dirac Point" *Phys. Rev. Lett.* **2016**, *116*, 126804.

(129) Aharonov, Y.; Bohm, D. "Significance of Electromagnetic Potentials in the Quantum Theory" *Phys. Rev.* **1959**, *115*, 485–491.

(130) Abrahams, E.; Anderson, P. W.; Licciardello, D. C.; Ramakrishnan, T. V. "Scaling Theory of Localization: Absence of Quantum Diffusion in Two Dimensions" *Phys. Rev. Lett.* **1979**, *42*, 673–676.

(131) Altshuler, B. L.; Khmel'nitzkii, D.; Larkin, A. I.; Lee, P. A. "Magnetoresistance and Hall effect in a disordered two-dimensional electron gas" *Phys. Rev. B* **1980**, *22*, 5142–5153.

(132) Altshuler, B. L.; Aronov, A. G.; Lee, P. A. "Interaction Effects in Disordered Fermi Systems in Two Dimensions" *Phys. Rev. Lett.* **1980**, *44*, 1288–1291.

(133) Bergmann, G. "Physical interpretation of weak localization: A time-of-flight experiment with conduction electrons" *Phys. Rev. B* **1983**, *28*, 2914–2920.

(134) Hikami, S.; Larkin, A. I.; Nagaoka, Y. "Spin-Orbit Interaction and Magnetoresistance in the 2 Dimensional Random System" *Prog. Theor. Phys.* **1980**, *63*, 707–710.

(135) Morozov, S. V.; Novoselov, K. S.; Katsnelson, M. I.; Schedin, F.; Ponomarenko, L. A.; Jiang, D.; Geim, A. K. "Strong suppression of weak localization in graphene" *Phys. Rev. Lett.* **2006**, *97*, 016801.

(136) Tikhonenko, F. V.; Horsell, D. W.; Gorbachev, R. V.; Savchenko, A. K. "Weak localization in graphene flakes" *Phys. Rev. Lett.* **2008**, *100*, 056802.

(137) Morpurgo, A. F.; Guinea, F. "Intervalley scattering, long-range disorder, and effective time-reversal symmetry breaking in graphene" *Phys. Rev. Lett.* **2006**, *97*, 196804.

(138) McClure, J. W. "Diamagnetism of Graphite" *Phys. Rev.* **1956**, *104*, 666–671.

(139) Hernangómez-Pérez, D.; Ulrich, J.; Florens, S.; Champel, T. "Spectral properties and local density of states of disordered quantum Hall systems with Rashba spin-orbit coupling" *Phys. Rev. B* **2013**, *88*, 245433.

(140) Briggs, A.; Guldner, Y.; Vieren, J. P.; Voos, M.; Hirtz, J. P.; Razeghi, M. "Low-Temperature Investigations of the Quantum Hall-Effect in $In_xGa_{1-x}As$-InP Heterojunctions" *Phys. Rev. B* **1983**, *27*, 6549–6552.

(141) Tsui, D. C.; Gossard, A. C. "Resistance Standard Using Quantization of the Hall Resistance of GaAs-$Al_xGa_{1-x}As$ Heterostructures" *Appl. Phys. Lett.* **1981**, *38*, 550–552.

(142) Shubnikov, L.; de Haas, W. J. *Leiden Commun.* **1930**, *207a, 207c, 207d, 210a.*

(143) Novoselov, K. S.; Jiang, Z.; Zhang, Y.; Morozov, S. V.; Stormer, H. L.; Zeitler, U.; Maan, J. C.; Boebinger, G. S.; Kim, P.; Geim, A. K. "Room-temperature quantum hall effect in graphene" *Science* **2007**, *315*, 1379–1379.

(144) Blake, P.; Hill, E. W.; Castro Neto, A. H.; Novoselov, K. S.; Jiang, D.; Yang, R.; Booth, T. J.; Geim, A. K. "Making graphene visible" *Appl. Phys. Lett.* **2007**, *91*, 063124.

(145) Fratini, S.; Guinea, F. "Substrate-limited electron dynamics in graphene" *Phys. Rev. B* **2008**, *77*, 195415.

(146) Chen, J. H.; Jang, C.; Xiao, S. D.; Ishigami, M.; Fuhrer, M. S. "Intrinsic and extrinsic performance limits of graphene devices on SiO2" *Nat. Nanotechnol.* **2008**, *3*, 206–209.

(147) Ishigami, M.; Chen, J. H.; Cullen, W. G.; Fuhrer, M. S.; Williams, E. D. "Atomic structure of graphene on SiO2" *Nano Lett.* **2007**, *7*, 1643–1648.

(148) Stolyarova, E.; Rim, K. T.; Ryu, S. M.; Maultzsch, J.; Kim, P.; Brus, L. E.; Heinz, T. F.; Hybertsen, M. S.; Flynn, G. W. "High-resolution scanning tunneling microscopy imaging of mesoscopic graphene sheets on an insulating surface" *Proc. Natl. Acad. Sci. U.S.A.* **2007**, *104*, 9209–9212.

(149) Zhang, Y. B.; Brar, V. W.; Wang, F.; Girit, C.; Yayon, Y.; Panlasigui, M.; Zettl, A.; Crommie, M. F. "Giant phonon-induced conductance in scanning tunnelling spectroscopy of gate-tunable graphene" *Nat. Phys.* **2008**, *4*, 627–630.

(150) Geringer, V.; Liebmann, M.; Echtermeyer, T.; Runte, S.; Schmidt, M.; Ruckamp, R.; Lemme, M. C.; Morgenstern, M. "Intrinsic and extrinsic corrugation of monolayer graphene deposited on SiO2" *Phys. Rev. Lett.* **2009**, *102*, 076102.

(151) Mashoff, T.; Pratzer, M.; Geringer, V.; Echtermeyer, T. J.; Lemme, M. C.; Liebmann, M.; Morgenstern, M. "Bistability and Oscillatory Motion of Natural Nanomembranes Appearing within Monolayer Graphene on Silicon Dioxide" *Nano Lett.* **2010**, *10*, 461–465.

(152) Jung, S. Y.; Rutter, G. M.; Klimov, N. N.; Newell, D. B.; Calizo, I.; Walker, A. R. H.; Zhitenev, N. B.; Stroscio, J. A. "Evolution of microscopic localization in graphene in a magnetic field from scattering resonances to quantum dots" *Nat. Phys.* **2011**, *7*, 245–251.

(153) Weitz, R. T.; Yacoby, A. "Nanomaterials: Graphene rests easy" *Nat. Nanotechnol.* **2010**, *5*, 699–700.

(154) Dean, C. R.; Young, A. F.; Meric, I.; Lee, C.; Wang, L.; Sorgenfrei, S.; Watanabe, K.; Taniguchi, T.; Kim, P.; Shepard, K. L.; Hone, J. "Boron nitride substrates for high-quality graphene electronics" *Nat. Nanotechnol.* **2010**, *5*, 722–726.

(155) Katsnelson, M. I.; Geim, A. K. "Electron scattering on microscopic corrugations in graphene" *Philos. Trans. A Math. Phys. Eng. Sci.* **2008**, *366*, 195–204.

(156) Paszkowicz, W.; Pelka, J. B.; Knapp, M.; Szyszko, T.; Podsiadlo, S. "Lattice parameters and anisotropic thermal expansion of hexagonal boron nitride in the 10-297.5 K temperature range" *Appl. Phys. a-Mater.* **2002**, *75*, 431–435.

(157) Pease, R. S. "Crystal Structure of Boron Nitride" *Nature* **1950**, *165*, 722–723.

(158) Constantinescu, G.; Kuc, A.; Heine, T. "Stacking in Bulk and Bilayer Hexagonal Boron Nitride" *Phys. Rev. Lett.* **2013**, *111*, 036104.

(159) Watanabe, K.; Taniguchi, T.; Kanda, H. "Direct-bandgap properties and evidence for ultraviolet lasing of hexagonal boron nitride single crystal" *Nat. Mater.* **2004**, *3*, 404–409.

(160) Young, A. F.; Dean, C. R.; Meric, I.; Sorgenfrei, S.; Ren, H.; Watanabe, K.; Taniguchi, T.; Hone, J.; Shepard, K. L.; Kim, P. "Electronic compressibility of layer-polarized bilayer graphene" *Phys. Rev. B* **2012**, *85*, 235458.

(161) Decker, R.; Wang, Y.; Brar, V. W.; Regan, W.; Tsai, H. Z.; Wu, Q.; Gannett, W.; Zettl, A.; Crommie, M. F. "Local Electronic Properties of Graphene on a BN Substrate via Scanning Tunneling Microscopy" *Nano Lett.* **2011**, *11*, 2291–2295.

(162) Deshpande, A.; LeRoy, B. J. "Scanning probe microscopy of graphene" *Phys. E (Amsterdam, Neth.)* **2012**, *44*, 743–759.

(163) Mayorov, A. S.; Gorbachev, R. V.; Morozov, S. V.; Britnell, L.; Jalil, R.; Ponomarenko, L. A.; Blake, P.; Novoselov, K. S.; Watanabe, K.; Taniguchi, T.; Geim, A. K. "Micrometer-scale ballistic transport in encapsulated graphene at room temperature" *Nano Lett.* **2011**, *11*, 2396–2399.

(164) Wang, L.; Meric, I.; Huang, P. Y.; Gao, Q.; Gao, Y.; Tran, H.; Taniguchi, T.; Watanabe, K.; Campos, L. M.; Muller, D. A.; Guo, J.; Kim, P.; Hone, J.; Shepard, K. L.; Dean, C. R. "One-Dimensional Electrical Contact to a Two-Dimensional Material" *Science* **2013**, *342*, 614–617.

(165) Taniguchi, T.; Watanabe, K. "Synthesis of high-purity boron nitride single crystals under high pressure by using Ba-BN solvent" *J. Cryst. Growth* **2007**, *303*, 525–529.

(166) Jun, L.; Velasco, J.; Huang, E.; Kahn, S.; Nosiglia, C.; Tsai, H. Z.; Yang, W.; Taniguchi, T.; Watanabe, K.; Zhang, Y.; Zhang, G.; Crommie, M.; Zettl, A.; Wang, F. "Photoinduced doping in heterostructures of graphene and boron nitride" *Nat. Nanotechnol.* **2014**, *9*, 348–352.

(167) Neumann, C.; Rizzi, L.; Reichardt, S.; Terres, B.; Khodkov, T.; Watanabe, K.; Taniguchi, T.; Beschoten, B.; Stampfer, C. "Spatial Control of Laser-Induced Doping Profiles in Graphene on Hexagonal Boron Nitride" *ACS Appl. Mater. Inter.* **2016**, *8*, 9377–9383.

(168) Velasco, J.; Ju, L.; Wong, D.; Kahn, S.; Lee, J.; Tsai, H. Z.; Germany, C.; Wickenburg, S.; Lu, J.; Taniguchi, T.; Watanabe, K.; Zettl, A.; Wang, F.; Crommie, M. F. "Nanoscale Control of Rewriteable Doping Patterns in Pristine Graphene/Boron Nitride Heterostructures" *Nano Lett.* **2016**, *16*, 1620–1625.

(169) Wong, D.; Velasco Jr., J.; Ju, L.; Lee, J.; Kahn, S.; Tsai, H. Z.; Germany, C.; Taniguchi, T.; Watanabe, K.; Zettl, A.; Wang, F.; Crommie, M. F. "Characterization and manipulation of individual defects in insulating hexagonal boron nitride using scanning tunnelling microscopy" *Nat. Nanotechnol.* **2015**, *10*, 949–953.

(170) Gutiérrez, C.; Brown, L.; Kim, C.-J.; Park, J.; Pasupathy, A. N. "Klein tunnelling and electron trapping in nanometre-scale graphene quantum dots" *Nat. Phys.* **2016**, *12*, 1069–1075.

(171) Lee, J.; Wong, D.; Velasco Jr, J.; Rodriguez-Nieva, J. F.; Kahn, S.; Tsai, H.-Z.; Taniguchi, T.; Watanabe, K.; Zettl, A.; Wang, F.; Levitov, L. S.; Crommie, M. F. "Imaging electrostatically confined Dirac fermions in graphene quantum dots" *Nat. Phys.* **2016**, *12*, 1032–1036.

(172) Reina, A.; Son, H.; Jiao, L.; Fan, B.; Dresselhaus, M. S.; Liu, Z.; Kong, J. "Transferring and Identification of Single- and Few-Layer Graphene on Arbitrary Substrates" *J. Phys. Chem. C* **2008**, *112*, 17741–17744.

(173) Zomer, P. J.; Dash, S. P.; Tombros, N.; van Wees, B. J. "A transfer technique for high mobility graphene devices on commercially available hexagonal boron nitride" *Appl. Phys. Lett.* **2011**, *99*, 232104.

(174) Zomer, P. J.; Guimarães, M. H. D.; Brant, J. C.; Tombros, N.; van Wees, B. J. "Fast pick up technique for high quality heterostructures of bilayer graphene and hexagonal boron nitride" *Appl. Phys. Lett.* **2014**, *105*, 013101.

(175) Yang, W.; Chen, G. R.; Shi, Z. W.; Liu, C. C.; Zhang, L. C.; Xie, G. B.; Cheng, M.; Wang, D. M.; Yang, R.; Shi, D. X.; Watanabe, K.; Taniguchi, T.; Yao, Y. G.; Zhang, Y. B.; Zhang, G. Y. "Epitaxial growth of single-domain graphene on hexagonal boron nitride" *Nat. Mater.* **2013**, *12*, 792–797.

(176) Wang, M.; Jang, S. K.; Jang, W.-J.; Kim, M.; Park, S.-Y.; Kim, S.-W.; Kahng, S.-J.; Choi, J.-Y.; Ruoff, R. S.; Song, Y. J.; Lee, S. "A Platform for Large-Scale Graphene Electronics - CVD Growth of Single-Layer Graphene on CVD-Grown Hexagonal Boron Nitride" *Adv. Mater.* **2013**, *25*, 2746–2752.

(177) Chen, X.; Wu, B.; Liu, Y. "Direct preparation of high quality graphene on dielectric substrates" *Chem. Soc. Rev.* **2016**, *45*, 2057–2074.

(178) Sun, J.; Zhang, Y.; Liu, Z. "Direct Chemical Vapor Deposition Growth of Graphene on Insulating Substrates" *ChemNanoMat* **2016**, *2*, 9–18.

(179) Girit, C. Ö.; Zettl, A. "Soldering to a single atomic layer" *Appl. Phys. Lett.* **2007**, *91*, 193512.

(180) Geringer, V.; Subramaniam, D.; Michel, A. K.; Szafranek, B.; Schall, D.; Georgi, A.; Mashoff, T.; Neumaier, D.; Liebmann, M.; Morgenstern, M. "Electrical transport and low-temperature scanning tunneling microscopy of microsoldered graphene" *Appl. Phys. Lett.* **2010**, *96*, 082114.

(181) Preston, T. H. "The International Temperature Scale of 1990 (ITS-90)" *Metrologia* **1990**, *27*, 3.

(182) Kretinin, A. V. et al. "Electronic properties of graphene encapsulated with different two-dimensional atomic crystals" *Nano Lett.* **2014**, *14*, 3270–3276.

(183) Woods, C. R. et al. "Commensurate-incommensurate transition in graphene on hexagonal boron nitride" *Nat. Phys.* **2014**, *10*, 451–456.

(184) Yankowitz, M.; Xue, J. M.; Cormode, D.; Sanchez-Yamagishi, J. D.; Watanabe, K.; Taniguchi, T.; Jarillo-Herrero, P.; Jacquod, P.; LeRoy, B. J. "Emergence of superlattice Dirac points in graphene on hexagonal boron nitride" *Nat. Phys.* **2012**, *8*, 382–386.

(185) Roth, S.; Matsui, F.; Greber, T.; Osterwalder, J. "Chemical Vapor Deposition and Characterization of Aligned and Incommensurate Graphene/Hexagonal Boron Nitride Heterostack on Cu(111)" *Nano Lett.* **2013**, *13*, 2668–2675.

(186) Tang, S.; Wang, H.; Zhang, Y.; Li, A.; Xie, H.; Liu, X.; Liu, L.; Li, T.; Huang, F.; Xie, X.; Jiang, M. "Precisely aligned graphene grown on hexagonal boron nitride by catalyst free chemical vapor deposition" *Sci. Rep.* **2013**, *3*, 2666.

(187) Yankowitz, M.; Xue, J.; LeRoy, B. J. "Graphene on hexagonal boron nitride" *J. Phys.-Condens. Mat.* **2014**, *26*, 303201.

(188) Gorbachev, R. V.; Song, J. C. W.; Yu, G. L.; Kretinin, A. V.; Withers, F.; Cao, Y.; Mishchenko, A.; Grigorieva, I. V.; Novoselov, K. S.; Levitov, L. S.; Geim, A. K. "Detecting topological currents in graphene superlattices" *Science* **2014**, *346*, 448–451.

(189) Sachs, B.; Wehling, T. O.; Katsnelson, M. I.; Lichtenstein, A. I. "Adhesion and electronic structure of graphene on hexagonal boron nitride substrates" *Phys. Rev. B* **2011**, *84*, 195414.

(190) Niquet, Y. M.; Fuchs, M.; Gonze, X. "Exchange-correlation potentials in the adiabatic connection fluctuation-dissipation framework" *Phys. Rev. A* **2003**, *68*, 032507.

(191) Xu, J.-R.; Song, Z.-Y.; Yuan, C.-G.; Zhang, Y.-Z. "Interaction-induced metallic state in graphene on hexagonal boron nitride" *Phys. Rev. B* **2016**, *94*, 195103.

(192) Bokdam, M.; Amlaki, T.; Brocks, G.; Kelly, P. J. "Band gaps in incommensurable graphene on hexagonal boron nitride" *Phys. Rev. B* **2014**, *89*, 201404.

(193) Van Wijk, M. M.; Schuring, A.; Katsnelson, M. I.; Fasolino, A. "Moire Patterns as a Probe of Interplanar Interactions for Graphene on h-BN" *Phys. Rev. Lett.* **2014**, *113*, 135504.

(194) Klimov, N. N.; Jung, S.; Zhu, S. Z.; Li, T.; Wright, C. A.; Solares, S. D.; Newell, D. B.; Zhitenev, N. B.; Stroscio, J. A. "Electromechanical Properties of Graphene Drumheads" *Science* **2012**, *336*, 1557–1561.

(195) Jung, J.; Raoux, A.; Qiao, Z. H.; MacDonald, A. H. "Ab initio theory of moire superlattice bands in layered two-dimensional materials" *Phys. Rev. B* **2014**, *89*, 205414.

(196) Chizhova, L. A.; Libisch, F.; Burgdörfer, J. "Graphene quantum dot on boron nitride: Dirac cone replica and Hofstadter butterfly" *Phys. Rev. B* **2014**, *90*, 165404.

(197) Rydberg, H.; Dion, M.; Jacobson, N.; Schröder, E.; Hyldgaard, P.; Simak, S. I.; Langreth, D. C.; Lundqvist, B. I. "Van der Waals Density Functional for Layered Structures" *Phys. Rev. Lett.* **2003**, *91*, 126402.

(198) Dobson, J. F.; White, A.; Rubio, A. "Asymptotics of the Dispersion Interaction: Analytic Benchmarks for van der Waals Energy Functionals" *Phys. Rev. Lett.* **2006**, *96*, 073201.

(199) Suzuura, H.; Ando, T. "Phonons and electron-phonon scattering in carbon nanotubes" *Phys. Rev. B* **2002**, *65*, 235412.

(200) Guinea, F.; Katsnelson, M. I.; Geim, A. K. "Energy gaps and a zero-field quantum Hall effect in graphene by strain engineering" *Nat. Phys.* **2010**, *6*, 30–33.

(201) Park, C.-H.; Yang, L.; Son, Y.-W.; Cohen, M. L.; Louie, S. G. "New Generation of Massless Dirac Fermions in Graphene under External Periodic Potentials" *Phys. Rev. Lett.* **2008**, *101*, 126804.

(202) Park, C. H.; Yang, L.; Son, Y. W.; Cohen, M. L.; Louie, S. G. "Anisotropic behaviours of massless Dirac fermions in graphene under periodic potentials" *Nat. Phys.* **2008**, *4*, 213–217.

(203) Moon, P.; Koshino, M. "Electronic properties of graphene/hexagonal-boron-nitride moire superlattice" *Phys. Rev. B* **2014**, *90*, 155406.

(204) Koshino, M.; Moon, P. "Electronic Properties of Incommensurate Atomic Layers" *J. Phys. Soc. Jpn.* **2015**, *84*, 121001.

(205) Wallbank, J. R.; Mucha-Kruczyński, M.; Fal'ko, V. I. "Moiré minibands in graphene heterostructures with almost commensurate $\sqrt{3} \times \sqrt{3}$ hexagonal crystals" *Phys. Rev. B* **2013**, *88*, 155415.

(206) Jung, J.; DaSilva, A. M.; MacDonald, A. H.; Adam, S. "Origin of band gaps in graphene on hexagonal boron nitride" *Nat. Commun.* **2015**, *6*, 6308.

(207) Meyer, J. C.; Girit, C. Ö.; Crommie, M. F.; Zettl, A. "Hydrocarbon lithography on graphene membranes" *Appl. Phys. Lett.* **2008**, *92*, 123110.

(208) Wallbank, J. R.; Patel, A. A.; Mucha-Kruczyński, M.; Geim, A. K.; Fal'ko, V. I. "Generic miniband structure of graphene on a hexagonal substrate" *Phys. Rev. B* **2013**, *87*, 245408.

(209) Bistritzer, R.; MacDonald, A. H. "Moiré butterflies in twisted bilayer graphene" *Phys. Rev. B* **2011**, *84*, 035440.

(210) Yan, W.; Liu, M.; Dou, R.-F.; Meng, L.; Feng, L.; Chu, Z.-D.; Zhang, Y.; Liu, Z.; Nie, J.-C.; He, L. "Angle-Dependent van Hove Singularities in a Slightly Twisted Graphene Bilayer" *Phys. Rev. Lett.* **2012**, *109*, 126801.

(211) Moon, P.; Koshino, M. "Optical properties of the Hofstadter butterfly in the moiré superlattice" *Phys. Rev. B* **2013**, *88*, 241412.

(212) Beechem, T. E.; Ohta, T.; Diaconescu, B.; Robinson, J. T. "Rotational Disorder in Twisted Bilayer Graphene" *ACS Nano* **2014**, *8*, 1655–1663.

(213) Cherkez, V.; de Laissardière, G. T.; Mallet, P.; Veuillen, J. Y. "Van Hove singularities in doped twisted graphene bilayers studied by scanning tunneling spectroscopy" *Phys. Rev. B* **2015**, *91*, 155428.

(214) Subramaniam, D.; Libisch, F.; Li, Y.; Pauly, C.; Geringer, V.; Reiter, R.; Mashoff, T.; Liebmann, M.; Burgdörfer, J.; Busse, C.; Michely, T.; Mazzarello, R.; Pratzer, M.; Morgenstern, M. "Wave-Function Mapping of Graphene Quantum Dots with Soft Confinement" *Phys. Rev. Lett.* **2012**, *108*, 046801.

(215) Jolie, W.; Craes, F.; Petrovic, M.; Atodiresei, N.; Caciuc, V.; Blugel, S.; Kralj, M.; Michely, T.; Busse, C. "Confinement of Dirac electrons in graphene quantum dots" *Phys. Rev. B* **2014**, *89*, 155435.

(216) Jolie, W.; Craes, F.; Busse, C. "Graphene on weakly interacting metals: Dirac states versus surface states" *Phys. Rev. B* **2015**, *91*, 115419.

(217) Eckmann, A.; Park, J.; Yang, H. F.; Elias, D.; Mayorov, A. S.; Yu, G. L.; Jalil, R.; Novoselov, K. S.; Gorbachev, R. V.; Lazzeri, M.; Geim, A. K.; Casiraghi, C. "Raman Fingerprint of Aligned Graphene/h-BN Superlattices" *Nano Lett.* **2013**, *13*, 5242–5246.

(218) Hofstadter, D. R. "Energy levels and wave functions of Bloch electrons in rational and irrational magnetic fields" *Phys. Rev. B* **1976**, *14*, 2239–2249.

(219) Hunt, B.; Sanchez-Yamagishi, J. D.; Young, A. F.; Yankowitz, M.; LeRoy, B. J.; Watanabe, K.; Taniguchi, T.; Moon, P.; Koshino, M.; Jarillo-Herrero, P.; Ashoori, R. C. "Massive Dirac fermions and Hofstadter butterfly in a van der Waals heterostructure" *Science* **2013**, *340*, 1427–1430.

(220) Dean, C. R.; Wang, L.; Maher, P.; Forsythe, C.; Ghahari, F.; Gao, Y.; Katoch, J.; Ishigami, M.; Moon, P.; Koshino, M.; Taniguchi, T.; Watanabe, K.; Shepard, K. L.; Hone, J.; Kim, P. "Hofstadter's butterfly and the fractal quantum Hall effect in moire superlattices" *Nature* **2013**, *497*, 598–602.

(221) Yu, G. L. et al. "Hierarchy of Hofstadter states and replica quantum Hall ferromagnetism in graphene superlattices" *Nat. Phys.* **2014**, *10*, 525–529.

(222) Ponomarenko, L. A. et al. "Cloning of Dirac fermions in graphene superlattices" *Nature* **2013**, *497*, 594–597.

(223) Usachov, D.; Adamchuk, V. K.; Haberer, D.; Grüneis, A.; Sachdev, H.; Preobrajenski, A. B.; Laubschat, C.; Vyalikh, D. V. "Quasifreestanding single-layer hexagonal boron nitride as a substrate for graphene synthesis" *Phys. Rev. B* **2010**, *82*, 075415.

(224) Amet, F.; Williams, J. R.; Watanabe, K.; Taniguchi, T.; Goldhaber-Gordon, D. "Insulating Behavior at the Neutrality Point in Single-Layer Graphene" *Phys. Rev. Lett.* **2013**, *110*, 216601.

(225) Chen, Z. G.; Shi, Z.; Yang, W.; Lu, X.; Lai, Y.; Yan, H.; Wang, F.; Zhang, G.; Li, Z. "Observation of an intrinsic bandgap and Landau level renormalization in graphene/boron-nitride heterostructures" *Nat. Commun.* **2014**, *5*, 4461.

(226) Giovannetti, G.; Khomyakov, P. A.; Brocks, G.; Kelly, P. J.; van den Brink, J. "Substrate-induced band gap in graphene on hexagonal boron nitride: Ab initio density functional calculations" *Phys. Rev. B* **2007**, *76*, 073103.

(227) Ortix, C.; Yang, L.; van den Brink, J. "Graphene on incommensurate substrates: Trigonal warping and emerging Dirac cone replicas with halved group velocity" *Phys. Rev. B* **2012**, *86*, 081405.

(228) Kindermann, M.; Uchoa, B.; Miller, D. L. "Zero-energy modes and gate-tunable gap in graphene on hexagonal boron nitride" *Phys. Rev. B* **2012**, *86*, 115415.

(229) Song, J. C. W.; Shytov, A. V.; Levitov, L. S. "Electron Interactions and Gap Opening in Graphene Superlattices" *Phys. Rev. Lett.* **2013**, *111*, 266801.

(230) Slotman, G. J.; van Wijk, M. M.; Zhao, P. L.; Fasolino, A.; Katsnelson, M. I.; Yuan, S. J. "Effect of Structural Relaxation on the Electronic Structure of Graphene on Hexagonal Boron Nitride" *Phys. Rev. Lett.* **2015**, *115*, 186801.

(231) DaSilva, A. M.; Jung, J.; Adam, S.; MacDonald, A. H. "Transport and particle-hole asymmetry in graphene on boron nitride" *Phys. Rev. B* **2015**, *91*, 245422.

(232) San-Jose, P.; Gutiérrez-Rubio, A.; Sturla, M.; Guinea, F. "Electronic structure of spontaneously strained graphene on hexagonal boron nitride" *Phys. Rev. B* **2014**, *90*, 115152.

(233) Yin, L. J.; Qiao, J. B.; Zuo, W. J.; Li, W. T.; He, L. "Experimental evidence for non-Abelian gauge potentials in twisted graphene bilayers" *Phys. Rev. B* **2015**, *92*, 081406.

(234) Carr, S.; Massatt, D.; Fang, S.; Cazeaux, P.; Luskin, M.; Kaxiras, E. "Twistronics: Manipulating the Electronic Properties of Two-dimensional Layered Structures through their Twist Angle" *ArXiv e-prints* **2016**, arXiv:1611.00649.

(235) Suŕez Morell, E.; Correa, J. D.; Vargas, P.; Pacheco, M.; Barticevic, Z. "Flat bands in slightly twisted bilayer graphene: Tight-binding calculations" *Phys. Rev. B* **2010**, *82*, 121407.

(236) Trambly de Laissardière, G.; Mayou, D.; Magaud, L. "Localization of Dirac Electrons in Rotated Graphene Bilayers" *Nano Lett.* **2010**, *10*, 804–808.

(237) Bistritzer, R.; MacDonald, A. H. "Moiré bands in twisted double-layer graphene" *Proc. Natl. Acad. Sci. U.S.A.* **2011**, *108*, 12233–12237.

(238) Sachs, B.; Wehling, T. O.; Katsnelson, M. â.; Lichtenstein, A. I. "Midgap states and band gap modification in defective graphene/h-BN heterostructures" *ArXiv e-prints* **2016**, arXiv:1611.98753.

(239) Tarucha, S.; Austing, D. G.; Honda, T.; van der Hage, R. J.; Kouwenhoven, L. P. "Shell filling and spin effects in a few electron quantum dot" *Phys. Rev. Lett.* **1996**, *77*, 3613–3616.

(240) Maksym, P. A.; Chakraborty, T. "Quantum Dots in a Magnetic-Field - Role of Electron-Electron Interactions" *Phys. Rev. Lett.* **1990**, *65*, 108–111.

(241) Kouwenhoven, L. P.; Austing, D. G.; Tarucha, S. "Few-electron quantum dots" *Rep. Prog. Phys.* **2001**, *64*, 701–736.

(242) Bischoff, D.; Krähenmann, T.; Dröscher, S.; Gruner, M. A.; Barraud, C.; Ihn, T.; Ensslin, K. "Reactive-ion-etched graphene nanoribbons on a hexagonal boron nitride substrate" *Appl. Phys. Lett.* **2012**, *101*, 203103.

(243) Engels, S.; Epping, A.; Volk, C.; Korte, S.; Voigtländer, B.; Watanabe, K.; Taniguchi, T.; Trellenkamp, S.; Stampfer, C. "Etched graphene quantum dots on hexagonal boron nitride" *Appl. Phys. Lett.* **2013**, *103*, 073113.

(244) Bischoff, D.; Simonet, P.; Varlet, A.; Overweg, H. C.; Eich, M.; Ihn, T.; Ensslin, K. "The importance of edges in reactive ion etched graphene nanodevices" *Phys. Status Solidi RRL* **2016**, *10*, 68–74.

(245) Zhao, Y.; Wyrick, J.; Natterer, F. D.; Rodriguez-Nieva, J. F.; Lewandowski, C.; Watanabe, K.; Taniguchi, T.; Levitov, L. S.; Zhitenev, N. B.; Stroscio, J. A. "Creating and probing electron whispering-gallery modes in graphene" *Science* **2015**, *348*, 672–675.

(246) Goossens, A. M.; Driessen, S. C. M.; Baart, T. A.; Watanabe, K.; Taniguchi, T.; Vandersypen, L. M. K. "Gate-Defined Confinement in Bilayer Graphene-Hexagonal Boron Nitride Hybrid Devices" *Nano Lett.* **2012**, *12*, 4656–4660.

(247) Allen, M. T.; Martin, J.; Yacoby, A. "Gate-defined quantum confinement in suspended bilayer graphene" *Nat. Commun.* **2012**, *3*, 934.

(248) Müller, A.; Kaestner, B.; Hohls, F.; Weimann, T.; Pierz, K.; Schumacher, H. W. "Bilayer graphene quantum dot defined by topgates" *J. Appl. Phys.* **2014**, *115*, 233710.

(249) Chen, H. Y.; Apalkov, V.; Chakraborty, T. "Fock-Darwin states of dirac electrons in graphene-based artificial atoms" *Phys. Rev. Lett.* **2007**, *98*, 186803.

(250) Giavaras, G.; Nori, F. "Tunable quantum dots in monolayer graphene" *Phys. Rev. B* **2012**, *85*, 165446.

(251) Huckestein, B. "Scaling Theory of the Integer Quantum Hall-Effect" *Rev. Mod. Phys.* **1995**, *67*, 357–396.

(252) Ilani, S.; Martin, J.; Teitelbaum, E.; Smet, J. H.; Mahalu, D.; Umansky, V.; Yacoby, A. "The microscopic nature of localization in the quantum Hall effect" *Nature* **2004**, *427*, 328–332.

(253) Martin, J.; Akerman, N.; Ulbricht, G.; Lohmann, T.; von Klitzing, K.; Smet, J. H.; Yacoby, A. "The nature of localization in graphene under quantum Hall conditions" *Nat. Phys.* **2009**, *5*, 669–674.

(254) Efros, A. L. "Non-Linear Screening and the Background Density of 2deg States in Magnetic-Field" *Solid State Commun.* **1988**, *67*, 1019–1022.

(255) Fogler, M. M.; Novikov, D. S.; Shklovskii, B. I. "Screening of a hypercritical charge in graphene" *Phys. Rev. B* **2007**, *76*, 233402.

(256) Fogler, M. M. "Neutrality Point of Graphene with Coplanar Charged Impurities" *Phys. Rev. Lett.* **2009**, *103*, 236801.

(257) Struck, A.; Kramer, B. "Electron correlations and single-particle physics in the integer quantum Hall effect" *Phys. Rev. Lett.* **2006**, *97*, 106801.

(258) Morgenstern, M.; Haude, D.; Gudmundsson, V.; Wittneven, C.; Dombrowski, R.; Wiesendanger, R. "Origin of Landau oscillations observed in scanning tunneling spectroscopy on n-InAs(110)" *Phys. Rev. B* **2000**, *62*, 7257–7263.

(259) Miller, D. L.; Kubista, K. D.; Rutter, G. M.; Ruan, M.; de Heer, W. A.; First, P. N.; Stroscio, J. A. "Observing the Quantization of Zero Mass Carriers in Graphene" *Science* **2009**, *324*, 924–927.

(260) Song, Y. J.; Otte, A. F.; Kuk, Y.; Hu, Y.; Torrance, D. B.; First, P. N.; de Heer, W. A.; Min, H.; Adam, S.; Stiles, M. D.; MacDonald, A. H.; Stroscio, J. A. "High-resolution tunnelling spectroscopy of a graphene quartet" *Nature* **2010**, *467*, 185–189.

(261) Li, G.; Andrei, E. Y. "Observation of Landau levels of Dirac fermions in graphite" *Nat. Phys.* **2007**, *3*, 623–627.

(262) Luican, A.; Li, G. H.; Andrei, E. Y. "Scanning tunneling microscopy and spectroscopy of graphene layers on graphite" *Solid State Commun.* **2009**, *149*, 1151–1156.

(263) Li, G. H.; Luican, A.; Andrei, E. Y. "Scanning Tunneling Spectroscopy of Graphene on Graphite" *Phys. Rev. Lett.* **2009**, *102*, 176804.

(264) Li, G. H.; Luican-Mayer, A.; Abanin, D.; Levitov, L.; Andrei, E. Y. "Evolution of Landau levels into edge states in graphene" *Nat. Commun.* **2013**, *4*, 1744.

(265) Luican, A.; Li, G. H.; Andrei, E. Y. "Quantized Landau level spectrum and its density dependence in graphene" *Phys. Rev. B* **2011**, *83*, 041405.

(266) Chae, J.; Jung, S.; Young, A. F.; Dean, C. R.; Wang, L.; Gao, Y.; Watanabe, K.; Taniguchi, T.; Hone, J.; Shepard, K. L.; Kim, P.; Zhitenev, N. B.; Stroscio, J. A. "Renormalization of the graphene dispersion velocity determined from scanning tunneling spectroscopy" *Phys. Rev. Lett.* **2012**, *109*, 116802.

(267) Niimi, Y.; Kambara, H.; Matsui, T.; Yoshioka, D.; Fukuyama, H. "Real-space imaging of alternate localization and extension of quasi-two-dimensional electronic states at graphite surfaces in magnetic fields" *Phys. Rev. Lett.* **2006**, *97*, 236804.

(268) Niimi, Y.; Matsui, T.; Kambara, H.; Tagami, K.; Tsukada, M.; Fukuyama, H. "Scanning tunneling microscopy and spectroscopy of the electronic local density of states of graphite surfaces near monoatomic step edges" *Phys. Rev. B* **2006**, *73*, 085421.

(269) Niimi, Y.; Kambara, H.; Fukuyama, H. "Localized Distributions of Quasi-Two-Dimensional Electronic States near Defects Artificially Created at Graphite Surfaces in Magnetic Fields" *Phys. Rev. Lett.* **2009**, *102*, 026803.

(270) Luican-Mayer, A.; Kharitonov, M.; Li, G.; Lu, C. P.; Skachko, I.; Goncalves, A. M.; Watanabe, K.; Taniguchi, T.; Andrei, E. Y. "Screening charged impurities and lifting the orbital degeneracy in graphene by populating Landau levels" *Phys. Rev. Lett.* **2014**, *112*, 036804.

(271) Miller, D. L.; Kubista, K. D.; Rutter, G. M.; Ruan, M.; de Heer, W. A.; Kindermann, M.; First, P. N.; Stroscio, J. A. "Real-space mapping of magnetically quantized graphene states" *Nat. Phys.* **2010**, *6*, 811–817.

(272) Zhu, S. Z.; Huang, Y.; Klimov, N. N.; Newell, D. B.; Zhitenev, N. B.; Stroscio, J. A.; Solares, S. D.; Li, T. "Pseudomagnetic fields in a locally strained graphene drumhead" *Phys. Rev. B* **2014**, *90*, 075426.

(273) Moriyama, S.; Morita, Y.; Watanabe, E.; Tsuya, D. "Field-induced confined states in graphene" *Appl. Phys. Lett.* **2014**, *104*, 053108.

(274) Tovari, E.; Makk, P.; Rickhaus, P.; Schönenberger, C.; Csonka, S. "Signatures of single quantum dots in graphene nanoribbons within the quantum Hall regime" *Nanoscale* **2016**, *8*, 11480–11486.

(275) Averin, D. V.; Nazarov, Y. V. "Virtual Electron-Diffusion during Quantum Tunneling of the Electric Charge" *Phys. Rev. Lett.* **1990**, *65*, 2446–2449.

(276) Weis, J.; Haug, R. J.; Vonklitzing, K.; Ploog, K. "Transport Spectroscopy of a Confined Electron-System under a Gate Tip" *Phys. Rev. B* **1992**, *46*, 12837–12840.

(277) Foxman, E. B.; Mceuen, P. L.; Meirav, U.; Wingreen, N. S.; Meir, Y.; Belk, P. A.; Belk, N. R.; Kastner, M. A.; Wind, S. J. "Effects of Quantum Levels on Transport through a Coulomb Island" *Phys. Rev. B* **1993**, *47*, 10020–10023.

(278) Weis, J.; Haug, R. J.; Vonklitzing, K.; Ploog, K. "Competing Channels in Single-Electron Tunneling through a Quantum-Dot" *Phys. Rev. Lett.* **1993**, *71*, 4019–4022.

(279) Johnson, A. T.; Kouwenhoven, L. P.; Dejong, W.; Vandervaart, N. C.; Harmans, C. J. P. M.; Foxon, C. T. "Zero-Dimensional States and Single Electron Charging in Quantum Dots" *Phys. Rev. Lett.* **1992**, *69*, 1592–1595.

(280) Nygard, J.; Cobden, D. H.; Lindelof, P. E. "Kondo physics in carbon nanotubes" *Nature* **2000**, *408*, 342–346.

(281) De Franceschi, S.; Sasaki, S.; Elzerman, J. M.; van der Wiel, W. G.; Tarucha, S.; Kouwenhoven, L. P. "Electron cotunneling in a semiconductor quantum dot" *Phys. Rev. Lett.* **2001**, *86*, 878–881.

(282) Schleser, R.; Ihn, T.; Ruh, E.; Ensslin, K.; Tews, M.; Pfannkuche, D.; Driscoll, D. C.; Gossard, A. C. "Cotunneling-mediated transport through excited states in the Coulomb-blockade regime" *Phys. Rev. Lett.* **2005**, *94*, 206805.

(283) Klein, O. "Die Reflexion von Elektronen an einem Potentialsprung nach der relativistischen Dynamik von Dirac" *Z. Phys.* **1929**, *53*, 157–165.

(284) Su, R. K.; Siu, G. G.; Chou, X. "Barrier Penetration and Klein Paradox" *J. Phys. A: Math. Gen.* **1993**, *26*, 1001–1005.

(285) Dombey, N.; Calogeracos, A. "Seventy years of the Klein paradox" *Phys. Rep.* **1999**, *315*, 41–58.

(286) Calogeracos, A.; Dombey, N. "History and physics of the Klein paradox" *Contemp. Phys.* **1999**, *40*, 313–321.

(287) Calogeracos, A. "Relativistic quantum mechanics - Paradox in a pencil" *Nat. Phys.* **2006**, *2*, 579–580.

(288) Katsnelson, M. I. "Graphene: carbon in two dimensions" *Mater. Today* **2007**, *10*, 20–27.

(289) Matulis, A.; Peeters, F. M. "Quasibound states of quantum dots in single and bilayer graphene" *Phys. Rev. B* **2008**, *77*, 115423.

(290) Beenakker, C. W. J. "Colloquium: Andreev reflection and Klein tunneling in graphene" *Rev. Mod. Phys.* **2008**, *80*, 1337–1354.

(291) Hewageegana, P.; Apalkov, V. "Trapping of an electron in coupled quantum dots in graphene" *Phys. Rev. B* **2009**, *79*, 115418.

(292) Giavaras, G.; Maksym, P. A.; Roy, M. "Electron confinement in single layer graphene quantum dots: Semiclassical approach" *Phys. E (Amsterdam, Neth.)* **2010**, *42*, 715–718.

(293) He, W.-Y.; Chu, Z.-D.; He, L. "Chiral Tunneling in a Twisted Graphene Bilayer" *Phys. Rev. Lett.* **2013**, *111*, 066803.

(294) Greenaway, M. T.; Vdovin, E. E.; Mishchenko, A.; Makarovsky, O.; Patane, A.; Wallbank, J. R.; Cao, Y.; Kretinin, A. V.; Zhu, M. J.; Morozov, S. V.; Fal'ko, V. I.; Novoselov, K. S.; Geim, A. K.; Fromhold, T. M.; Eaves, L. "Resonant tunnelling between the chiral Landau states of twisted graphene lattices" *Nat. Phys.* **2015**, *11*, 1057–1062.

(295) Cheianov, V. V.; Fal'ko, V. I. "Selective transmission of Dirac electrons and ballistic magnetoresistance of *n*-*p* junctions in graphene" *Phys. Rev. B* **2006**, *74*, 041403.

(296) Downing, C. A.; Stone, D. A.; Portnoi, M. E. "Zero-energy states in graphene quantum dots and rings" *Phys. Rev. B* **2011**, *84*, 155437.

(297) Tworzydlo, J.; Trauzettel, B.; Titov, M.; Rycerz, A.; Beenakker, C. W. J. "Sub-Poissonian shot noise in graphene" *Phys. Rev. Lett.* **2006**, *96*, 246802.

(298) Kim, M.; Choi, J.-H.; Lee, S.-H.; Watanabe, K.; Taniguchi, T.; Jhi, S.-H.; Lee, H.-J. "Valley-symmetry-preserved transport in ballistic graphene with gate-defined carrier guiding" *Nat. Phys.* **2016**, *12*, 1022–1026.

(299) Rickhaus, P.; Liu, M.-H.; Makk, P.; Maurand, R.; Hess, S.; Zihlmann, S.; Weiss, M.; Richter, K.; Schönenberger, C. "Guiding of Electrons in a Few-Mode Ballistic Graphene Channel" *Nano Lett.* **2015**, *15*, 5819–5825.

(300) Mayorov, A. S.; Elias, D. C.; Mukhin, I. S.; Morozov, S. V.; Ponomarenko, L. A.; Novoselov, K. S.; Geim, A. K.; Gorbachev, R. V. "How Close Can One Approach the Dirac Point in Graphene Experimentally?" *Nano Lett.* **2012**, *12*, 4629–4634.

(301) Ohta, T.; Bostwick, A.; Seyller, T.; Horn, K.; Rotenberg, E. "Controlling the electronic structure of bilayer graphene" *Science* **2006**, *313*, 951–954.

(302) Zhang, Y. B.; Tang, T. T.; Girit, C.; Hao, Z.; Martin, M. C.; Zettl, A.; Crommie, M. F.; Shen, Y. R.; Wang, F. "Direct observation of a widely tunable bandgap in bilayer graphene" *Nature* **2009**, *459*, 820–823.

(303) Oostinga, J. B.; Heersche, H. B.; Liu, X.; Morpurgo, A. F.; Vandersypen, L. M. "Gate-induced insulating state in bilayer graphene devices" *Nat Mater* **2008**, *7*, 151–157.

(304) Jing, L.; Velasco J., J.; Kratz, P.; Liu, G.; Bao, W.; Bockrath, M.; Lau, C. N. "Quantum transport and field-induced insulating states in bilayer graphene pnp junctions" *Nano Lett.* **2010**, *10*, 4000–4004.

(305) Taychatanapat, T.; Jarillo-Herrero, P. "Electronic Transport in Dual-Gated Bilayer Graphene at Large Displacement Fields" *Phys. Rev. Lett.* **2010**, *105*, 166601.

(306) Shimazaki, Y.; Yamamoto, M.; Borzenets, I. V.; Watanabe, K.; Taniguchi, T.; Tarucha, S. "Generation and detection of pure valley current by electrically induced Berry curvature in bilayer graphene" *Nat. Phys.* **2015**, *11*, 1032–1036.

(307) Sui, M.; Chen, G.; Ma, L.; Shan, W.-Y.; Tian, D.; Watanabe, K.; Taniguchi, T.; Jin, X.; Yao, W.; Xiao, D.; Zhang, Y. "Gate-tunable topological valley transport in bilayer graphene" *Nat. Phys.* **2015**, *11*, 1027–1031.

(308) Giesbers, A. J. M.; Zeitler, U.; Neubeck, S.; Freitag, F.; Novoselov, K. S.; Maan, J. C. "Nanolithography and manipulation of graphene using an atomic force microscope" *Solid State Commun.* **2008**, *147*, 366–369.

(309) Morgenstern, M.; Freitag, N.; Vaid, A.; Pratzer, M.; Liebmann, M. "Graphene quantum dots: wave function mapping by scanning tunneling spectroscopy and transport spectroscopy of quantum dots prepared by local anodic oxidation" *Phys. Status Solidi RRL* **2016**, *10*, 24–38.

(310) Bell, D. C.; Lemme, M. C.; Stern, L. A.; Williams, J. R.; Marcus, C. M. "Precision cutting and patterning of graphene with helium ions" *Nanotechnology* **2009**, *20*, 455301.

(311) Qi, Z. J.; Daniels, C.; Hong, S. J.; Park, Y. W.; Meunier, V.; Drndic, M.; Johnson, A. T. "Electronic transport of recrystallized freestanding graphene nanoribbons" *ACS Nano* **2015**, *9*, 3510–3520.

(312) Vicarelli, L.; Heerema, S. J.; Dekker, C.; Zandbergen, H. W. "Controlling defects in graphene for optimizing the electrical properties of graphene nanodevices" *ACS Nano* **2015**, *9*, 3428–3435.

(313) Liu, Z.; Ma, L.; Shi, G.; Zhou, W.; Gong, Y.; Lei, S.; Yang, X.; Zhang, J.; Yu, J.; Hackenberg, K. P.; Babakhani, A.; Idrobo, J. C.; Vajtai, R.; Lou, J.; Ajayan, P. M. "In-plane heterostructures of graphene and hexagonal boron nitride with controlled domain sizes" *Nat. Nanotechnol.* **2013**, *8*, 119–124.

(314) Kan, M.; Li, Y. W.; Sun, Q. "Recent advances in hybrid graphene-BN planar structures" *Wires. Comput. Mol. Sci.* **2016**, *6*, 65–82.

(315) Güttinger, J.; Molitor, F.; Stampfer, C.; Schnez, S.; Jacobsen, A.; Dröscher, S.; Ihn, T.; Ensslin, K. "Transport through graphene quantum dots" *Rep. Prog. Phys.* **2012**, *75*, 126502.

(316) White, C. T.; Li, J. W.; Gunlycke, D.; Mintmire, J. W. "Hidden one-electron interactions in carbon nanotubes revealed in graphene nanostrips" *Nano Lett.* **2007**, *7*, 825–830.

(317) Peres, N. M. R.; Castro Neto, A. H.; Guinea, F. "Conductance quantization in mesoscopic graphene" *Phys. Rev. B* **2006**, *73*, 195411.

(318) Gunlycke, D.; Areshkin, D. A.; White, C. T. "Semiconducting graphene nanostrips with edge disorder" *Appl. Phys. Lett.* **2007**, *90*, 142104.

(319) Fernández-Rossier, J.; Palacios, J. J.; Brey, L. "Electronic structure of gated graphene and graphene ribbons" *Phys. Rev. B* **2007**, *75*, 205441.

(320) Yang, L.; Park, C.-H.; Son, Y.-W.; Cohen, M. L.; Louie, S. G. "Quasiparticle Energies and Band Gaps in Graphene Nanoribbons" *Phys. Rev. Lett.* **2007**, *99*, 186801.

(321) Molitor, F.; Stampfer, C.; Güttinger, J.; Jacobsen, A.; Ihn, T.; Ensslin, K. "Energy and transport gaps in etched graphene nanoribbons" *Semicond. Sci. Technol.* **2010**, *25*, 034002.

(322) Stampfer, C.; Güttinger, J.; Hellmüller, S.; Molitor, F.; Ensslin, K.; Ihn, T. "Energy Gaps in Etched Graphene Nanoribbons" *Phys. Rev. Lett.* **2009**, *102*, 056403.

(323) Han, M. Y.; Özyilmaz, B.; Zhang, Y.; Kim, P. "Energy Band-Gap Engineering of Graphene Nanoribbons" *Phys. Rev. Lett.* **2007**, *98*, 206805.

(324) Bischoff, D.; Varlet, A.; Simonet, P.; Ihn, T.; Ensslin, K. "Electronic triple-dot transport through a bilayer graphene island with ultrasmall constrictions" *New J. Phys.* **2013**, *15*, 083029.

(325) Moser, J.; Bachtold, A. "Fabrication of large addition energy quantum dots in graphene" *Appl. Phys. Lett.* **2009**, *95*, 173506.

(326) Güttinger, J.; Stampfer, C.; Frey, T.; Ihn, T.; Ensslin, K. "Graphene quantum dots in perpendicular magnetic fields" *Physica Status Solidi B-Basic Solid State Physics* **2009**, *246*, 2553–2557.

(327) Güttinger, J.; Stampfer, C.; Libisch, F.; Frey, T.; Burgdörfer, J.; Ihn, T.; Ensslin, K. "Electron-Hole Crossover in Graphene Quantum Dots" *Phys. Rev. Lett.* **2009**, *103*, 046810.

(328) Schnez, S.; Molitor, F.; Stampfer, C.; Güttinger, J.; Shorubalko, I.; Ihn, T.; Ensslin, K. "Observation of excited states in a graphene quantum dot" *Appl. Phys. Lett.* **2009**, *94*, 012107.

(329) Elzerman, J. M.; Hanson, R.; Greidanus, J. S.; Willems van Beveren, L. H.; De Franceschi, S.; Vandersypen, L. M. K.; Tarucha, S.; Kouwenhoven, L. P. "Few-electron quantum dot circuit with integrated charge read out" *Phys. Rev. B* **2003**, *67*, 161308.

(330) Güttinger, J.; Stampfer, C.; Hellmuller, S.; Molitor, F.; Ihn, T.; Ensslin, K. "Charge detection in graphene quantum dots" *Appl. Phys. Lett.* **2008**, *93*, 212102.

(331) Wang, L. J.; Cao, G.; Tu, T.; Li, H. O.; Zhou, C.; Hao, X. J.; Su, Z.; Guo, G. C.; Jiang, H. W.; Guo, G. P. "A graphene quantum dot with a single electron transistor as an integrated charge sensor" *Appl. Phys. Lett.* **2010**, *97*, 262113.

(332) Volk, C.; Neumann, C.; Kazarski, S.; Fringes, S.; Engels, S.; Haupt, F.; Müller, A.; Stampfer, C. "Probing relaxation times in graphene quantum dots" *Nat. Commun.* **2013**, *4*, 1753.

(333) Neumann, C.; Volk, C.; Engels, S.; Stampfer, C. "Graphene-based charge sensors" *Nanotechnology* **2013**, *24*, 444001.

(334) Neubeck, S.; Ponomarenko, L. A.; Freitag, F.; Giesbers, A. J. M.; Zeitler, U.; Morozov, S. V.; Blake, P.; Geim, A. K.; Novoselov, K. S. "From One Electron to One Hole: Quasiparticle Counting in Graphene Quantum Dots Determined by Electrochemical and Plasma Etching" *Small* **2010**, *6*, 1469–1473.

(335) Güttinger, J.; Frey, T.; Stampfer, C.; Ihn, T.; Ensslin, K. "Spin states in graphene quantum dots" *Phys. Rev. Lett.* **2010**, *105*, 116801.

(336) Puddy, R. K.; Scard, P. H.; Tyndall, D.; Connolly, M. R.; Smith, C. G.; Jones, G. A. C.; Lombardo, A.; Ferrari, A. C.; Buitelaar, M. R. "Atomic force microscope nanolithography of graphene: Cuts, pseudocuts, and tip current measurements" *Appl. Phys. Lett.* **2011**, *98*, 133120.

(337) Molitor, F.; Dröscher, S.; Güttinger, J.; Jacobsen, A.; Stampfer, C.; Ihn, T.; Ensslin, K. "Transport through graphene double dots" *Appl. Phys. Lett.* **2009**, *94*, 222107.

(338) Volk, C.; Fringes, S.; Terres, B.; Dauber, J.; Engels, S.; Trellenkamp, S.; Stampfer, C. "Electronic excited states in bilayer graphene double quantum dots" *Nano Lett.* **2011**, *11*, 3581–3586.

(339) Chen, Z.; Lin, Y.-M.; Rooks, M. J.; Avouris, P. "Graphene nano-ribbon electronics" *Phys. E (Amsterdam, Neth.)* **2007**, *40*, 228–232.

(340) Tapasztó, L.; Dobrik, G.; Lambin, P.; Biro, L. P. "Tailoring the atomic structure of graphene nanoribbons by scanning tunnelling microscope lithography" *Nat. Nano.* **2008**, *3*, 397–401.

(341) Han, M. Y.; Brant, J. C.; Kim, P. "Electron Transport in Disordered Graphene Nanoribbons" *Phys. Rev. Lett.* **2010**, *104*, 056801.

(342) Dauber, J.; Terres, B.; Volk, C.; Trellenkamp, S.; Stampfer, C. "Reducing disorder in graphene nanoribbons by chemical edge modification" *Appl. Phys. Lett.* **2014**, *104*, 083105.

(343) Adam, S.; Cho, S.; Fuhrer, M. S.; Das Sarma, S. "Density Inhomogeneity Driven Percolation Metal-Insulator Transition and Dimensional Crossover in Graphene Nanoribbons" *Phys. Rev. Lett.* **2008**, *101*, 046404.

(344) Wharam, D. A.; Thornton, T. J.; Newbury, R.; Pepper, M.; Ahmed, H.; Frost, J. E. F.; Hasko, D. G.; Peacock, D. C.; Ritchie, D. A.; Jones, G. A. C. "One-Dimensional Transport and the Quantization of the Ballistic Resistance" *J. Phys. C Solid State* **1988**, *21*, L209–L214.

(345) Nakada, K.; Fujita, M.; Dresselhaus, G.; Dresselhaus, M. S. "Edge state in graphene ribbons: Nanometer size effect and edge shape dependence" *Phys. Rev. B* **1996**, *54*, 17954–17961.

(346) Wakabayashi, K. "Electronic transport properties of nanographite ribbon junctions" *Phys. Rev. B* **2001**, *64*, 125428.

(347) Brey, L.; Fertig, H. A. "Electronic states of graphene nanoribbons studied with the Dirac equation" *Phys. Rev. B* **2006**, *73*, 235411.

(348) Muñoz-Rojas, F.; Jacob, D.; Fernandez-Rossier, J.; Palacios, J. J. "Coherent transport in graphene nanoconstrictions" *Phys. Rev. B* **2006**, *74*, 195417.

(349) Tombros, N.; Veligura, A.; Junesch, J.; Guimaraes, M. H. D.; Vera-Marun, I. J.; Jonkman, H. T.; van Wees, B. J. "Quantized conductance of a suspended graphene nanoconstriction" *Nat. Phys.* **2011**, *7*, 697–700.

(350) Girit, Ç. Ö.; Meyer, J. C.; Erni, R.; Rossell, M. D.; Kisielowski, C.; Yang, L.; Park, C.-H.; Crommie, M. F.; Cohen, M. L.; Louie, S. G.; Zettl, A. "Graphene at the Edge: Stability and Dynamics" *Science* **2009**, *323*, 1705–1708.

(351) Koskinen, P.; Malola, S.; Häkkinen, H. "Evidence for graphene edges beyond zigzag and armchair" *Phys. Rev. B* **2009**, *80*, 073401.

(352) Kobayashi, Y.; Fukui, K.-i.; Enoki, T.; Kusakabe, K. "Edge state on hydrogen-terminated graphite edges investigated by scanning tunneling microscopy" *Phys. Rev. B* **2006**, *73*, 125415.

(353) Evaldsson, M.; Zozoulenko, I. V.; Xu, H.; Heinzel, T. "Edge-disorder-induced Anderson localization and conduction gap in graphene nanoribbons" *Phys. Rev. B* **2008**, *78*, 161407.

(354) Chuvilin, A.; Meyer, J. C.; Algara-Siller, G.; Kaiser, U. "From graphene constrictions to single carbon chains" *New J. Phys.* **2009**, *11*, 083019.

(355) Suenaga, K.; Koshino, M. "Atom-by-atom spectroscopy at graphene edge" *Nature* **2010**, *468*, 1088–1090.

(356) Zan, R.; Ramasse, Q. M.; Bangert, U.; Novoselov, K. S. "Graphene Reknits Its Holes" *Nano Lett.* **2012**, *12*, 3936–3940.

(357) Pan, M.; Girão, E. C.; Jia, X.; Bhaviripudi, S.; Li, Q.; Kong, J.; Meunier, V.; Dresselhaus, M. S. "Topographic and Spectroscopic Characterization of Electronic Edge States in CVD Grown Graphene Nanoribbons" *Nano Lett.* **2012**, *12*, 1928–1933.

(358) Libisch, F.; Rotter, S.; Burgdörfer, J. "Coherent transport through graphene nanoribbons in the presence of edge disorder" *New J. Phys.* **2012**, *14*, 123006.

(359) Bischoff, D.; Libisch, F.; Burgdörfer, J.; Ihn, T.; Ensslin, K. "Characterizing wave functions in graphene nanodevices: Electronic transport through ultrashort graphene constrictions on a boron nitride substrate" *Phys. Rev. B* **2014**, *90*, 115405.

(360) Hubacek, J. S.; Brockenbrough, R. T.; Gammie, G.; Skala, S. L.; Lyding, J. W.; Latten, J. L.; Shapley, J. R. "Scanning Tunnelling Microscopy of Graphite-Adsorbed Molecular-Species" *J. Microsc.-Oxford* **1988**, *152*, 221–227.

(361) McDermott, M. T.; McCreery, R. L. "Scanning-Tunneling-Microscopy of Ordered Graphite and Glassy-Carbon Surfaces - Electronic Control of Quinone Adsorption" *Langmuir* **1994**, *10*, 4307–4314.

(362) Fang, M.; Wang, K.; Lu, H.; Yang, Y.; Nutt, S. "Covalent polymer functionalization of graphene nanosheets and mechanical properties of composites" *J. Mater. Chem.* **2009**, *19*, 7098–7105.

(363) Georgakilas, V.; Otyepka, M.; Bourlinos, A. B.; Chandra, V.; Kim, N.; Kemp, K. C.; Hobza, P.; Zboril, R.; Kim, K. S. "Functionalization of Graphene: Covalent and Non-Covalent Approaches, Derivatives and Applications" *Chem. Rev.* **2012**, *112*, 6156–6214.

(364) Layek, R. K.; Nandi, A. K. "A review on synthesis and properties of polymer functionalized graphene" *Polymer* **2013**, *54*, 5087–5103.

(365) Xiang, Z.; Dai, Q.; Chen, J.-F.; Dai, L. "Edge Functionalization of Graphene and Two-Dimensional Covalent Organic Polymers for Energy Conversion and Storage" *Adv. Mater.* **2016**, *28*, 6253–6261.

(366) Cai, J.; Ruffieux, P.; Jaafar, R.; Bieri, M.; Braun, T.; Blankenburg, S.; Muoth, M.; Seitsonen, A. P.; Saleh, M.; Feng, X.; Mullen, K.; Fasel, R. "Atomically precise bottom-up fabrication of graphene nanoribbons" *Nature* **2010**, *466*, 470–473.

(367) Jiao, L.; Wang, X.; Diankov, G.; Wang, H.; Dai, H. "Facile synthesis of high-quality graphene nanoribbons" *Nat. Nano.* **2010**, *5*, 321–325.

(368) Kosynkin, D. V.; Higginbotham, A. L.; Sinitskii, A.; Lomeda, J. R.; Dimiev, A.; Price, B. K.; Tour, J. M. "Longitudinal unzipping of carbon nanotubes to form graphene nanoribbons" *Nature* **2009**, *458*, 872–876.

(369) Tao, C.; Jiao, L.; Yazyev, O. V.; Chen, Y.-C.; Feng, J.; Zhang, X.; Capaz, R. B.; Tour, J. M.; Zettl, A.; Louie, S. G.; Dai, H.; Crommie, M. F. "Spatially resolving edge states of chiral graphene nanoribbons" *Nat. Phys.* **2011**, *7*, 616–620.

(370) Wang, X.; Ouyang, Y.; Jiao, L.; Wang, H.; Xie, L.; Wu, J.; Guo, J.; Dai, H. "Graphene nanoribbons with smooth edges behave as quantum wires" *Nat. Nanotechnol.* **2011**, *6*, 563–567.

(371) McCann, E. "Asymmetry gap in the electronic band structure of bilayer graphene" *Phys. Rev. B* **2006**, *74*, 161403.

(372) Min, H.; Sahu, B.; Banerjee, S. K.; MacDonald, A. H. "*Ab initio* theory of gate induced gaps in graphene bilayers" *Phys. Rev. B* **2007**, *75*, 155115.

(373) Castro, E. V.; Novoselov, K. S.; Morozov, S. V.; Peres, N. M. R.; dos Santos, J. M. B. L.; Nilsson, J.; Guinea, F.; Geim, A. K.; Neto, A. H. C. "Biased Bilayer Graphene: Semiconductor with a Gap Tunable by the Electric Field Effect" *Phys. Rev. Lett.* **2007**, *99*, 216802.

(374) Weitz, R. T.; Allen, M. T.; Feldman, B. E.; Martin, J.; Yacoby, A. "Broken-Symmetry States in Doubly Gated Suspended Bilayer Graphene" *Science* **2010**, *330*, 812–816.

(375) Velasco, J.; Lee, Y.; Zhao, Z.; Jing, L.; Kratz, P.; Bockrath, M.; Lau, C. N. "Transport Measurement of Landau Level Gaps in Bilayer Graphene with Layer Polarization Control" *Nano Lett.* **2014**, *14*, 1324–1328.

(376) Ki, D. K.; Fal'ko, V. I.; Abanin, D. A.; Morpurgo, A. F. "Observation of Even Denominator Fractional Quantum Hall Effect in Suspended Bilayer Graphene" *Nano Lett.* **2014**, *14*, 2135–2139.

(377) Zou, K.; Zhu, J. "Transport in gapped bilayer graphene: The role of potential fluctuations" *Phys. Rev. B* **2010**, *82*, 081407.

(378) Rutter, G. M.; Jung, S. Y.; Klimov, N. N.; Newell, D. B.; Zhitenev, N. B.; Stroscio, J. A. "Microscopic polarization in bilayer graphene" *Nat. Phys.* **2011**, *7*, 649–655.

(379) Li, J.; Martin, I.; Buttiker, M.; Morpurgo, A. F. "Topological origin of subgap conductance in insulating bilayer graphene" *Nat. Phys.* **2011**, *7*, 38–42.

(380) Vaezi, A.; Liang, Y.; Ngai, D. H.; Yang, L.; Kim, E.-A. "Topological Edge States at a Tilt Boundary in Gated Multilayer Graphene" *Phys. Rev. X* **2013**, *3*, 021018.

(381) San-Jose, P.; Gorbachev, R. V.; Geim, A. K.; Novoselov, K. S.; Guinea, F. "Stacking Boundaries and Transport in Bilayer Graphene" *Nano Lett.* **2014**, *14*, 2052–2057.

(382) Ju, L.; Shi, Z. W.; Nair, N.; Lv, Y. C.; Jin, C. H.; Velasco Jr., J.; Ojeda-Aristizabal, C.; Bechtel, H. A.; Martin, M. C.; Zettl, A.; Analytis, J.; Wang, F. "Topological valley transport at bilayer graphene domain walls" *Nature* **2015**, *520*, 650–655.

(383) Yan, J.; Fuhrer, M. S. "Charge transport in dual gated bilayer graphene with Corbino geometry" *Nano Lett.* **2010**, *10*, 4521–4525.

(384) Engels, S. *Limitations to charge carrier transport in high quality single- and bi-layer graphene*, Ph. D. Thesis, 2016.

(385) Giavaras, G.; Maksym, P. A.; Roy, M. "Magnetic field induced confinement-deconfinement transition in graphene quantum dots" *J. Phys.-Condens. Mat.* **2009**, *21*, 102201.

(386) Giavaras, G.; Nori, F. "Graphene quantum dots formed by a spatial modulation of the Dirac gap" *Appl. Phys. Lett.* **2010**, *97*, 243106.

(387) Maksym, P. A.; Roy, M.; Craciun, M. F.; Russo, S.; Yamamoto, M.; Tarucha, S.; Aoki, H. "Proposal for a magnetic field induced graphene dot" *J. Phys. Conf. Ser.* **2010**, *245*, 012030.

(388) Park, P. S.; Kim, S. C.; Yang, S. R. E. "Scaling properties of induced density of chiral and nonchiral Dirac fermions in magnetic fields" *Phys. Rev. B* **2011**, *84*, 085405.

(389) Park, P. S.; Kim, S. C.; Yang, S. R. E. "Comment on "Fock-Darwin States of Dirac Electrons in Graphene-Based Artificial Atoms"" *Phys. Rev. Lett.* **2012**, *108*, 169701.

(390) Maksym, P. A.; Aoki, H. "Magnetic-field-controlled vacuum charge in graphene quantum dots with a mass gap" *Phys. Rev. B* **2013**, *88*, 081406.

(391) Orlof, A.; Shylau, A. A.; Zozoulenko, I. V. "Electron-electron interactions in graphene field-induced quantum dots in a high magnetic field" *Phys. Rev. B* **2015**, *92*, 075431.

(392) Landau, L. "Diamagnetismus der Metalle" *Z. Phys.* **1930**, *64*, 629–637.

(393) Fock, V. "Bemerkung zur Quantelung des harmonischen Oszillators im Magnetfeld" *Z. Phys.* **1928**, *47*, 446–448.

(394) Darwin, C. G. "The Diamagnetism of the Free Electron" *Math. Proc. Cambridge Philos. Soc.* **1930**, *27*, 86–90.

(395) Dingle, R. B. "Some Magnetic Properties of Metals .1. General Introduction, and Properties of Large Systems of Electrons" *Proc. R. Soc. London, Ser. A* **1952**, *211*, 500–516.

(396) Yoshioka, D. "Local density of states around impurity in a strong magnetic field: I. Two-dimensional system with parabolic dispersion" *J. Phys. Soc. Jpn.* **2007**, *76*, 024718.

(397) Schnez, S.; Ensslin, K.; Sigrist, M.; Ihn, T. "Analytic model of the energy spectrum of a graphene quantum dot in a perpendicular magnetic field" *Phys. Rev. B* **2008**, *78*, 195427.

(398) Hashimoto, K.; Champel, T.; Florens, S.; Sohrmann, C.; Wiebe, J.; Hirayama, Y.; Römer, R. A.; Wiesendanger, R.; Morgenstern, M. "Robust Nodal Structure of Landau Level Wave Functions Revealed by Fourier Transform Scanning Tunneling Spectroscopy" *Phys. Rev. Lett.* **2012**, *109*, 116805.

(399) Bindel, J. R.; Ulrich, J.; Liebmann, M.; Morgenstern, M. "Probing the nodal structure of Landau level wave functions in real space" *Phys. Rev. Lett.* **2016**, in press.

(400) Morgenstern, M.; Gudmundsson, V.; Dombrowski, R.; Wittneven, C.; Wiesendanger, R. "Nonlocality of the exchange interaction probed by scanning tunneling spectroscopy" *Phys. Rev. B* **2001**, *63*, 201301.

(401) Shevchenko, S. N.; Ashhab, S.; Nori, F. "Landau-Zener-Stuckelberg interferometry" *Phys. Rep.* **2010**, *492*, 1–30.

(402) Stehlik, J.; Dovzhenko, Y.; Petta, J. R.; Johansson, J. R.; Nori, F.; Lu, H.; Gossard, A. C. "Landau-Zener-Stückelberg interferometry of a single electron charge qubit" *Phys. Rev. B* **2012**, *86*, 121303.

(403) Wu, G. Y.; Lue, N. Y. "Graphene-based qubits in quantum communications" *Phys. Rev. B* **2012**, *86*, 045456.

(404) Rohling, N.; Burkard, G. "Universal quantum computing with spin and valley states" *New J. Phys.* **2012**, *14*, 083008.

(405) Rohling, N.; Russ, M.; Burkard, G. "Hybrid Spin and Valley Quantum Computing with Singlet-Triplet Qubits" *Phys. Rev. Lett.* **2014**, *113*, 176801.

(406) Libisch, F.; Rotter, S.; Güttinger, J.; Stampfer, C.; Burgdörfer, J. "Transition to Landau levels in graphene quantum dots" *Phys. Rev. B* **2010**, *81*, 245411.

(407) Britnell, L.; Gorbachev, R. V.; Jalil, R.; Belle, B. D.; Schedin, F.; Katsnelson, M. I.; Eaves, L.; Morozov, S. V.; Mayorov, A. S.; Peres, N. M. R.; Neto, A. H. C.; Leist, J.; Geim, A. K.; Ponomarenko, L. A.; Novoselov, K. S. "Electron Tunneling through Ultrathin Boron Nitride Crystalline Barriers" *Nano Lett.* **2012**, *12*, 1707–1710.

(408) Averin, D. V.; Likharev, K. K. "Coulomb Blockade of Single-Electron Tunneling, and Coherent Oscillations in Small Tunnel-Junctions" *J. Low Temp. Phys.* **1986**, *62*, 345–373.

(409) Hanna, A. E.; Tinkham, M. "Variation of the Coulomb Staircase in a 2-Junction System by Fractional Electron Charge" *Phys. Rev. B* **1991**, *44*, 5919–5922.

(410) Nagel, J. R. "Solving the Generalized Poisson Equation Using the Finite-Difference Method (FDM)" *Lecture Notes, Dept. of Electrical and Computer Engineering, University of Utah* **2011**.

(411) Fang, T.; Konar, A.; Xing, H.; Jena, D. "Carrier statistics and quantum capacitance of graphene sheets and ribbons" *Appl. Phys. Lett.* **2007**, *91*, 092109.

(412) Xia, J.; Chen, F.; Li, J.; Tao, N. "Measurement of the quantum capacitance of graphene" *Nat. Nanotechnol.* **2009**, *4*, 505–509.

(413) Dröscher, S.; Roulleau, P.; Molitor, F.; Studerus, P.; Stampfer, C.; Ensslin, K.; Ihn, T. "Quantum capacitance and density of states of graphene" *Appl. Phys. Lett.* **2010**, *96*, 152104.

(414) Martinez-Gordillo, R.; Roche, S.; Ortmann, F.; Pruneda, M. "Transport fingerprints at graphene superlattice Dirac points induced by a boron nitride substrate" *Phys. Rev. B* **2014**, *89*, 161401(R).

(415) Chen, Y. C.; Zhao, C. C.; Huang, F.; Zhan, R. Z.; Deng, S. Z.; Xu, N. S.; Chen, J. "In Situ Characterization of the Local Work Function along Individual Free Standing Nanowire by Electrostatic Deflection" *Sci. Rep.* **2016**, *6*, 21270.

(416) Dial, O. E.; Ashoori, R. C.; Pfeiffer, L. N.; West, K. W. "High-resolution spectroscopy of two-dimensional electron systems" *Nature* **2007**, *448*, 176–179.

(417) Landau, L. "On the theory of transfer of energy at collisions I" *Phys. Z. Sowjetunion* **1932**, *1*, 88.

(418) Landau, L. "On the theory of transfer of energy at collisions II" *Phys. Z. Sowjetunion* **1932**, *2*, 46.

(419) Zener, C. "Non-Adiabatic Crossing of Energy Levels" *Proc. R. Soc. London, Ser. A* **1932**, *137*, 696–702.

(420) Stückelberg, E. C. G. "Theorie der unelastischen Stösse zwischen Atomen" *Helv. Phys. Acta* **1932**, *5*, 369–422.

(421) Majorana, E. "Atomi orientati in campo magnetico variabile" *Il Nuovo Cimento (1924-1942)* **1932**, *9*, 43–50.

(422) Kayanuma, Y. "Phase coherence and nonadiabatic transition at a level crossing in a periodically driven two-level system" *Phys. Rev. B* **1993**, *47*, 9940–9943.

(423) Oliver, W. D.; Yu, Y.; Lee, J. C.; Berggren, K. K.; Levitov, L. S.; Orlando, T. P. "Mach-Zehnder interferometry in a strongly driven superconducting qubit" *Science* **2005**, *310*, 1653–1657.

(424) Teichmann, K.; Wenderoth, M.; Loth, S.; Ulbrich, R. G.; Garleff, J. K.; Wijnheijmer, A. P.; Koenraad, P. M. "Controlled charge switching on a single donor with a scanning tunneling microscope" *Phys. Rev. Lett.* **2008**, *101*, 076103.

(425) Li, S.-Y.; Bai, K.-K.; Yin, L.-J.; Qiao, J.-B.; Wang, W.-X.; He, L. "Observation of unconventional splitting of Landau levels in strained graphene" *Phys. Rev. B* **2015**, *92*, 245302.

(426) Wang, W.-X.; Yin, L.-J.; Qiao, J.-B.; Cai, T.; Li, S.-Y.; Dou, R.-F.; Nie, J.-C.; Wu, X.; He, L. "Atomic resolution imaging of the two-component Dirac-Landau levels in a gapped graphene monolayer" *Phys. Rev. B* **2015**, *92*, 165420.

(427) Altimiras, C.; le Sueur, H.; Gennser, U.; Cavanna, A.; Mailly, D.; Pierre, F. "Non-equilibrium edge-channel spectroscopy in the integer quantum Hall regime" *Nat. Phys.* **2010**, *6*, 34–39.

(428) Choi, H. K.; Sivan, I.; Rosenblatt, A.; Heiblum, M.; Umansky, V.; Mahalu, D. "Robust electron pairing in the integer quantum hall effect regime" *Nat. Commun.* **2015**, *6*, 7435.

(429) Sabo, R.; Gurman, I.; Rosenblatt, A.; Lafont, F.; Banitt, D.; Park, J.; Heiblum, M.; Gefen, Y.; Umansky, V.; Mahalu, D. "A New Paradigm for Edge Reconstruction in Fractional Quantum Hall States" *ArXiv e-prints* **2016**, arXiv:1603.06908.

(430) Handschin, C.; Fülöp, B.; Makk, P.; Blanter, S.; Weiss, M.; Watanabe, K.; Taniguchi, T.; Csonka, S.; Schönenberger, C. "Point contacts in encapsulated graphene" *Appl. Phys. Lett.* **2015**, *107*, 183108.

(431) Liao, Y.; Tu, K.; Han, X.; Hu, L.; Connell, J. W.; Chen, Z.; Lin, Y. "Oxidative Etching of Hexagonal Boron Nitride Toward Nanosheets with Defined Edges and Holes" *Sci. Rep.* **2015**, *5*, 14510.

(432) Wang, J. I. J.; Yang, Y.; Chen, Y.-A.; Watanabe, K.; Taniguchi, T.; Churchill, H. O. H.; Jarillo-Herrero, P. "Electronic Transport of Encapsulated Graphene and WSe2 Devices Fabricated by Pick-up of Prepatterned hBN" *Nano Lett.* **2015**, *15*, 1898–1903.

(433) Day, H. C.; Allee, D. R. "Selective Area Oxidation of Silicon with a Scanning Force Microscope" *Appl. Phys. Lett.* **1993**, *62*, 2691–2693.

(434) Snow, E. S.; Campbell, P. M. "Fabrication of Si Nanostructures with an Atomic-Force Microscope" *Appl. Phys. Lett.* **1994**, *64*, 1932–1934.

(435) Campbell, P. M.; Snow, E. S.; McMarr, P. J. "Fabrication of nanometer-scale side-gated silicon field effect transistors with an atomic force microscope" *Appl. Phys. Lett.* **1995**, *66*, 1388–1390.

(436) Held, R.; Heinzel, T.; Studerus, P.; Ensslin, K.; Holland, M. "Semiconductor quantum point contact fabricated by lithography with an atomic force microscope" *Appl. Phys. Lett.* **1997**, *71*, 2689–2691.

(437) Lüscher, S.; Heinzel, T.; Ensslin, K.; Wegscheider, W.; Bichler, M. "Signatures of Spin Pairing in Chaotic Quantum Dots" *Phys. Rev. Lett.* **2001**, *86*, 2118–2121.

(438) Heinzel, T.; Held, R.; Lüscher, S.; Ensslin, K.; Wegscheider, W.; Bichler, M. "Electronic properties of nanostructures defined in Ga[Al]As heterostructures by local oxidation" *Phys. E (Amsterdam, Neth.)* **2001**, *9*, 84–93.

(439) Kim, D.-H.; Koo, J.-Y.; Kim, J.-J. "Cutting of multiwalled carbon nanotubes by a negative voltage tip of an atomic force microscope: A possible mechanism" *Phys. Rev. B* **2003**, *68*, 113406.

(440) Dagata, J. A.; Schneir, J.; Harary, H. H.; Evans, C. J.; Postek, M. T.; Bennett, J. "Modification of hydrogen-passivated silicon by a scanning tunneling microscope operating in air" *Appl. Phys. Lett.* **1990**, *56*, 2001–2003.

(441) Kellner, J. *Strukturierung von Graphen mittels AFM*, BSc Thesis, 2010.

(442) Nent, A. *Herstellung von Nanostrukturen mittels anodischer Oxidation*, BSc Thesis, 2011.

(443) Van Bebber, J. *Schneiden von Graphenflocken mittels AFM*, BSc Thesis, 2011.

(444) Jung, L. *Systematische Untersuchung von mittels AFM hergestellten Schnitten in Graphen*, BSc Thesis, 2011.

(445) Hecking, T. *Nanostrukturierung von Graphen mittels anodischer Oxidation*, BSc Thesis, 2012.

(446) Jekat, F. *Lokale Anodische Oxidation von Graphen und deren Raman-Untersuchung*, BSc Thesis, 2013.

(447) Zijlstra, D. *Herstellung von Graphen-Nanostrukturen mittels lokaler anodischer Oxidation*, BSc Thesis, 2013.

(448) Shedd, G. M.; Russell, P. "The scanning tunneling microscope as a tool for nanofabrication" *Nanotechnology* **1990**, *1*, 67–80.

(449) Tseng, A. A.; Notargiacomo, A.; Chen, T. P. "Nanofabrication by scanning probe microscope lithography: A review" *J. Vac. Sci. Technol. B* **2005**, *23*, 877–894.

(450) Xie, X. N.; Chung, H. J.; Sow, C. H.; Wee, A. T. S. "Nanoscale materials patterning and engineering by atomic force microscopy nanolithography" *Mat. Sci. Eng. R* **2006**, *54*, 1–48.

(451) Kurra, N.; Reifenberger, R. G.; Kulkarni, G. U. "Nanocarbon-Scanning Probe Microscopy Synergy: Fundamental Aspects to Nanoscale Devices" *ACS Appl. Mater. Inter.* **2014**, *6*, 6147–6163.

(452) Weeks, B. L.; Vaughn, M. W.; DeYoreo, J. J. "Direct imaging of meniscus formation in atomic force microscopy using environmental scanning electron microscopy" *Langmuir* **2005**, *21*, 8096–8098.

(453) Wastl, D. S.; Weymouth, A. J.; Giessibl, F. J. "Optimizing atomic resolution of force microscopy in ambient conditions" *Phys. Rev. B* **2013**, *87*, 245415.

(454) Stiévenard, D.; Fontaine, P. A.; Dubois, E. "Nanooxidation using a scanning probe microscope: An analytical model based on field induced oxidation" *Appl. Phys. Lett.* **1997**, *70*, 3272–3274.

(455) Kinser, C. R.; Schmitz, M. J.; Hersam, M. C. "Kinetics and mechanism of atomic force microscope local oxidation on hydrogen-passivated silicon in inert organic solvents" *Adv. Mater.* **2006**, *18*, 1377–1380.

(456) Neubeck, S.; Freitag, F.; Yang, R.; Novoselov, K. S. "Scanning probe lithography on graphene" *Phys. Status Solidi B* **2010**, *247*, 2904–2908.

(457) Arai, M.; Masubuchi, S.; Nose, K.; Mitsuda, Y.; Machida, T. "Fabrication of 10-nm-scale nanoconstrictions in graphene using atomic force microscopy-based local anodic oxidation lithography" *Jpn. J. Appl. Phys.* **2015**, *54*, 04DJ06.

(458) Weng, L.; Zhang, L.; Chen, Y. P.; Rokhinson, L. P. "Atomic force microscope local oxidation nanolithography of graphene" *Appl. Phys. Lett.* **2008**, *93*, 093107.

(459) Masubuchi, S.; Ono, M.; Yoshida, K.; Hirakawa, K.; Machida, T. "Fabrication of graphene nanoribbon by local anodic oxidation lithography using atomic force microscope" *Appl. Phys. Lett.* **2009**, *94*, 082107.

(460) Ko, S.; Lee, S. j.; Son, M.; Ahn, D.; Lee, S.-W. "Investigation of humidity-dependent size control of local anodic oxidation on graphene by using atomic force microscopy" *Journal of the Korean Physical Society* **2015**, *66*, 617–620.

(461) Masubuchi, S.; Arai, M.; Machida, T. "Atomic Force Microscopy Based Tunable Local Anodic Oxidation of Graphene" *Nano Lett.* **2011**, *11*, 4542–4546.

(462) Byun, I.-S.; Yoon, D.; Choi, J. S.; Hwang, I.; Lee, D. H.; Lee, M. J.; Kawai, T.; Son, Y.-W.; Jia, Q.; Cheong, H.; Park, B. H. "Nanoscale Lithography on Monolayer Graphene Using Hydrogenation and Oxidation" *ACS Nano* **2011**, *5*, 6417–6424.

(463) Neubeck, S. *Scanning probe investigations on graphene*, Ph. D. Thesis, 2010.

(464) Park, J.; Kim, K. B.; Park, J. Y.; Choi, T.; Seo, Y. "Graphite patterning in a controlled gas environment" *Nanotechnology* **2011**, *22*, 335304.

(465) Yong, H.; Kim, K.; Choi, W.; Park, J.; Ahmad, M.; Seo, Y. "The production of a cellular graphene array by scanning probe lithography and its ability to store electrical charge" *Carbon* **2012**, *50*, 4640–4647.

(466) Wei, Z.; Wang, D.; Kim, S.; Kim, S.-Y.; Hu, Y.; Yakes, M. K.; Laracuente, A. R.; Dai, Z.; Marder, S. R.; Berger, C.; King, W. P.; de Heer, W. A.; Sheehan, P. E.; Riedo, E. "Nanoscale Tunable Reduction of Graphene Oxide for Graphene Electronics" *Science* **2010**, *328*, 1373–1376.

(467) Zhang, K.; Fu, Q.; Pan, N.; Yu, X.; Liu, J.; Luo, Y.; Wang, X.; Yang, J.; Hou, J. "Direct writing of electronic devices on graphene oxide by catalytic scanning probe lithography" *Nat. Commun.* **2012**, *3*, 1194.

(468) Brintlinger, T.; Chen, Y.-F.; Dürkop, T.; Cobas, E.; Fuhrer, M. S.; Barry, J. D.; Melngailis, J. "Rapid imaging of nanotubes on insulating substrates" *Appl. Phys. Lett.* **2002**, *81*, 2454–2456.

(469) Ehrenberg, W.; Siday, R. E. "The Refractive Index in Electron Optics and the Principles of Dynamics" *Proc. Phys. Soc. London, Sect. B* **1949**, *62*, 8–22.

(470) Aharonov, Y.; Bohm, D. "Further Considerations on Electromagnetic Potentials in the Quantum Theory" *Phys. Rev.* **1961**, *123*, 1511–1524.

(471) Webb, R. A.; Washburn, S.; Umbach, C. P.; Laibowitz, R. B. "Observation of H/E Aharonov-Bohm Oscillations in Normal-Metal Rings" *Phys. Rev. Lett.* **1985**, *54*, 2696–2699.

(472) Recher, P.; Trauzettel, B.; Rycerz, A.; Blanter, Y. M.; Beenakker, C. W. J.; Morpurgo, A. F. "Aharonov-Bohm effect and broken valley degeneracy in graphene rings" *Phys. Rev. B* **2007**, *76*, 235404.

(473) Zarenia, M.; Pereira, J. M.; Peeters, F. M.; Farias, G. A. "Electrostatically Confined Quantum Rings in Bilayer Graphene" *Nano Lett.* **2009**, *9*, 4088–4092.

(474) Zarenia, M.; Pereira, J. M.; Chaves, A.; Peeters, F. M.; Farias, G. A. "Simplified model for the energy levels of quantum rings in single layer and bilayer graphene" *Phys. Rev. B* **2010**, *81*, 045431.

(475) Zarenia, M.; Pereira, J. M.; Chaves, A.; Peeters, F. M.; Farias, G. A. "Erratum: Simplified model for the energy levels of quantum rings in single layer and bilayer graphene [Phys. Rev. B **81** , 045431 (2010)]" *Phys. Rev. B* **2010**, *82*, 119906.

(476) Timp, G.; Chang, A. M.; Cunningham, J. E.; Chang, T. Y.; Mankiewich, P.; Behringer, R.; Howard, R. E. "Observation of the Aharonov-Bohm Effect for Omega-C-Tau Greater Than 1" *Phys. Rev. Lett.* **1987**, *58*, 2814–2817.

(477) Ishibashi, K.; Takagaki, Y.; Gamo, K.; Namba, S.; Ishida, S.; Murase, K.; Aoyagi, Y.; Kawabe, M. "Observation of Aharonov-Bohm Magnetoresistance Oscillations in Selectively Doped Gaas-Algaas Submicron Structures" *Solid State Commun.* **1987**, *64*, 573–576.

(478) Ford, C. J. B.; Thornton, T. J.; Newbury, R.; Pepper, M.; Ahmed, H.; Foxon, C. T.; Harris, J. J.; Roberts, C. "The Aharonov-Bohm Effect in Electrostatically Defined Heterojunction Rings" *J. Phys. C Solid State* **1988**, *21*, L325–L331.

(479) Schelter, J.; Recher, P.; Trauzettel, B. "The Aharonov-Bohm effect in graphene rings" *Solid State Commun.* **2012**, *152*, 1411–1419.

(480) Russo, S.; Oostinga, J. B.; Wehenkel, D.; Heersche, H. B.; Sobhani, S. S.; Vandersypen, L. M. K.; Morpurgo, A. F. "Observation of Aharonov-Bohm conductance oscillations in a graphene ring" *Phys. Rev. B* **2008**, *77*, 085413.

(481) Huefner, M.; Molitor, F.; Jacobsen, A.; Pioda, A.; Stampfer, C.; Ensslin, K.; Ihn, T. "Investigation of the Aharonov-Bohm effect in a gated graphene ring" *Phys. Status Solidi B* **2009**, *246*, 2756–2759.

(482) Huefner, M.; Molitor, F.; Jacobsen, A.; Pioda, A.; Stampfer, C.; Ensslin, K.; Ihn, T. "The Aharonov-Bohm effect in a side-gated graphene ring" *New J. Phys.* **2010**, *12*, 043054.

(483) Yoo, J. S.; Park, Y. W.; Skakalova, V.; Roth, S. "Shubnikov-de Haas and Aharonov Bohm effects in a graphene nanoring structure" *Appl. Phys. Lett.* **2010**, *96*, 143112.

(484) Smirnov, D.; Schmidt, H.; Haug, R. J. "Aharonov-Bohm effect in an electron-hole graphene ring system" *Appl. Phys. Lett.* **2012**, *100*, 203114.

(485) Nam, Y.; Yoo, J. S.; Park, Y. W.; Lindvall, N.; Bauch, T.; Yurgens, A. "The Aharonov-Bohm effect in graphene rings with metal mirrors" *Carbon* **2012**, *50*, 5562–5568.

(486) Rahman, A.; Guikema, J. W.; Lee, S. H.; Markovic, N. "Transmission of phase information between electrons and holes in graphene" *Phys. Rev. B* **2013**, *87*, 081401.

(487) Shen, T.; Wu, Y. Q.; Capano, M. A.; Rokhinson, L. P.; Engel, L. W.; Ye, P. D. "Magnetoconductance oscillations in graphene antidot arrays" *Appl. Phys. Lett.* **2008**, *93*, 122102.

(488) Shaw, R. W.; Mapother, D. E.; Hopkins, D. C. "Critical Fields of Superconducting Tin, Indium, and Tantalum" *Phys. Rev.* **1960**, *120*, 88–91.

(489) Altshuler, B. L.; Khmelnitskii, D. E. "Fluctuation Properties of Small Conductors" *Jetp Lett.* **1985**, *42*, 359–363.

(490) Lee, P. A.; Stone, A. D.; Fukuyama, H. "Universal conductance fluctuations in metals: Effects of finite temperature, interactions, and magnetic field" *Phys. Rev. B* **1987**, *35*, 1039–1070.

(491) Kechedzhi, K.; Kashuba, O.; Fal'ko, V. I. "Quantum kinetic equation and universal conductance fluctuations in graphene" *Phys. Rev. B* **2008**, *77*, 193403.

(492) Kechedzhi, K.; Horsell, D. W.; Tikhonenko, F. V.; Savchenko, A. K.; Gorbachev, R. V.; Lerner, I. V.; Fal'ko, V. I. "Quantum Transport Thermometry for Electrons in Graphene" *Phys. Rev. Lett.* **2009**, *102*, 066801.

(493) Güttinger, J. *Graphene Quantum Dots*, Ph. D. Thesis, 2011.

(494) Ihn, T., *Electronic Quantum Transport in Mesoscopic Semiconductor Structures*; Springer Tracts Mod. Phys. Vol. 192; Springer: 2004.

(495) Stampfer, C.; Schurtenberger, E.; Molitor, F.; Güttinger, J.; Ihn, T.; Ensslin, K. "Tunable graphene single electron transistor" *Nano Lett.* **2008**, *8*, 2378–2383.

(496) Stampfer, C.; Güttinger, J.; Molitor, F.; Graf, D.; Ihn, T.; Ensslin, K. "Tunable Coulomb blockade in nanostructured graphene" *Appl. Phys. Lett.* **2008**, *92*, 012102.

(497) Molitor, F.; Jacobsen, A.; Stampfer, C.; Güttinger, J.; Ihn, T.; Ensslin, K. "Transport gap in side-gated graphene constrictions" *Phys. Rev. B* **2009**, *79*, 075426.

(498) Ponomarenko, L. A.; Schedin, F.; Katsnelson, M. I.; Yang, R.; Hill, E. W.; Novoselov, K. S.; Geim, A. K. "Chaotic dirac billiard in graphene quantum dots" *Science* **2008**, *320*, 356–358.

(499) Byon, H. R.; Choi, H. C. "Carbon nanotube guided formation of silicon oxide nanotrenches" *Nat. Nanotechnol.* **2007**, *2*, 162–166.

(500) Nemes-Incze, P.; Magda, G.; Kamaras, K.; Biro, L. P. "Crystallographically selective nanopatterning of graphene on SiO2" *Nano Res.* **2010**, *3*, 110–116.

(501) Krauss, B.; Nemes-Incze, P.; Skakalova, V.; Biro, L. P.; Klitzing, K.; Smet, J. H. "Raman scattering at pure graphene zigzag edges" *Nano Lett.* **2010**, *10*, 4544–4548.

(502) Biro, L. P.; Nemes-Incze, P.; Lambin, P. "Graphene: nanoscale processing and recent applications" *Nanoscale* **2012**, *4*, 1824–39.

(503) Dobrik, G.; Tapaszto, L.; Biro, L. P. "Selective etching of armchair edges in graphite" *Carbon* **2013**, *56*, 332–338.

(504) Oberhuber, F.; Blien, S.; Heydrich, S.; Yaghobian, F.; Korn, T.; Schuller, C.; Strunk, C.; Weiss, D.; Eroms, J. "Weak localization and Raman study of anisotropically etched graphene antidots" *Appl. Phys. Lett.* **2013**, *103*, 143111.

(505) Kaufmann, B. *Strukturierung von Graphen durch Oxidation*, Diploma Thesis, 2014.

(506) Son, Y. W.; Cohen, M. L.; Louie, S. G. "Half-metallic graphene nanoribbons" *Nature* **2006**, *444*, 347–349.

(507) Son, Y. W.; Cohen, M. L.; Louie, S. G. "Energy gaps in graphene nanoribbons" *Phys. Rev. Lett.* **2006**, *97*, 216803.

(508) Wang, Z. F.; Li, Q.; Zheng, H.; Ren, H.; Su, H.; Shi, Q. W.; Chen, J. "Tuning the electronic structure of graphene nanoribbons through chemical edge modification: A theoretical study" *Phys. Rev. B* **2007**, *75*, 113406.

(509) Wassmann, T.; Seitsonen, A. P.; Saitta, A. M.; Lazzeri, M.; Mauri, F. "Structure, Stability, Edge States, and Aromaticity of Graphene Ribbons" *Phys. Rev. Lett.* **2008**, *101*, 096402.

(510) Cervantes-Sodi, F.; Csányi, G.; Piscanec, S.; Ferrari, A. C. "Edge-functionalized and substitutionally doped graphene nanoribbons: Electronic and spin properties" *Phys. Rev. B* **2008**, *77*, 165427.

(511) Grob, M. *Implementing vertical resolution and in-situ manipulation of samples within a scanning electron microscope: The Nanofinger ®*, Ph. D. Thesis, 2016.